

# **STOCHASTIC MOLECULAR DYNAMICS IN PICOSECONDS TIME SCALE: NEUTRON SCATTERING AND MOLECULAR DYNAMICS SIMULATION STUDIES**

*By*

**VEERENDRA KUMAR SHARMA**

**(PHYS01201004017)**

Bhabha Atomic Research Centre, Mumbai

*A thesis submitted to the*

*Board of Studies in Physical Sciences*

*In partial fulfillment of requirements*

*For the Degree of*

**DOCTOR OF PHILOSOPHY**

*of*

**HOMI BHABHA NATIONAL INSTITUTE**



**May, 2013**

# Homi Bhabha National Institute

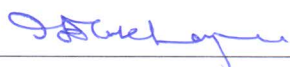
## Recommendations of the Viva Voce Board

As members of the Viva Voce Board, we certify that we have read the dissertation prepared by **Veerendra Kumar Sharma** entitled "*Stochastic Molecular Dynamics in Picoseconds Time Scale: Neutron Scattering and Molecular Dynamics Simulation Studies*" and recommend that it may be accepted as fulfilling the dissertation requirement for the Degree of Doctor of Philosophy.



Date: 19/10/13

Chairman- **Prof. S. L. Chaplot**



Date: 19/10/13

Guide / Convener- **Prof. R. Mukhopadhyay**

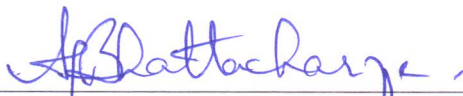
Date: 19/10/13

Member 1- **Prof. A. K. Arora**



Date: 19/10/13

Member 2- **Prof. A. K. Tyagi**



Date: 19/10/13

External Examiner- **Prof. Aninda J. Bhattacharyya**

Final approval and acceptance of this dissertation is contingent upon the candidate's submission of the final copies of the dissertation to HBNI.

I hereby certify that I have read this dissertation prepared under my direction and recommend that it may be accepted as fulfilling the dissertation requirement.

Date: 19<sup>th</sup> October 2013

Place: Mumbai

 19/10/2013  
R. Mukhopadhyay

(Guide)

## **STATEMENT BY AUTHOR**

This dissertation has been submitted in partial fulfillment of requirements for an advanced degree at Homi Bhabha National Institute (HBNI) and is deposited in the Library to be made available to borrowers under rules of the HBNI.

Brief quotations from this dissertation are allowable without special permission, provided that accurate acknowledgement of source is made. Requests for permission for extended quotation from or reproduction of this manuscript in whole or in part may be granted by the Competent Authority of HBNI when in his or her judgment the proposed use of the material is in the interests of scholarship. In all other instances, however, permission must be obtained from the author.

**Veerendra Kumar Sharma**

# **DECLARATION**

I, hereby declare that the investigation presented in the thesis has been carried out by me.

The work is original and has not been submitted earlier as a whole or in part for a degree / diploma at this or any other Institution / University.

**Veerendra Kumar Sharma**

**DEDICATED  
TO  
MY PARENTS**

# ACKNOWLEDGEMENTS

First and foremost, I would like to express my deep and sincere gratitude to my supervisor Prof. R. Mukhopadhyay, for his invaluable guidance, constant encouragement, unstinted inspiration, keen interest and good wishes. His perpetual energy and enthusiasm constantly motivated me. His wide knowledge and his logical way of thinking on critical scientific problems have been of great value for me. I am also grateful to him for being patient while critically reviewing this thesis.

This thesis would not have been possible without the guidance, help, support, critical analysis and valuable suggestions from Dr. S. Mitra who has been truly invaluable to me both on an academic and a personal level, for which I am extremely grateful. I am also thankful to him for sharing his excellent knowledge and scientific understanding with me.

It gives me immense pleasure to thank Prof. S. L. Chaplot, Head, SSPD, BARC, for continuous encouragement and never ending support since my joining this department. I would also like to express my gratitude to the members of doctoral committee; Prof. S. L. Chaplot, Prof. A. K. Arora and Prof. A. K. Tyagi for their input, valuable discussions and accessibility.

I would like to gratefully acknowledge and thank my all collaborators for their cooperation, support and many fruitful scientific discussions. I also gratefully acknowledge the help rendered by all the members of SSPD, BARC.

And last but not the least, I would like to thank all my family members specially my brothers, Vimal and Ajay for being supportive in my effort and extending encouragement. I would like to express special thanks to my wife, Neha for her encouragement and patience during the writing of this thesis. I express my sincere thanks to all my friends for their numerous help, support and enjoyable company for making the life pleasant.

# CONTENTS

	Page No.
<b>Synopsis</b> .....	i
<b>List of Figures</b> .....	xv
<b>List of Tables</b> .....	xxix
<b>Chapter 1: Introduction</b> .....	1
1.1. Theoretical Formalism of Quasielastic Neutron Scattering.....	4
1.1.1. Scattering Length and Cross-Section.....	4
1.1.2. Neutron Scattering Function.....	6
1.1.3. Different Types of Motions and Contributions to the Scattering Law...	10
1.1.4. Translational Motion.....	14
1.1.4.1. Brownian Diffusion (Continuous Diffusion) Model.....	14
1.1.4.2. Jump Diffusion Model.....	16
1.1.4.3. Localized Translational Diffusion.....	19
1.1.5. Rotational Motion.....	22
1.1.5.1. Isotropic Rotational Diffusion on a Surface of a Sphere.....	22
1.1.5.2. Continuous Rotational Diffusion on a Circle.....	23
1.1.5.3. Jump Rotation Among $N$ Equivalent Sites on a Circle.....	24
1.2. Instruments and Methods for Quasielastic Neutron Scattering.....	25
1.2.1. Triple Axis Spectrometer.....	26
1.2.2. MARX spectrometer.....	28
1.2.3. IN5 Spectrometer.....	29
1.2.4. FOCUS Spectrometer.....	31
1.2.5. IRIS Spectrometer.....	32

1.2.6. Data Analysis-General Aspects.....	34
1.3. Molecular Dynamics Simulation.....	37
1.3.1. Building Model.....	39
1.3.2. Evaluation of forces or potential energy.....	39
1.3.3. Boundary conditions.....	41
1.3.4. Integration algorithms.....	42
1.3.4.1. The Verlet algorithm.....	42
1.3.4.2. Gear predictor-corrector algorithm.....	45
1.4. Time correlation functions.....	45
1.4.1 Velocity auto correlation functions .....	46
1.4.2 Mean-Square Displacement.....	47
1.4.3 Intermediate Scattering Function.....	48
1.5. Overview of the thesis.....	49
<b>Chapter 2: Dynamical Motions in Anionic Sodium Dodecyl Sulfate Based</b>	
<b>Micelles .....</b>	<b>51</b>
2.1. Introduction .....	51
2.2. Experimental Details.....	54
2.3. MD Simulation Details.....	56
2.4. Results and Discussion.....	57
2.4.1. Results From Data Obtained Using IRIS Spectrometer.....	59
2.4.2. Results from Data obtained using Dynamic Light Scattering.....	68
2.4.3. Results from MD Simulation.....	71
2.4.4. Results from Data obtained using IN5 spectrometer.....	81
2.5. Conclusions.....	83
<b>Chapter 3: Molecular Mobility in Solid Sodium Dodecyl Sulfate.....</b>	<b>85</b>



3.1. Introduction .....	85
3.2. Experimental Details .....	86
3.3. Results and Discussion.....	87
3.4. Conclusions.....	102
<b>Chapter 4: Dynamical Landscape in CTAB Micelles.....</b>	<b>104</b>
4.1 Introduction.....	104
4.2. Experimental Details .....	105
4.3. Results and Discussion.....	106
4.3.1. Results From Data Obtained Using IRIS Spectrometer.....	106
4.3.1.1. Global Motion.....	109
4.3.1.2. Segmental Motion.....	111
4.3.2. Results From Data Obtained Using FOCUS Spectrometer.....	117
4.4. Conclusions.....	124
<b>Chapter 5: Effect of Molecular Architecture on the Dynamics of the Ionic Micelles .....</b>	<b>125</b>
5.1. Introduction .....	125
5.2. Experimental Details.....	128
5.3. Results and Discussion.....	129
5.3.1. Effect of Chain Length on the Dynamics of Cationic CnTAB Micelles	129
5.3.2. Effect of Phenyl ring on the Dynamics of Anionic Micelles.....	142
5.4. Conclusions.....	149
<b>Chapter 6: Dynamics of Water in Restricted Geometries: Polyamide Membranes, Prussian Blue and its Analogues.....</b>	<b>151</b>
6.1. Introduction .....	151
6.2. Dynamics of Water in Nanoporous Polyamide Membranes .....	152

6.2.1. Experimental Details .....	155
6.2.2. Results and Discussions .....	156
6.2.2.1. SEM and PALS Studies.....	156
6.2.2.2. QENS Results.....	159
6.3. Dynamics of Water in Prussian Blue and Its Analogues.....	169
6.3.1. Experimental Details.....	172
6.3.2 Results and Discussion.....	173
6.4. Conclusions.....	188
<b>Chapter 7: Dynamics of Adsorbed Molecules in Nanoporous Zeolitic Framework.....</b>	<b>191</b>
7.1. Introduction.....	191
7.2. Experimental Details.....	194
7.3. MD Simulation Details.....	194
7.4. Results and Discussion.....	196
7.4.1 Dynamics of Propylene in ZSM5 Zeolite.....	196
7.4.2. Dynamics of Ethylene Glycol (EG) in ZSM5 Zeolite.....	217
7.5. Conclusions.....	222
<b>Chapter 8: Summary and Future Direction.....</b>	<b>225</b>
8.1. Summary.....	225
8.2. Future Direction.....	230
<b>References.....</b>	<b>233</b>
<b>List of Publications.....</b>	<b>246</b>

# SYNOPSIS

Neutron scattering is an excellent way to study dynamics of atoms and molecules in condensed matter since energy of thermal neutron matches closely with the excitations [1]. Dynamics reflect the intermolecular or intramolecular interaction, which are the key factor for the properties of materials. In an inelastic neutron scattering experiment where a finite energy is exchanged between neutron and system, the scattered intensity is analysed as function of both energy transfer and wave vector transfer. Periodic motions (e.g., oscillating with characteristic frequency  $\omega_i$ ), give inelastic peaks at  $\omega = \pm\omega_i$  in the energy spectrum. However, thermally activated stochastic motions (diffusion, reorientation, etc.) lead to broadening of the elastic peak ( $\omega=0$ ) over and above to the instrument resolution. This broadening is known as quasielastic broadening and by examining this one can extract information about the stochastic motions occurring typically in picoseconds time scale. Thus, Quasi-elastic Neutron Scattering (QENS) technique involves the measurement of spectra centered at zero energy transfer. With advancement in instrumentation worldwide the time range that can be probed by QENS has been widened considerably. At present QENS spectrometers exist which can probe molecular dynamics on the time scales  $\sim 10^{-9}$ - $10^{-13}$  sec. Further, because of a large neutron scattering cross-section of hydrogen, QENS is especially suited to study the diffusive motion of hydrogenous molecules.

Optical spectroscopy, NMR and dielectric relaxation measurements are the other complementary experimental technique to QENS. However, scattering techniques have a significant advantage due to an additional variable, wave vector transfer  $Q$ , which provides spatial information related to the geometry of the motion. The time-scale of the dynamical motion, its geometry as well as the nature of the hindering potential can all be obtained from QENS experiments. Classical molecular dynamics (MD) simulation provides an excellent

tool to supplement the results obtained from QENS experiment due to overlap of the time and length scale it can access [2]. Thus, there is a mutual advantage in combining data from these two methods; experimental scattering data can be used as a gauge for the MD force field that is the central input for the simulation and trajectories obtained from the simulation can be used to interpret data from neutron scattering experiments providing deeper insights of the dynamical process. Further MD simulation does not suffer from the limitation of an experiment. This thesis reports study of stochastic molecular motion that exists in various complex molecular systems including self-assembled aggregates like micelles and fluids confined in restricted geometries.

Amphiphilic molecules such as surfactants and lipids undergo self-association under specific conditions to form aggregates such as micelles, vesicles, wormlike micelles, etc. Though the structure and macroscopic behavior of micelles has been studied extensively, the fast local dynamics of surfactant molecules in these assemblies and their correlation with microstructure is not investigated in detail. Hence, it is of great interest to obtain a detailed description of the internal dynamics in micelles. Local dynamics of such assemblies are important in understanding various properties such as the mechanism in releasing the solubilized drugs, micellar breaking time, etc. The dynamical processes in the micelles are very complex and the microscopic mechanisms of many of these remain poorly understood [3-10]. In general, dynamics of micellar system include multiple relaxation processes on local and global scales. The detailed dynamical landscape of anionic sodium dodecyl sulphate (SDS) micelles has been investigated by combining the results obtained from QENS experiments carried out at two different spectrometers having different energy resolutions, which enable us to cover wide range of time scales [5-7]. We have successfully modeled the internal motions of the micelles. In parallel, MD simulation has been carried out which provide further insight of the complex dynamics exists in the micelles [7]. Dynamics of

cetyltrimethylammonium bromide (CTAB) based cationic micelles has been also investigated [8]. CTAB molecule contains a head group, consisting of three methyl units unlike SDS. Therefore, head group dynamics may also contribute to the internal motion of the monomer. Four distinct relaxation processes that involve molecular motions at different time and length scale, from slow and global micellar motion to fast and local CH<sub>2</sub> group rotation are observed [8]. All of these relaxation processes reflect molecular motion in a very complex potential energy landscape with a large distribution of energy minima and energy barrier separating the energy states. Effect of molecular architecture of the surfactant (such as varying chain length [9], presence of phenyl ring [10], etc) on the dynamics of micelles is also studied and reported here.

Fluids under the constraints of spatial restrictions within a medium are called confined fluids. The behaviour of fluids in restricted geometries is mainly determined by the two-factors; spatial constraint and guest-host interaction [11]. The modification in dynamical behaviour of fluid in confined geometry compared to its bulk has considerable interest in scientific research, not only for fundamental aspects but also for practical applications in petroleum industries, catalysis, water purification and so forth. The dynamics of adsorbed species is indeed complex and depend upon a number of factors like the size and shape of the molecule, pore topology, guest-host interaction, and temperature [12-20]. Here we have investigated some of these effects on dynamics of adsorbed species. In many common situations water is found to be occupied in cavities like water in, rocks or clays, living cells, macromolecules, etc. This confined water plays a crucial role in the stability and the catalytic function of biological macromolecules. Therefore it is of interest to study the dynamical behaviour of water in confined media. Nanoporous polyamide membranes, which are widely used for water filtration, provide an opportunity to study the dynamics of water in confined media. Another example of a confining medium is that of zeolites, which are microporous

aluminosilicates with a regular pore structure. Because of their properties like high pore volume, acid strength, thermodynamic stability etc., they are very useful in industry as catalysts and molecular sieves. Since the properties of catalysis and molecular sieving depend upon diffusivity of the adsorbed molecules, a study of the dynamics of guest molecules confined in zeolitic materials is imperative to understand these properties. This thesis deals with the stochastic molecular motions in picoseconds time scale as studied using QENS and MD simulation techniques. It consists of eight chapters.

**Chapter 1** gives a brief overview of stochastic molecular motions along with details of QENS and MD simulation techniques. The theoretical formalism of quasielastic neutron scattering is discussed here. Two different features of the neutron scattering, namely, the coherent and incoherent scattering are discussed. The scattering function or scattering law is the relevant expression to be evaluated for a microscopic interpretation of the experimental data. Scattering law is separated into the coherent and incoherent parts. Contributions from various types of motion in the scattering law are discussed in detail on the basis of various dynamical models. The formalism involved in the determination of dynamical properties from the experimental data is also given here. The instruments used for the QENS studies are also described in this chapter.

As discussed earlier, neutron spectroscopy and molecular dynamics simulation are highly complementary. Trajectories obtained from MD simulation can be analyzed in details and provides information, which is not accessible in the experiments. Moreover, for complex system, dynamical processes are complex and exist in wide time scale range. In such cases molecular dynamics (MD) simulations are very useful for providing deep insight on the dynamical process. The link between the MD simulation and experimental data is established by a specific time correlation function, which is either measured directly, or indirectly in form of a Fourier spectrum. Several relevant time correlation functions are discussed here.

**Chapter 2** presents the dynamics in anionic SDS micellar system as investigated using QENS and MD simulation techniques [5-7]. Preliminary QENS experiment has been carried out on MARX spectrometer at BARC. Significant quasielastic broadening which corresponds to the localized motion within the micelles is observed for SDS micelles [5]. In order to gain further insight, QENS experiments have been carried out on high energy resolution ( $\Delta E \sim 17.5 \mu\text{eV}$ ) backscattering spectrometer, IRIS at ISIS. Data analysis clearly shows presence of two distinct motions; whole micellar motion or global diffusion and segmental motion of the SDS monomer [6]. The global diffusion associated with the whole micelle is found to be Fickian in nature and the corresponding diffusion coefficients are found to be consistent with those obtained from dynamic light scattering measurements [6]. A model in which the hydrogen atoms undergo localised translational diffusion confined within spherical volumes successfully describes segmental dynamics of the SDS molecules. This volume increases linearly along the SDS chain such that the hydrogen atoms closer to the head group move within smaller spheres with lower diffusion constant than the hydrogen atoms away from the head group. Diffusivity and the volume of the spheres are found to increase with temperature. MD simulation indicates an additional faster component, which is not expected to be observed within the energy window of IRIS spectrometer [7]. Therefore, QENS experiment was carried out using time of flight spectrometer IN5 ( $\Delta E \sim 60 \mu\text{eV}$ ) at ILL, Grenoble which provides a wider energy window. The observed data could be consistently described by taking into account the dynamics observed with IRIS and a faster dynamical component as indicated in MD simulation [7]. Therefore a detailed dynamical landscape in the SDS micellar solution has been investigated using different QENS spectrometers covering wide time scale range.

**Chapter 3** discusses molecular mobility in solid crystalline SDS as observed using high resolution QENS technique [21]. It was of interest to check whether SDS molecules in

the solid phase show any dynamical motion as observed in micelles. At ambient conditions, the crystal structure of anhydrous SDS has been found to be monoclinic with a single molecule in the asymmetric unit. While the quasielastic data showed the presence of dynamical motion at and above 210 K, the fixed energy window data indicated that the dynamics is present even at lower temperatures. The fixed energy window data showed that the dynamics evolves monotonically with increasing temperature until 360 K where a dynamical transition takes place. A similar signature is also found in the differential scanning calorimetry data. The analysis of the QENS data showed that at  $T < 360$  K, SDS molecules undergo fractional reorientational motion about the molecular axis. With increase in temperature, it is found that dynamical contribution increases, which presumably start from the tail and progresses toward head of the alkyl chain. While 11% of the molecule is found to be mobile at 210 K, at 350 K it grows to 60 % indicating a gradual melting. The same set of parameters obtained from analysis of the QENS spectra describes the elastic scan data as well. Above the dynamical transition ( $T > 360$  K), the observed dynamics found to be describable with localised translational diffusion of the hydrocarbon chain of the SDS molecule. It is interesting to note that the dynamical behaviour of SDS in the high temperature chain-melt state is very similar to that observed for the monomer dynamics in SDS micelles [6].

**Chapter 4** describes the dynamics in cationic CTAB micelles as obtained by combining the data from two different QENS spectrometers (IRIS at ISIS and FOCUS at PSI) covering wide energy transfer range which is suitable to probe motions in broad range of time scale [8]. CTAB molecule consists of a head group, consisting of three methyl units (unlike SDS) and a long alkyl chain. Therefore, apart from the dynamics of the chain, head group dynamics may also contribute to the internal motion of the monomer. IRIS data ( $\Delta E \sim 17.5$   $\mu\text{eV}$ ) show the presence of two distinct motions; global diffusion (Fickian type), and the



segmental motion of the CTAB monomers. The segmental dynamics of CTAB molecules within a micelle has been described with a model considering the motion of the head group and the hydrophobic alkyl chain separately. It is found that the data is consistent with a model in which the methyl groups in the head group undergo 3-fold jump rotations and the hydrogen atoms belonging to the alkyl chain perform localized translational diffusion. Localized translational diffusion is manifestation of the flexibility involved in the chain, where hydrogen atoms move within a spherical volume, the size of which increases linearly from the top to the bottom. This linear description fits the data well. Diffusivity also follows the same architecture. QENS data at FOCUS ( $\Delta E \sim 55 \mu\text{eV}$ ) indicate an additional faster dynamical component over and above that observed with IRIS. Data analysis shows that this faster component may ascribe to torsional isomerisation of some of the  $\text{CH}_2$  groups in the hydrocarbon chain. Four distinct relaxation processes in CTAB micelles that involve molecular motions at different time and length scales are observed [8]. Therefore, a comprehensive description of the complex dynamics exists in CTAB micelle has been provided.

**Chapter 5** presents the effect of molecular architecture on the dynamics of the ionic micelles [9,10]. Molecular architecture of the surfactant is one of the parameters that control the structural arrangement in a micellar system. While there are reports on many such studies to understand the structural details [22,23], effect towards dynamical behaviour is not known. We have studied the effect of different chain length on the dynamical behaviour of alkyl trimethylammonium bromide ( $\text{C}_n\text{TAB}$ ) micelles ( $n=10, 12, 14$  and  $16$ ) by QENS technique [9]. The data analysis clearly shows that with increasing chain length, dynamics of  $\text{C}_n\text{TAB}$  monomer is greatly affected; within the localized translational diffusion model the diffusion is found to be reduced and occurs in smaller spheres, and also the residence times increased. Global motion is also found to be hindered with increased chain length. Results are explained

on the basis of enhancement of counterions condensation with the increase of the chain length. Other aspect of variation in the molecular architecture is presence of phenyl ring near to the head group of a surfactant. Two surfactants namely, sodium dodecyl benzene sulfonate (SDBS) and SDS have been chosen for this purpose. It is found that due to phenyl group, dodecyl chains in SDBS micelles are less flexible than SDS micelles [10]. Results could be understood with the fact that dodecyl chains in the SDBS micelles are more tightly packed than SDS micelles. Small angle neutron scattering experiments also showed that fractional charge of SDBS micelles is smaller vis-à-vis SDS micelles. Results of both scattering techniques are found to be consistent with each other. MD simulation results published recently also indicated similar behaviour.

**Chapter 6** describes the dynamics of water in nanoporous systems. This chapter is divided into two parts. The first part of this chapter focuses on the nanoporous polyamide membranes, which are mainly used for water filtrations. Efficiency of these membranes for filtration process depends upon their ability for water uptake. Therefore it is of interest to study the dynamical behaviour of water inside these membranes. In our study we have focused on two following polyamide membranes (i) Trimesoyl chloride -m-phenylene diamine based reverse osmosis (RO) membrane and (ii) Trimesoyl chloride - piperazine based nanofiltration (NF) membrane. Both membranes are synthesized by interfacial polymerization technique at Central Salt and Marine Chemicals Research Institute, Bhavnagar, India. Both membranes are subsequently characterized by Positron Annihilation Lifetime Spectroscopy and Scanning Electron Microscope (SEM) techniques. Positron lifetime spectroscopy shows that both membranes have pore size of  $\sim 5$  Å [12-14]. SEM pictures indicate that NF membrane has relatively smoother surface microstructure compared to RO membrane, which has relatively rough surface, showing hill–valley microstructure morphology. Dynamics of water sorbed in RO and NF membrane is studied using QENS

technique. QENS experiments have been carried out on both hydrated as well as dehydrated membranes using MARX spectrometer at BARC, Trombay [13-14] and FOCUS at PSI, Switzerland [12]. QENS data indicates that translational motion of water confined in these membranes gets modified compared to the bulk water whereas rotational motion remains unaltered. Translational motion of water in RO and NF membranes follows random jump diffusion with lower diffusivity compared to the bulk water.

The second part of this chapter is on dynamics of water in Prussian blue and its analogues molecular magnet which are represented by a general formula  $A_x[B(CN)_6]_y \cdot zH_2O$  where A and B are 3d or 4d magnetic ions [15,16]. When  $x/y=1$ , for example, in case of ferriferrocyanide,  $Fe(II)[Fe(II)(CN)_6] \cdot 4H_2O$ , the 4 water molecules are noncoordinated. But when  $x/y>1$ , some of the  $\{B(CN)_6\}$  sites remain vacant for example,  $M_3[Fe(CN)_6]_2 \cdot 14-16 H_2O$ , 33% of the building unit  $(Fe(CN)_6)$  sites remain vacant in the material framework creating spherical cavities. There exists, three structurally distinguishable water molecules: (i) coordinated water molecules which are coordinated to A octahedra at empty nitrogen site, (ii) non-coordinated water molecules connected by hydrogen bonds to the coordinated ones in the spherical cavity of  $[B(CN)_6]$  and (iii) non-coordinated water at 8c (1/4, 1/4, 1/4) interstitial site of the unit cell. It is found that one can tune physical as well as the magnetic properties of these compounds via changing the relative humidity; the interest here is to investigate the dynamical behaviour of these water molecules. Dynamical behaviour of water in Prussian blue  $(Fe(III)_4[Fe(II)(CN)_6]_3 \cdot 15H_2O)$  and its analogues,  $Fe(II)[Fe(II)(CN)_6] \cdot 4H_2O$ ,  $M_3[Fe(CN)_6]_2 \cdot 14-16 H_2O$  (with  $M=Cu$  or  $Mn$ ) have been studied using QENS technique. QENS experiments have been carried out using FOCUS spectrometer at PSI, Switzerland. Data analysis showed that dynamics of water is highly dependent on its location as well as the interaction to the surrounding environment. It is found that overall dynamics of water in  $Fe(II)[Fe(II)(CN)_6] \cdot 4H_2O$  ( $x/y=1$ ) is much localized and restricted compared to other

compounds ( $x/y > 1$ ). Activation energy for water diffusion in  $\text{Fe(II)[Fe(II)(CN)}_6\text{]} \cdot 4\text{H}_2\text{O}$  is found to be higher than other compounds ( $x/y > 1$ ). Results are found to be consistent with the thermal gravimetric measurements. A complete dynamical picture of water molecules in such systems is provided.

**Chapter 7** presents dynamics of adsorbed species (propylene [17-19], ethylene glycol [20]) in the ZSM5 zeolites. Interconnecting channel networks typify the structures of ZSM5 zeolite. Our MD simulation studies suggest that rotational motion of propylene is almost an order of magnitude faster than the translational motion. Therefore, spectrometers (MARX and TAS at BARC) having different energy resolutions were used to study the translational and rotational motion of propylene in ZSM5 zeolite [17,18]. Translational motion, being slower, was distinctly observed in a narrower window MARX spectrometer while both contribute to the wider one. Diffusion of propylene in the channels of ZSM5 zeolite was found to follow jump diffusion model. Variation of elastic incoherent structure factor suggests that rotational motion of propylene is isotropic [17,18]. However, intermediate scattering functions corresponding to the rotational motion indicate a complex and anisotropic rotational motion of the propylene molecule at short times. Orientational correlation functions indicate that propylene molecule performs librations at short times [19]. Calculated rotational density of states and dynamic structure factor further confirmed this. It is also observed that while diffusing, propylene molecules prefer an orientation in which the long molecular axis aligns along the channel. Detailed analysis reveals that preferred orientation of propylene is because of the shape of the host matrix rather than spatial restriction.

Another guest species is ethylene glycol, which can form hydrogen bond with the oxygen of the host zeolitic ZSM5 and is of interest to see the effect on the dynamical behaviour of ethylene glycol. QENS experiments have been carried out on ethylene glycol

adsorbed in ZSM5 zeolite using MARX spectrometer at BARC. Analysis of QENS data revealed that observed dynamics correspond to isotropic rotational motion of ethylene glycol [20]. Rotational diffusion coefficient of ethylene glycol adsorbed in ZSM5 zeolite is found to be slower compared to bulk ethylene glycol. Comparing the results with the other guest species, propylene, benzene in ZSM5, it is found that rotational diffusion coefficient of ethylene glycol is an order of magnitude smaller than propylene and almost comparable to benzene. In spite of the fact that ethylene glycol has lower moment of inertia and less symmetric than benzene. Therefore, main cause of hindered rotation may be the strong attractive interaction between ethylene glycol molecules and ZSM5 zeolite. This should reflect in freezing behavior of ethylene glycol /benzene confined in ZSM5 zeolite, as freezing temperature of fluids in confined media is strongly affected by the strength of forces between fluid molecules and the pore walls. Positron annihilation spectroscopy technique is used to understand the nature of guest-host interaction and the results of both QENS and positron annihilation spectroscopy are found to be consistent with each other [20].

Finally in **Chapter 8**, I conclude the thesis with a brief summary of the results along with a brief discussion on possible future work. The work reported in this thesis shows that quasielastic neutron scattering has successfully been used to study stochastic motions present in complex molecular systems including micelles and fluids in the restricted geometry. It has been also shown that how one can enrich the information obtained from QENS experiment by supplementing the results obtained from MD simulation technique. Suitable theoretical models are explored and compared to the experimental data to understand the dynamics in detail. The experimental data validated the models and the models in turn have been fruitfully used to calculate the characteristic time, diffusion constant and the geometry of motion. The specific systems studied here have technological relevance and promise potential industrial applications. Complex dynamical behaviour including various motions in different time

scales are observed for anionic as well as cationic micellar systems using different spectrometers covering wide energy transfer range. It is found that dynamics of micelles is affected by changing the molecular architecture of the surfactants. In parallel, MD simulation helps a lot to understand and visualization of the stochastic motions in complex micellar systems.

It has been shown that the diffusivity in the confined media is affected by a variety of factors including the shape and size of the guest molecules and the interaction between the confined and the confining species. It is found that dynamics of water in Prussian blue analogous compounds is found to be dependent on the location of the water molecules. The experience gained during thesis work would be useful for studying the dynamics of more complex biological systems. I, have recently taken up other issues of practical interest, which can be studied with the QENS techniques. For example, dynamics in vesicles, effect of external confinement on the dynamics of micelles, effect of location of phenyl ring on the dynamics of micelles, role of water molecules in the gelation of aluminium slurry, dynamics of water in clays, diffusion of adsorbed species in the metal organic framework etc. I have planned to carry out such studies in the future.

## Reference:

1. M. Bée, *Quasielastic Neutron Scattering*, Adam Hilger: Bristol 1988.
2. M. P. Allen and D. J. Tildesley, *Computer Simulation of Liquids*, Oxford Science Publications, Oxford 1989.
3. V. G. Sakai, C. A. Simionescu and S. H. Chen, *Dynamics of Soft Matter: Neutron Applications*, Springer: New York, 2012.
4. Y. Gerelli, V. Garcia Sakai, J. Ollivier and A. Deriuab, *Soft Matter*, **7** (2011) 3929.
5. V. K. Sharma, Gunjan Verma, S. Gautam, P. A. Hassan, S. Mitra and R. Mukhopadhyay *Z. Phys. Chem.*, **224** (2010) 253.
6. V. K. Sharma, S. Mitra, G. Verma, P. A. Hassan, V. Garcia Sakai, R. Mukhopadhyay, *J. Phys. Chem. B*, **114** (2010) 17049.
7. B. Aoun, V. K. Sharma, S. Mitra, M. Johnson and R. Mukhopadhyay (To be submitted).
8. V. K. Sharma, S. Mitra, V. Garcia Sakai, P.A. Hassan, J. Peter Embs and R. Mukhopadhyay, *Soft Matter*, **8** (2012) 7151.
9. V. K. Sharma, S. Mitra, V. Garcia Sakai and R. Mukhopadhyay, *J. Phys. Chem. B*, **116** (2012) 9007.
10. V. K. Sharma, S. Mitra, M. Johnson and R. Mukhopadhyay (To be submitted).
11. D. R. Cole, E. Mamontov, G. Rother, Chapter 19, *In Neutron Applications in Earth, Energy and Environmental Sciences; Eds. L. Liang, R. Rinaldi, H. Schober*, Springer-Verlag: Berlin, 2009.
12. V. K. Sharma, S. Mitra, Puyam Singh, Fanni Jura'ny, and R. Mukhopadhyay, *Euro. Phys. Journal ST*, **189** (2010) 217.
13. V. K. Sharma, P.S. Singh, S. Gautam, P. Maheshwari, D. Dutta and R. Mukhopadhyay, *J. Membrane Science*, **326** (2009) 667.
14. V. K. Sharma, P.S. Singh, S. Gautam, S. Mitra and R. Mukhopadhyay, *Chem. Phys. Lett.*, **478** (2009) 56.
15. V. K. Sharma, S. Mitra, Amit Kumar, S. M. Yusuf, Fanni Juranyi and R. Mukhopadhyay, *J. Phys. Cond. Mat.*, **23** (2011) 446002.
16. V. K. Sharma, S. Mitra, N. Thakur, S. M. Yusuf, Fanni Juranyi and R. Mukhopadhyay (To be submitted).
17. V.K. Sharma, S. Gautam, S. Mitra, Mala N. Rao, A. K. Tripathi, S. L. Chaplot and R. Mukhopadhyay, *J. Phys. Chem. B*, **113** (2009) 8066.
18. V. K. Sharma, S. Gautam, S. Mitra and R. Mukhopadhyay, *Z. Phys. Chem.*, **224** (2010)

133.

19. Siddharth Gautam, V. K. Sharma, S. Mitra, S. L. Chaplot and R. Mukhopadhyay, *Chem. Phys. Lett*, **501** (2011) 345.

20. V. K. Sharma, S. Mitra, P. Maheshwari, D. Dutta, P. K. Pujari, and R. Mukhopadhyay, *Euro. Phys. Journal ST*, **189**, 273 (2010).

21. S. Mitra, V. K. Sharma, V. Garcia Sakai, J. Peter Embs and R. Mukhopadhyay, *J. Phys. Chem. B*, **115** (2011) 9732.

22. S. S. Berr, *J. Phys. Chem.*, **91** (1987) 4760.

23. Swati De, V.K. Aswal and S. Ramakrishnan, *Langmuir*, **26** (2010) 17882.



# LIST OF FIGURES

		Page No.
1.1	A Schematic diagram showing the Triple Axis Spectrometer installed at Dhruva, Trombay. The lower half of the figure shows the rotation along the three axes and the vector diagram defining the wave vector transfer.	27
1.2	A Schematic diagram of the QENS spectrometer installed at Dhruva, Trombay	29
1.3	A Schematic diagram of multichopper IN5 spectrometer at Institut Laue-Langevin, France.	30
1.4	A Schematic diagram of the FOCUS instrument at SINQ, Paul Scherrer Institute, Switzerland.	31
1.5	A Schematic diagram of the IRIS instrument at ISIS facility, Rutherford Appleton laboratory, United Kingdom.	33
2.1	Schematic of an anionic SDS micellar solution	54
2.2	Observed quasielastic broadening for 10% (w/w) SDS micelles over the instrument resolution at MARX spectrometer at $Q=1.32 \text{ \AA}^{-1}$	58
2.3	Typical fitted QENS spectra for 10% (w/w) SDS micelles observed at MARX spectrometer. Solid lines are the fits. Dashed and dashed-dotted lines represent quasielastic and elastic part respectively	59
2.4	QENS spectra measured for the 20% (w/w) SDS micelles at IRIS spectrometer at different temperatures at $Q = 1.2 \text{ \AA}^{-1}$ . The instrument resolution is shown with the black dashed line. Spectra have been normalised to maximum peak intensity	60

2.5	QENS spectra from the 20% (w/w) SDS micellar solution observed at IRIS spectrometer at 300K fitted using two Lorentzian functions at some typical $Q$ values.	61
2.6	Variation of HWHM of the Lorentzian representing global motion, $\Gamma_G$ for 20% (w/w) SDS micellar solution with $Q^2$ at temperatures of 300 K, 315 K and 330 K. The lines correspond to a fit with Fick's diffusion. HWHM's of Lorentzian correspond to global motion for 10% (w/w) SDS micellar solution at 300 K is also shown by open circle.	62
2.7	Variation of EISF for 20% (w/w) SDS micellar solution with $Q$ . The solid lines represent calculated EISF for a model described in the text. EISF observed for 10% (w/w) SDS micellar solution at 300 K is also shown by open circle.	64
2.8	Schematic showing the model in which hydrogen atoms of a SDS chain moving in spheres of different radii. The radii of sphere are shown to increase linearly along the SDS chain.	65
2.9	Variation of the HWHM of the Lorentzian representing the segmental motion, for the 20% (w/w) SDS micellar solution with $Q$ . The solid lines are fits with a model in which the hydrogen atoms at the different $\text{CH}_2$ positions along the of SDS chain are moving within spheres of varying radii and with varying diffusion coefficients. HWHM of the Lorentzian correspond to segmental motion for the 10% (w/w) SDS micellar solution at 300 K is also shown by open circle	66
2.10	Electric field correlation function obtained from 20% (w/w) SDS solution at a scattering angle of $130^\circ$ . Only long time behaviour of $g^{(1)}(\tau)$ by cumulant method as shown by the solid line.	70

2.11	Variation of the mean relaxation rate ( $\Gamma_{DLS}$ ) of correlation functions with $Q^2$ for 20% (w/w) SDS solution at 300 K, as measured by DLS. The line corresponds to the fit assuming Fickian diffusion	71
2.12	Probability distributions for the distance from an atom to the centre of the mass, COM, of the SDS micelle at 300K	73
2.13	Probability distribution of (a) the angle of all SDS molecules formed between the vectors connecting C2 to C12 and C2 to center of mass of the micelles at 300 as well as 320 K (b) the end-to-end distances (S-C12) of all the SDS molecules inside the micelles.	74
2.14	Variation of mean-square displacement of center of mass of SDS micelles with time at 300 and 320 K	75
2.15	The $I^H_{inc}(Q,t)$ vs time plot at some typical $Q$ values. The solid line is that obtained by least squares fit using Eq (2.15)	77
2.16	(a) Three different components of $I^H_{inc}(Q,t)$ are obtained from the fit for a typical $Q$ at 300 K. (b) Intermediate scattering function $I^H_{inc}(Q,t)$ calculated at 300 and 320 K for a typical $Q$ value.	78
2.17	Variation of the three different decay constants, $\Gamma$ as obtained from the fits of $I^H_{inc}(Q,t)$ using Eq. (2.15) with $Q$ . Open symbols show HWHM of Lorentzian functions correspond to global, segmental and torsional motion as obtained from QENS experiment.	79
2.18	The behavior of weight factors $A(Q)$ in Eq. (2.15) corresponding to the three components of the intermediate scattering function $I^H_{inc}(Q,t)$ with $Q$ .	79

2.19	Trajectory of a H3 (hydrogen attached to 3rd carbon atom from head group) of a particular SDS molecule after filtration out of the global motion in the (a) X-Y plane and (b) X-Z plane.	80
2.20	QENS spectra recorded for 10 % (w/w) SDS micellar solution from IN5 after subtracting the contribution from the solvent at the temperature 300 K at typical $Q = 1.1 \text{ \AA}^{-1}$ and $1.6 \text{ \AA}^{-1}$ . The phenomenological fit represented by the solid line is based on Eq. (2.18) sum of three Lorentzian functions. The broadest component corresponds to the fast motion and is shown by the dash-dotted line. Other components correspond to the global and segmental motions are shown by dashed and short dashed line respectively.	82
3.1	Unit cell of anhydrous SDS.	86
3.2	Temperature dependence of elastic intensity (normalised to lowest temperature studied) for, (a) average over $Q = 0.45$ to $1.84 \text{ \AA}^{-1}$ and (b) for different $Q$ values. The inset represents a DSC scan at 5 K/min. A melting transition is evident.	88
3.3	QENS spectra observed using (a) the IRIS and (b) the FOCUS spectrometers at different temperatures at typical $Q$ values. Data shown are normalised to peak amplitude. The dashed line shows the instrument resolution.	90
3.4	Typical fitted QENS spectra as observed for anhydrous SDS powder using (a) the IRIS spectrometer at 300 K and (b) the FOCUS spectrometer at 370 K at different $Q$ values. The dashed line shows the instrument resolution in the middle panel.	91

3.5	Variation of EISF for SDS powder with $Q$ at different temperatures. Solid and empty circles represent data obtained with IRIS and FOCUS respectively. The solid lines represent calculated EISF for fractional uniaxial rotational diffusion model as described in text. Dashed-dotted line is for $T=280$ K as per calculation based on fractional uniaxial rotational model (assuming $p_x = 0.33$ & $a = 1.55$ Å).	93
3.6	Variation of fractional dynamic component ( $p_x$ ) of the chains and radius of rotation ( $a$ ) of the chain as obtained from the least squares fit of the EISF assuming uniaxial rotational model in the temperature range 210-350 K.	95
3.7	Variation of HWHM of a Lorentzian representing internal motion SDS powder with $Q$ . Solid and empty circles represent data obtained with IRIS and FOCUS respectively. Solid lines are the fits with a fractional uniaxial rotational model.	95
3.8	Variation of rotational diffusion constant ( $D_r$ ) in the temperature range 210-350 K. Arrhenius behaviour is evident.	96
3.9	Variation of EISF for SDS powder with $Q$ at 370 and 400 K. The solid lines represent calculated EISF for localised translational diffusion model as described in text.	99
3.10	Variation of HWHM of a Lorentzian representing internal motion SDS powder with $Q$ at 370 and 400 K. Solid lines are the fits with localised translational diffusion model.	100

3.11	Schematic model of the motion in solid SDS (a) below the transition temperature ( $T=360$ K) uniaxial rotation along the molecular axis is observed and (b) above $T=360$ K, localized translational diffusion in which hydrogen atoms of a SDS chain moving in spheres of different radii is observed. The radii of sphere are shown to increase linearly along the SDS chain.	101
4.1	Schematic of cationic CTAB ( $C_{16}H_{33}N^+(CH_3)_3Br^-$ ) micellar solution.	105
4.2	(a) QENS spectra from IRIS for a $\sim 10$ % (w/w) CTAB micellar solution and $D_2O$ at 300 K at $Q=1.2 \text{ \AA}^{-1}$ . The contribution from the $D_2O$ and that from the pure micelles after the $D_2O$ subtraction are also shown (b) shows the subtracted QENS spectra at different temperatures at a typical $Q$ -value. The instrument resolution is shown by black dashed line.	107
4.3	Typical fitted $S(Q, \omega)$ for 10 % (w/w) CTAB micelles at 330 K, as obtained from IRIS spectrometer, assuming model function given in Eq. (4.1).	109
4.4	Variation of half width at half maxima, $\Gamma_G$ , of the Lorentzian $L_G(\Gamma_G, \omega)$ , which accounts for global motion of micelles in solution with $Q^2$ at temperatures of 300 K, 315 K and 330 K. It appears that $\Gamma_G(Q)$ is a quadratic function of $Q$ , as expected for continuous diffusion. The solid lines correspond to a fit with Fick's law of diffusion.	110
4.5	Variation of EISF for CTAB micellar solution with $Q$ at temperatures of 300 K, 315 K and 330 K. The solid lines represent calculated EISF for a model described in the text.	115

4.6	Schematic of the proposed model for the segmental motion of the monomer in CTAB micelles. Hydrogen atoms of the alkyl chain diffuse within spheres of different sizes, radii of the spheres increase linearly from head towards tail. Hydrogen atoms belong to the methyl group existing in the head group performs 3-fold jump rotation.	115
4.7	Variation of the half width at half maxima, $\Gamma_{\text{seg}}$ , of the Lorentzian $L_{\text{seg}}(\Gamma_{\text{seg}}, \omega)$ , which accounts for segmental motion of the monomer with $Q$ at different measured temperatures. Solid lines are the fits assuming the model as described in the text.	116
4.8	QENS spectra recorded for 10 % (w/w) CTAB micelles from FOCUS at the temperature 330 K. The phenomenological fit represented by the solid line is based on Eq.(4.12) sum of three Lorentzian functions. The broadest component corresponds to the torsional motion and is shown by the dashed ( <i>dark yellow color</i> ) line. Other components correspond to the global and segmental motions are shown by short dashed ( <i>magenta color</i> ) and dash-dotted ( <i>blue color</i> ) line respectively.	120
4.9	Variation of effective EISF with $Q$ for CTAB micellar solution at 330 K. The solid lines represent the calculated EISF (Eq. 4.15) for a model described in the text.	122
4.10	Variation of the half width at half maxima, $\Gamma_{\text{tor}}$ , with $Q$ , of the Lorentzian $L_{\text{tor}}(\Gamma_{\text{tor}}, \omega)$ , corresponding to torsional motion.	122
5.1	Schematic of cationic surfactants $C_n\text{TAB}$ having different chain length and anionic SDS and SDBS molecules.	128

- 5.2 Typical QENS spectra for 0.3 M  $C_n$ TAB micellar solution, (a) for different chain lengths at typical value of  $Q = 1.2 \text{ \AA}^{-1}$ , (b) for  $C_{10}$ TAB and  $C_{16}$ TAB micelles at  $Q = 1.8 \text{ \AA}^{-1}$ , (c) for  $C_{14}$ TAB micelles at  $Q = 1.2 \text{ \AA}^{-1}$  at different temperatures. All the spectra are normalised to peak amplitude. The instrument resolution is shown by dashed line. 130
- 5.3 Typical fitted  $S_{\text{micelles}}(Q, \omega)$  for 0.3 M  $C_{14}$ TAB micelles, (a) at different temperatures at  $Q = 1.0 \text{ \AA}^{-1}$  and (b) for different  $Q$  values at  $T = 300 \text{ K}$ , assuming model function given in Eq. (5.1). 132
- 5.4 Typical fitted  $S_{\text{micelles}}(Q, \omega)$  for 0.3 M  $C_n$ TAB micellar solution at a typical value of  $Q = 1.2 \text{ \AA}^{-1}$  at 300 K, assuming model function given in Eq. (5.1). 133
- 5.5 Variation of half width at half maxima,  $\Gamma_G$ , of the Lorentzian  $L_G(\Gamma_G, \omega)$ , corresponds to the global motion of  $C_n$ TAB micelles (for  $n = 10, 12, 14$  and  $16$ ) with  $Q^2$  at 300 K. The solid lines correspond to fits with Fick's law of diffusion. 134
- 5.6 Variation of global diffusivity,  $D_G$  for different  $C_n$ TAB micelles with the alkyl chain length at 300 K. The temperature dependence of  $D_G$  for  $C_{14}$ TAB is also shown. 135
- 5.7 Variation of EISF for  $C_n$ TAB micelles ( $n = 10, 12, 14$  and  $16$ ) at 300 K. Solid lines represent calculated EISF for the model described in the text. 138
- 5.8 Variation of the HWHM,  $\Gamma_{\text{in}}$ , of the Lorentzian corresponds to segmental motion of the monomer for  $C_n$ TAB micelles with  $Q$  for different chain lengths at 300 K. 139



5.9	Comparison of QENS spectra as obtained using IN5 spectrometer at ILL for (a) 0.3 M micellar solution of SDBS and SDS at $Q=1.2 \text{ \AA}^{-1}$ at 300 K and (b) 0.3 M SDBS micellar solution at different temperatures at $Q=1.2 \text{ \AA}^{-1}$ . The instrument resolution is also shown by dashed line.	142
5.10	Typical fitted $S(Q, \omega)$ for 0.3 M SDBS micelles at 330 K, as obtained using IN5 spectrometer at ILL, assuming scattering function given in Eq. (5.6).	144
5.11	Variation of half width at half maxima, $\Gamma_G$ , corresponds to global motion, with $Q^2$ for SDBS and SDS micelles at 300 K. Inset shows the variation of $\Gamma_G$ at different temperature for SDBS micelle. The solid lines are the fits with Fick's law of diffusion.	145
5.12	Variation of EISF for SDBS and SDS micellar solution with $Q$ at 300 K. It is evident that internal dynamics of SDS micelle is more disordered than SDBS micelle at 300 K. Inset shows the EISF for SDBS micelles at different temperatures.	146
5.13	Variation of the HWHM, $\Gamma_{in}$ , which correspond to the internal motion of the monomer for SDBS micelles with $Q$ for SDS and SDBS micelle at 300 K. Inset shows the temperature dependence of $\Gamma_{in}$ for SDBS micelle. Lines show the fits using Fick's law.	148
6.1	Chemical structure of reverse osmosis (RO) polyamide membrane.	153
6.2	Chemical structure of nanofiltration (NF) polyamide membrane.	154
6.3	SEM micrograph of (a) RO and (b) NF polyamide membranes.	157

6.4	Fitted QENS spectra from the water-sorbed RO polyamide membrane using MARX spectrometer at some typical $Q$ -values. Instrument resolution is shown by dashed line in the middle panel.	159
6.5	Fitted QENS spectra from the water sorbed NF polyamide membrane using MARX spectrometer at some typical $Q$ values. Instrument resolution is shown by dashed line in the middle panel.	160
6.6	Variation of HWHM ( $\Gamma$ ), as obtained from QENS experiment on water sorbed in (a) RO and (b) NF polyamide membranes. The symbols represent experimental $\Gamma$ values while the solid line is the fit with Singwi-Sjölander model.	162
6.7	Typical measured QENS spectra for (a) water sorbed RO membrane and (b) water sorbed NF membrane using FOCUS spectrometer at a particular $Q=1.0 \text{ \AA}^{-1}$ .	164
6.8	Fitted QENS spectra for water-sorbed RO polyamide membrane using Eq. (6.5) at some typical $Q$ values.	165
6.9	Fitted QENS spectra for water-sorbed NF polyamide membrane using Eq. (6.5) at some typical $Q$ values.	166
6.10	Variation of HWHM of Lorentzian corresponds to translation motion of water in RO membrane with $Q^2$ at different temperatures. The solid line corresponds to the fit as per the random jump diffusion model.	167
6.11	Variation of HWHM of Lorentzian corresponds to translation motion of water in NF membrane with $Q^2$ at different temperatures. The solid line corresponds to the fit using Eq. (6.3) as per the random jump diffusion model.	167

- 6.12 Unit cell of (a) PBA-II ( $\text{Cu}_2\text{Mn}_2[\text{Fe}(\text{CN})_6]_{2.67} \cdot 19\text{H}_2\text{O}$ ) and (b) PBA-I ( $\text{Fe}_4(\text{II})[\text{Fe}(\text{II})(\text{CN})_6]_{4.16}\text{H}_2\text{O}$ ) and as obtained from the structural analysis [140,142]. The spherical cavity formed by coordinated water molecules in PBA-II is also indicated. The non-coordinated water molecules within the cavity as well as at octants are omitted for clarity. 171
- 6.13 Vibrational DOS for PBA-II ( $\text{Cu}_2\text{Mn}_2[\text{Fe}(\text{CN})_6]_{2.67} \cdot 19\text{H}_2\text{O}$ ) and its dehydrated form at 300 K. A peak around 8 meV in  $\text{Cu}_2\text{Mn}_2[\text{Fe}(\text{CN})_6]_{2.67} \cdot 19\text{H}_2\text{O}$  is not seen in the dehydrated sample. 174
- 6.14 Comparison of QENS spectra as obtained for PB, PBA-I and PBA-II at  $Q=1.0 \text{ \AA}^{-1}$  at 330 K. The instrument resolution as obtained from a standard vanadium sample is shown by a dashed line. Spectra have been normalized to maximum peak intensity of vanadium. 175
- 6.15 QENS spectra recorded for (a) PB and (b) PBA-I at different temperatures at  $Q=1.0 \text{ \AA}^{-1}$ . Contribution from dehydrated sample has been subtracted. A dashed line shows the instrument resolution. Spectra have been normalized to maximum peak intensity. 175
- 6.16 Fitted subtracted QENS spectra for PB ( $\text{Fe}_4(\text{II})[\text{Fe}(\text{II})(\text{CN})_6]_{3.14}\text{H}_2\text{O}$ ) at some typical Q values. Instrument resolution is shown by the dashed line in the middle panel. 177
- 6.17 Fitted subtracted QENS spectra for PBA-I ( $\text{Fe}_4(\text{II})[\text{Fe}(\text{II})(\text{CN})_6]_{4.16}\text{H}_2\text{O}$ ) at some typical Q values. Instrument resolution is shown by the dashed line in the middle panel. 177
- 6.18 Fitted subtracted QENS spectra for PBA-II ( $\text{Cu}_2\text{Mn}_2[\text{Fe}(\text{CN})_6]_{2.67} \cdot 19\text{H}_2\text{O}$ ) at some typical Q values. Instrument resolution is shown by the dashed line in the middle panel. 178

- 6.19 Variation of EISF for (a) PB ( $\text{Fe}_4(\text{II})[\text{Fe}(\text{II})(\text{CN})_6]_3 \cdot 14\text{H}_2\text{O}$ ), (b) PBA-I ( $\text{Fe}_4(\text{II})[\text{Fe}(\text{II})(\text{CN})_6]_4 \cdot 16\text{H}_2\text{O}$ ) and (c) PBA-II ( $\text{Cu}_2\text{Mn}_2[\text{Fe}(\text{CN})_6]_{2.67} \cdot 19\text{H}_2\text{O}$ ) as obtained from QENS data with  $Q$  at different temperatures. Solid lines show the fits to the EISF using a localized translational diffusion model with immobile fraction [Eq.(6.9)] of water molecules. A dashed line shows the calculated EISF as per the model based on isotropic rotation just for comparison. 180
- 6.20 Variation of fraction of water molecules taking part in the dynamics in PB ( $\text{Fe}_4(\text{II})[\text{Fe}(\text{II})(\text{CN})_6]_3 \cdot 14\text{H}_2\text{O}$ ), PBA-I ( $\text{Fe}_4(\text{II})[\text{Fe}(\text{II})(\text{CN})_6]_4 \cdot 16\text{H}_2\text{O}$ ) and PBA-II ( $\text{Cu}_2\text{Mn}_2[\text{Fe}(\text{CN})_6]_{2.67} \cdot 19\text{H}_2\text{O}$ ) as obtained from the model fit in the temperature range 260–360 K. 181
- 6.21 Variation of half width at half maxima (HWHM) of a Lorentzian representing water dynamics in (a) PB ( $\text{Fe}_4(\text{II})[\text{Fe}(\text{II})(\text{CN})_6]_3 \cdot 14\text{H}_2\text{O}$ ), (b) PBA-I ( $\text{Fe}_4(\text{II})[\text{Fe}(\text{II})(\text{CN})_6]_4 \cdot 16\text{H}_2\text{O}$ ) and (c) PBA-II ( $\text{Cu}_2\text{Mn}_2[\text{Fe}(\text{CN})_6]_{2.67} \cdot 19\text{H}_2\text{O}$ ) with  $Q$ . Solid lines are the fit with a model based on localized translational diffusion as described in Eq. (6.10). 184
- 6.22 Variation of localized diffusion constant ( $D_{\text{loc}}$ ) of water in (a) PB( $\text{Fe}_4(\text{II})[\text{Fe}(\text{II})(\text{CN})_6]_3 \cdot 14\text{H}_2\text{O}$ ) and PBA-I ( $\text{Fe}_4(\text{II})[\text{Fe}(\text{II})(\text{CN})_6]_4 \cdot 16\text{H}_2\text{O}$ ) and (b) PBA-II ( $\text{Cu}_2\text{Mn}_2[\text{Fe}(\text{CN})_6]_{2.67} \cdot 19\text{H}_2\text{O}$ ) in the temperature range 260–360 K. Arrhenius behaviour is evident within the measured temperature range. 186

6.23	Thermo-gravimetric curves for $\text{PB}(\text{Fe}_4(\text{II})[\text{Fe}(\text{II})(\text{CN})_6]_3 \cdot 14\text{H}_2\text{O})$ , PBA-I $(\text{Fe}_4(\text{II})[\text{Fe}(\text{II})(\text{CN})_6]_4 \cdot 16\text{H}_2\text{O})$ and PBA-II $(\text{Cu}_2\text{Mn}_2[\text{Fe}(\text{CN})_6]_{2.67} \cdot 19\text{H}_2\text{O})$ compounds. Sharp loss in weight of PB compared to PBA-I and PBA-II is evident.	187
7.1	(a) Straight and sinusoidal channel structure of ZSM5 zeolite (b) Propylene molecule as a united atom model as used in simulation.	193
7.2	Fitted QENS spectra from the propylene adsorbed in ZSM5 zeolite using MARX spectrometer at some typical $Q$ values. Instrument resolution is shown by dashed line.	196
7.3	Variation of HWHM ( $\Gamma_T$ ) with $Q^2$ . The lines correspond to the fit assuming different models as described in the text.	197
7.4	Variation of (a) translational and (b) rotational intermediate scattering functions calculated from MD simulation trajectories with time $t$ at $Q=0.45 \text{ \AA}^{-1}$ .	200
7.5	QENS spectra from the propylene adsorbed in ZSM5 zeolite at TAS at some typical $Q$ -values. Instrument resolution is shown by dash dot dotted line in middle panel.	202
7.6	Variation of EISF for propylene adsorbed in ZSM5 zeolite as obtained from QENS data using TAS with respect to wave vector $Q$ . The solid line corresponds to the isotropic rotational diffusion model.	203
7.7	Variation of quasielastic structure factor $(2l+1)j_l^2(Qr)$ with $Qr$ at some typical $l$ values.	204
7.8	Typical fitted experimental data observed with TAS assuming isotropic rotational diffusion model for propylene adsorbed in ZSM5 zeolite at some typical $Q$ values.	205

7.9	Variation of rotational diffusion coefficient ( $D_R$ ) with $Q$ .	205
7.10	Trajectory of the CH <sub>3</sub> site with respect to the center of mass of the molecule for (a) 1311 ps, (b) first 140 ps and (c) first 200 ps of the simulation production run in X-Y plane.	206
7.11	Variation of $EISF$ as obtained from long time behaviour of $I^R(Q, t)$ calculated using MD simulation trajectories of the propylene molecules in ZSM5 zeolite. The solid curve corresponds to the calculated variation for isotropic rotational diffusion.	207
7.12	Variation of $I^R(Q, t)$ of propylene molecules within ZSM5 zeolite at typical $Q$ values.	208
7.13	The behavior of the first six orientational correlation functions, $\langle P_l(\mathbf{e}(t) \cdot \mathbf{e}(0)) \rangle$ with time.	209
7.14	(a) Fourier Transform of $I^R(Q, t)$ for propylene in ZSM5 zeolite at typical $Q$ -value of $1.8 \text{ \AA}^{-1}$ . A peak around $\sim 7 \text{ meV}$ is observed. (b) Fourier Transform of AVACF for propylene in ZSM5 zeolite. Inset: FT of AVACF in an expanded scale, the peak around $\sim 7 \text{ meV}$ is evident.	210
7.15	(a) Torque auto correlation function (TACF) for propylene in ZSM5 zeolite. Presence of oscillations is observed. (b) TACF for due to guest-guest as well as guest host interaction. TACF due to guest-host interaction is seen to be responsible for the oscillations.	211
7.16	(a) Projection of a unit vector $\mathbf{e}$ (directed towards CH <sub>3</sub> site) with respect to center of mass in space fixed coordinate for short time for a tagged molecule in ZSM5 zeolite. (b) Torque exerted on the molecules in the X direction due to guest-guest interaction.	213

7.17	(a) Histogram of the distribution of projection angles of unit vector (from center of mass to a CH <sub>3</sub> site) to different axis in case of propylene adsorbed in ZSM5 zeolite. (b) Schematic of a sphere covered by the tip of a unit vector $\mathbf{e}$ performing isotropic rotation.	216
7.18	Histograms of the distribution of projection angles of unit vector (from center of mass to a CH <sub>3</sub> site) to different axis in case of propylene adsorbed in (a) Na-Y and (b) AlPO <sub>4</sub> -5 zeolites.	217
7.19	Fitted QENS spectra from EG adsorbed in ZSM5 zeolite at some typical $Q$ values. Solid lines represent the fit while dash-dot and dash-dot-dot lines represent quasielastic and elastic components respectively. Instrument resolution is shown by dashed line in middle panel.	218
7.20	(a) Variation of EISF as obtained from QENS data of EG loaded in ZSM5 using MARX spectrometer with respect to wave vector $Q$ . The solid line corresponds to the isotropic rotational diffusion model. (b) Schematic of EG molecule.	219
7.21	Typical fitted QENS spectra for EG sorbed in ZSM5 zeolite assuming isotropic rotational diffusion model at some typical $Q$ values.	220
7.22	Variation of rotational diffusion coefficient, $D_R$ of EG sorbed in ZSM5 with $Q$ .	221

# LIST OF TABLES

		Page No.
2.1	Radii of spheres, $R_{\min}$ and $R_{\max}$ and corresponding diffusion constants, $D_{\min}$ and $D_{\max}$ as obtained from the least square fitting of the data with a model discussed in the text for different temperatures.	68
3.1	Radii of spheres, $R_{\min}$ and $R_{\max}$ , and corresponding diffusion coefficients, $D_{\min}$ and $D_{\max}$ , as obtained by least squares fitting of the data at high temperatures ( $>360$ K) with localized translational diffusion model.	102
4.1	Diffusion coefficients ( $D_G$ ) corresponding to the global motion of CTAB micelles at different temperatures. Global diffusion coefficient observed for other micelles and proteins using QENS techniques [21,30,53] are also given for the comparison.	111
4.2	Radii of spheres, $R_{\min}$ and $R_{\max}$ , and associated diffusion coefficients, $D_{\min}$ and $D_{\max}$ for hydrocarbon chain and mean residence time ( $\tau_1$ ) for the hydrogen atoms in the head group, as obtained from the least square fitting of the data (Fig. 4.5 & 4.7) with a model discussed in the text, at different temperatures.	117
5.1	Various parameters related to shape and size of the 0.1 M $C_n$ TAB micelles for different chain lengths as obtained using Small Angle Neutron Scattering (SANS) experiment at 298 K as taken from Ref. [93].	136



5.2	Radii of spheres, $R_{min}$ and $R_{max}$ , and associated diffusion coefficients, $D_{min}$ and $D_{max}$ for hydrocarbon chain and mean residence time ( $\tau$ ) for the hydrogen atoms in the head group, as obtained from the least square fitting of the data (Figs. 5.7 & 5.8) with a model discussed in the text, for different chain length $n$ of the molecules $C_nTAB$ . Global diffusion coefficient ( $D_G$ ) for $C_nTAB$ ( $n=10,12,14$ and $16$ ) micelles is also compared.	140
6.1	Pick-off life time ( $\tau_p$ ), intensities ( $I$ ), and calculated radii ( $R, R_0$ ) of the cavities or voids in the RO and NF polyamide membranes.	158
6.2	Values of translational diffusion coefficient ( $D_T$ ), residence time ( $\tau$ ) and rotational diffusion coefficient ( $D_R$ ) of water sorbed in RO and NF membranes at different temperatures.	168
6.3	Fraction of water molecules taking part in the dynamics ( $p_x$ ) and localization radius of sphere ( $a$ ) for PB ( $Fe_4(II)[Fe(II)(CN)_6]_3 \cdot 14H_2O$ ), PBA-I ( $Fe_4(II)[Fe(II)(CN)_6]_4 \cdot 16H_2O$ ) and PBA-II ( $Cu_2Mn_2[Fe(CN)_6]_{2.67} \cdot 19H_2O$ ) as obtained from the least square fitting of the data (Fig. 6.19) with a model discussed in the text, in the temperature range 260-360 K.	181
6.4	Localised Diffusion coefficients, $D_{loc}$ of water in PB, PBA-I and PBA-II compounds as obtained from the least square fitting of the data (Fig. 6.21) with the localised translational diffusion model as discussed in the text.	188

7.1	Root mean square jump length ( $l$ ) and translational diffusion coefficient ( $D_T$ ) for propylene in ZSM5 zeolite as obtained from the fits shown in Fig 7.3.	199
-----	--	-----

# CHAPTER 1

## Introduction

Neutron scattering is an excellent technique to study both structure and dynamics of condensed matter on atomic scale. This is because wavelength and the energy of thermal and cold neutrons match closely with the interatomic spacing and the excitations in solid [1-4]. Neutron being a neutral particle scattered majorly by the nuclei of the atom via strong neutron-nuclear interaction. Therefore, neutron scattering is an isotropic scattering (since wavelength of neutron is much larger than the size of the nucleus) and scattering amplitude varies irregularly with the atomic number of the scatterer. This is in contrast to X-ray scattering where scattering amplitude highly depend on the scattering angle and proportional to the atomic number of the scatterer. Thus, study of lighter elements in presence of heavy elements or distinguishing the adjacent atoms is possible via neutron scattering technique. Moreover, scattering cross section is not the same for different isotopes. Therefore, neutron scattering experiments can be used to distinguish the isotopic contributions. All these properties make neutron scattering technique a powerful experimental tool to investigate structure and dynamics of the materials. Dynamics reflect the intermolecular or intramolecular interaction, which are the key factor for the properties of materials. In an inelastic neutron scattering experiment, where a finite energy is exchanged between neutron and system, the scattered intensity is analysed as function of both the energy transfer  $\hbar\omega$  ( $= E_0 - E$ , where  $E_0$  and  $E$  are initial and final energies of neutrons) and wave-vector transfer  $\mathbf{Q}$  ( $= \mathbf{k}_0 - \mathbf{k}$ , where  $\mathbf{k}_0$  and  $\mathbf{k}$  are initial and final wave vectors of neutrons). Periodic motions (e.g., oscillating with characteristic frequencies  $\omega_i$ ), give rise to characteristic inelastic lines at  $\omega = \pm\omega_i$  in the energy spectrum. However, in a real neutron scattering experiment, these

lines will be broadened due to finite instrumental resolution. Unlike the periodic motions where peaks corresponds to characteristic frequencies in the measured spectrum, stochastic motions lead to broadening of the elastic peak ( $\omega=0$ ) over and above the instrument resolution. This broadening is known as quasielastic broadening and by examining this, one can extract information about the stochastic motions occurring typically in picoseconds time scale. Thus, Quasi-elastic Neutron Scattering (QENS) technique involves the measurement of spectra centered at zero energy transfer. With advancement in instrumentation and availability of high neutron flux from spallation source and nuclear reactors, the time range that can be probed by QENS has been widened considerably. At present QENS spectrometers exist which can probe molecular dynamics on the time scales  $\sim 10^{-9}$ - $10^{-13}$  sec. Both quantitative as well as qualitative information about the molecular motion can be obtained by this technique. Qualitative information pertains to the geometrical mechanism of the motion while quantitative information means about the correlation times and length scales of the motion. In addition to this, QENS technique can also be used to determine the hindering potential by investigating the temperature dependence of the correlation time. Therefore, all three main information's (the time-scale of the dynamical motion, its geometry as well as the nature of the hindering potential) of the stochastic motion can be obtained from the QENS experiments.

Nuclear magnetic resonance and dielectric relaxation measurements are two other complementary experimental techniques to QENS. However, scattering techniques have a significant advantage due to an additional variable, wave vector transfer  $\mathbf{Q}$ , which provides spatial information related to the geometry of the motion. An alternative to neutrons seems to be the photons. Although X-rays have wavelengths of the order of 1 Å and used widely for structure analysis but their energy is very large ( $\sim$ keV) and hence unsuitable for quasielastic scattering experiments with  $\mu$ eV-meV resolution. Lasers provide an extremely good energy

resolution, but their wavelength ( $\sim 5000 \text{ \AA}$ ) only allows excitations to be studied at very small wave vectors. Classical molecular dynamics (MD) simulation provides an excellent tool to supplement the results obtained from QENS experiment due to overlap of the time and length scale it can access. Thus, there is a mutual advantage in combining data from QENS experiments and MD simulations; experimental scattering data can be used as a gauge for the MD force field that is the central input for the simulation and the trajectories obtained from the simulation can be used to interpret data from neutron scattering experiments providing deeper insights of the dynamical process. Further, MD simulation does not suffer from the limitation of an experiment. Simulations are ideally suited for problems, which cannot be tackled by experiment due to physical constraints. Extreme temperatures and pressures can be simulated without having to deal with the physical difficulties involved. In this chapter we shall briefly describe the techniques of QENS experiment and MD simulation.

The organization of this chapter is as follows: the theoretical formalism of quasielastic neutron scattering technique is discussed in 1.1. Coherent and incoherent neutron scattering length and corresponding scattering cross-section are discussed in section 1.1.1. Neutron scattering function and its relation with scattered neutron intensity have been discussed in section 1.1.2. Various kinds of stochastic motions and their contribution to the scattering function are described in 1.1.3. In section 1.1.4, different models for translational motion and related scattering functions are discussed. Similarly, models for rotational motions are discussed in 1.1.5. Details about the instruments and methods for quasielastic neutron scattering are described in sections 1.2. In section 1.3, brief introduction of classical MD simulation is discussed. Different aspects of the simulation like initial condition, evaluation of force and potential energy, periodic boundary condition and integration algorithm are discussed in this section. Once the trajectories are obtained various quantities of

interest can be calculated using time correlation functions. Various time correlation functions are discussed in section 1.4. Finally overview of the thesis is discussed in section 1.5.

## 1.1. THEORETICAL FORMALISM OF QUASIELASTIC NEUTRON SCATTERING

### 1.1.1. Scattering Length and Cross-Section

As mentioned earlier, neutron scatters from a nucleus isotropically and therefore, neutron scattering is described by a scattering length  $b$  that is not a function of scattering angle, and scattering cross-section of a nucleus is given by [1-4]

$$\sigma = 4\pi b^2 \quad (1.1)$$

Scattering length depends on the nature of the scattering nucleus. Let's consider an atom having several isotopes with scattering lengths  $b_1, b_2, \dots$  and corresponding abundance  $c_1, c_2, \dots$ . The average of the scattering length over all the isotopes of a species is called the coherent scattering length of that atom whereas its root mean square deviation over the average is called incoherent scattering length. Therefore, coherent and incoherent scattering lengths can be written as [1-4]

$$b_{coh} = \langle b \rangle = \sum_k c_k b_k \quad (1.2)$$

and

$$b_{inc} = [\langle b^2 \rangle - \langle b \rangle^2]^{1/2} \quad (1.3)$$

where the average value of squared scattering lengths is given by  $\langle b^2 \rangle = \sum_k c_k b_k^2$ . The

incoherent scattering length can only be zero for single isotope with zero nuclear spin. For nuclei with nuclear spin  $I \neq 0$  there appears an additional contribution in incoherent scattering, called spin incoherent scattering. Let us consider a single isotope specimen with nuclear spin  $I$ . The interaction of neutron (spin=1/2) with the nuclear spins produces two

compound nuclear states with total spins parallel  $I + 1/2$  and anti parallel  $I - 1/2$  with different scattering length respectively. The corresponding average scattering lengths are then given by

$$\langle b \rangle = \left( \frac{I+1}{2I+1} \right) b^+ + \left( \frac{I}{2I+1} \right) b^- \quad (1.4)$$

$$\langle b^2 \rangle = \left( \frac{I+1}{2I+1} \right) (b^+)^2 + \left( \frac{I}{2I+1} \right) (b^-)^2 \quad (1.5)$$

For the hydrogen/proton with  $I = 1/2$ ,  $b^+ = 1.08 \times 10^{-12} \text{ cm}$  and  $b^- = -4.74 \times 10^{-12} \text{ cm}$ . The opposite sign of  $b^+$  and  $b^-$  causes the large difference between  $\sigma_{inc}(\text{H}) = 79.9$  barn and  $\sigma_{coh}(\text{H}) = 1.8$  barn. In fact the incoherent neutron scattering cross-section for hydrogen atoms (79.9 barns) is almost an order of magnitude larger than that from other species. This makes incoherent neutron scattering a unique tool for the study of the self-diffusion in hydrogenous materials. Considering the case of deuterium,  $I = 1$ , one obtains  $\sigma_{inc}(\text{D}) = 2.0$  barns and  $\sigma_{coh}(\text{D}) = 5.6$  barns. Therefore, deuterium is very useful in neutron scattering experiment for the contrast matching as can be seen in later chapters. Moreover, this can be used to distinguish between different chemical groups by selective deuteration. The spin dependent scattering can be utilized to separate coherent and spin incoherent quasi-elastic scattering by means of polarized neutrons. When an incident neutron beam with spin ‘up’ polarization fall on the sample, coherent QENS does not flip the polarization, however in spin incoherent QENS one third of the scattering intensity is non-spin flip and two thirds are spin flip scattering [5]

$$\left( \frac{d\sigma}{d\omega} \right)^{\uparrow\uparrow} = \left( \frac{d\sigma}{d\omega} \right)_{coh} + \frac{1}{3} \left( \frac{d\sigma}{d\omega} \right)_{spin-inc} \quad (1.6)$$

$$\left( \frac{d\sigma}{d\omega} \right)^{\uparrow\downarrow} = \frac{2}{3} \left( \frac{d\sigma}{d\omega} \right)_{spin-inc} \quad (1.7)$$

Hence

$$\left(\frac{d\sigma}{d\omega}\right)_{coh} = \left(\frac{d\sigma}{d\omega}\right)^{\uparrow\uparrow} - \frac{1}{2}\left(\frac{d\sigma}{d\omega}\right)^{\uparrow\downarrow} \quad (1.8)$$

$$\left(\frac{d\sigma}{d\omega}\right)_{spin-inc} = \frac{3}{2}\left(\frac{d\sigma}{d\omega}\right)^{\uparrow\downarrow} \quad (1.9)$$

In this thesis we shall be concerned mainly with incoherent neutron scattering. Two other elements, which are of importance in QENS experiments, are aluminium and vanadium. Aluminium is used to make sample containers because of its extremely weak absorbing power for neutrons (1% per mm). Vanadium is a purely incoherent scatterer with  $\sigma_{inc}=5.1$  barns and  $\sigma_{coh}=0.03$  barns. It can therefore be used for calibration purposes.

### 1.1.2. Neutron Scattering Function

When a monochromatic beam of neutrons with energy  $E_0$  and wave vector  $\mathbf{k}_0$ , are scattered from a sample with a final energy  $E=E_0+\hbar\omega$  and a final wave vector  $\mathbf{k}$ , into a direction  $\mathbf{\Omega}$ . The double differential cross section  $\frac{\partial^2\sigma}{\partial\mathbf{\Omega}\partial E} (= \frac{1}{h} \frac{\partial^2\sigma}{\partial\mathbf{\Omega}\partial\omega})$  gives the probability that a neutron with incident energy  $E_0$ , scattered within a solid angle element  $d\mathbf{\Omega}$  and with an energy transfer  $\hbar\omega=E-E_0$  and can be written as [3-4]

$$\frac{\partial^2\sigma}{\partial\mathbf{\Omega}\partial\omega} = \frac{k}{k_0} \frac{1}{2\pi} \sum_i \sum_j \int_{-\infty}^{\infty} \frac{1}{N} \left\langle b_i b_j \exp\{i\mathbf{Q}\cdot\mathbf{R}_i(t)\} \times \exp\{-i\mathbf{Q}\cdot\mathbf{R}_j(0)\} \right\rangle \exp(-i\omega t) dt \quad (1.10)$$

Here  $b_i$  is the scattering length of the  $i^{\text{th}}$  atomic species, each of them being a mixture of several isotopes possessing a nuclear spin.  $\mathbf{R}_i(t)$  is the position of  $i^{\text{th}}$  atomic species at time  $t$  and  $\mathbf{Q} (= \mathbf{k}-\mathbf{k}_0)$  is the wave vector transfer. The summation is for 1 to  $N$ , where  $N$  is the total number of nuclei in the sample.  $\langle \rangle$  denotes thermal average holds not only for the positions of the sample nuclei but also for all the spin states. In fact, it is in general, assumed that there



is no coupling between the actual scattering length of a nucleus and its position. Under this condition averaging can be done independently on the spin states and location of the nucleus.

$$\frac{\partial^2 \sigma}{\partial \mathbf{Q} \partial \omega} = \frac{k}{k_0} \frac{1}{2\pi} \sum_i \sum_j \int_{-\infty}^{\infty} \langle b_i b_j \rangle \left\langle \exp\{i\mathbf{Q} \cdot \mathbf{R}_i(t)\} \times \exp\{-i\mathbf{Q} \cdot \mathbf{R}_j(0)\} \right\rangle \exp(-i\omega t) dt \quad (1.11)$$

To introduce the definitions of the coherent and incoherent scattering length [Eqs. (1.2) and (1.3)] into Eq. (1.10), we must make explicit in the double summation the terms, which corresponds to the nuclei of identical nature. Let us assume that sample is formed of  $n$  different types of atoms (i.e. H, D, C, etc.) and let  $N_\alpha$  and  $N_\beta$  be number of atoms of type  $\alpha$  and  $\beta$ . If there is no correlation between the values of the scattering length for different isotopes, the Eq. (1.11) can be split into two parts as,

$$\frac{\partial^2 \sigma}{\partial \mathbf{Q} \partial \omega} = \left( \frac{\partial^2 \sigma}{\partial \mathbf{Q} \partial \omega} \right)_{coh} + \left( \frac{\partial^2 \sigma}{\partial \mathbf{Q} \partial \omega} \right)_{inc} \quad (1.12)$$

The two terms on the right hand side of Eq. (1.12) are the coherent and incoherent parts of the double differential cross section. The coherent part can be written as

$$\left( \frac{\partial^2 \sigma}{\partial \mathbf{Q} \partial \omega} \right)_{coh} = \frac{1}{N} \frac{k}{k_0} \sum_{\alpha=1}^n \sum_{\beta=1}^n b_\alpha^{coh} b_\beta^{coh} \sqrt{N_\alpha N_\beta} S_{coh}^{\alpha\beta}(\mathbf{Q}, \omega) \quad (1.13)$$

here  $b_\alpha^{coh}$  and  $b_\beta^{coh}$  are the coherent scattering lengths relative to isotopes  $\alpha$  and  $\beta$ . The function  $S_{coh}^{\alpha\beta}(\mathbf{Q}, \omega)$  is called the scattering function (or the scattering law) relative to the components  $\alpha$  and  $\beta$ . It is the time Fourier transform of the intermediate scattering function and can be written as

$$S_{coh}^{\alpha\beta}(\mathbf{Q}, \omega) = \frac{1}{2\pi \sqrt{N_\alpha N_\beta}} \int_{-\infty}^{\infty} \sum_{i_\alpha=1}^{N_\alpha} \sum_{j_\beta=1}^{N_\beta} \left\langle \exp\{i\mathbf{Q} \cdot \mathbf{R}_{i_\alpha}(t)\} \times \exp\{-i\mathbf{Q} \cdot \mathbf{R}_{j_\beta}(0)\} \right\rangle \exp(-i\omega t) dt \quad (1.14)$$

where

$$I_{coh}^{\alpha\beta}(\mathbf{Q}, t) = \frac{1}{\sqrt{N_\alpha N_\beta}} \sum_{i_\alpha=1}^{N_\alpha} \sum_{j_\beta=1}^{N_\beta} \left\langle \exp\{i\mathbf{Q} \cdot \mathbf{R}_{i_\alpha}(t)\} \times \exp\{-i\mathbf{Q} \cdot \mathbf{R}_{j_\beta}(0)\} \right\rangle \quad (1.15)$$

Similarly for the incoherent scattering cross section, we can write

$$\left( \frac{\partial^2 \sigma}{\partial \mathbf{Q} \partial \omega} \right)_{inc} = \frac{1}{N} \frac{k}{k_0} \sum_{\alpha=1}^n b_{\alpha}^{inc} S_{inc}^{\alpha}(\mathbf{Q}, \omega) \quad (1.16)$$

The function  $S_{inc}^{\alpha}(\mathbf{Q}, \omega)$  is the incoherent scattering law relative to the species  $\alpha$ . It is the time Fourier transform of the incoherent intermediate scattering function and can be written as

$$S_{inc}^{\alpha}(\mathbf{Q}, \omega) = \frac{1}{2\pi N_{\alpha}} \int_{-\infty}^{\infty} \sum_{i_{\alpha}=1}^{N_{\alpha}} \left\langle \exp\{i\mathbf{Q} \cdot \mathbf{R}_{i_{\alpha}}(t)\} \times \exp\{-i\mathbf{Q} \cdot \mathbf{R}_{i_{\alpha}}(0)\} \right\rangle \exp(-i\omega t) dt \quad (1.17)$$

where

$$I_{inc}^{\alpha}(\mathbf{Q}, t) = \frac{1}{N_{\alpha}} \sum_{i_{\alpha}=1}^{N_{\alpha}} \left\langle \exp\{i\mathbf{Q} \cdot \mathbf{R}_{i_{\alpha}}(t)\} \times \exp\{-i\mathbf{Q} \cdot \mathbf{R}_{i_{\alpha}}(0)\} \right\rangle \quad (1.18)$$

It may be noted that  $S_{coh}^{\alpha\beta}(\mathbf{Q}, \omega)$  in Eq. (1.14) involves sum over the phase shifts of different atoms and thus results in interference effects. On the other hand, the positions in the exponential terms in Eq. (1.18) refer to the same nucleus at different times  $0$  and  $t$ . Thus, scattered neutron intensity is separated into two terms *coherent* and *incoherent* as shown in Eq. (1.12). In coherent scattering, the total intensity observed results from the sum of the different intensities scattered from the different atoms. Thus by measuring coherent scattering law one can get information on correlated motions. Whereas incoherent scattering involves the same nucleus at two different times, so there is no interference effects between the amplitudes scattered by different nuclei. Thus by measuring incoherent scattering law one can get information on uncorrelated motions or single particle dynamics.

In case of a single isotope ( $n=1$ ), the double differential cross section can be written as

$$\frac{\partial^2 \sigma}{\partial \mathbf{Q} \partial \omega} = \frac{1}{4\pi N} \frac{k}{k_0} [\sigma_{coh} S_{coh}(\mathbf{Q}, \omega) + \sigma_{inc} S_{inc}(\mathbf{Q}, \omega)] \quad (1.19)$$

where  $\sigma_{\text{coh}}$  and  $\sigma_{\text{inc}}$  are coherent and incoherent scattering cross section respectively. The scattering functions  $S_{\text{coh}}(\mathbf{Q}, \omega)$  and  $S_{\text{inc}}(\mathbf{Q}, \omega)$  are the time Fourier transforms of intermediate scattering functions and can be written as

$$S_{\text{coh}}(\mathbf{Q}, \omega) = \frac{1}{2\pi} \int_{-\infty}^{\infty} I_{\text{coh}}(\mathbf{Q}, t) \exp(-i\omega t) dt \quad (1.20)$$

and

$$S_{\text{inc}}(\mathbf{Q}, \omega) = \frac{1}{2\pi} \int_{-\infty}^{\infty} I_{\text{inc}}(\mathbf{Q}, t) \exp(-i\omega t) dt \quad (1.21)$$

with intermediate scattering functions

$$I_{\text{coh}}(\mathbf{Q}, t) = \frac{1}{N} \sum_i \sum_j \langle \exp\{i\mathbf{Q} \cdot \mathbf{R}_i(t)\} \times \exp\{-i\mathbf{Q} \cdot \mathbf{R}_j(0)\} \rangle \quad (1.22)$$

$$I_{\text{inc}}(\mathbf{Q}, t) = \frac{1}{N} \sum_{i=1} \langle \exp\{i\mathbf{Q} \cdot \mathbf{R}_i(t)\} \times \exp\{-i\mathbf{Q} \cdot \mathbf{R}_i(0)\} \rangle \quad (1.23)$$

One can return to the real space by taking the space Fourier transform of intermediate scattering function as follows,

$$G(\mathbf{r}, t) = \frac{1}{(2\pi)^3} \int_{-\infty}^{\infty} I_{\text{coh}}(\mathbf{Q}, t) \exp(-i\mathbf{Q} \cdot \mathbf{r}) d\mathbf{Q} \quad (1.24)$$

By using Eq. (1.22) one can get the definition of pair-correlation function as

$$G(\mathbf{r}, t) = \frac{1}{N} \sum_i \sum_j \int \langle \delta(\mathbf{r} - \mathbf{r}' + \mathbf{R}_i(0)) \delta(\mathbf{r}' - \mathbf{R}_j(t)) \rangle d\mathbf{r}' \quad (1.25)$$

with the normalization condition  $\int G(\mathbf{r}, t) d\mathbf{r} = N$ .

One can also get the definition of self-correlation function by using Eq. (1.23) as

$$G_s(\mathbf{r}, t) = \frac{1}{N} \sum_i \int \langle \delta(\mathbf{r} - \mathbf{r}' + \mathbf{R}_i(0)) \delta(\mathbf{r}' - \mathbf{R}_i(t)) \rangle d\mathbf{r}' \quad (1.26)$$

with the normalization condition  $\int G_s(\mathbf{r}, t) d\mathbf{r} = 1$ .

The scattering functions defined in Eq. (1.14) and (1.17) satisfy the following detailed balance condition

$$S(-\mathbf{Q}, -\omega) = \exp\left(-\frac{\hbar\omega}{2k_B T}\right) S(\mathbf{Q}, \omega) \quad (1.27)$$

This shows that function  $S(\mathbf{Q}, \omega)$  is not symmetric with respect to  $\omega$ . This is due to the fact that probability of finding the system in the lower energy state is greater by the Boltzmann factor  $\exp(\hbar\omega/2k_B T)$  than that of in the higher energy state. Here  $k_B$  is the Boltzmann constant and  $T$  is the temperature of the system. Therefore, transitions from lower energy state to the higher energy state are more probable than the inverse.

In case of hydrogenous systems, total scattering of thermal neutron is dominated by the incoherent scattering of protons as  $\sigma_{\text{coh}}$  or  $\sigma_{\text{inc}}$  (any element)  $\ll \sigma_{\text{inc}}$  (proton). So in case of hydrogenous systems one can write,

$$\frac{\partial^2 \sigma}{\partial \mathbf{Q} \partial \omega} = \frac{1}{4\pi} \frac{k}{k_0} \sigma_{\text{inc}} S_{\text{inc}}(\mathbf{Q}, \omega) \quad (1.28)$$

Thus, neutron scattering technique yields a powerful way of investigating the motions of one individual proton and therefore the incoherent scattering law is analyzed in terms of single particle motions. Since all the work reported in this thesis pertained to hydrogenous systems, only the incoherent scattering law will be considered for discussion in the subsequent sections.

### 1.1.3. Different Types of Motions and Contributions to the Scattering Law

For a molecular system several kinds of motions viz. translational, rotational and vibrational can exist. In general diffusional (translational or rotational) and vibrational motions are assumed dynamically independent of each other because they occur on clearly different time

scale. Further, dynamical coupling between translational and rotational motion is neglected.

In that case one can write incoherent part of the intermediate scattering function [3] as,

$$I_{inc}(\mathbf{Q}, t) = I_{inc}^T(\mathbf{Q}, t) \cdot I_{inc}^R(\mathbf{Q}, t) \cdot I_{inc}^V(\mathbf{Q}, t) \quad (1.29)$$

where the superscripts  $T$ ,  $R$  and  $V$  refer to the translational, rotational and vibrational components respectively. The above equation can be written also in terms of  $S_{inc}(\mathbf{Q}, \omega)$  as,

$$S_{inc}(\mathbf{Q}, \omega) = S_{inc}^T(\mathbf{Q}, \omega) \otimes S_{inc}^R(\mathbf{Q}, \omega) \otimes S_{inc}^V(\mathbf{Q}, \omega) \quad (1.30)$$

where the symbol  $\otimes$  stands for a convolution product. The scattering function of the vibrations contains an elastic term (associated with neutrons scattered without energy transfer) and inelastic terms (at the certain characteristic frequencies) and can be written as [3]

$$S_{inc}^V(\mathbf{Q}, \omega) = \exp\{-2W(Q)\} [\delta(\omega) + S_{inel}^{V'}(\mathbf{Q}, \omega)] \quad (1.31)$$

Here,  $W(Q)$  is the Debye-waller factors and can be written as

$$2W(Q) = \frac{1}{3} \langle u^2 \rangle Q^2 \quad (1.32)$$

$\langle u^2 \rangle$  denote mean square displacements of the atoms.  $S_{inel}^{V'}(\mathbf{Q}, \omega)$  is composed of a series of sharp peaks occurring at characteristic frequency  $\omega_i$  of the system. From Eqs. (1.30) and (1.31), scattering law can be written as

$$S_{inc}(\mathbf{Q}, \omega) = \exp\{-2W\} [S_{inc}^T(\mathbf{Q}, \omega) \otimes S_{inc}^R(\mathbf{Q}, \omega) + S_{inc}^I(\mathbf{Q}, \omega)] \quad (1.33)$$

The term  $S_{inc}^I(\mathbf{Q}, \omega)$  is an inelastic term that results from convolution of  $S_{inc}^{V'}(\mathbf{Q}, \omega)$  with  $S_{inc}^T(\mathbf{Q}, \omega) \otimes S_{inc}^R(\mathbf{Q}, \omega)$ . This term contributes very little in the quasielastic region ( $\sim \pm 2$  meV) apart from possible increase in the background. Therefore, in the quasielastic regime the Eq.(1.33) can be written as,

$$S_{inc}(\mathbf{Q}, \omega) = \exp(-2W(Q)) [S_{inc}^T(\mathbf{Q}, \omega) \otimes S_{inc}^R(\mathbf{Q}, \omega)] \quad (1.34)$$

Therefore, in the quasielastic regime, the vibrational contribution will be only through the Debye-Waller factor, which is simply a scaling factor that does not modify the shape of the scattering function.

It is interesting to study the behaviour of the scattering functions in the limit  $t \rightarrow \infty$ . The intermediate scattering function can therefore be written as a sum of two parts as

$$I_{inc}(\mathbf{Q}, t) = I_{inc}(\mathbf{Q}, \infty) + I'_{inc}(\mathbf{Q}, t) \quad (1.35)$$

where the first term is independent of time whereas the second term is time dependent part. One can obtain the corresponding scattering law by taking Fourier transform of the above equation as

$$S_{inc}(\mathbf{Q}, \omega) = I_{inc}(\mathbf{Q}, \infty)\delta(\omega) + S'_{inc}(\mathbf{Q}, \omega) \quad (1.36)$$

The  $S_{inc}(\mathbf{Q}, \omega)$  has been separated into purely elastic component,  $I_{inc}(\mathbf{Q}, \infty)\delta(\omega)$ , and another one called quasielastic term which possesses a non-vanishing broadening since it is the time Fourier transform of a time dependent term. The coefficient of delta function is the space Fourier transforms of the scatterer distribution, taken at infinite time and averaged over all the possible initial positions. It has the dimension of a structure factor and gives the fraction of elastic component in total scattering function. Therefore, this coefficient is called Elastic Incoherent Structure Factor (EISF), which provides information about the geometry of the molecular motion.

In case the motion is non-localized in space (like translational motion of bulk liquid) the probability of finding the particle at particular position  $\mathbf{r}$  at long time  $t \rightarrow \infty$  is zero provided that same particles was at  $\mathbf{r}=0$  at time  $t=0$ . Therefore, one can write

$$G_s(\mathbf{r}, \infty) = 0 \quad (1.37)$$

or

$$I_{inc}(\mathbf{Q}, \infty) = 0 \quad (1.38)$$

Therefore, a characteristic feature of the scattered intensity from a liquid or any material with translational disorder is the absence of elastic peak. Conversely the existence of an elastic component in the scattered intensity clearly indicates the presence of localized motion provided that elastic scattering is not due to immobile host.

In practice QENS experiment the instrumental resolution is finite and if represented by  $R(\omega)$ , the scattered intensity can be represented as

$$I = S_{inc}(\mathbf{Q}, \omega) \otimes R(\omega) = I_{inc}(\mathbf{Q}, \infty)R(\omega) + S'_{inc}(\mathbf{Q}, \omega) \otimes R(\omega) \quad (1.39)$$

$R(\omega)$  is generally obtained by measuring spectra from the standard vanadium sample which is pure incoherent scatterer. Eq. (1.39) indicates that the elastic peak in the spectra does not appear as an infinitely sharp line but as a peak shaped curve, often approximated by some function (e.g. Gaussian) with an energy width characteristic of the instrument. This width ( $\Delta E \sim 1/\Delta t$ ) defines the magnitude of the time-scale over which the motions are observable. As can be seen in later section width of the quasielastic component in Eq. (1.39) is inversely proportional to the characteristic time of the motion. This means that the very slow motion corresponding to large characteristic time leads to negligible quasielastic broadening over the instrument resolution function. Therefore, corresponding scattered intensity is almost elastic. On the other hand, very fast motions produce considerable very large broadening comparison to the resolution function and will contribute to a flat background in the quasielastic region (depending on the available energy transfer range of the instrument). Thus the energy resolution functions and available energy transfer range of instrument defines both upper and lower limits on the time scale of motion that can be observed with the instrument. Therefore, it is very important to choose an appropriate instrument. It is possible to separate the contributions from slow and fast motions by using instruments having different energy resolutions. The slow motion could be investigated with high resolution instrument where the faster motion would contribute as background. The data with poor resolution instrument will

have contribution from both slow and fast motions, but in the analysis one could use the information as obtained from the high resolution instrument for the slower motion and obtain information pertaining to that of the faster one. This methodology has been employed in many cases [6-10] to separate out different dynamical motions.

#### **1.1.4. Translational Motion**

As discussed in earlier section the observed dynamics may have contribution from translational and rotational motion leaving away the vibration part. In this section various models of long range as well as localized translational motion will be discussed.

##### **1.1.4.1. Brownian Diffusion (Continuous Diffusion) Model**

The simplest translational motion is Brownian motion, which was first described quantitatively by Einstein in 1905. This motion occurs when the interaction between the particles is weak. In that situation, the particles move under the influence of the forces arising from the collisions between them. Between two collisions one particle moves along a straight line. After collision it goes in another random direction, independent of the previous one: the particle has forgotten its previous history. In this case, one can show that the self-correlation function as defined in Eq. (1.26) follows the equation

$$\frac{\partial G_s(\mathbf{r}, t)}{\partial t} = D \nabla^2 G_s(\mathbf{r}, t) \quad (1.40)$$

where  $D$  is the diffusion coefficient. The differential equation above is called Fick's law and is satisfied by the self-correlation function under the following two conditions

$$G_s(\mathbf{r}, 0) = \delta(\mathbf{r})$$

and

$$\int G_s(\mathbf{r}, t) d\mathbf{r} = 1$$



The solution of the diffusion equation [11] is

$$G_s(\mathbf{r}, t) = (4\pi Dt)^{-3/2} \exp(-r^2 / 4Dt) \quad (1.41)$$

One can obtain expressions for the corresponding intermediate scattering function  $I_{inc}(\mathbf{Q}, t)$  and the scattering law  $S_{inc}(\mathbf{Q}, \omega)$  by taking Fourier transforms as

$$I_{inc}(\mathbf{Q}, t) = \exp(-DQ^2 t) \quad (1.42)$$

and

$$S_{inc}(\mathbf{Q}, \omega) = \frac{1}{\pi} \frac{DQ^2}{\omega^2 + (DQ^2)^2} \quad (1.43)$$

Thus for simple Brownian diffusion, the intermediate scattering function is a Gaussian function with respect to  $Q$  while the scattering law is a Lorentzian with half-width at half-maxima (HWHM)  $DQ^2$ . In a neutron scattering experiment, on a sample exhibiting this kind of motion, the line width is therefore expected to be proportional to  $Q^2$ . For this reason it is also called the  $DQ^2$  law. Example of perfect stochastic diffusive motion is rare. Nevertheless such a situation is encountered in the case of the liquid phase of Argon. Dasannacharya and Rao [12] have observed continuous diffusion in liquid phase of Argon as studied using neutron scattering technique. The diffusion coefficient can be expressed in terms of the ‘distance’ that a molecule covers between two successive collisions,  $l$ , and the ‘time interval’ between the collisions,  $\tau$ , using the Einstein relation,

$$D = \frac{\langle l^2 \rangle}{6\tau} \quad (1.44)$$

In Brownian motion, the distance travels by a particle between any two successive collisions or jump length  $|l|$  is assumed to be small compared to the distance  $|r|$  of this particle from the origin. Therefore this model is also known as continuous diffusion model. This assumption is satisfied if we are concerned only at small  $Q$  values where the exact

mechanisms of diffusion are not revealed and Fick's law is satisfied. At large momentum transfer, which essentially corresponds to motion at smaller distance the continuous diffusion model appears no more appropriate and we need to describe the diffusion process in more detail.

#### 1.1.4.2. Jump Diffusion Model

This model assumes that for a time interval  $\tau$ , an atom remains on a given site, vibrating about a center of equilibrium, building up a thermal cloud. After this time, the atom moves rapidly to another site, in a negligible jump time. The length of the jump vector between these two sites,  $|l|$ , is assumed to be much larger than the dimensions of the thermal cloud. The time  $\tau$ , taken by the particle in between jumps is also called residence time. A scattering law can be calculated based on random walk diffusion, which is characterized by distribution of jump lengths. Basic assumption in this model is that the jump diffusion is a Markovian process, according to which successive jumps are uncorrelated but governed by a spatial probability distribution  $\rho(r)$ .

Chudley and Elliott [13] and also Egelstaff [14] have shown that for an isotropic distribution of jump length  $\rho(r)$ , the scattering law is a Lorentzian with a HWHM,  $\Gamma(Q)$  given by,

$$\Gamma(Q) = \frac{1}{\tau} \frac{\int_0^{\infty} \left[ 1 - \frac{\sin(Qr)}{Qr} \right] \rho(r) dr}{\int_0^{\infty} \rho(r) dr} \quad (1.45)$$

Chudley and Elliott [13] calculated the scattering law for a fixed jump length  $l$  i.e., all the jumps are identical and hence there is no distribution in jump length. So the distribution  $\rho(r)$  can be represented as

$$\rho(r) = \delta(r - l) \quad (1.46)$$

Then the variation of HWHM becomes

$$\Gamma(Q) = \frac{1}{\tau} \left[ 1 - \frac{\sin(Ql)}{Ql} \right] \quad (1.47)$$

In the low  $Q$  limit Eq. (1.47) reduces to

$$\Gamma(Q) = \frac{Q^2 l^2}{6\tau} \quad (1.48)$$

and using Einstein relation  $D = \frac{l^2}{6\tau}$  one obtain the  $DQ^2$  variation of half width at half maxima of the scattering function.

Constant jump length situation may well suitable in crystalline solids where the molecule is expected to jump between sites of potential minima, which are very regularly distributed. Diffusion of hydrogen in palladium provides an example of constant jump diffusion model as studied by Rowe et al [15]. On the other hand if the equipotential sites are not very well ordered as one might expect in case of a liquid, the jump lengths are no longer constant but rather distributed. A Gaussian distribution of jump length was taken by Hall and Ross in their model [16]. The jump length distribution in this model is then

$$\rho(r) = \frac{1}{(l_0 \sqrt{2\pi})^3} \exp\left(-\frac{r^2}{2l_0^2}\right)$$

which corresponds to scalar distribution of jump lengths of the form

$$\rho(r) = 4\pi r^2 \rho(r) = \frac{2r^2}{l_0^3 \sqrt{2\pi}} \exp\left(-\frac{r^2}{2l_0^2}\right) \quad (1.49)$$

where  $l_0$  is the standard deviation. This is a normalized distribution since

$$\int_0^\infty \rho(r) dr = 1$$

and corresponding mean square jump length would be,

$$\langle r^2 \rangle = \int_0^\infty r^2 \rho(r) dr = 3l_0^2 \quad (1.50)$$

HWHM of the Lorentzian function corresponding to H-R model would be,

$$\Gamma(Q) = \frac{1}{\tau} \left[ 1 - \exp\left(-\frac{Q^2 l_0^2}{2}\right) \right] \quad (1.51)$$

In the low  $Q$  limit Eq. (1.51) reduces to  $\Gamma(Q) = \frac{Q^2 l_0^2}{2\tau}$  and using Einstein relation from Eq.

(1.44) one obtains the  $DQ^2$  variation of half width at half maxima of the scattering function.

Singwi and Sjölander, employed a different distribution of jump lengths to explain the diffusion of water. They assumed jump lengths are distributed randomly as [17],

$$\rho(r) = \frac{r}{l_0^2} \exp(-r/l_0) \quad (1.52)$$

This distribution is also normalized as

$$\int_0^\infty \rho(r) dr = 1$$

and it corresponds to a mean square jump length

$$\langle r^2 \rangle = \int_0^\infty r^2 \rho(r) dr = 6l_0^2 \quad (1.53)$$

HWHM of the Lorentzian function corresponding to S-S model would be

$$\Gamma(Q) = \frac{1}{\tau} \left[ 1 - \frac{1}{1 + l_0^2 Q^2} \right] = \frac{l_0^2 Q^2 / \tau}{1 + l_0^2 Q^2} \quad (1.54)$$

By using Einstein relation  $D = \frac{\langle r^2 \rangle}{6\tau}$  one can rewrite the above equation as,

$$\Gamma(Q) = \frac{DQ^2}{1 + DQ^2 \tau} \quad (1.55)$$

This model has been used to describe the translational diffusion of bulk water [18]. For  $Q \rightarrow 0$ ,  $DQ^2\tau$  can be approximated negligible compared to one and Eq. (1.55) reduces to  $\Gamma(Q) = DQ^2$  same as the Ficks law. It may be noted that in all these jump diffusion models, the difference is microscopic. In case the system is studied at a larger length scales or equivalently at small  $Q$  values, the information about the finer details is lost and the diffusion process looks very much like the Brownian diffusion. The variation of  $\Gamma(Q)$  with  $Q^2$  is therefore linear at low  $Q$  values and the diffusion coefficient can be obtained simply from the slope of this curve in the region of small  $Q$  values. At higher  $Q$  values however, as finer details of the jump diffusion start to emerge, the variation of  $\Gamma(Q)$  with  $Q^2$  is no more linear and saturates to a value, which is indicative of the residence times involved in the jump process.

#### 1.1.4.3. Localized Translational Diffusion

Scattering laws so far discussed are calculated assuming the particles are moving in the infinite media and there is no boundaries which can restrict their motion. But in many occasions, motions of the particles are found to be restricted. For example, translational motions of water molecules adsorbed in the cavity of porous media [6] etc. Scattering laws describing this type of motion will be different than the scattering laws described above. Volino and Dianoux [19] showed that for particle diffusion under the influence of spherical symmetry potential with,

$$\begin{aligned} V(r) &= 0 & \text{for } 0 < r < a \\ \text{and} & & \\ V(r) &= \infty & \text{for } r > a \end{aligned} \tag{1.56}$$

the intermediate scattering function can be written as

$$I_{inc}(\mathbf{Q}, t) = \sum_{l=0}^{\infty} (2l+1) \sum_{n=0}^{\infty} A_n^l(\mathbf{Q}) \exp(-D\lambda_n^l t) \tag{1.57}$$

where  $\lambda_n^l$  is the  $(l,n)^{\text{th}}$  eigen value of a one-dimensional steady state Schrödinger like equation derived from Smoluchowski equation and which is real and non-negative,  $D$  is the diffusion coefficient and  $A_n^l(Q)$  are the weight factors. The scattering law is the Fourier transform of Eq. (1.57) and can be written as

$$S_{inc}(Q, \omega) = A_0^0(Q) \delta(\omega) + \frac{1}{\pi} \sum_{\{l,n\} \neq \{0,0\}} (2l+1) A_n^l(Q) \frac{(x_n^l)^2 D / a^2}{\left[ (x_n^l)^2 D / a^2 \right]^2 + \omega^2} \quad (1.58)$$

here  $x_n^l = a\sqrt{\lambda_n^l}$  are dimensionless numbers and the values of first 99 of them are tabulated in ref. [19]. The most important observation is the appearance of the elastic component in the scattering law. This is derived from the fact that the probability for a particle confined by a potential does not decay to zero at infinite time but instead approaches to a stationary distribution. So,  $A_0^0(Q)$  in Eq. (1.58) is the fraction of elastic component in the total spectra and can be called EISF. The EISF for particle confined within a sphere of radius ‘ $a$ ’ can be written as [19]

$$A_0^0(Qa) = \left[ \frac{3j_1(Qa)}{Qa} \right]^2 \quad (1.59)$$

In the limit  $Qa \rightarrow \infty$ , the scattering law described in Eq. (1.58) reduces to Eq. (1.43), which means that in the limit  $Qa \rightarrow \infty$ , the effects of the walls become insignificant and the  $DQ^2$  law is retrieved. Volino and Dianoux also showed that in the limit  $Qa \ll \pi$ , the half width at half maxima of the quasielastic component is practically constant and can be written as

$$(HWHM)_{Qa \ll \pi} = (x_0^1)^2 D / a^2 = 4.33296 D / a^2 \quad (1.60)$$

So, in order to calculate the diffusion constant ( $D$ ), measurement of half width at half maxima of the quasielastic component at very low  $Q$  values is required.

In a more general case, particles may undergo localized diffusive motion in the spheres having different radii. For example long alkyl chain molecules having hydrogen

atoms distributed along the main molecular axis. Thus, the confining radii of all hydrogen atoms is not expected to be same. As an another example, Dellerue et al. [20] have shown for C-phycocyanin that the confinement radii of backbone protons and of side-chain protons were different. They have also shown that the confinement radii depend on the distance from the center of mass of the molecules. Therefore, a model in which the radii are distributed would be more realistic to describe the dynamics of such complex systems. The major difficulty arises from the relative weight to attribute to each of the individual scattering laws in the averaging process. Various distribution functions such as linear, Gaussian, lognormal, etc are used [10, 21, 22]. Here we discuss the simplest distribution function consists of a linear variation of the radii of the spherical volumes for a long alkyl chain exists in micellar system. [22]. Individual EISF curves corresponding to different hydrogen atoms can then be averaged to get the overall contribution. In addition to the variation of spherical volume (within which diffusion of hydrogen atom occurs) along the chain there may also be a variation in time scale of diffusion – i.e. a distribution of diffusion coefficients along the chain. For simplicity, we assume a similar variation for diffusion coefficient, as assumed for radii of the spheres, i.e. diffusivity of hydrogen atom increases linearly from the head towards tail.

The resultant scattering law for such a model can be obtained by averaging the scattering laws for hydrogen atoms belonging to different carbon atoms, generating spheres of different radii and diffusivities. The scattering law in this case can be written after modifying the Volino and Dianoux model [19] as,

$$S_{inc}(Q, \omega) = \frac{1}{N} \sum_{i=1}^N \left[ A_0^0(QR_i) \delta(\omega) + \frac{1}{\pi} \sum_{\{l,n\} \neq \{0,0\}} (2l+1) A_n^l(QR_i) \frac{(x_n^l)^2 D_i / R_i^2}{\left[ (x_n^l)^2 D_i / R_i^2 \right]^2 + \omega^2} \right] \quad (1.61)$$

where  $R_i$  is the radius of the  $i^{\text{th}}$  sphere and is equal to

$$R_i = \frac{i-1}{N-1} [R_{\max} - R_{\min}] + R_{\min} \quad (1.62)$$

and  $D_i$  is the diffusivity of hydrogen atoms belonging to  $i^{\text{th}}$  position along the alkyl chain and can be written as

$$D_i = \frac{i-1}{N-1} [D_{\max} - D_{\min}] + D_{\min} \quad (1.63)$$

where  $N$  is total number of  $\text{CH}_2$  units in the alkyl chain, which are participating in the motion. Therefore, the averaged EISF can be written as

$$A_{\text{av}}(Q) = \frac{1}{N} \sum_{i=1}^N A_0^0(QR_i) = \frac{1}{N} \sum_{i=1}^N \left[ \frac{3j_1(QR_i)}{QR_i} \right]^2 \quad (1.64)$$

Based on this model, the hydrogen atoms associated with the first carbon atom will move within the smallest sphere of radius  $R_{\min}$  and with the smallest diffusion coefficient  $D_{\min}$ . And as one goes towards other end of the chain, both diffusivity and radius of the sphere increase and the hydrogen atoms at the end of the tail and furthest from the head group (the  $\text{CH}_3$  unit) will move within the largest sphere of radius  $R_{\max}$  and with diffusion coefficient  $D_{\max}$ .

### 1.1.5. Rotational Motion

In a molecular system, in addition to translation motion of the whole molecules, rotational motion is also expected to be present. Here, we discuss various models related to the rotational motion.

#### 1.1.5.1. Isotropic Rotational Diffusion on a Surface of a Sphere

In this model, molecular reorientation is assumed to take place through small-angle random rotations on surface of a sphere i.e. on a time average, molecule does not have a preferred axis of rotation. For such a case there is no difference between a single crystal scattering law and a powder scattering law since the motion of each individual molecule is already spatially



isotropic. Sears has shown that the intermediate scattering function for a molecule undergoing isotropic rotational diffusion can be written as [23]

$$I_{inc}(Q, t) = \sum_{l=0}^{\infty} (2l+1) j_l^2(Qr) F_l(t) \quad (1.65)$$

where  $j_l(Qr)$  are the spherical Bessel functions of order  $l$ ,  $r$  is the radius of gyration and

$$F_l(t) = \langle P_l[\mathbf{u}(t) \cdot \mathbf{u}(0)] \rangle \quad (1.66)$$

Here  $P_l$  are the Legendre polynomials and  $\mathbf{u}$  is a unit vector fixed to the molecule and can be used to specify the orientation of the molecule. The first term in the summation of Eq. 1.69 with  $l=0$  gives the EISF. The EISF for isotropic rotational motion is thus simply  $j_0^2(Qr)$ . The  $F_l(t)$  contain the details of the motion and for isotropic rotational diffusion, all  $F_l(t)$  decay to zero at long times except  $F_0(t)$  ( $=1$ ) and can be written as [23]

$$F_l(t) = \exp[-l(l+1)D_R t] \quad (1.67)$$

where  $D_R$  is the rotational diffusion constant. By taking time-Fourier transform of Eq. (1.65), scattering law can be obtained as

$$S_{inc}(Q, \omega) = j_0^2(Qr) \delta(\omega) + \frac{1}{\pi} \sum_{l=1}^{\infty} (2l+1) j_l^2(Qr) \frac{l(l+1)D_R}{\omega^2 + (l(l+1)D_R)^2} \quad (1.68)$$

#### 1.1.5.2. Continuous Rotational Diffusion on a Circle

In case of some molecular systems, existence of anisotropy in the potential energy landscape gives rise to a preferred orientation. In such cases, it becomes easier for the molecule to rotate about one axis of rotation rather than others. This may give rise to a uniaxial rotation of the molecule with the individual atoms performing motion along a circle. The intermediate scattering function in this case can be written as [24]

$$I_{inc}(Q, t) = \sum_{l=0}^{\infty} j_l^2(Qr \sin \theta) \exp(-D_R l^2 |t|) \quad (1.69)$$

where  $\theta$  is the angle between the  $Q$  vector and the axis of rotation.

The scattering law corresponding to this can be obtained by taking time Fourier transform as

$$S_{inc}(\mathbf{Q}, \omega) = j_0^2(Qr \sin \theta) \delta(\omega) + 2 \sum_{l=1}^{\infty} j_l^2(Qr \sin \theta) \frac{1}{\pi} \frac{D_R l^2}{(D_R l^2)^2 + \omega^2} \quad (1.70)$$

It may be noted here that the above expression unlike the case of isotropic rotation does not give the powder averaged scattering law. No analytical expression for the powder averaged scattering law exists in this case. However, we shall see in the next section that it is possible to use the expressions for jump model by making large number of equally spaced sites.

### 1.1.5.3. Jump Rotation Among $N$ Equivalent Sites on a Circle

In this model, it is assumed that particle is allowed to have any position among  $N$  equivalent sites equally distributed on a circle of radius  $r$ . The particle is allowed to perform a random walk among these sites but jumps are restricted to neighbouring sites only. The common example of jump model is 3-fold jump rotation of methyl group about their three-fold symmetry axis [10]. In this model jumps are characterized by an angle  $\alpha$  ( $=2\pi/N$ ). The average time spent at a site between two successive jumps is  $\tau$ , which is also called the residence time. It is also assumed that the jumps are instantaneous i.e. there is no time spent while jumping from one site to the other. In this case the powder averaged scattering law is written as [24]

$$S_{inc}(Q, \omega) = B_0(Qr) \delta(\omega) + \frac{1}{\pi} \sum_{n=1}^{N-1} B_n(Qr) \frac{1/\tau_n}{(1/\tau_n)^2 + \omega^2} \quad (1.71)$$

with

$$B_n(Qr) = \frac{1}{N} \sum_{p=1}^N j_0(2Qr \sin \frac{\pi p}{N}) \cos(\frac{2\pi np}{N}) \quad (1.72)$$

$$\tau_n = \frac{\tau}{1 - \cos n\alpha} = \frac{\tau}{2 \sin^2(n\pi / N)} \quad (1.73)$$

Dianoux et al. [24], showed that for sufficiently large  $N$  ( $>6$ ) and in the region  $Qr \leq \pi$  this model gives a good approximation to the uniaxial rotational diffusion model for which the rotational diffusion coefficient can be calculated as  $D_r = 1/\tau_1 = (2/\tau) \sin^2(\pi/N)$ .

## 1.2. INSTRUMENTS AND METHODS FOR QUASIELASTIC NEUTRON SCATTERING

Neutron spectroscopy involves measurement of changes in both energy and momentum of neutrons interacting with matter, in order to obtain information about the time scale and geometry of dynamics of constituent atoms. Thus, in quasielastic neutron scattering experiment one must need to know the energy of both incident and scattered neutrons, to obtain the energy ( $\hbar\omega = E_0 - E$ ) transfer. Energy of neutron can be determined by two different methods. The first one is based on the fact that the neutron, being a wave follows Bragg's law when diffracted by crystal. By orienting a suitable single crystal, one can determine the energy of the neutrons. Triple Axis Spectrometer (TAS) is typical example based on this method. The second method is based on the fact that neutrons, being a particle follow the laws of kinematics. Neutrons wavelength ( $\lambda$ ) can be measured by measuring its velocity ( $v$ ) using the relation  $\lambda = h/mv$ , where  $h$  is the Planck constant. Since neutron flight time can be determined on sufficiently large lengths, one can analyze the energy of neutrons by using velocity selectors or choppers. The latter technique is known as time-of-flight (TOF) technique. TOF spectrometers are the example based on this method in which the energy of neutrons is determined through a direct measurement of their velocities.

Neutron spectrometers can either have direct or inverted geometry. In direct geometry spectrometers initial energy ( $E_0$ ) of neutron is kept fixed and the final energy of neutrons is

allowed to vary. On the other hand in inverted geometry where incident energy of the neutrons is varied and the final energy of the neutrons is kept fixed.

In this thesis, spectrometers having different configuration starting from conventional TAS to TOF backscattering spectrometers having instrument energy resolution (full width at half maxima) in the range of 3 meV to 17  $\mu$ eV are used to study the stochastic motions present in the system of interest. QENS experiments were carried out using in-house facility (at Dhruva reactor, Bhabha Atomic Research Centre, Trombay, India) as well as at the various mega facilities (such as Institute Laue Langevin, France; SINQ, Paul Scherrer Institute (PSI), Switzerland and ISIS at the Rutherford Appleton Laboratory, United Kingdom). Brief descriptions of spectrometers used for carrying out quasielastic measurements reported in this thesis are discussed here.

### **1.2.1. Triple Axis Spectrometer**

This spectrometer is installed at a radial beam in Dhruva reactor, Trombay [25]. Fig. 1.1 shows the schematic diagram of the triple-axis spectrometer. As the name implies, this instrument comprises three axes. A crystal monochromator situated at the first axis helps to select a monochromatic neutron beam from the Maxwellian spectrum of neutrons from the reactor. These monochromatic neutrons are incident on a sample mounted on the second axis. As the neutrons undergo energy and momentum exchange during the scattering, one can measure the spectrum of neutrons scattered at any scattering angle by means of an analyzing crystal mounted on the third axis followed by a neutron detector.

Some of the quasielastic experiments for propylene in ZSM5 zeolite have been performed using triple axis spectrometer. Experiments have been performed in inverted geometry where the final energy is kept fixed using pyrolytic graphite (002) analyzer, while the incident energy is varied using a copper (111) monochromator. By changing the Bragg angle ( $\theta_m$ ) at the monochromator, incident energies of neutrons were varied. Final energy of

neutrons is kept fixed by keeping the Bragg angle ( $\theta_A$ ) between the scattered neutron beam and analyzer fixed.

### TRIPLE AXIS SPECTROMETER

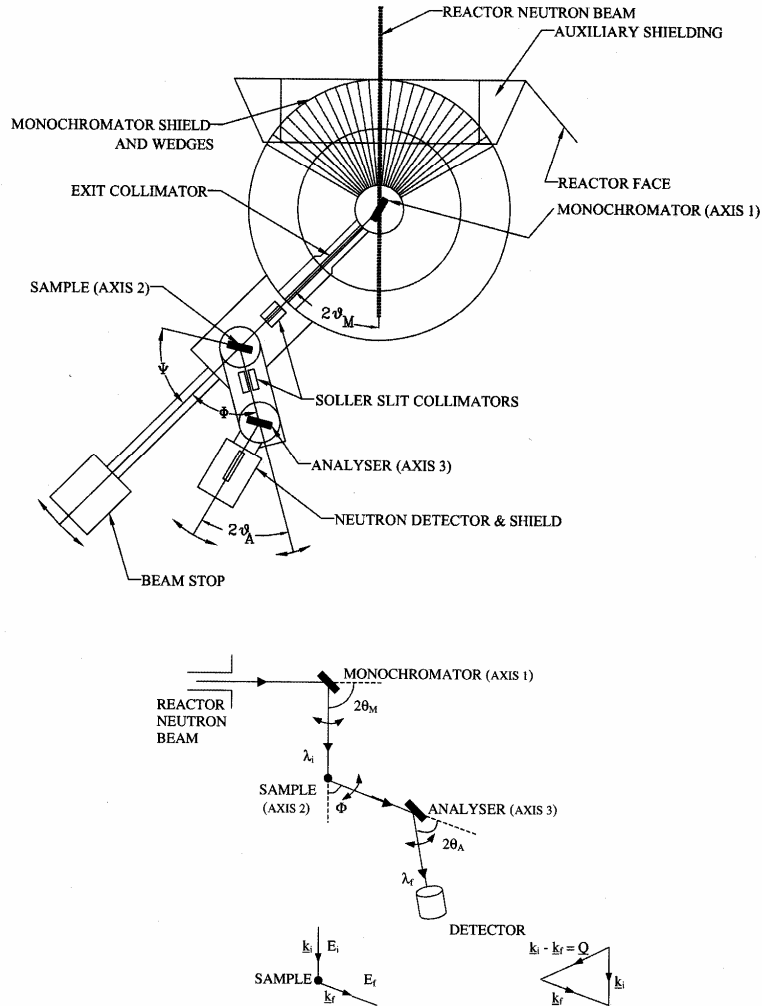


**Fig. 1.1** A Schematic diagram showing the Triple Axis Spectrometer installed at Dhruva, Trombay. The lower half of the figure shows the rotation along the three axes and the vector diagram defining the wave vector transfer.

A series of measurements, called a scan is performed with constant  $Q$ , which is obtained by suitably changing the scattering angle ( $\phi$ ) at par with changing the incident wave vector of neutrons. The spectrometer covers scattering angles ranging from  $10^\circ$  to  $100^\circ$ . At final energy of neutrons is kept fixed at 20 meV, triple axis spectrometer provides energy

resolution [full width at half-maximum (FWHM)] of  $\sim 3.3$  meV at elastic position in the  $Q$  range of  $0.8\text{--}2.5 \text{ \AA}^{-1}$ , as obtained from the measurements on a standard vanadium sample.

### 1.2.2. MARX Spectrometer

The MARX (Multi Angle Reflecting X-tal) spectrometer is, in principle, similar to a conventional triple axis spectrometer except that it measures the scattered neutrons in a larger solid angle. This is possible by using a combination of large analyzer crystal and position sensitive detector. Since the analyzer crystal is large, each point along the length of the analyzer crystal will provide a different Bragg angle and reflect neutrons with different final energies. Thus an energy scale is set up along the length of the detector and the spectrometer provides a broad energy spectrum for one instrumental configuration. The instrument is installed at the end of through tube TT1004 at the Dhruva reactor at Trombay [26]. A schematic diagram of this instrument is shown in Fig. 1.2. This instrument consists of a double monochromators (pyrolytic graphite (0002) crystals) placed inside the biological shield providing a closer approach to the source. These monochromators used in tandem for varying the incident energy of neutrons. The second monochromator is vertically bent to focus the neutron beam at the sample position. A beryllium filter, to remove neutrons of wavelength smaller than  $4 \text{ \AA}$  is installed at the end of the out of pile shielding before the sample. The sample table, the analyzer crystal and the detector are all kept in modules standing on air pads on machined and polished mild steel plates that act as the floor for the air cushion. In all the experiments performed with this instrument and reported in this thesis, the wavelength of the neutron is kept fixed at  $4 \text{ \AA}$  with incident energy of  $5.11$  meV. In this case the resolution of the instrument is about  $200 \mu\text{eV}$ . The wave vector transfer range available is  $0.6\text{--}1.8 \text{ \AA}^{-1}$ .

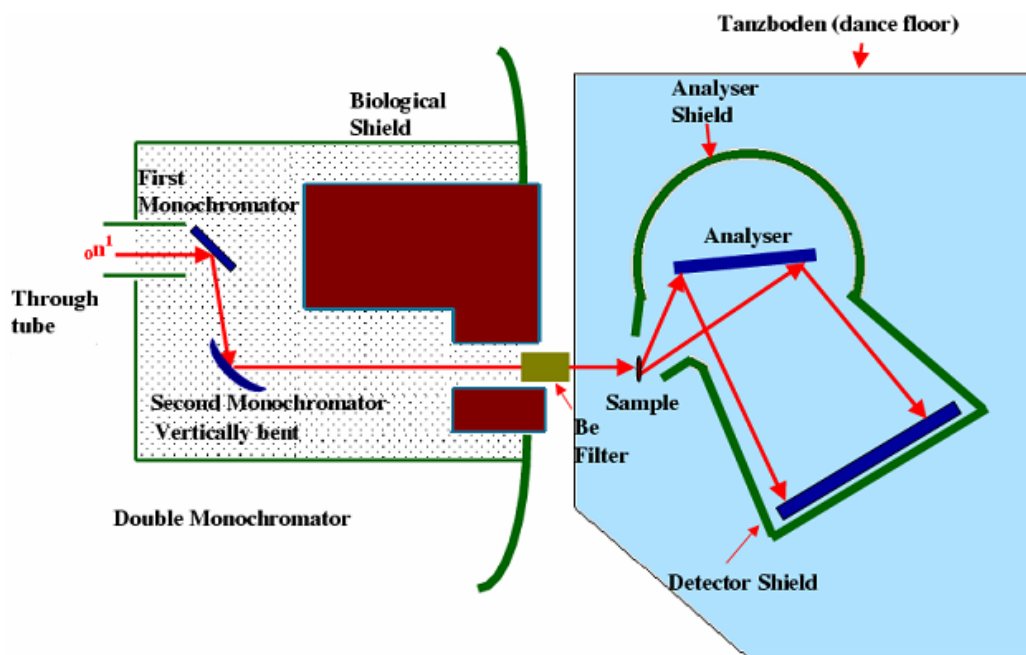


**Fig. 1.2** A Schematic diagram of the QENS spectrometer installed at Dhruva, Trombay.

### 1.2.3. IN5 Spectrometer

IN5 is a high precision direct geometry multichoppers-based Time-of-flight (TOF) spectrometer, is located at the cold neutron guide of Institut Laue-Langevin (ILL) Grenoble, France [27]. ILL is the worlds highest neutron flux research reactor. Nowadays, there are two different ways used in direct geometry TOF spectrometers for monochromatizing the beam. The first type of spectrometer uses several disk choppers separated from each other (as in present case). The other method of monochromatizing and pulsing a neutron beam is the use of a curved crystal monochromator in combination with Fermi chopper (ex. FOCUS spectrometer as will be discussed in the next section). In IN5 spectrometer, to increase the flux at sample the total beam cross-section ( $30 \times 200 \text{ mm}^2$ ) before the instrument guide is focused to a reasonable size ( $15 \times 50 \text{ mm}^2$ ) at sample position by use of tapered super-mirror guides.

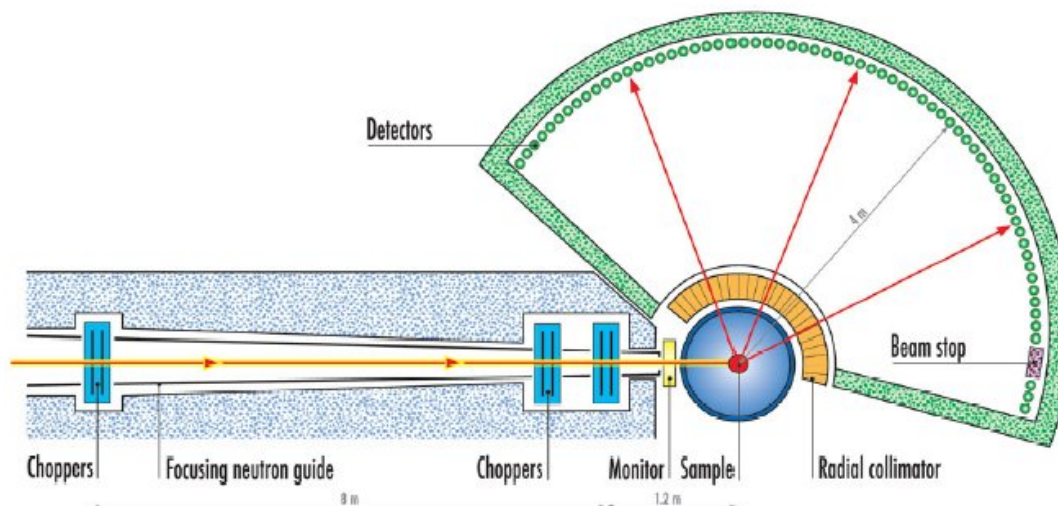
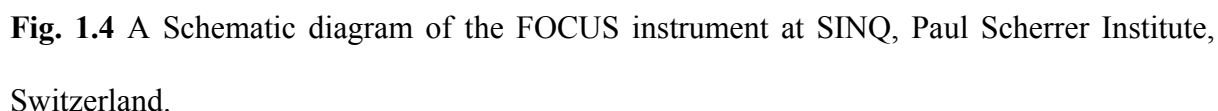


**Fig. 1.3** A Schematic diagram of multichopper IN5 spectrometer at Institut Laue-Langevin, France.

The chopper system consists of 2 counter-rotating pairs for primary pulsing and monochromatization and two additional choppers, one for control of frame overlap (fast neutron of later pulse overtake the slow neutrons from the preceding one) the other for suppression of contamination by harmonics. This offers total flexibility of wavelength selection and chopper speed, which permits considerable optimization of the energy range, energy resolution, momentum-transfer range and count rate. A schematic of IN5 spectrometer is shown in Fig. 1.3. The most outstanding concept of the new design is an array of position-sensitive detectors (PSD) inside a vacuum flight chamber. The aim was to obtain a large gapless detection surface with a spatial resolution comparable to triple-axis instruments. The PSDs allow the construction of seamless detector surfaces over large areas minimizing gaps in the spectra. Detectors of IN5 are grouped in 12 modules of 32 tubes, each module sharing the same gas with 26 mm between the axes of each one-inch (25.4 mm) diameter tube.



This instrument installed at the Swiss spallation neutron source SINQ is a direct geometry hybrid time of flight instrument, which combines a curved crystal monochromator with a Fermi Chopper [28]. A schematic of this instrument is shown in Fig. 1.4.



31

the detectors. The theta angle of the monochromator can be varied continuously from 17.5 to 70 degree. For incident wavelengths larger than 4 Å, a Be-filter is used together with the first chopper to suppress higher order contamination. The disc chopper also acts as anti-overlap chopper. There are about 375  $^3\text{He}$  counter tubes with rectangular cross-section covering scattering angle range of 10 to 130°. To prevent scattering from air, the space between the sample and the detectors is occupied by an Ar-filled box. In addition there is a 2D-multidetector covering angular range -5 to -24 degree.

### 1.2.5. IRIS Spectrometer

The IRIS time of flight backscattering spectrometer installed at the ISIS facility (Rutherford Appleton Laboratory, UK) works in inverted geometry: the final energy of the neutrons, which are detected, is in a narrow band of energy about some precise value [29]. ISIS is a spallation neutron source situated near Oxford in the United Kingdom. The backscattering principle is based on the fact that the best energy resolution from a monochromator can be obtained in backscattering geometry i.e. scattering angle  $\rightarrow 180^\circ$ . IRIS is designed for quasi-elastic and low-energy high-resolution inelastic spectroscopy. This instrument is located at N6 beam line viewing a liquid hydrogen moderator cooled to 25 K. A schematic of the spectrometer is shown in Fig 1.5. The two choppers located at 6.3 m and 10 m from the moderator respectively are used to define the energy range of incident neutrons. Both choppers are operating at 50, 25, 16.6 or 10 Hz in synchronization with ISIS operating frequency. Neutron beam transport, from the moderator to the sample position, is achieved using a neutron guide, which is terminated by a 2.5m long converging nickel titanium super mirror. The super mirror component not only helps to focus the beam at the sample position [32 mm (h) x 21 mm (w)] but also serves to increase incident flux on the sample position. Neutrons scattered from the sample are energy-analysed by means of Bragg reflection from

one of two large single crystal arrays (pyrolytic graphite and muscovite mica) in close to backscattering geometry. Each analyzer is associated with its own bank of 51 ZnS scintillator detectors. The two analyzer banks, which can operate simultaneously, afford high resolution over wide energy and momentum transfer ranges. Beryllium filter cooled at 25 K is also available when using the graphite analyzer to extend the accessible energy transfer range. Furthermore, the graphite analyzer bank itself is cooled close to liquid helium temperature to reduce background contributions from thermal diffuse scattering. The diffraction detector bank at two theta  $\sim 170^\circ$  can be used either as a diagnostic tool for samples under spectroscopic study or as a dedicated long d-spacing diffractometer with good resolution and high intensity.

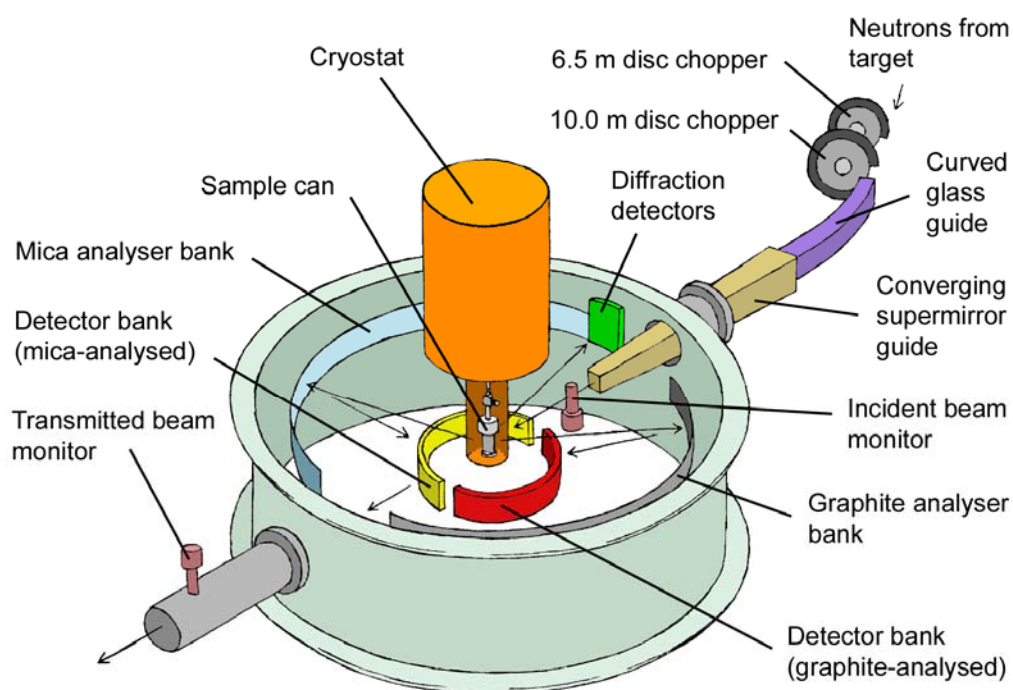


**Fig. 1.5** A Schematic diagram of the IRIS instrument at ISIS facility, Rutherford Appleton laboratory, United Kingdom.

### 1.2.6. Data Analysis-General Aspects

In the present thesis, the systems of interest are hydrogenous and as we mentioned earlier the scattered intensity from such samples are mainly from the incoherent scattering of hydrogen's. To start with, the raw data as obtained from experiment are corrected for air scattering and the energy dependent detector efficiency etc. Scattered intensity (or  $\frac{\partial^2 \sigma}{\partial \Omega \partial \omega}$ ) obtained by a quasielastic spectrometer is converted to  $S_{inc}(Q, \omega) \otimes R(\omega)$ , since the scattered intensity is proportional to the convolution product of  $S_{inc}(Q, \omega)$  and  $R(\omega)$ , where  $R(\omega)$  is the instrumental resolution function. The Detail balance condition is taken into account while converting the raw data to  $S_{inc}(Q, \omega)$ . QENS data from standard sample vanadium are used to determine the instrumental resolution.

In absence of any specific information on the nature of the dynamics present in the system,  $S_{inc}(Q, \omega)$  is approximated to a sum of elastic and quasielastic parts convoluted with the instrumental resolution

$$S_{inc}(Q, \omega) = A_0(Q)\delta(\omega) + (1 - A_0(Q))L(\Gamma, \omega) \quad (1.74)$$

where  $A_0(Q)$  is the EISF and  $L(\Gamma, \omega)$  is a Lorentzian function and represents the quasielastic part of the scattered intensity. Eq. (1.74) is then fitted to the experimentally observed data by least square fitting method with  $A_0(Q)$  and  $\Gamma(Q)$  as the fitting parameters.

In case the *EISF* obtained is not negligible, i.e. experimentally observed spectra contain significant elastic components, which suggest localized motion. For instance in case of rotational motion the EISF is not negligible and shows a typical variation with  $Q$ . The variation of EISF obtained from the foresaid fits are then compared with that according to various models of rotational motion as discussed in section 1.1.5. Once a particular model of molecular motion is found to describe this variation satisfactorily, the experimental data is

then fitted with the scattering law describing that model and the parameters of interest viz. the correlation times and lengths etc. are obtained.

In case the EISF obtained is negligible and observed spectra is described by a single Lorentzian. This indicates the presence of a pure long-range translational motion. Variation of observed HWHM of the Lorentzian with  $Q^2$  can be compared with various models of translational motion and thereby obtaining the correlation times and jump lengths along with the diffusion coefficient.

However, in the case of molecular liquids (such as water or hydrocarbons) both translational and rotational motions could be present. Observed scattering law can be written as the convolution of scattering law correspond to both motions

$$S_{inc}(Q, \omega) = S_{inc}^T(Q, \omega) \otimes S_{inc}^R(Q, \omega) \quad (1.75)$$

Here  $S_{inc}^T(Q, \omega)$  and  $S_{inc}^R(Q, \omega)$  are the scattering law for translational and rotational (localized) motion respectively. As discussed in section 1.1.3 scattering function for pure translational motion and rotational motion can be written as

$$S_{inc}^T(Q, \omega) = \frac{1}{\pi} \frac{\Gamma_T(Q)}{(\Gamma_T(Q))^2 + \omega^2} \quad (1.76)$$

$$S_{inc}^R(Q, \omega) = \left[ A_0(Q)\delta(\omega) + (1 - A_0(Q)) \frac{1}{\pi} \frac{\Gamma_R(Q)}{(\Gamma_R(Q))^2 + \omega^2} \right] \quad (1.77)$$

where  $\Gamma_T(Q)$  and  $\Gamma_R(Q)$  are the half width at half maximum of the Lorentzian functions corresponding to translational and rotational quasielastic components respectively. Therefore, Eq.(1.75) can be written as

$$\begin{aligned} S_{inc}(Q, \omega) &= \left[ A_0(Q)\delta(\omega) + (1 - A_0(Q)) \frac{1}{\pi} \frac{\Gamma_R(Q)}{(\Gamma_R(Q))^2 + \omega^2} \right] \otimes \frac{1}{\pi} \frac{\Gamma_T(Q)}{(\Gamma_T(Q))^2 + \omega^2} \\ &= \left[ A_0(Q) \frac{1}{\pi} \frac{\Gamma_T(Q)}{(\Gamma_T(Q))^2 + \omega^2} + (1 - A_0(Q)) \frac{1}{\pi^2} \frac{[\Gamma_T(Q) + \Gamma_R(Q)]}{[\Gamma_T(Q) + \Gamma_R(Q)]^2 + \omega^2} \right] \end{aligned} \quad (1.78)$$

Therefore, resulting scattering law consists of sum of two Lorentzians and a background. If both the motions occur in the same time scale, it is generally difficult to separate  $\Gamma_T(Q)$  and  $\Gamma_R(Q)$ . However, if these two motions are in different time scale (i.e. one is much slower than the other), it is possible to separate the two motions by using two different instrumental resolutions. Slower motions will contribute to high-resolution spectra and both slow and fast motion will contribute to poor resolution spectra.

Scattering law will be more complex for the system such as dispersion of spherical nanometer sized molecular aggregates (Ex. micelles, reverse micelles, proteins etc.) in the solution, due to existence of at least three distinct motions namely translational and rotation of the whole molecular aggregates in the solution and internal motion within the molecular aggregates. In that case, assuming these dynamical processes are independent to each other, resulting scattering law can be written as

$$S_{inc}(Q, \omega) = S_{inc}^T(Q, \omega) \otimes S_{inc}^R(Q, \omega) \otimes S_{inc}^{int}(Q, \omega) + B(Q) \quad (1.79)$$

Here  $S_{inc}^{int}(Q, \omega)$  is the scattering function correspond to the internal motion within the molecular aggregates. The internal motions of the aggregates involve localized dynamics of the hydrogens. This gives rise to the elastic contribution in the scattering law. Therefore, scattering law for internal motion can be expressed as

$$S_{inc}^{int}(Q, \omega) = A_{int}(Q) \delta(\omega) + (1 - A_{int}(Q)) L_{int}(\Gamma_{int}, \omega) \quad (1.80)$$

where  $\Gamma_{int}(Q)$  is the half width at half maximum of the Lorentzian function corresponding to internal motion of the molecular aggregates. The scattering function of the translational motion of whole aggregates can be represented as a Lorentzian function [30,31]. For isotropic rotational diffusion of whole aggregates scattering law can be given by sum of an elastic line and infinite series of the Lorentzians weighted by  $(2l+1)j_l^2(Qr)$  factor [30,31]. It may be noted that these weight factors are independent of the rotational diffusion constant and only depend on the radius of rotation. Analytically it has been shown that the convolution of independent

translational and rotational motions of a dense nanometer sized hard sphere particle can be well approximated by a single effective Lorentzian whose width is consistently larger than that of the sole translational contribution [30,31].

$$S_{inc}^T(Q, \omega) \otimes S_{inc}^R(Q, \omega) = L_G(\Gamma_G, \omega) = \frac{1}{\pi} \frac{\Gamma_G}{\Gamma_G^2 + \omega^2} \quad (1.81)$$

Here  $\Gamma_G$  is an effective half width at half maxima that describes the global motion of the whole aggregates (which include both translation and rotation of the whole molecular aggregates) through the solvent. Therefore, here rotational diffusion does not modify the shape of the scattering function as assumed for translational motion, or its  $Q$ -variation, but leads to an apparent diffusion coefficient, slightly higher than self diffusion coefficient for pure translational motion. Therefore, total scattering law for molecular aggregates can be written as sum of two Lorentzians and a background.

$$\begin{aligned} S_{inc}(Q, \omega) &= L_G(\Gamma_G, \omega) \otimes \left[ A_{int}(Q) \delta(\omega) + (1 - A_{int}(Q)) L_{int}(\Gamma_{int}, \omega) \right] + B(Q) \\ &= \left[ A_{int}(Q) L_G(\Gamma_G, \omega) + (1 - A_{int}(Q)) L_{tot}(\Gamma_G + \Gamma_{int}, \omega) \right] + B(Q) \end{aligned} \quad (1.82)$$

### 1.3. MOLECULAR DYNAMICS SIMULATION

Scopes of the experiments are limited by used instrument. Some materials and extreme conditions (high temperature or pressure etc.) are inaccessible to experiments. In such cases, computer simulations are useful. Simulations are helpful not only when the experiment is not feasible but also to gain deeper insights into the molecular processes involved. The aim of computer simulation is to study a system by recreating it on the computer as close to nature as possible, i.e. by simulating the dynamics of a system in all microscopic detail over a time relevant to the properties of interest. Computer simulation generates detailed information at the microscopic level and the conversion of this information into macroscopic level is the province of statistical mechanics. Another advantage of computer simulations over an

experiment is that while in an experiment it is difficult to specify all the factors, which constitute experimental environments, in a simulation, the input conditions are control of at our disposal. However, in spite of all the advantages computer simulations have over experiments, they are also not free from limitations. Major limitations of a computer simulation are the finite size effect. It is not possible to simulate a macroscopic material in a simulation. Periodic boundary conditions are applied to the system in order to simulate a large system. However some physical quantities are too sensitive to the finite size effects. The same is true for the effects due to finite time. Any two trajectories, which are initially very close to, each other, begin to diverge exponentially after some time and eventually become uncorrelated. No integration algorithm can therefore provide an exact solution to the equation of motion over a large interval time. A simulation therefore cannot run for large times. However, to simulate the physical properties of interest it is enough to run a simulation for times larger than the typical correlation times of the system.

Classical molecular dynamics (MD) simulation [32] is a technique, in which phase space trajectories are generated by integrating the Newtonian equations of motion for a system of  $N$  particles. MD simulation provides an excellent tool to supplement the results obtained from neutron scattering experiments due to overlap of the time and length scale it can access. The differential scattering cross section can be expressed in terms of time correlation functions of the spatially Fourier transformed particle density. The corresponding time correlation function can be easily obtained from molecular dynamics simulations. This enables a direct comparison between simulated and measured neutron scattering intensities. Thus, there is a mutual advantage in combining data from these two methods; experimental scattering data can be used as a gauge for the MD force field and trajectories obtained from the simulation can be used to interpret data obtained from neutron scattering experiments providing deeper insights of the dynamical process. MD simulation needs a set of initial



conditions (positions and velocities of each particle), an accurate force field to represent the interaction acting between the particles and the boundary conditions to be employed. Then solve the classical eq. of motion

$$m_i \frac{d^2 r_i}{dt^2} = f_i = -\frac{\partial}{\partial r_i} U(r_1, r_2, \dots, r_N) \quad (1.83)$$

where  $m_i$  and  $r_i$  are the mass and position of the  $i^{\text{th}}$  particle,  $U(r_1, r_2, \dots, r_N)$  is the potential energy depending on the coordinates of the  $N$  particles and  $f_i$  is the force acting on the  $i^{\text{th}}$  particle. This is a system of coupled second order non-linear differential equations and can be solved numerically. A variety of algorithms are in vogue to solve the equations of motion. They can be characterized by how accurate their results are and how much computational time is required to run an MD program using them. In the following section we will discuss briefly each ingredients of the classical MD simulation.

### 1.3.1. Building Model

Before starting MD simulation one need to develop a microscopic model of the system. In fact appropriate model building for a given system is one of the key challenges in the whole area of molecular simulation. Selection of the model (such as fully atomistic, united atom, coarse gained etc.) depends on the properties of the system to be studied and length scale and time scale to be explored. Initial position and velocities of each particle constituting the system is needed. If a system is crystalline, the atomic positions will be available form a crystallographic data. However, for a disordered system, the atomic positions can be generated randomly. The velocities of each particle can be assigned randomly from a Maxwellian distribution centered on the desired temperature.

### 1.3.2. Evaluation of Forces or Potential Energy

Lets us assume a system containing N particles. The potential energy may be divided into terms depending on the coordinates of individual particles, pairs, triplet, etc.

$$V = \sum_i v_1(r_i) + \sum_i \sum_{j>i} v_2(r_i, r_j) + \sum_i \sum_{j>i} \sum_{k>j>i} v_3(r_i, r_j, r_k) + \dots \quad (1.84)$$

The  $\sum_i \sum_{j>i}$  notation indicates a summation over all distinct pairs i and j without counting any pair twice. First term in Eq. (1.84) represent the effect of external field. The second term is pair potential, which is the most important and depends only on the magnitude of the pair separation  $r_{ij} = |r_i - r_j|$ . The  $v_3$  term in above equation involve triplet of atoms. Four body and higher terms are expected to be small (specially at liquid densities) in comparison with  $v_2$  and  $v_3$  and are neglected. However, calculation of triplet term, which involves a sum over triplet of particles, will be very time consuming on a computer. Fortunately, the pair wise approximation gives a remarkably good description of liquid properties because the average three body effects can be partially included by defining an effective pair potential. Therefore one can rewrite Eq. (1.84)

$$V = \sum_i v_1(r_i) + \sum_i \sum_{j>i} v_2^{eff}(r_i, r_j) \quad (1.85)$$

The pair potential appearing in computer simulations is generally regarded as effective pair potentials, representing many body effects. Commonly used pair potentials are Lennard-Jones 12-6, hard –sphere, square well etc. For charged particles, one should also include long-range Coulombic interactions. These potentials represent mainly the non-bonded interactions. For molecular systems, apart from these various non-bonded interactions, one must also consider intramolecular bond interactions to maintain the molecular topology. Potential parameters are the basic input to a MD simulation. The parameters are typically obtained either from *ab-initio* or semi-empirical quantum mechanical calculation or by fitting to experimental data such as neutron or X-ray diffraction, phonon dispersion curve, NMR, infrared, Raman etc.

### 1.3.3. Boundary Conditions

Due to limited available memory and calculation time MD simulation are usually performed with small number of particles,  $10 \leq N \leq 10000$ . But as in most of the cases we are interested on the bulk properties of solids or liquids therefore, need to impose some boundary conditions. However computer represents a system of  $N$  particles in isolation or surrounded by vacuum. These arrangements are not satisfactory for the simulation of bulk liquid or solid due to surface effects. This is because a large fraction of particles (49 % for  $N=1000$ ) lie on the surface. The particles on the surface experience quite different interaction from the particles in the bulk. The problem of surface effects can be overcome by implementing periodic boundary conditions (PBC) in which it is assumed that a simulation box is surrounded by an infinite number of replicas of itself. Only the  $N$  particles inside the central cell are considered explicitly, but as soon as one of the particles leaves the cell an image particle enter from the opposite side to replace it. It is important to check that if the properties of a small infinitely periodic system and the macroscopic real system, which it represents, are the same. This will depend both on the properties under investigation and the range of intermolecular interactions. If the size of simulation box is sufficiently large, the effects are normally not important, but one need to be careful when considering any properties that depend on long range correlations. Only those fluctuations are allowed which have wavelengths that are compatible with the box size.

PBC are used together with minimum image convention means that only the interaction with the nearest image is considered. However time needed to compute the force is proportional to  $N^2$ . The largest contribution to potential or force comes from neighbouring particles and for short range force we normally apply a spherical cut-off i.e. for  $r \geq r_c$ , pair potential  $U(r)$  is set to zero, where  $r_c$  is the cut-off distance. It may be noted that the cutoff

distance must not be greater than half of the simulation box length, for consistency with the minimum image convention.

### 1.3.4. Integration Algorithms

A standard method for solving a differential equation (Eq. (1.83)) is the finite difference method. A variety of integration algorithms are in vogue. The algorithm used to solve the equations of motion is chosen to optimize for computational time and accuracy. The central idea is to obtain the positions, velocities and other dynamical properties at time  $t+\delta t$ , given that the positions of the particles and their velocities are known at time  $t$ . The equations are solved a step-by-step basis. The time step chosen should be significantly smaller than the time taken by the molecule to travel a distance equal to its own size. Some of the commonly used algorithms are described below in brief.

#### 1.3.4.1. The Verlet Algorithm

Verlet algorithm [33] is based on the positions  $r(t)$ , accelerations  $a(t)$  and the positions at the previous time step  $r(t-\delta t)$ . The positions are advanced using the equation

$$r(t + \delta t) = 2r(t) - r(t - \delta t) + \delta t^2 a(t) \quad (1.86)$$

The velocities are not used here to compute the trajectories. They have been eliminated by addition of the equations obtained by Taylor expansion about  $r(t)$

$$r(t + \delta t) = r(t) + \delta t v(t) + \frac{1}{2} \delta t^2 a(t)$$

$$r(t - \delta t) = r(t) - \delta t v(t) + \frac{1}{2} \delta t^2 a(t)$$

However velocities are useful for estimating the kinetic energy (and hence the total energy) and can be calculated as

$$\mathbf{v}(t) = \frac{\mathbf{r}(t + \delta t) - \mathbf{r}(t - \delta t)}{2\delta t} \quad (1.87)$$

It may be noted here that although the positions are calculated here accurately with errors of order  $\delta t^4$ , the velocities are prone to errors of order  $\delta t^2$ . To estimate the velocities more accurately, more variables need to be stored. The Verlet algorithm thus requires only  $9N$  words to be stored, making it very compact and simple to program. The Verlet algorithm is symmetrical in time and given conservative forces is guaranteed to conserve linear momentum. The advancement of the positions takes place at a single step. However, for all the benefits this algorithm has, the handling of the velocities is rather awkward and because to advance the positions, a small term ( $a(t) \delta t^2$ ) is added to the difference of two large terms (Eq. 1.86), some numerical imprecision may be added.

The deficiency of the Verlet algorithm is tackled in a half-step ‘leap-frog’ scheme [32]. In this scheme, the positions are advanced as

$$\mathbf{r}(t + \delta t) = \mathbf{r}(t) + \delta t^2 \mathbf{v} \left( t + \frac{1}{2} \delta t \right) \quad (1.88)$$

$$\mathbf{v} \left( t + \frac{1}{2} \delta t \right) = \mathbf{v} \left( t - \frac{1}{2} \delta t \right) + \delta t a(t) \quad (1.89)$$

For this the mid-step velocities,  $\mathbf{v}(t-1/2\delta t)$  in addition to the current positions and accelerations are to be stored. The velocity equation (Eq. 1.89) is applied first and the velocities leap over the coordinates to give the mid step velocities hence the name leap-frog. During this step, the current velocities may be calculated as

$$\mathbf{v}(t) = \frac{1}{2} \left( \mathbf{v} \left( t - \frac{1}{2} \delta t \right) + \mathbf{v} \left( t + \frac{1}{2} \delta t \right) \right) \quad (1.90)$$

This is necessary so that total energy as well as any other quantities that require positions and velocities at time  $t$  can be calculated. Elimination of velocities from these equations shows that the method is algebraically equivalent to Verlet’s algorithm. This form

of the Verlet algorithm thus has an advantage over the conventional form outlined above since at no stage is a difference between two large quantities taken to calculate a smaller quantity thereby minimizing the precision loss. Moreover, since many a times the temperature is adjusted in a simulation by scaling of the velocities it is advantageous to calculate the velocities explicitly as is done here.

Velocities are handled in a more satisfactory way in yet another algorithm the ‘velocity Verlet’ algorithm, which does store positions, velocities, and accelerations all at the same time  $t$  [32]. This algorithm takes the form

$$\mathbf{r}(t + \delta t) = \mathbf{r}(t) + \delta t \mathbf{v}(t) + \frac{1}{2} \delta t^2 \mathbf{a}(t) \quad (1.91)$$

$$\mathbf{v}(t + \delta t) = \mathbf{v}(t) + \frac{1}{2} \delta t (\mathbf{a}(t) + \mathbf{a}(t + \delta t)) \quad (1.92)$$

The algorithm involves two stages of calculation with the evaluation of force performed in between. Firstly, the new positions are calculated at time  $t + \delta t$ . The velocities are then calculated at mid step as

$$\mathbf{v}\left(t + \frac{1}{2} \delta t\right) = \mathbf{v}(t) + \frac{1}{2} \delta t \mathbf{a}(t) \quad (1.93)$$

The forces and accelerations are then calculated at time  $t + \delta t$  and the velocity move completed as

$$\mathbf{v}(t + \delta t) = \mathbf{v}\left(t + \frac{1}{2} \delta t\right) + \frac{1}{2} \delta t \mathbf{a}(t + \delta t) \quad (1.94)$$

The method thus uses 9N words of storage. Because of its numerical stability, convenience and simplicity, this algorithm has been used extensively.

### 1.3.4.2. Gear Predictor-Corrector Algorithm

The other type of algorithms used often in MD simulations is the Gear predictor-corrector algorithm [34]. The basic algorithm predicts the values of positions, velocities, accelerations etc. at time  $t+\delta t$  from the corresponding values at time  $t$ . Forces and hence accelerations are then calculated from the new positions of the molecules. These are then compared with the predicted values to estimate the size of the error in the prediction step. A corrector step is then applied to obtain correct positions, velocities etc. Any thermodynamical quantity of interest can then be calculated from these corrected variables. For small time steps this algorithm is more accurate than the Verlet algorithms but is neither time reversible nor simple to program.

Once the trajectories have been obtained from a simulation run, various quantities of interest can be calculated from them. For most spectroscopic experiments the link between MD simulation and experimental data is established by a specific time correlation function, which is either measured directly or indirectly in form of a Fourier spectrum. One can obtain information about the system under study by studying these functions in detail. The integration of time correlation functions gives a measure of the transport coefficients of the system while their Fourier transform is related to the power spectra of the system. For example one may calculate the diffusion coefficient by integrating the velocity autocorrelation function (VACF) and the Fourier transform of VACF provide the density of states, which can be observed by an inelastic neutron scattering experiment. Here we will discuss in brief about some relevant time correlation functions.

## 1.4. TIME CORRELATION FUNCTIONS

Time correlation functions (TCF) provide a statistical description of the time-evolution of a variable for an ensemble at thermal equilibrium. TCF are special form of thermal averages, in

which the quantity to be averaged is the product of two dynamical variables, each taken at a different time. TCF between two quantities A and B is given as

$$C_{AB}(\tau) = \langle A(t_0)B(t_0 + \tau) \rangle \quad (1.95)$$

the brackets indicate an average over different time origins  $t_0$ . If both quantities A and B are same then

$$C_{AA}(\tau) = \langle A(t_0)A(t_0 + \tau) \rangle \quad (1.96)$$

$C_{AA}(\tau)$  is called auto correlation function of A.

In the following we describe, in brief, typical TCF's that have relevance with neutron scattering experiments. Let's assume a system of interest having N number of particles. The particles are labeled by indices  $\alpha, \beta$ . Their positions are denoted by  $R_\alpha$  and their velocities by  $V_\alpha$ .

### 1.4.1 Velocity Auto Correlation Function (VACF)

The velocity autocorrelation function (VACF) is usually defined as

$$C_{vv}(t) = \frac{1}{N} \sum_{\alpha=1}^N \frac{1}{3} \langle \mathbf{v}_\alpha(0) \cdot \mathbf{v}_\alpha(t) \rangle \quad (1.97)$$

Fourier transform of VACF is the density of states  $G(\omega)$

$$G(\omega) = \frac{1}{\pi} \int_{-\infty}^{+\infty} dt \exp[-i\omega t] C_{vv}(t) \quad (1.98)$$

Neutron weighted density of states  $G_{NW}(\omega)$  can be obtained as

$$G_{NW}(\omega) = \frac{1}{N} \sum_{\alpha=1}^N b_{\alpha,inc}^2 G_\alpha(\omega) \quad 1.99$$

$$G_\alpha(\omega) = \frac{1}{\pi} \int_{-\infty}^{+\infty} dt \exp[-i\omega t] C_{vv;\alpha}(t) \quad (1.100)$$

where  $b_{\alpha,inc}$  is the incoherent neutron scattering length of  $\alpha$  atom. Neutron weighted density of states  $G_{NW}(\omega)$  is directly related to the incoherent dynamic structure factor



$$\lim_{q \rightarrow 0} \frac{\omega^2}{q^2} S(\mathbf{q}, \omega) = G_{NW}(\omega) \quad (1.101)$$

#### 1.4.2 Mean-Square Displacement (MSD)

Another important quantity describing the dynamics of an atomic or molecular system is the mean-square displacement (MSD) of a particle. Defining

$$\delta \mathbf{R}_\alpha(t) = \mathbf{R}_\alpha(t) - \mathbf{R}_\alpha(0) \quad (1.102)$$

the MSD of particle  $\alpha$  is given by

$$\begin{aligned} \Delta^2(t) &= \frac{1}{N} \sum_{\alpha=1}^N \langle \delta \mathbf{R}_\alpha^2(t) \rangle \\ &= \frac{1}{N} \sum_{\alpha=1}^N \langle R_\alpha^2(t) \rangle + \langle R_\alpha^2(0) \rangle - 2 \langle R_\alpha(t) \cdot R_\alpha(0) \rangle \end{aligned} \quad (1.103)$$

MSD is not a time correlation function, but can be written as the autocorrelation function of  $\mathbf{R}(t)$  plus two time-dependent functions that are simple to calculate.

If the particles under consideration perform diffusive motion, the long-time limit of MSD is related to the diffusion constant,  $D$  according to the following Einstein relation

$$D = \lim_{t \rightarrow \infty} \frac{1}{6t} \Delta^2(t) \quad (1.104)$$

The diffusion constant can also be obtained by the integration of VACF using Green-Kubo relation

$$D = \int_0^\infty C_{vv}(t) dt \quad (1.105)$$

From Eqs. (1.98) and (1.105) value of DOS at  $\omega=0$  also gives diffusion constant

$$D = G(0) = \int_0^\infty C_{vv}(t) dt \quad (1.106)$$

### 1.4.3 Intermediate Scattering Function

Single particle correlations are described by the incoherent intermediate scattering function,  $I_{\text{inc}}(Q, t)$  [Eq. (1.23)] and that is of direct relevance to QENS experiments. As clear from Eq. (1.23) that  $I_{\text{inc}}(Q, t)$  contains only self terms and thus gives only information about single particle motions. It is easy to calculate  $I_{\text{inc}}(Q, t)$  from the trajectories obtained from simulation. The position vector of an interacting site of the molecule can be written as a sum of the position vector of the centre of mass of the molecule,  $\mathbf{r}_i^{\text{CM}}$  and the position vector of the site with respect to the centre of mass of the molecule  $\mathbf{d}_i$

$$\mathbf{r}_i = \mathbf{r}_i^{\text{CM}} + \mathbf{d}_i \quad (1.107)$$

This separation of the position vector gives rise to a decomposition of the intermediate scattering function into the centre of mass or translational motion and rotational motion. The corresponding intermediate scattering functions can thus be written as

$$I_{\text{inc}}^T(Q, t) = \frac{1}{N} \sum_i \overline{\left\langle \exp \left[ i\mathbf{Q} \cdot (\mathbf{r}_i^{\text{CM}}(t + t_0) - \mathbf{r}_i^{\text{CM}}(t_0)) \right] \right\rangle} \quad (1.108)$$

$$I_{\text{inc}}^R(Q, t) = \frac{1}{N} \sum_i \overline{\left\langle \exp \left[ i\mathbf{Q} \cdot (\mathbf{d}_i(t + t_0) - \mathbf{d}_i(t_0)) \right] \right\rangle} \quad (1.109)$$

Here the bar denotes average over different orientations of the  $\mathbf{Q}$  vector. This is useful to make comparison with the experimental data from the powder sample. As has been discussed earlier, the Fourier transform of this function is the scattering law that is proportional to the measured scattered neutron intensity in a QENS experiment.

The EISF is defined as the limit of the incoherent intermediate scattering function for long time,

$$EISF(Q) = \lim_{t \rightarrow \infty} I_{\text{inc}}(Q, t) \quad (1.110)$$

EISF can also be observed directly in QENS experiment, which is the fraction of elastic contribution, observed in the spectra and provide information about the geometry of the motion.

Use of Fast Fourier transforms (FFT) [35] has made the calculation of these autocorrelation functions faster and convenient. This correspondence between the functions calculated in MD simulation and the QENS experimental data has resulted in a large number of comparative studies between MD simulation and QENS experiments as discussed in the next chapters.

## **1.5. OVERVIEW OF THE THESIS**

As has been shown above, QENS and MD simulation are two techniques that can be used as complimentary tools to study stochastic molecular motion in condensed matter occurring typically in picoseconds time scale. These two techniques have been used effectively to study stochastic molecular motion that exists in various complex molecular systems including micelles and fluids confined in restricted geometries, the results of which are reported in this thesis. Amphiphilic molecules such as surfactants and lipids undergo self-association under specific conditions to form aggregates such as micelles, vesicles, wormlike micelles, etc. It is of interest to obtain a detailed description of the internal dynamics in micelles. The information about the mobility of the hydrocarbon chains is useful in understanding how a particle diffuses inside a micelle through its interior. This information can be utilized in many applications such as drug delivery, synthesis and design of nano particles, etc. Dynamical motions present in anionic sodium dodecyl sulphate (SDS) micelles have been studied and described in next chapter. It was of interest to check whether SDS molecules in the solid phase show any dynamical motion as observed in micelles. Chapter 3 describe the dynamics in crystalline SDS powder. Dynamics of cetyltrimethylammonium bromide (CTAB) based cationic micelles has also been investigated and presented in chapter 4. CTAB molecule

contains a head group, consisting of three methyl units unlike SDS. Therefore, head group dynamics may also contribute to the internal motion of the monomer. The detailed dynamical landscape has been investigated by combining the results obtained from QENS experiments carried out using two spectrometers with different energy resolutions to cover wide dynamical range. Four distinct relaxation processes that involve molecular motions at different time and length scale, from slow and global micellar motion to fast and local CH<sub>2</sub> group rotation are observed. All these relaxation processes reflect molecular motion in a very complex potential energy landscape with a large distribution of energy minima and energy barrier separating the energy states. Effect of molecular architecture of the surfactant (such as varying chain length, presence of phenyl ring, etc) on the dynamics of micelles is also studied and described in chapter 5. Fluids under the constraints of spatial restrictions within a medium are called confined fluids. The modification in dynamical behaviour of fluid in confined geometry compared to its bulk has considerable interest in scientific research, not only for fundamental aspects but also for practical applications in petroleum industries, catalysis, water purification and so forth. The dynamics of adsorbed species is indeed complex and depend upon a number of factors like the size and shape of the molecule, pore topology, guest-host interaction, and temperature [36]. Dynamics of water molecules has been investigated in nanoporous polyamide membranes, which are widely used for water filtration and in various Prussian blue analogous compounds. Chapter 6, describes water dynamics in these systems. In chapter 7, dynamics of guest molecules (propylene, ethylene glycol) adsorbed in ZSM5 zeolite is presented. Zeolites are microporous aluminosilicates with a regular pore structure, are very useful in industry as catalysts and molecular sieves. Chapter 8 provides a summary of the main results. Some future plans have also been discussed in this chapter.

## CHAPTER 2

# Dynamical Motions in Anionic Sodium Dodecyl

## Sulfate Based Micelles

### 2.1. INTRODUCTION

Surfactants are among the most versatile products in chemistry since the last century both from the point of view of their interesting properties and applications; therefore it is not surprising that they are being investigated extensively. Surfactants have a wide range of applications, for example, pharmaceutical, medical, food industries, material synthesis and so forth [37-41]. Surfactant molecules typically comprise a hydrophobic hydrocarbon chain covalently bonded to a hydrophilic group (polar, ionic or zwitterionic). In aqueous solution at a concentration above the critical micellar concentration (CMC), surfactant molecules are known to self-aggregate to form micelles. The CMC depends on various parameters such as the size of the head group, length of the hydrophobic tail, temperature, etc. Formation of micelle is a result of the delicate balance between two opposing forces, namely, the attractive hydrophobic interaction of the tails, and the ionic or steric repulsion of the head groups [41,42]. The attractive tail-tail hydrophobic interaction provides the driving force for the aggregation of surfactant molecules, while the electrostatic repulsion between the head group puts a lower limit on the size that a micelle can attain. The surfactant molecules adopt a preferential orientation with their hydrophilic head group pointing towards the aqueous phase, while their hydrophobic tails are pointing away from it. By tailoring the molecular architecture and interaction between the surfactant molecules, discrete structures with specific size, shape and order can be created [41,42] Information about the size and shape of the micelles can be obtained using small angle scattering technique [41,42]. Charged

spherical micelles can grow into elliptical rod like structures by addition of electrolytes that screen the electrostatic repulsion. Formation of worm like micelles can be induced in ionic micellar solutions by changing the electrostatic interaction between the head groups of individual amphiphiles. Addition of electrolytes in the micellar solution affects the interaction between the charged head groups and this lead to transition from spherical to rod like micelles. The shape of the aggregates has been quantitatively described in terms of the surfactant packing parameter ( $p$ ), which is the ratio of hydrocarbon chain volume and the product of effective head group area and chain length. Low packing parameter (around  $1/3$ ) prefers spherical aggregates while a value close to  $1/2$  favors rod-like aggregates [41]. Though the structure and macroscopic behavior of micelles has been studied extensively [39-42], the fast local dynamics of surfactant molecules in these assemblies and their correlation with microstructure is not investigated in detail. Local dynamics of such assemblies are important in understanding various properties such as the mechanism in releasing the solubilized drugs, micellar breaking time etc. Hence, it is of great interest to obtain a detailed description of the molecular dynamics in such systems. Different kinds of motion exist in micellar solution such as the global motion of whole aggregates, segmental motion of monomers within micelles and so forth. These can be studied experimentally using techniques such as Nuclear Magnetic Resonance (NMR) [43-45], Dynamic Light Scattering (DLS) [46-48] and Quasi-elastic Neutron Scattering (QENS) [31,49-55] etc. DLS technique is limited to time scale of global diffusion of the micelles. To probe the faster dynamical process both NMR and QENS are well suited, but the access of QENS to the spatial dimension of the motion is much more direct. QENS technique has been extensively used in the study of soft matter systems including micelles, proteins, membrane, etc. [21,30,31,49-55]. Taboney et al [49] had reported monomer dynamics in tetradecyl trimethyl ammonium bromide (TTAB) micelles and sodium bis (2 ethylhexyl) sulfosuccinate (AOT) reverse

micelles in deuterated cyclohexane ( $C_6D_{12}$ ) using QENS technique. In block copolymer micelles, Castelletto et al [50] have observed two dynamical modes e.g., fast and slow modes. The slow mode that weight factor dominates at low scattering angle corresponds to the translational diffusion of micelles whereas the fast mode is ascribed to internal motion of micelles [50]. Internal dynamics of ganglioside micellar solutions had been studied and described in terms of a simple model of confined diffusion within a sphere [51]. As discussed in chapter 1, classical molecular dynamics (MD) simulation is an excellent technique to supplement the QENS results and provide more detailed microscopic understanding about the dynamical processes present in a system. MD simulation studies have been performed on a variety of micellar systems, including sodium dodecyl sulfate (SDS), AOT reverse micelles, cetyltrimethylammonium bromide and so forth [56-61]. Recently, structure and dynamics of SDS and sodium dodecyl benzene sulfonate (SDBS) micelles have been studied in detail using MD simulation technique [59]. It was found that SDBS micelle is more spherical than SDS micelles. The mean micellar radius was found to be similar for the both micelles however analysis of the solvent accessible surface area, chain direction, and end-to-end distances showed that the hydrophobic core made by the dodecyl chains of SDBS was more tightly packed than SDS. The mobility of alkyl chain in SDS micelles was found to be larger than that of in SDBS micelles. It was shown that for both the micelles the tail end of hydrocarbon chain has larger segmental mobility than the other part of the chain. The dihedral angle distribution and the density of gauche defects can characterize the conformational motions. An increased probability of gauche defects at the terminal part of the hydrophobic alkyl chain was found in both the micelles [59].

This chapter discusses dynamical motions of SDS ( $C_{12}H_{25}OSO_3^-Na^+$ ) micelles as studied using QENS, DLS and MD simulation techniques. The alkyl chain of SDS molecule has 12 carbon atoms, attached to a sulfate group as shown in Fig. 2.1. It has been shown that

the experimental data is well described by a quantitative model that takes into account the nature of internal motions of SDS micelles. The details of the experiments are given in section 2.2 and details of the MD simulation are given in section 2.3. Results and discussion are given in section 2.4. The conclusions are depicted in section 2.5.

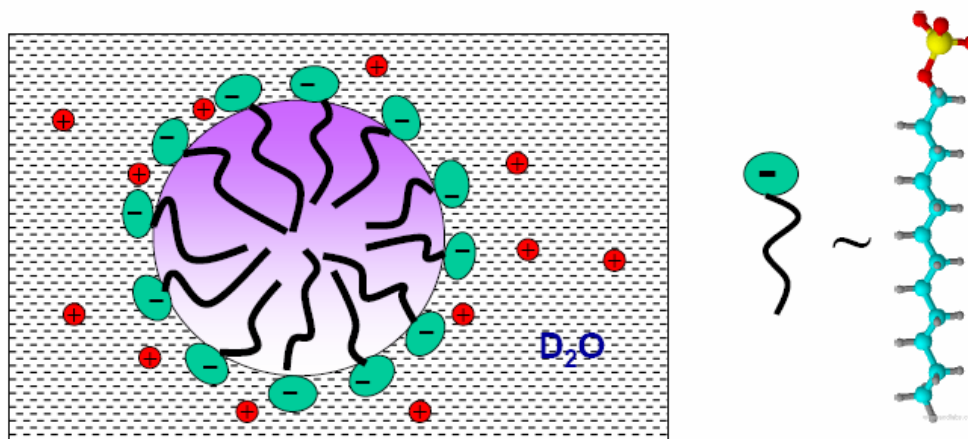


**Fig. 2.1** Schematic of an anionic SDS micellar solution.

## 2.2. EXPERIMENTAL DETAILS

SDS (electrophoresis grade) was obtained from Sisco Research Labs, Mumbai, India. As discussed in Chapter 1, for a hydrogenous sample, neutron scattering is mainly incoherent, as the incoherent scattering cross section of H atom is much greater than the coherent or incoherent scattering cross section of any other atom. Specifically for the system under study here, we are interested in the dynamics of hydrogenated micelles in solution, and thus use deuterated water to minimize the scattering contribution from the solvent. Therefore, micellar solutions were prepared by dissolving SDS in D<sub>2</sub>O (99.4% atom D purity) for QENS measurements. Preliminary QENS experiments were carried out on 10% (w/w) aqueous SDS solution in D<sub>2</sub>O at 300 K using the MARX spectrometer, (at Dhruva reactor, Trombay) which has an energy resolution of  $\Delta E \sim 200 \mu\text{eV}$  (full width at half maxima) Subsequently, QENS experiments were carried out using the high-energy resolution ( $\Delta E \sim 17.5 \mu\text{eV}$ )



backscattering spectrometer IRIS at the ISIS facility, United Kingdom. IRIS spectrometer was used in the offset mode with an energy transfer range of  $-0.3$  to  $1.2$  meV. The quasi-elastic spectra were recorded in the  $Q$  range of  $0.5 \text{ \AA}^{-1}$  to  $1.8 \text{ \AA}^{-1}$ . The samples were placed in an annular aluminum can with an internal spacing of  $1$  mm chosen to achieve no more than 10% scattering such that multiple scattering is avoided. QENS measurements were carried out on 20% as well as 10 % (w/w) SDS micellar solution in the temperature range of 300-330K in which micelles are thermodynamically stable. Measurements were also carried out on pure  $D_2O$  at each temperature to estimate the contribution of pure solvent. The ISIS QENS data analysis package, MODES [62] was used to carry out background subtraction and detector efficiency corrections.

As we shall see later, MD simulation indicates an additional faster component vis-à-vis those observed with IRIS spectrometer. To observe this faster component, further QENS experiments have been carried out using the time of flight spectrometer IN5 at the Institute Laue Langvin, Gernoble, France. IN5 offers a much larger energy transfer range compared to IRIS, suitable to observe these faster motion ( $0.1$  ps -  $30$  ps). IN5 was operated with the incident wavelength  $6 \text{ \AA}$  providing an energy resolution of  $\Delta E \sim 60 \text{ \mu eV}$  (full width at half-maximum, FWHM). Measurements were carried out on 10% (w/w) SDS micellar solution at  $300$  K in the wave-vector transfer ( $Q$ ) range  $0.3$ - $1.7 \text{ \AA}^{-1}$ . Data were collected for pure  $D_2O$  also at each temperature to estimate the contribution of pure solvent. The ILL data analysis package, LAMP [63] was used to carry out data reduction involving background subtraction, detector efficiency corrections, etc

DLS measurements were carried out for the 20 % (w/w) SDS micellar solution at  $300$ K using a Malvern 4800 Autosizer employing a 7132 digital correlator at BARC, Trombay, India. The light source was an Ar-ion laser operated at a wavelength of  $514.5$  nm

with a maximum power output of 2W. The samples of micellar solutions were filtered through 0.2- $\mu\text{m}$  filters (Acrodisc) to avoid interference from dust particles.

### 2.3. MD SIMULATION DETAILS

MD simulations studies of an SDS based micelle system were carried out in collaboration with Prof. M. Johnson, ILL, Grenoble, France. MD simulations are performed at 300K and 320K. The most probable mean aggregation number of sixty molecules for SDS micelles is determined experimentally [64-66] and used in recent SDS simulations [56,59,60,67,68]. The simulations were carried out using NAMD simulation software [69] and CHARMM 2.2 force-field parameters [70]. Our aim was to compare the results obtained from QENS data and to get deep insight on the dynamical process. A simulation box of 60 micellar like pre-assembled SDS molecules solvated with 11637 water molecules was chosen as starting configuration for the simulations. The default CHARMM 2.2 force-field parameters and charges for SDS molecules and the TIP3P [71] water model were applied. The generated  $(77\text{\AA})^3$  cubic initial structure was subjected to 10000 minimization steps using rigid bonds conditions and a 12  $\text{\AA}$  non-bonded cut-off in order to relax all the van der Waals contacts associated with the all trans geometries of the alkyl chains. After removing all restraints, the systems were equilibrated through a 10 nanoseconds (ns) long simulation carried out in isothermal–isobaric (NPT) ensemble [72]. The final equilibrated system size was about  $(71.8\text{\AA})^3$  at 300K and  $(72.3\text{\AA})^3$  at 320K. At the end, a production run of 2ns was performed in the NPT ensemble. The equations of motions were integrated with a time-step of 1 femtosecond for all the interactions, which gave good energy conservation. The electrostatic interactions were calculated using the Particle Mesh Ewald algorithm [72] with a grid spacing of 1 $\text{\AA}$ . The constant pressure was maintained to 1 atm or 1.01325 bar using Langevin piston [73].

## 2.4. RESULTS AND DISCUSSION

QENS data recorded from the pure solvent (D<sub>2</sub>O) were subtracted from that measured QENS data for the micellar solution, rather than modeling it with a separate scattering function. To minimize the systematic errors, the measurements were performed in the same sample cell first for the D<sub>2</sub>O and then for the micellar solution. Both spectra were normalized to monitor counts and the final scattered intensity from the micelles was obtained using the following relation,

$$\phi I_{micelles}(Q, \omega) = I_{solution}(Q, \omega) - (1 - \phi) I_{D_2O}(Q, \omega) \quad (2.1)$$

where  $\phi$  is the volume fraction of SDS in the D<sub>2</sub>O and can be estimated as,

$$\phi = \frac{M_{SDS} \times v}{V_{solv} + M_{SDS} \times v}, \text{ where } M_{SDS} \text{ and } V_{solv} \text{ are the mass of SDS and volume of the solvent}$$

(D<sub>2</sub>O) respectively and  $v$  is specific volume of the SDS.. The factor  $\phi$  accounts for the fact that the amount of D<sub>2</sub>O in micellar solution is less than that measured in the pure D<sub>2</sub>O sample.

Preliminary QENS experiments were performed at Dhruva, Trombay using MARX spectrometer. Significant quasielastic broadening was observed for SDS micelles suggesting dynamical motion in the time scale of the spectrometer. The data for SDS micelles are shown in Fig. 2.2 at  $Q=1.32 \text{ \AA}^{-1}$  at 300 K.

Micelles in solution have the freedom to undergo a variety of motions including whole body translational diffusion, rotation of the micelles and segmental motions of the monomer within the micelle [31,43-51]. As discussed in section 1.2.6 of chapter 1 that translation and rotation of the whole micelles can be well approximated by a single Lorentzian representing the global motion. As we shall see later global diffusion of the SDS

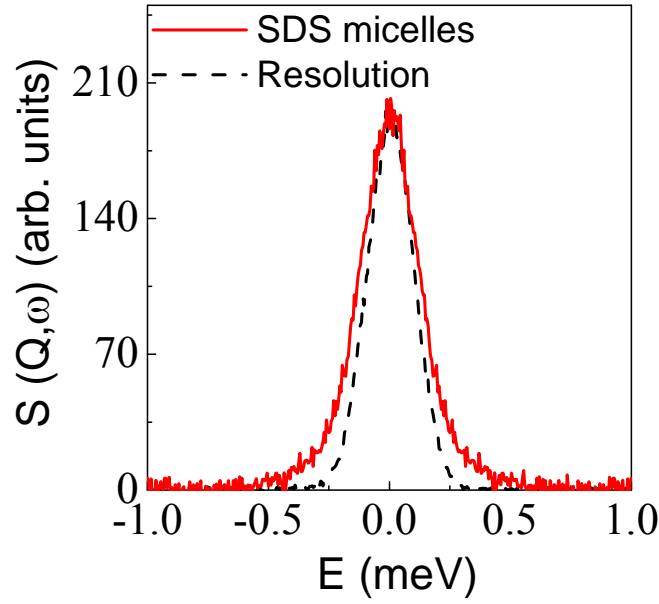


**Fig. 2.2** Observed quasielastic broadening for 10% (w/w) SDS micelles over the instrument resolution at MARX spectrometer at  $Q=1.32 \text{ \AA}^{-1}$ .

micelles is found to be order of  $\sim 2 \times 10^{-6} \text{ cm}^2/\text{s}$  which is an order of magnitude slower than the observable motions at MARX spectrometer (FWHM  $\sim 200 \text{ } \mu\text{eV}$ ) which description is given in section 1.2.2 of chapter 1. Therefore, global diffusion of the micelles is not expected to be observed at the MARX spectrometer. Thus, observed quasielastic broadening correspond to the segmental motion of the monomers.

To proceed with the analysis, it is required to separate the elastic and quasielastic components. For that, the model scattering law [Eq. (1.74)] was convoluted by the instrumental resolution function and used to describe the observed data. Observed QENS spectra are separated into elastic and quasielastic components as shown in Fig. 2.3. Significant elastic fraction is observed in the observed QENS data, which indicates the presence of localized motion. To characterize this localized motion and to get more insight, further QENS experiments have been carried out on high-energy resolution (FWHM  $\sim 17.5 \text{ } \mu\text{eV}$ ) IRIS spectrometer at ISIS facility, UK (Chapter 1, section 1.2.5).

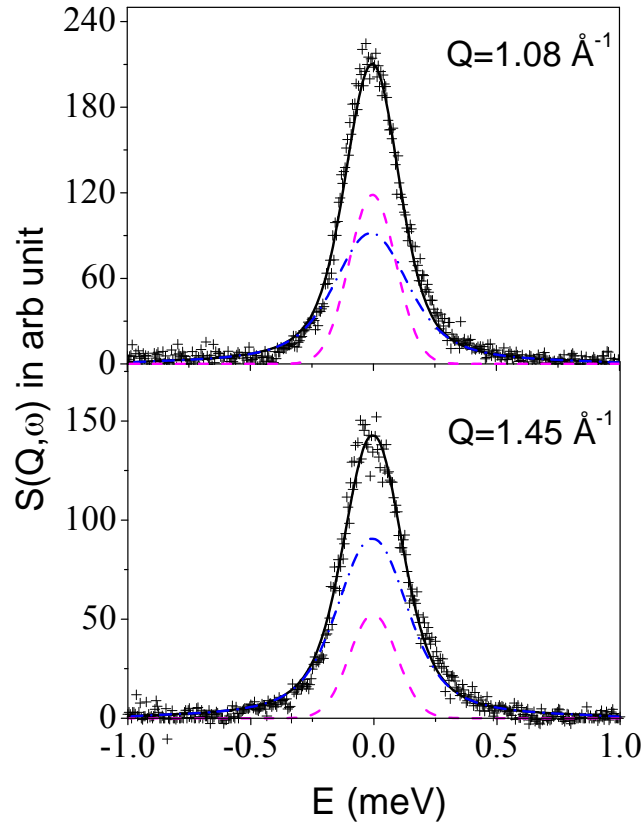


**Fig. 2.3** Typical fitted QENS spectra for 10% (w/w) SDS micelles observed at MARX spectrometer. Solid lines are the fits. Dashed and dashed-dotted lines represent quasielastic and elastic part respectively.

#### 2.4.1. Results From Data Obtained Using IRIS Spectrometer

QENS spectra for 20 % (w/w) SDS micelles are obtained using Eq. (2.1) and are shown in Fig. 2.4 at typical  $Q=1.2 \text{ \AA}^{-1}$  at different temperatures. The instrumental resolution, as measured using standard vanadium sample, is also shown in the figure for comparison. Significant quasielastic (QE) broadening over the instrumental resolution is evident at all the measured temperatures.

Both global as well as the segmental motion may contribute to the observed QENS data.. Therefore, combining these dynamical processes, the scattering law for micelles can be written as (section 1.2.6 of chapter 1)

$$S_{micelles}(Q, \omega) = \left[ A_{seg}(Q) L_G(\Gamma_G, \omega) + (1 - A_{seg}(Q)) L_{G+Seg}(\Gamma_{G+Seg}, \omega) \right] \quad (2.2)$$

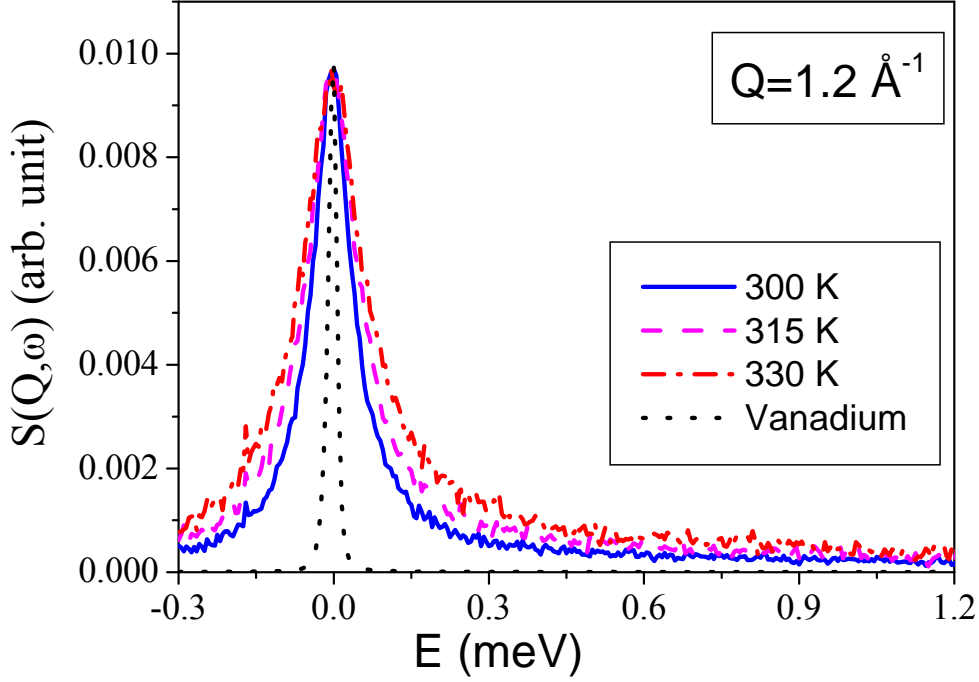


**Fig. 2.4** QENS spectra measured for the 20% (w/w) SDS micelles at IRIS spectrometer at different temperatures at  $Q = 1.2 \text{ \AA}^{-1}$ . The instrument resolution is shown with the black dashed line. Spectra have been normalised to maximum peak intensity.

Here, the Lorentzian,  $L_G(\Gamma_G, \omega)$  corresponds to the global motion of the whole micelle and the Lorentzian,  $L_{G+Seg}(\Gamma_{G+Seg}, \omega)$  represents the combination of global micellar motion and segmental motions of the micelle.  $A_{seg}(Q)$  represents the ESIF correspond to the segmental motion and can be extracted from the integrated areas of the two Lorentzian functions. Eq. (2.2) convoluted with the instrumental resolution is used to describe the QENS data corresponding to the micelles. A least square fitting method is used to fit the spectra with parameters,  $A_{seg}(Q)$ ,  $\Gamma_G$  and  $\Gamma_{G+seg}$ . No *a priori* model for the  $Q$  dependence is introduced into the fit, neither for the weight factor, nor for the HWHM of the Lorentzian functions. Therefore, the behaviour of the fit parameters can be used to verify different theoretical

models. The QENS data were analyzed using the program DAVE [74] developed at the NIST Center for Neutron Research.

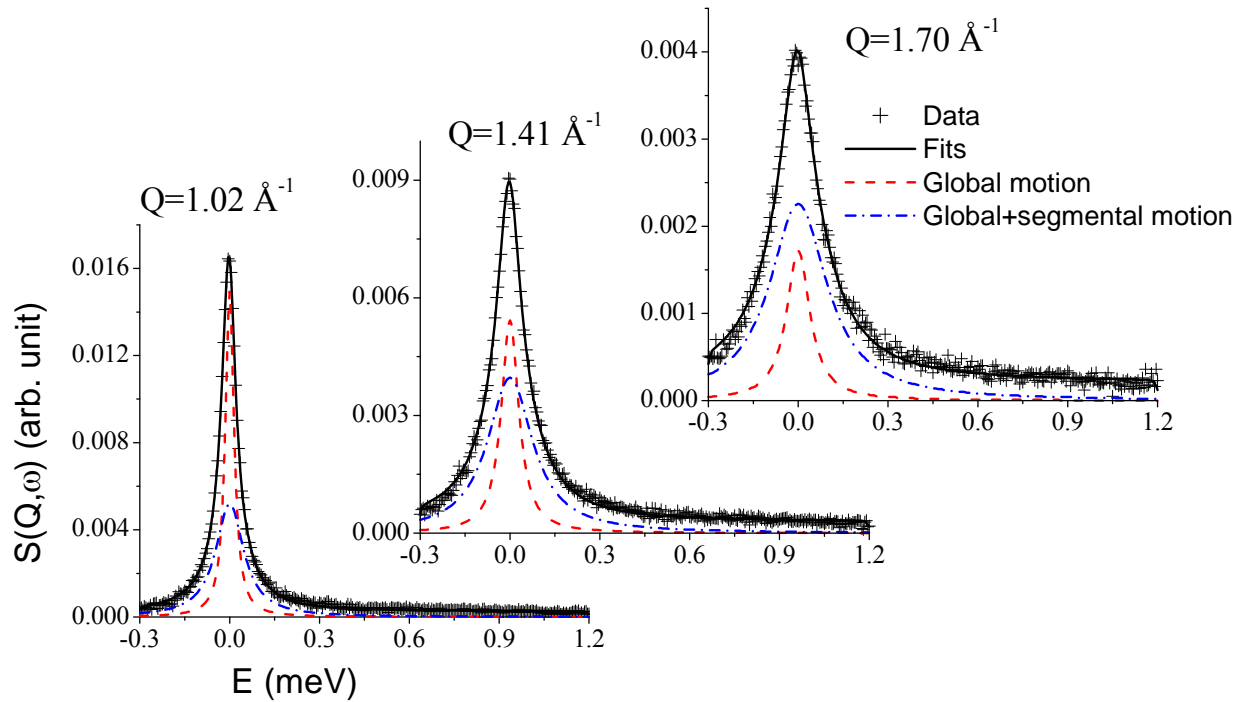


**Fig. 2.5** QENS spectra from the 20% (w/w) SDS micellar solution observed at IRIS spectrometer at 300K fitted using two Lorentzian functions at some typical  $Q$  values.

It is found that observed QENS spectra could be described very well by the model scattering function [Eq. (2.2)] as shown in Fig. 2.5 at some typical  $Q$  values. To gain more insight into the nature of the dynamical processes, the behaviour of the parameters correspond to Lorentzian functions were investigated. As given in Eq. (2.2), narrower Lorentzian function (hereafter referred as 1<sup>st</sup> Lorentzian) corresponds to the global motion only, whereas broader Lorentzian function (hereafter referred as a 2<sup>nd</sup> Lorentzian) represents the convolution of two Lorentzian functions (global micellar motion convoluted with the segmental motion of the monomer with the micelles). The variation of the HWHM,  $\Gamma_G$ , of the 1<sup>st</sup> Lorentzian with  $Q^2$  at each temperature is shown in Fig. 2.6. The data is described very well by simple Brownian motion using Ficks law,  $\Gamma_G = D_G Q^2$ . The diffusion constant for

the global micellar motion,  $D_G$ , as obtained from the slope is found to be  $(2.5 \pm 0.1) \times 10^{-6}$  cm<sup>2</sup>/sec at 300K. As expected,  $D_G$  increases with increasing temperature and at 330 K it is found to be  $3.1 \pm 0.2 \times 10^{-6}$  cm<sup>2</sup>/sec. Global diffusion has also been observed for other micelles, proteins in solutions etc. using QENS technique [21,30,31,50]. For example, Perez et al [30] studied the global diffusion of myoglobin and lysozyme proteins and found diffusion constants of  $(8.2 \pm 0.2) \times 10^{-7}$  cm<sup>2</sup>/sec and  $(9.1 \pm 0.2) \times 10^{-7}$  cm<sup>2</sup>/sec respectively at 298 K. This is slower than SDS micelles by a factor of 3, most likely owing to the difference in hydrodynamic diameters between proteins and micellar aggregates.

Having characterized the global diffusion, data are now analyzed for the segmental motion of the monomers. The  $Q$ -dependence of the EISF,  $A_{\text{seg}}(Q)$  at different temperatures is shown in Fig. 2.7. Internal motion of a micelle involves bending, stretching of chemical bonds,

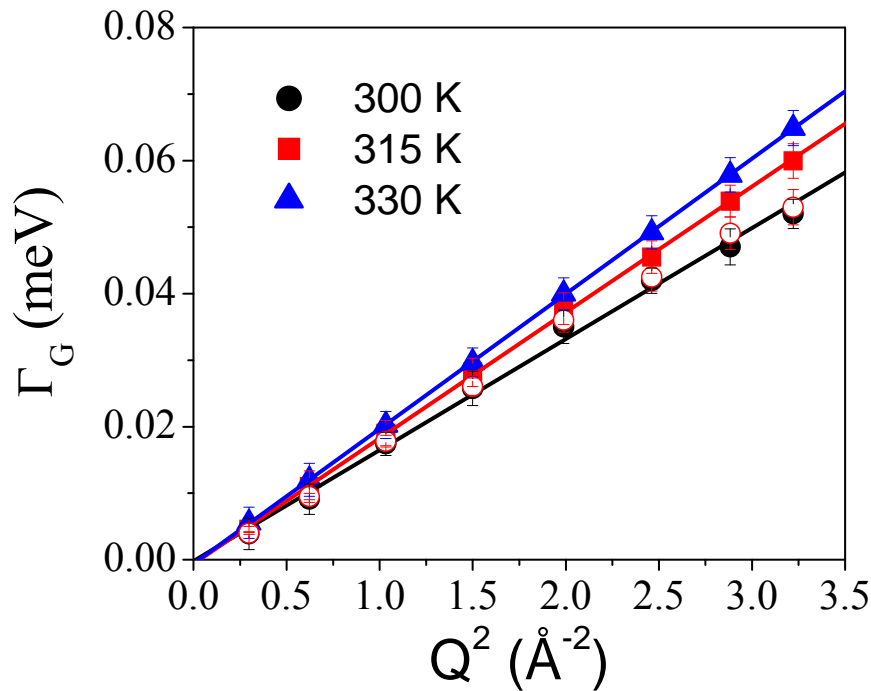


**Fig. 2.6** Variation of HWHM of the Lorentzian representing global motion,  $\Gamma_G$  for 20% (w/w) SDS micellar solution with  $Q^2$  at temperatures of 300 K, 315 K and 330 K. The lines



correspond to a fit with Fick's diffusion. HWHM's of Lorentzian correspond to global motion for 10% (w/w) SDS micellar solution at 300 K is also shown by open circle.

large amplitude oscillations, reorientation of alkyl chain etc. All these various motions can effectively modeled by localized translational diffusion within a sphere. For a long alkyl chain system, the flexibility of the chain demands that the hydrogen atoms at different positions along the chain move in spheres having different radii and diffusivities (section 1.1.4.3 in chapter 1). The distribution of radii and diffusivities could be linear, Gaussian, lognormal function, etc. [21,22,55]. We adopt a simple linear distribution which was also used to describe dynamics of alkyl chain in dicopper tetrapalmitate [22], phospholipid liposomes [55] etc., whereas lognormal distribution was used to describe the internal motion in the more complex calmodulin protein [21]. Our model seems more appropriate since it takes into account that different protons along the SDS chains undergo diffusive motion over significantly different spatial extents. Therefore, scattering law for alkyl chain motion is given as in Eq. (1.61) of chapter 1.

$$S_{seg}(Q, \omega) = \frac{1}{N} \sum_{i=1}^N \left[ A_0^0(QR_i) \delta(\omega) + \frac{1}{\pi} \sum_{\{l,n\} \neq \{0,0\}} (2l+1) A_n^l(QR_i) \frac{(x_n^l)^2 D_i / R_i^2}{\left[ (x_n^l)^2 D_i / R_i^2 \right]^2 + \omega^2} \right] \quad (2.3)$$

$R_i$  is the radius of the  $i^{\text{th}}$  sphere and is equal to

$$R_i = \frac{i-1}{N-1} [R_{\max} - R_{\min}] + R_{\min} \quad (2.4)$$

where  $D_i$  is the diffusivity of hydrogen atoms belonging to  $i^{\text{th}}$  position along the SDS chain and can be written as

$$D_i = \frac{i-1}{N-1} [D_{\max} - D_{\min}] + D_{\min} \quad (2.5)$$

where  $N$  is total number of  $\text{CH}_2$  units, which are taking part in the motion. In SDS ( $\text{C}_{12}\text{H}_{25}\text{OSO}_3^- \text{Na}^+$ ),  $N$  equals to 12. Therefore, the averaged EISF can be written as

$$A_{av}(Q) = \frac{1}{12} \sum_{i=1}^{12} A_0^0(QR_i) = \frac{1}{12} \sum_{i=1}^{12} \left[ \frac{3j_1(QR_i)}{QR_i} \right]^2 \quad (2.6)$$

Based on this model, the hydrogen atoms belonging to different  $CH_2$  units will move within spheres; size of confining spheres and associated diffusivities vary linearly from a minimum to a maximum value. Given the structure of SDS molecules, it is expected that minimum value of radius ( $R_{min}$ ) and diffusivity ( $D_{min}$ ) would correspond to  $CH_2$  unit nearest the head group. As one goes away from the head group along the SDS chain, both diffusivity and radius of the sphere increase and the hydrogen atoms at the end of the tail and furthest from the head group (the  $CH_3$  unit) will move within the largest sphere of radius  $R_{max}$  and with diffusion coefficient  $D_{max}$ .  $R_{min}$  and  $R_{max}$  are determined by least squares fit of the extracted EISF as described in Eqs. (2.4) and (2.6).

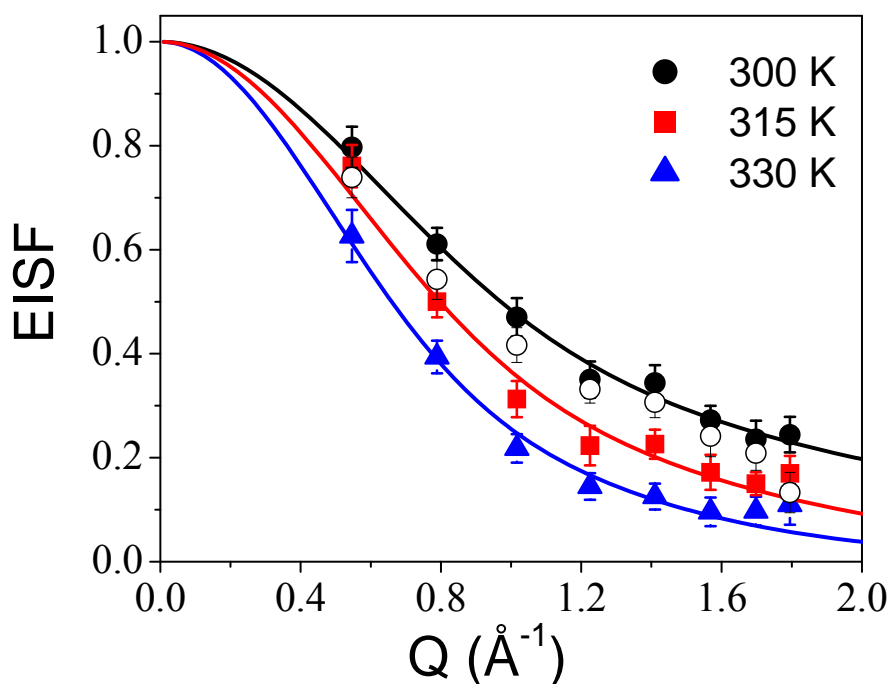


**Fig. 2.7** Variation of EISF for 20% (w/w) SDS micellar solution with  $Q$ . The solid lines represent calculated EISF for a model described in the text. EISF observed for 10% (w/w) SDS micellar solution at 300 K is also shown by open circle.

Fits are found to be reasonably good at all the temperatures as shown in Fig. 2.7 which confirms that a linear variation is a reasonable description of the internal dynamics of the SDS monomers in the micelles. A sketch to demonstrate the proposed model is shown in Fig. 2.8 where the hydrogen atoms in the monomer are shown to diffuse within a spherical volume of different sizes, which increases linearly from the head towards tail.

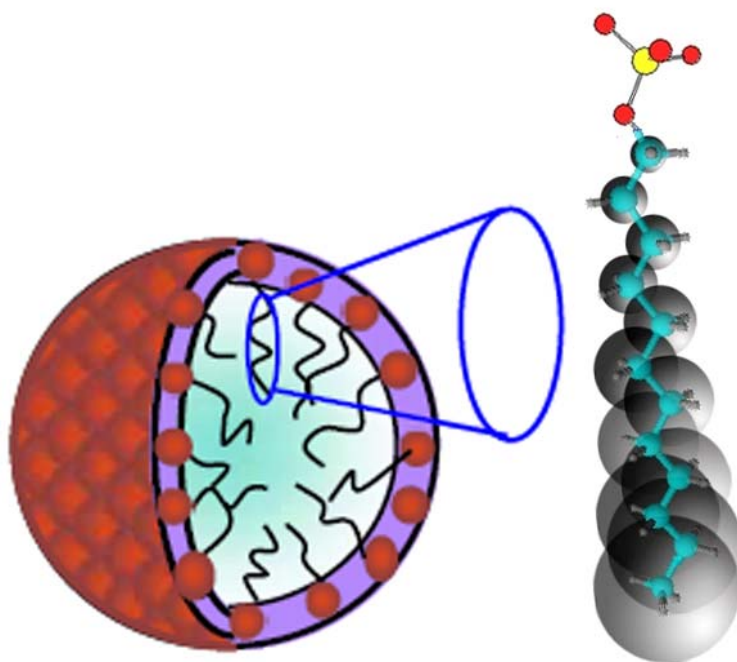


**Fig. 2.8** Schematic showing the model in which hydrogen atoms of a SDS chain moving in spheres of different radii. The radii of sphere are shown to increase linearly along the SDS chain.

This picture is consistent with that emerging from NMR spectral investigations and fluorescence decay measurements of micellar solutions [43,45,75]. Bockstaele et al [75] demonstrated that the segmental mobility of the chains of micelle-forming molecules seems to increase from the polar head to the non-polar tail. However, in these studies no quantitative estimate of the microscopic length scales of diffusion was provided. Here we have obtained a

quantitative estimate of the length scale of localized motions for individual protons.  $R_{\min}$  and  $R_{\max}$  for all the systems studied at different temperatures are given in Table 2.1. At 300 K, the localized motions of hydrogen atoms along the SDS chain are found to be restricted to spheres of radii between  $0.4 \pm 0.1$  Å to  $3.4 \pm 0.1$  Å, and increase to  $1.2 \pm 0.1$  Å and  $4.4 \pm 0.2$  Å at the highest temperature measured of 330 K. The exact values for  $R_{\min}$  should be taken with care as they are unrealistically small, and thus indicate that there is negligible movement of the protons in the first carbon position held by the head-group.

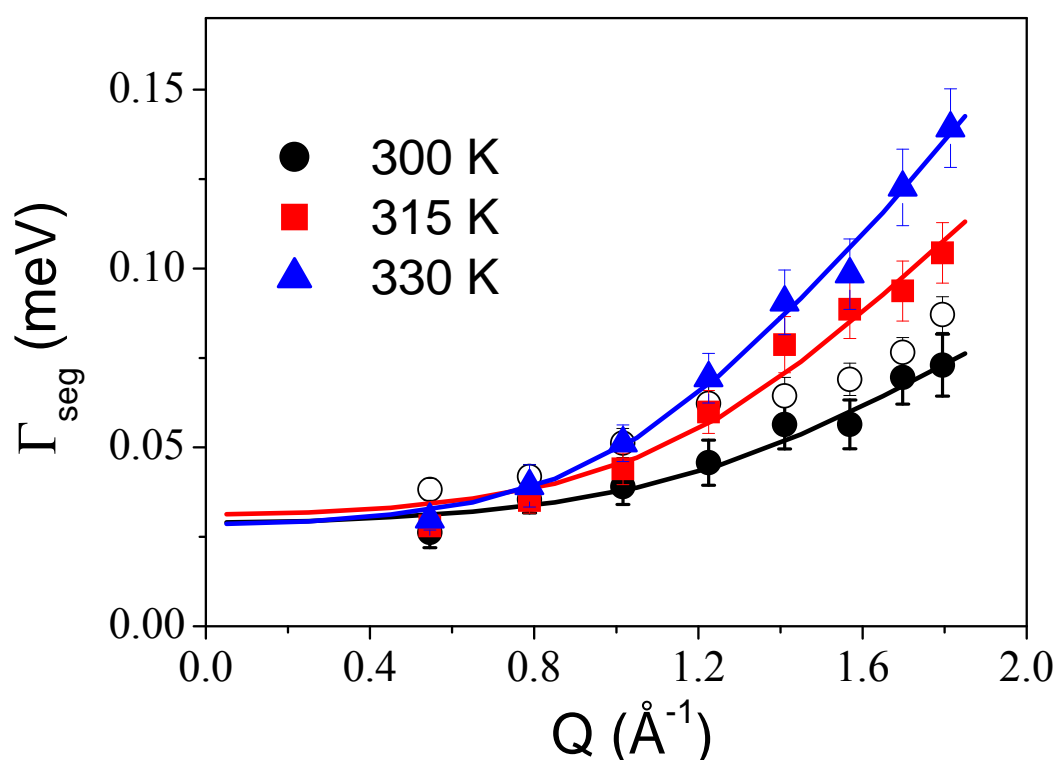


**Fig. 2.9** Variation of the HWHM of the Lorentzian representing the segmental motion, for the 20% (w/w) SDS micellar solution with  $Q$ . The solid lines are fits with a model in which the hydrogen atoms at the different  $\text{CH}_2$  positions along the of SDS chain are moving within spheres of varying radii and with varying diffusion coefficients. HWHM of the Lorentzian correspond to segmental motion for the 10% (w/w) SDS micellar solution at 300 K is also shown by open circle.

We now turn to examine the variation of the width of the Lorentzian corresponding to the segmental motion as a function of  $Q$  as another important test of the validity of our model. Behaviour of width correspond to segmental motion,  $\Gamma_{\text{seg}}(Q)$  with  $Q$  is shown in Fig. 2.9 at different temperatures. At low  $Q$ , where the motion essentially corresponds to motion at larger distance, behaviour of HWHM approaches a constant value, which is independent of  $Q$ . This can be explained in terms of steric hindrance between the stacked molecules in the micelles.  $\text{CH}_2$  units are not able to move far from the chain axes and therefore, HWHM tends to a constant value at lower  $Q$ . As it is not possible to get an analytical expression for the HWHM of the quasielastic part for the present model, one can calculate the same numerically for given values of  $R_{\text{min}}$ ,  $R_{\text{max}}$ ,  $D_{\text{min}}$  and  $D_{\text{max}}$  using Eqs. (2.3) and (2.5). The least squares fitting method is used to describe the observed QE width correspond to segmental motion with  $D_{\text{min}}$  and  $D_{\text{max}}$  as parameters while the values of  $R_{\text{min}}$  and  $R_{\text{max}}$  are already known from the fit of the EISF (Fig. 2.7). Solid lines in Fig. 2.9 represent the fit as obtained from the above description. As can be seen from the Fig. 2.9 the model provides a very good description of the data. The obtained values of  $D_{\text{min}}$  and  $D_{\text{max}}$  at different temperature are given in Table 2.1. At 300K,  $D_{\text{min}}$  and  $D_{\text{max}}$  for the 20% (w/w) SDS micellar solution are found to be  $(0.1 \pm 0.1) \times 10^{-5} \text{ cm}^2/\text{s}$  and  $(0.9 \pm 0.1) \times 10^{-5} \text{ cm}^2/\text{s}$  respectively. Diffusivity is found to increase with temperature, with values at 330K being  $(0.7 \pm 0.1) \times 10^{-5} \text{ cm}^2/\text{s}$  and  $(1.5 \pm 0.2) \times 10^{-5} \text{ cm}^2/\text{s}$  respectively.

To understand the effect of surfactant concentration on the dynamics of the micelles QENS measurements were also carried out on 10% (w/w) SDS micellar solution at 300 K. QENS spectra for 10% (w/w) SDS micelles are very well described by two Lorentzians similar to the case of 20% (w/w) SDS solution. The *HWHM* of first Lorentzian, which correspond to the global motion found to be similar to that of 20% (w/w) SDS micellar solution and shows Fickian type behaviour (Fig. 2.6). The extracted EISF and HWHM

correspond to segmental motion are shown in Figs. 2.7 & 2.9 respectively. Both EISF as well as HWHM are found to be more or less similar to 20% (w/w) SDS micelles at the same temperature. The fact that very similar nature of the global as well as segmental motion implies that dynamics of SDS micelles is not very sensitive to the surfactant concentration, at least, in the present range of the measurements. Finally, a good description of the QENS data for two different surfactant concentrations at different temperatures with the same model verifies the consistency of the model.

**Table 2.1** Radii of spheres,  $R_{\min}$  and  $R_{\max}$  and corresponding diffusion constants,  $D_{\min}$  and  $D_{\max}$  as obtained from the least square fitting of the data with a model discussed in the text for different temperatures.

Sample	$T$ (K)	$R_{\min}$ (Å)	$R_{\max}$ (Å)	$D_{\min}$ ( $\times 10^{-5}$ cm <sup>2</sup> /s)	$D_{\max}$ ( $\times 10^{-5}$ cm <sup>2</sup> /s)
20 % SDS	300	$0.4 \pm 0.1$	$3.4 \pm 0.1$	$0.1 \pm 0.1$	$0.9 \pm 0.1$
-do-	315	$0.9 \pm 0.1$	$3.8 \pm 0.1$	$0.5 \pm 0.1$	$1.2 \pm 0.1$
-do-	330	$1.2 \pm 0.1$	$4.4 \pm 0.2$	$0.7 \pm 0.1$	$1.5 \pm 0.2$

#### 2.4.2. Results from Data obtained using Dynamic Light Scattering

The results obtained for the global motion with QENS are compared with those from dynamic light scattering (DLS) studies. In DLS technique, a laser beam illuminates sample and the fluctuations of the scattered light are detected at a particular wave vector transfer,  $Q$  by a fast photon detector. Fluctuations in the scattering intensity arise due to the Brownian motion of particles (micelles, polymers, proteins, etc.) in the solution. DLS technique is also known as photon correlation spectroscopy and quasielastic light scattering. It is possible to

directly measure the intensity fluctuations with time. However, the best way is to extract usable information from the fluctuating intensity by constructing its auto correlation function. The normalized second order auto correlation function of the scattered intensity,  $g^2(Q, \tau)$  can be written as

$$g^2(Q, \tau) = \frac{\langle I(Q, t)I(Q, t + \tau) \rangle}{\langle I(Q, t) \rangle^2} \quad (2.7)$$

where  $\tau$  is the correlator delay time.  $I(Q, t)$  and  $I(Q, \tau)$  represents the scattered light intensity at any arbitrary time  $t$  and at a later time  $\tau$ . For photo counts obeying Gaussian statistics  $g^2(Q, \tau)$  is related to the first order auto correlation function of the electric field  $g^1(Q, \tau)$  by the Siegert relationship

$$g^2(Q, \tau) = \beta + A |g^1(Q, \tau)|^2 \quad (2.8)$$

where  $\beta$  is the baseline and  $A$  is an adjustable parameter dependent on the scattering geometry and independent of  $\tau$ . In a suspension of mono disperse particles, in the low concentration regime, undergoing Brownian diffusion,  $g^1(Q, \tau)$  can be written as a single exponential.

$$g^1(Q, \tau) = \exp(-\Gamma_{DLS} \tau) \quad (2.9)$$

where  $\Gamma_{DLS}$  is the relaxation rate of the correlation function given by  $\Gamma_{DLS} = D_c Q^2$ ;  $D_c$  being the collective translational diffusion coefficient [48].

However, in most of the cases, samples are polydispersed. Thus, the first order autocorrelation function is a sum of the exponential decay functions corresponding to each of the species in the population. In that case, Eq. (2.9) can be written as

$$g^1(Q, \tau) = \int_0^\infty G(\Gamma_{DLS}) \exp(-\Gamma_{DLS} \tau) d\Gamma_{DLS} \quad (2.10)$$

where  $G(\Gamma_{DLS})$  represents the distribution of relaxation rate and is function of the number and size of the scatterers. For narrow polydispersity and non-interacting particles, the above expression can be simplified to the well-known cumulant expansion [76].

$$\ln(g^{(1)}(Q, \tau)) = b - \overline{\Gamma_{DLS}}\tau + \frac{\mu_2\tau^2}{2} \quad (2.11)$$

The first cumulant ( $\overline{\Gamma_{DLS}}$ ) and the second cumulant ( $\mu_2$ ) give the mean and variance of the relaxation rate respectively.

However, in case of charged and concentrated particles in the solution, it has been shown [47,48] that the autocorrelation function,  $g^{(1)}(Q, \tau)$  can be described by a sum of two single exponentials. It has been also shown [47,48] that fast and slow components are related to collective and self-diffusion of the particle respectively.

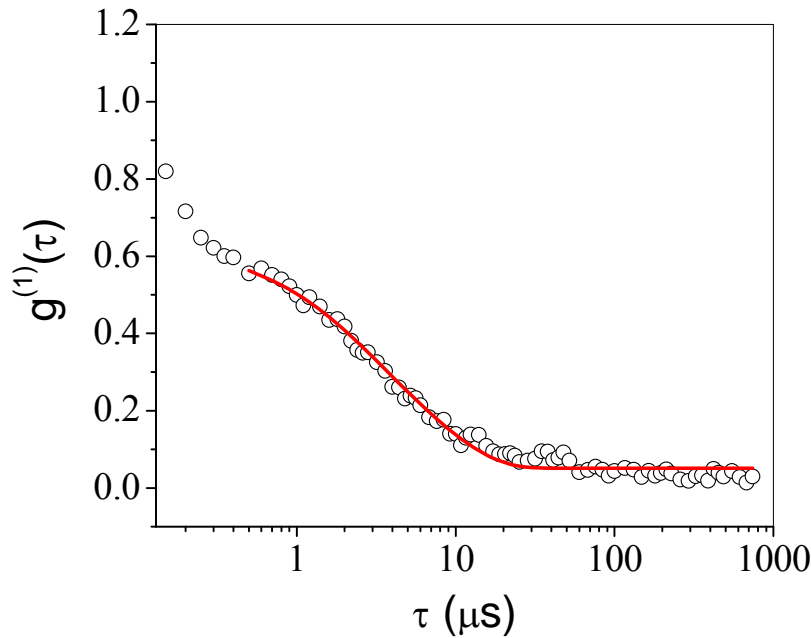


**Fig. 2.10** Electric field correlation function obtained from 20% (w/w) SDS micellar solution at a scattering angle of  $130^\circ$ . Only long time behaviour of  $g^{(1)}(\tau)$  is fitted by cumulant method as shown by the solid line.

Fig. 2.10 shows a typical scattered field correlation function measured from 20% (w/w) SDS solution at a scattering angle of  $130^\circ$ . The long time behavior of the correlation function can be analyzed using the cumulants method [76] (solid line) while the data at very short times suggest the occurrence of an additional relaxation. Due to the limited number of data points at very short time and poor statistics, no attempts were made to evaluate the



collective diffusion coefficient of the micelles for the fast component. Thus, the major relaxation process observed here corresponds to self-diffusion coefficient of the micelles arising from the slow component.

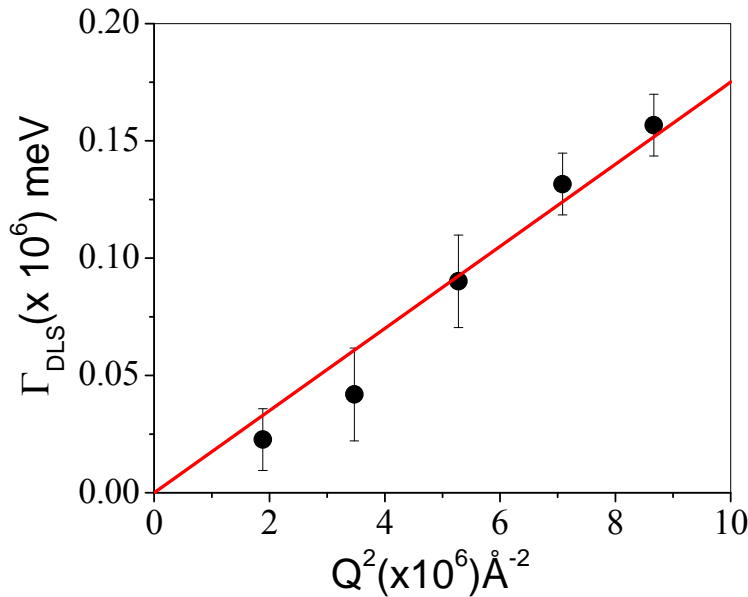


**Fig. 2.11** Variation of the mean relaxation rate ( $\Gamma_{DLS}$ ) of correlation functions with  $Q^2$  for 20% (w/w) SDS solution at 300 K, as measured by DLS. The line corresponds to the fit assuming Fickian diffusion.

Fig. 2.11 shows the  $Q^2$  dependence of the mean relaxation rate as obtained for the 20% (w/w) SDS solution, at 300K.  $\Gamma_{DLS}$  vs  $Q^2$  show linear behaviour (Fig. 2.11), as expected for Brownian motion. Self-diffusion coefficient,  $D_{DLS} = (2.7 \pm 0.3) \times 10^{-6} \text{ cm}^2/\text{s}$  is obtained and this is in agreement to that obtained from QENS measurements.

### 2.4.3. Results from MD Simulation

To get more insight on the dynamical processes that might exist in micelles, classical MD simulation of SDS micellar solution has been carried out at two different temperatures 300 and 320 K. A vast amount of information can be extracted from the full phase space simulation trajectory of the micellar solution. Firstly structure and geometry of the micelles is

characterized to validate the simulation outcomes. Once agreement between simulation and experiment is verified, analysis of the quantities related to the dynamical properties of the micelle at the atomic scale has been carried out. The shape of a micelle can be characterized by examining the eccentricity,  $e$ , defined as

$$e = 1 - \frac{I_{\min}}{I_{\text{avg}}} \quad (2.12)$$

where  $I_{\min}$  is the smallest moment of inertia of the SDS micelles along the x, y, or z axis and  $I_{\text{avg}}$  is the average of all three moments of inertia. It may be noted that for perfect sphere the eccentricity is zero, whereas  $e \sim 1.0$  for a flat like object. The average value of eccentricity obtained for present case is  $\sim 0.1$ . This is consistent with the SANS data on SDS micelles [77] in which scattering data were analyzed using models for oblate or tablet-shaped micelles in the entire regime of scattering vectors that are relevant for determining the structure of the micelles. The micelle is not rigid, but kept inflating and deflating during the simulation in breathing-like manner. This is in good agreement with recent work done by F. Palazzesi et al [59]. The average radius of gyration of the SDS micelle is obtained as 16.3 Å, which is consistent with the earlier simulation studies on the SDS micelles [56,59,60]. The micelle structure can be analyzed in terms of the probability distribution of the distance of selected atoms from its center of mass. The probability distribution analysis of the distance of selected atoms of SDS molecules from the center of mass of the micelle have been calculated and shown in Fig. 2.12. It is evident from Fig. 2.12 that as the distance from the head group increases the probability distribution of the carbon atoms gets broadened. For the ‘C1’ atom (closest to head group) the distribution is similar to that of sulfur atom in the head group. An increase in the distribution occurs upon going from ‘C1’ to ‘C6’ atom and it becomes largest for the ‘C12’ belonging to the methyl group at the tail end. The head groups shown here is the geometric center of all of the four oxygen atoms and the sulfur. We have found that the maximum probability for the head group is at 19.5 Å distance from center of mass of

micelles and it decreases rapidly on either sides of the maximum as shown in Fig. 2.12. These results are in good agreement with the earlier MD simulation studies on SDS micelles [56,59,60]. Bendedouch et al. [78] reported a mean micellar radius of 18.9 Å for lithium dodecyl sulfate using small angle neutron scattering, which is also consistent with the present observation.

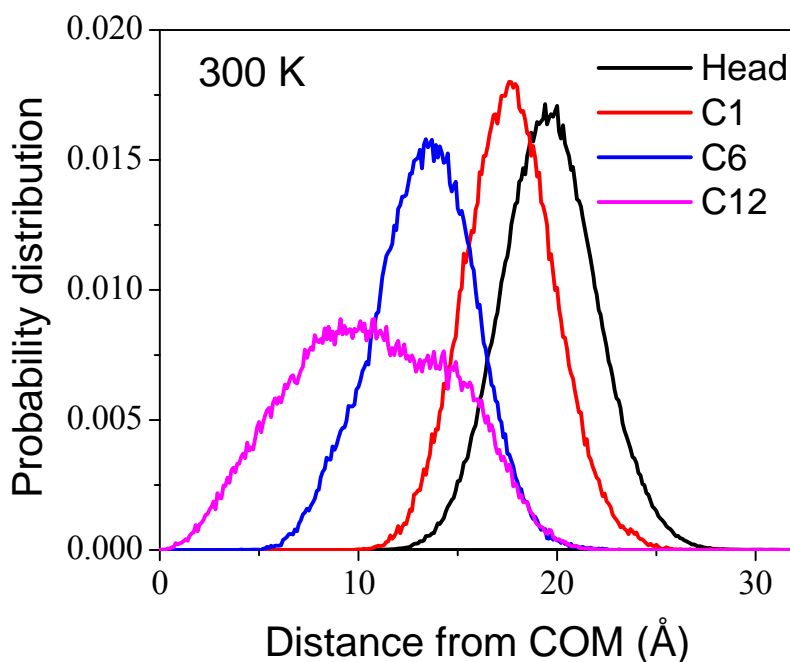


**Fig. 2.12** Probability distributions for the distance from an atom to the centre of the mass, COM, of the SDS micelle at 300K.

Orientation of the chain or direction in the micelles is calculated by examining the angle formed by the first vector that joins C2 (the 2<sup>nd</sup> carbon atom from head group) to C12 (the carbon of the terminal methyl group) and the second vector from C2 to the micelle center of mass. When this angle is zero it implies that alkyl chain points towards the center of the micelle. It is found that the probability is maximum at 25° as shown in Fig. 2.13(a), which indicates that the molecules are roughly oriented with their tails toward the center of the micelle. This is consistent with the other studies on the SDS micelles [56,60].

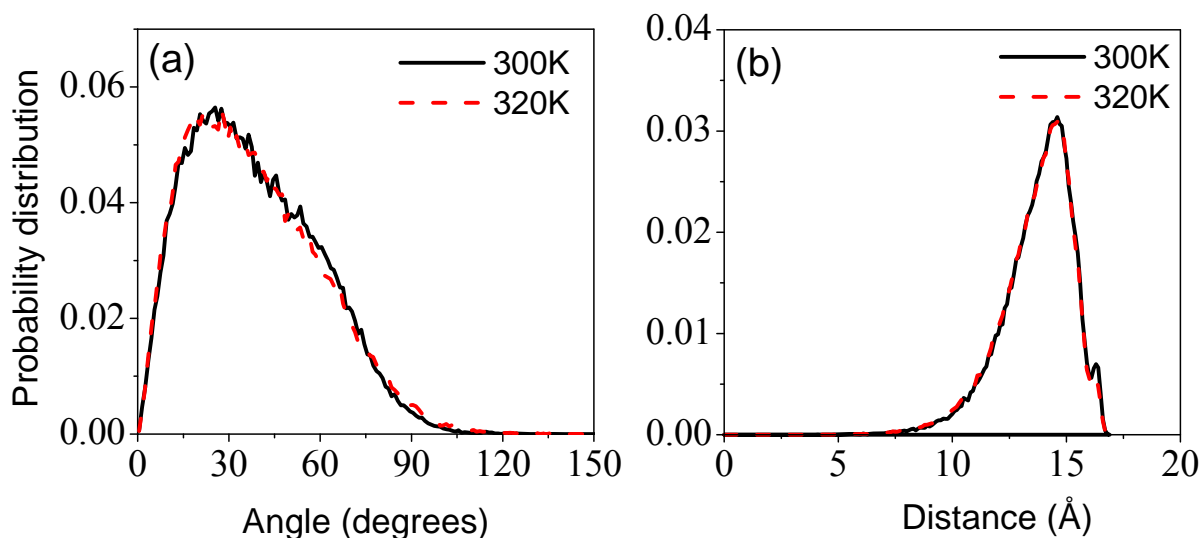


**Fig. 2.13** Probability distribution of (a) the angle of all SDS molecules formed between the vectors connecting C2 to C12 and C2 to center of mass of the micelles at 300 as well as 320 K (b) the end-to-end distances (S-C12) of all the SDS molecules inside the micelles.

The conformations of the SDS molecules in the micelles can be characterized by intra-molecular distance distribution between sulfur atom and carbon atom at the terminal of the alkyl chain. This analysis allows us to estimate the flexibility of the chain inside the micelles. The distribution shows some intensity at small values starting from 7 Å up to the maximum at 14.5 Å as shown in Fig. 2.13(b). The intensity decreases rapidly after the maximum and slightly increases again at 16.2 Å, corresponding to the extended, pure trans conformation, making a small shoulder before falling completely to 0 at 17 Å. It is found that peak corresponds to all- trans conformation is weaker than peak related alkyl chain having conformation defects such as one or more dihedral angle in the gauche conformation. This indicates that alkyl chains are flexible inside the micelles of SDS surfactants.

Now we turn to examine the dynamical aspects of the SDS micelles. Coordinates of the center of mass (COM) of SDS micelles have been calculated for each time steps. Self-

diffusion coefficient of the whole micelles ( $D_s$ ) can be calculated from the Mean squared displacement (MSD) of the COM using Einstein's relation (Eq. (1.104) of chapter 1)

$$6tD_s = \left\langle \left| \mathbf{r}^{COM}(t+t_0) - \mathbf{r}^{COM}(t_0) \right|^2 \right\rangle \quad (2.13)$$

Here,  $\mathbf{r}^{COM}$  is the position vector of the centre of mass of the micelles. MSD calculated from the centre of mass trajectories of the micelles is shown in Fig. 2.14. One may note from Eq. (2.13) that the diffusion coefficient of the whole micelles can be directly obtained from the plot of MSD vs. time and found to be  $2.3 \times 10^{-6} \text{ cm}^2/\text{s}$  at 300 K. At 320 K self-diffusion of the whole micelles increases and found to be  $2.7 \times 10^{-6} \text{ cm}^2/\text{s}$ . It may be noted that although the statistics in the calculation of the diffusion constant from MD simulation is poor (one single SDS micelles in a box of water) but the simulation results are in good agreement with the observation of DLS and QENS experimental techniques.

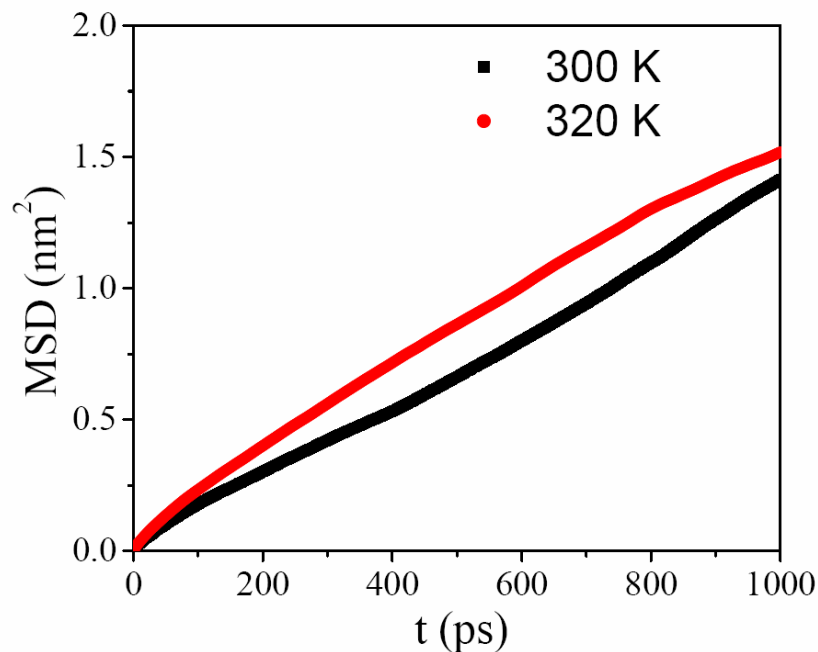


**Fig. 2.14** Variation of mean-square displacement of center of mass of SDS micelles with time at 300 and 320 K.

Incoherent intermediate scattering function corresponds to the hydrogen atoms of SDS molecules,  $I_{\text{inc}}^H(Q, t)$  are calculated from the trajectories of the MD simulation in order to compare with QENS techniques more directly. As discussed earlier in a QENS experiment from a hydrogenous sample, the scattering is predominantly incoherent, due to high incoherent scattering cross section of hydrogen atoms. Therefore, observed intensity is directly proportional to incoherent scattering law which is temporal Fourier transform of  $I_{\text{inc}}^H(Q, t)$  as discussed in section 1.1.2.  $I_{\text{inc}}^H(Q, t)$  can be calculated from MD simulation trajectories using following equation

$$I_{\text{inc}}^H(Q, t) = \frac{1}{N_H} \sum_{i=1}^{N_H} \overline{\langle \exp[i\mathbf{Q} \cdot (\mathbf{r}_i(t+t_0) - \mathbf{r}_i(t_0))] \rangle} \quad (2.14)$$

where bar denotes the average over all  $\mathbf{Q}$  vectors with the same magnitude allowed by periodic boundary conditions and  $N_H$  is number of hydrogen atoms (i.e.  $N_H=25$ ) in the SDS molecule. In the present case, the  $I_{\text{inc}}^H(Q, t)$  were calculated for different  $Q$  values within the range of 0.5-2.1  $\text{\AA}^{-1}$ , the limit chosen according to QENS experiments. Generally, for stochastic motion the behaviour of the intermediate scattering function is described by an exponential or Gaussian function in time domain [14]. However, in the present case the intermediate scattering functions could not be fitted by a single exponential or Gaussian. Various combinations of exponentials and Gaussian functions were therefore tried to describe the  $I_{\text{inc}}^H(Q, t)$  and it was observed that  $I_{\text{inc}}^H(Q, t)$  could be modelled by a combination of three exponentials as given below over the entire  $Q$  and  $t$  range.

$$I_{\text{inc}}^H(Q, t) = A_1(Q)e^{(-t\Gamma_1(Q))} + A_2(Q)e^{(-t\Gamma_2(Q))} + A_3(Q)e^{(-t\Gamma_3(Q))} \quad (2.15)$$

$I_{\text{inc}}^H(Q, t)$  functions as obtained from the simulation using Eq. (2.14) at different  $Q$  are shown in Fig. 2.15. The fit of the same with the Eq. (2.15), is also shown by solid lines in the figure. Evidently it is clear that model function as given in Eq. (2.15) describe the  $I_{\text{inc}}^H(Q, t)$

calculated from the simulation data in this  $Q$  range very well. This indicates that three distinct motions occurring in different time scales exist in the SDS micelles. All three components corresponding to these motions are shown in Fig. 2.16(a) at a typical  $Q=1.1 \text{ \AA}^{-1}$ . With increase in temperature  $I^H_{\text{inc}}(Q,t)$  decay more rapidly indicating faster motion as shown in Fig. 2.16(b) at a particular  $Q$  value .

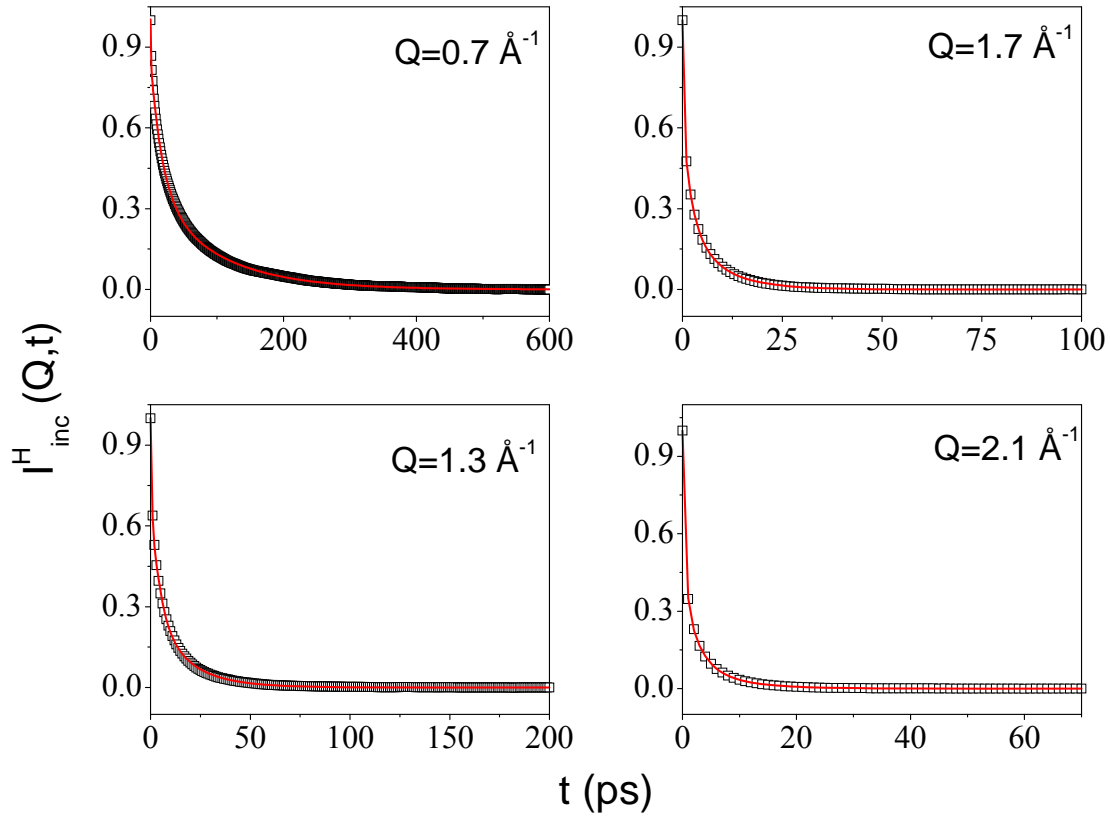


**Fig. 2.15** The  $I^H_{\text{inc}}(Q,t)$  vs time plot at some typical  $Q$  values. The solid line is that obtained by least squares fit using Eq (2.15).

The behaviour of the widths of the three exponential functions with  $Q$  at 300 K is shown in Fig. 2.17. HWHM's of both the Lorentzian functions correspond to global and segmental motions respectively as observed with IRIS spectrometer are also shown in the Fig. 2.17. It is found that two components,  $\Gamma_1$  and  $\Gamma_2$  of  $I^H_{\text{inc}}(Q,t)$  match very closely with the components observed with IRIS spectrometer.

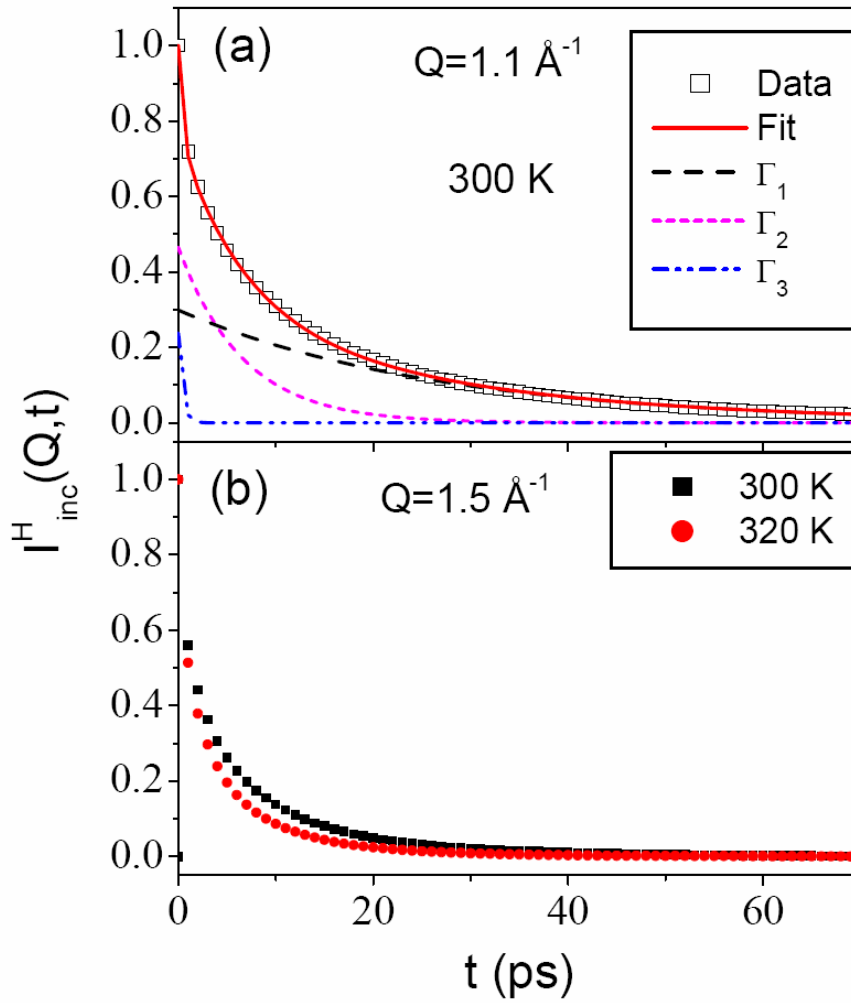


**Fig. 2.16** (a) Three different components of  $I^H_{\text{inc}}(Q, t)$  are obtained from the fit for a typical  $Q$  at 300 K. (b) Intermediate scattering function  $I^H_{\text{inc}}(Q, t)$  calculated at 300 and 320 K for a typical  $Q$  value.

Therefore, one may conclude that these two observed components correspond to global and segmental motion respectively. Third exponentials ( $\Gamma_3 \sim 1.5$  meV) is more or less constant with  $Q$  and too fast to be observed within the time window of the IRIS spectrometer. However, it would be possible to observe the same in a wider time window instrument and we shall discuss this later. Variation of weight factors of these three components ( $A_1$ ,  $A_2$  and  $A_3$ ) with  $Q$  is shown in Fig. 2.18. The weight factor corresponding to the faster component ( $A_3$ ) is very small at low  $Q$  and it dominates at larger  $Q$  values or equivalently at shorter length scales indicating that it correspond to some fast localized motion.



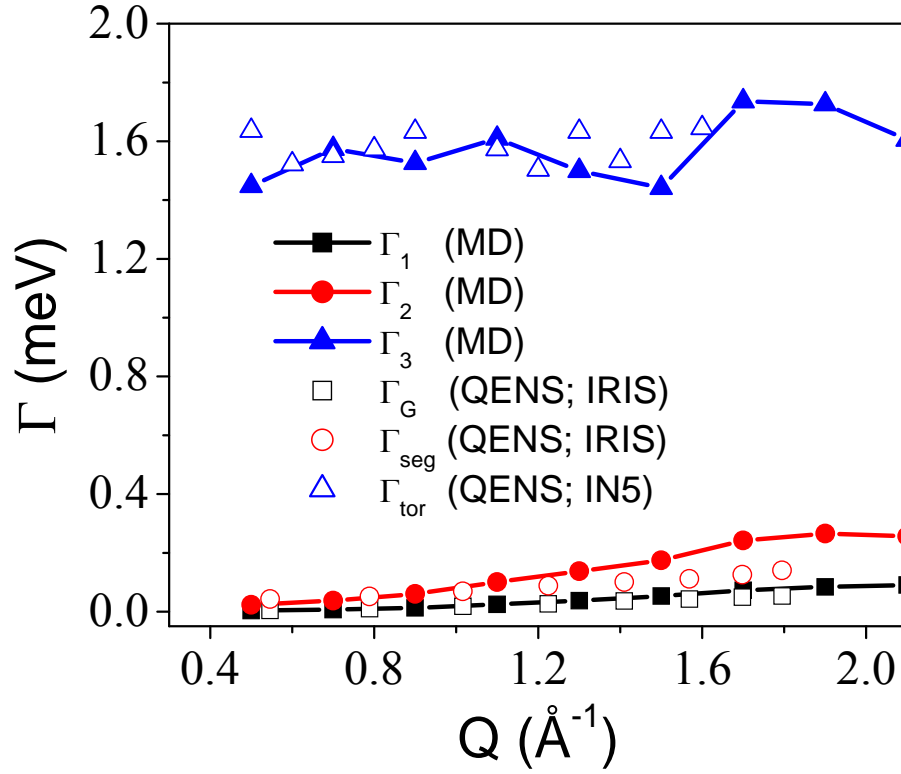


**Fig. 2.17** Variation of the three different decay constants,  $\Gamma$  as obtained from the fits of  $I_{\text{inc}}^H(Q, t)$  using Eq. (2.15) with  $Q$ . Open symbols show HWHM of Lorentzian functions correspond to global, segmental and torsional motion as obtained from QENS experiment.

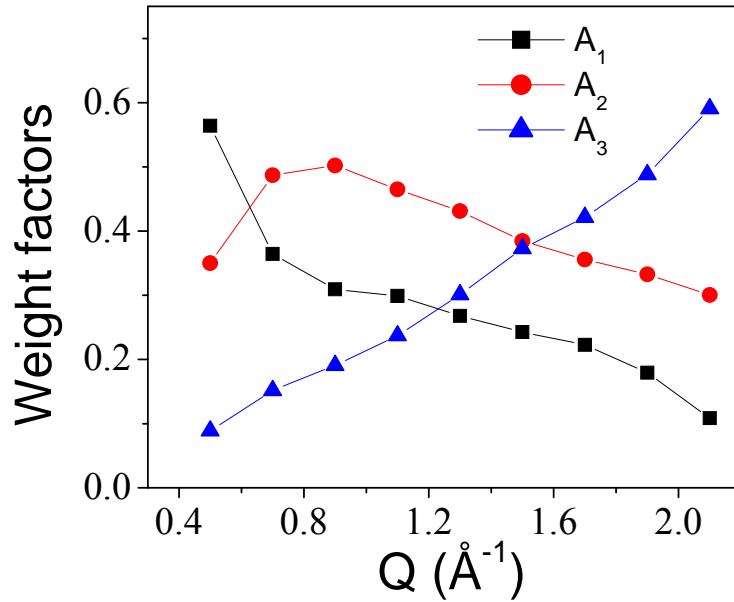


**Fig. 2.18** The behavior of weight factors  $A(Q)$  in Eq. (2.15) corresponding to the three components of the intermediate scattering function  $I_{\text{inc}}^H(Q, t)$  with  $Q$ .

To characterize the internal motion of the micelles, global motion filtered trajectories have been calculated using n-Moldyn [79]. Global motion filtered trajectory of a typical hydrogen atom attached to C3 of the SDS molecules is shown in Fig. 2.19. As can be seen from the figure that the internal motion is more or less localized in nature, the hydrogen atoms undergo localized diffusion within a confined space. Typical distance covered by particular hydrogen atom is about 6 Å, which is consistent with the diameter of the confining volume of segmental motion as obtained from QENS data [53].

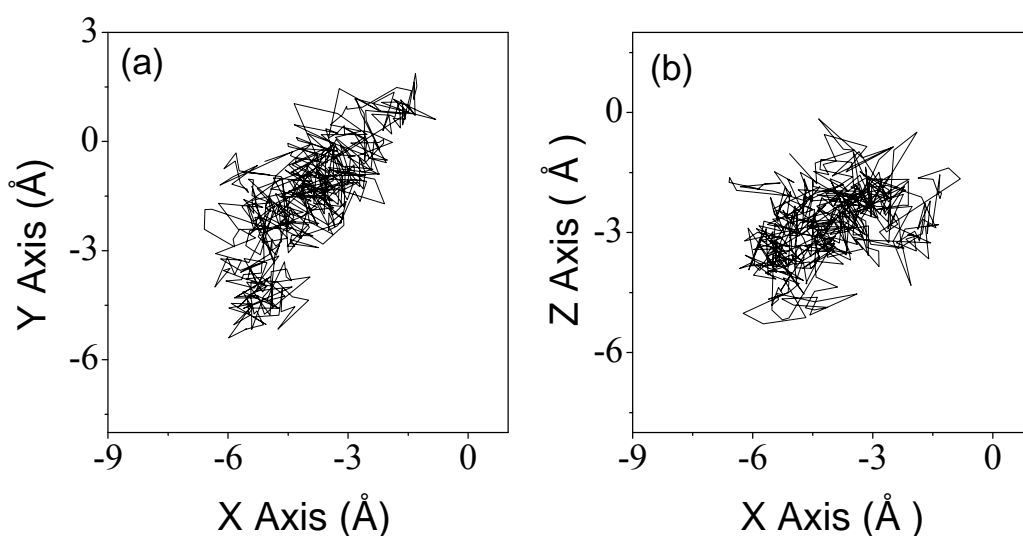


**Fig. 2.19** Trajectory of a H3 (hydrogen attached to 3rd carbon atom from head group) of a particular SDS molecule after filtration out of the global motion in the (a) X-Y plane and (b) X-Z plane.

It is of interest to investigate the distribution of the time scale or diffusivity as well as the spatial volume covered by the alkyl chain in SDS micelles. The local dynamics along the alkyl chain is of interest since it provides the information towards the diffusion of guest species inside the micelles through interior. MSD and intermediate scattering functions for the hydrogen atoms attached to each carbon along the alkyl chain are calculated from the global motion filtered trajectories. MSDs as well as intermediate scattering functions clearly reveals that there is a distribution in the spatial volume encompassed by the hydrogens atoms as well as in their diffusivity along the alkyl chain. These observations are consistent

with the QENS experimental results, which indicate that uniform diffusivity, and radius for all the protons could not describe the observed data.

#### 2.4.4. Results from Data obtained using IN5 Spectrometer

MD simulation predicts an additional faster motion ( $\Gamma_3 \sim 1.5$  meV) than observed at IRIS spectrometer and is found to be  $Q$  independent and corresponding weight factor ( $A_3$ ) increases with the momentum transfer. This fast dynamics is most probably due to the torsional motion, which dominate at high momentum transfer and observed for alkyl chain in many other systems including phospholipids membranes [55, 80, 81]. To observe this fast component, QENS experiments have been carried out using IN5 ( $\Delta E \sim 60$   $\mu$ eV) spectrometer at ILL Grenoble, which has a wider energy transfer range compared to IRIS spectrometer. The formalism used to describe the data as obtained from IRIS spectrometer was found to be inadequate for that obtained from IN5 spectrometer. An additional broad quasielastic component is observed suggesting presence of a faster dynamical component, beyond the dynamical range of IRIS spectrometer. To develop the formalism for analyzing the data involving the global, segmental as well as torsional motion, we have assumed that these motions are independent of each other. Therefore resultant scattering law can be written as

$$S_{micelles}(\mathbf{Q}, \omega) = S_G(Q, \omega) \otimes S_{seg}(\mathbf{Q}, \omega) \otimes S_{tor}(\mathbf{Q}, \omega) \quad (2.16)$$

Since torsional motion is localized in nature, the scattering law can be represented by a sum of elastic and quasielastic component.

$$S_{tor}(Q, \omega) = A_{tor}(Q) \delta(\omega) + (1 - A_{tor}(Q)) L_{tor}(\Gamma_{tor}, \omega) \quad (2.17)$$

Since the torsional motion is expected to be much faster than segmental motion or global motion of the whole micelle ( $\Gamma_{tor} \gg \Gamma_{seg}$  and  $\Gamma_G$ ), Eq. (2.16) can be written as [using Eq.

(2.2) and (2.17)]

$$S_{micelles}(Q, \omega) = B_1 L_G(\Gamma_G, \omega) + B_2 L_{G+seg}(\Gamma_{seg} + \Gamma_G, \omega) + B_3 L_{tor}(\Gamma_{tor}, \omega) \quad (2.18)$$

which comprises three Lorentzian functions. It may be noted that information about the global and segmental dynamics is already known from the analysis of IRIS data and that can be used to extract the information about the fastest component. QENS data observed with IN5 spectrometer is successfully described by the scattering law as given in Eq. (2.18). Typical fitted QENS spectra observed with IN5 spectrometer are shown in Fig. 2.20.

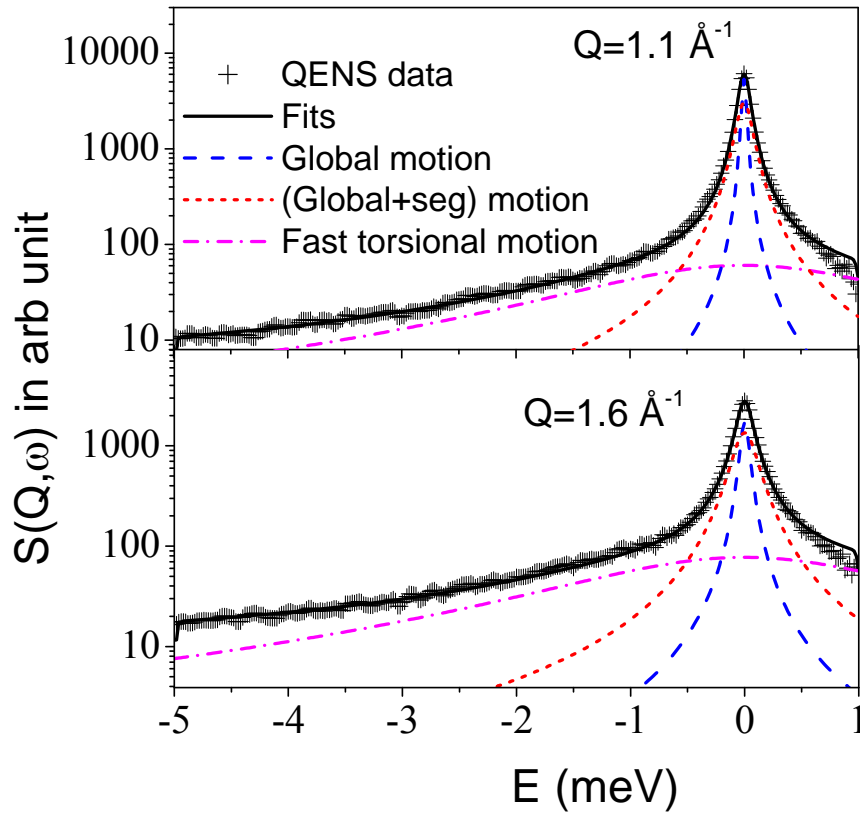


**Fig. 2.20** QENS spectra recorded for 10 % (w/w) SDS micellar solution from IN5 after subtracting the contribution from the solvent at the temperature 300 K at typical  $Q = 1.1 \text{ \AA}^{-1}$  and  $1.6 \text{ \AA}^{-1}$ . The phenomenological fit represented by the solid line is based on Eq. (2.18) sum of three Lorentzian functions. The broadest component corresponds to the fast motion

and is shown by the dash-dotted line. Other components correspond to the global and segmental motions are shown by dashed *and* short dashed *line* respectively.

HWHM of the fastest component observed with IN5 is compared with the decay constants [ $\Gamma$ 's as extracted from  $I^H_{\text{inc}}(Q,t)$ ] as shown in Fig. 2.17. It is found that HWHM of the broad component observed at IN5 spectrometer is very similar to the decay constant  $\Gamma_3$  and also found to be more or less independent of  $Q$ .  $B_3$ , the area corresponds to the broad component is found to increase with  $Q$ , which is consistent with the MD simulation results. All three distinct dynamical components as observed in both QENS and MD simulation studies are found to be consistent with each other.

## 2.5. CONCLUSIONS

The dynamics of sodium dodecyl sulfate (SDS) micelles have been investigated at a molecular scale using combination of quasielastic neutron scattering (QENS), dynamic light scattering (DLS) and molecular dynamics (MD) simulation studies [52,53,82]. Data observed at IRIS spectrometer indicates presence of two distinct motions; whole micellar motion or global diffusion and segmental motion of the SDS monomer [53]. The global diffusion associated with the whole micelle is found to be Fickian in nature and the corresponding diffusion coefficients are found to be consistent with those obtained from DLS measurements and MD simulation results. A model in which the hydrogen atoms undergo localised translational diffusion confined within spherical volumes successfully describes segmental dynamics of the SDS molecules. The volume and the associated diffusivity of the confining sphere found to have linear relationship with the position of hydrogen atom on the alkyl chain. Diffusivity and the volume of the spheres are found to increase with temperature. Intermediate scattering functions as calculated from the trajectories as obtained from MD simulation indicates that there exists three distinct motions in different time scales exist [82].

Two of them match closely with those observed with the IRIS spectrometer i.e. global and segmental motions. Remaining motion is found too fast to be observable at the IRIS spectrometer. Therefore, QENS experiments have been carried out using time of flight spectrometer IN5 at ILL which provides a wider energy window. The observed data could be consistently described by taking into account the dynamics observed with IRIS and a faster dynamical component as indicated in MD simulation. This fast component could be one correspond to torsional motion of an alkyl chain as indicated by the other studies on similar systems. Therefore, a detailed dynamical landscape in the SDS micellar solution has been investigated covering wide range of time scale. It is of interest to check whether SDS molecules in the solid phase show any dynamical motion as observed in micelles, which will be discussed, in next chapter.

## CHAPTER 3

# Molecular Mobility in Solid Sodium Dodecyl Sulfate

### 3.1. INTRODUCTION

After successfully unraveling the complex dynamical landscape in SDS based micelles [52,53,82], it was of interest to study the dynamics that may exist in the solid phase of SDS. The crystal structure of SDS powder has been investigated in detail through a combination of synchrotron, x-ray diffraction and molecular modeling techniques [83-84]. At ambient conditions, the crystal structure of anhydrous SDS has been found to be monoclinic with a single molecule in the asymmetric unit. An electrostatic interaction between the head groups dominates the packing and largely determines the alignment of the hydrocarbon chains with respect to the long axis of the unit cell. The SDS molecules are arranged tail to tail in double layers having a tilt angle of  $15^\circ$  with respect to the long axis of the unit cell (Fig. 3.1). There exists an alternating 2 Å displacement of adjacent molecules perpendicular to the layer plane. This arrangement of the polar head groups determines the lateral packing of the molecules and leaves the hydrocarbon chains with about 10 % larger cross sectional area than is usual in solid state chain packing arrangements [84]. This could perhaps leads to disorder in the conformation of the chain and allow reorientation of the hydrocarbon chains. Picquert [85] had shown the existence of rotational disorder in anhydrous SDS powder using Raman spectroscopy.

In this chapter, molecular mobility in SDS powder as studied by high-resolution QENS technique in the temperature range 175- 400 K is discussed. The details of the experiments are given in section 3.2. Results and discussion are given in section 3.3. The conclusions are depicted in section 3.4.

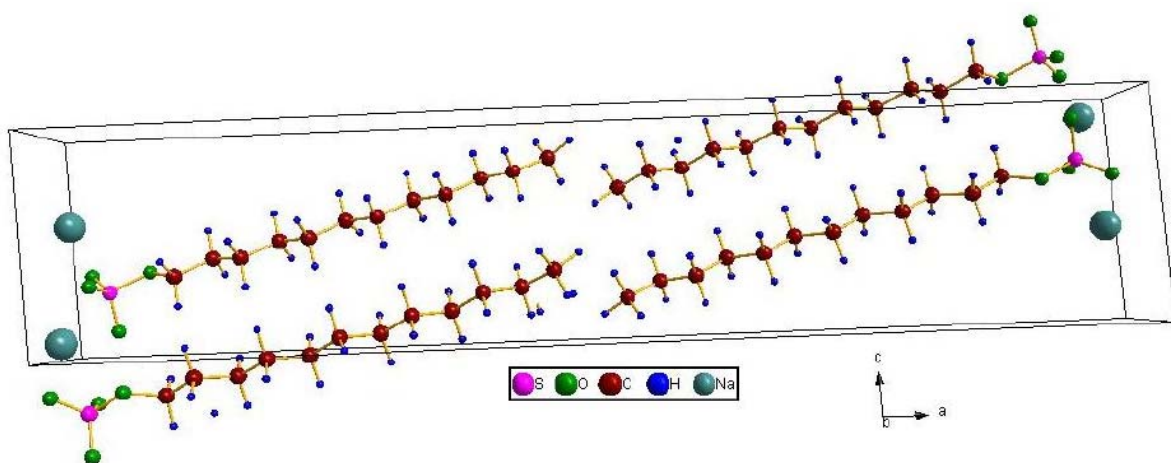


**Fig. 3.1** Unit cell of anhydrous SDS.

### 3.2. EXPERIMENTAL DETAILS

SDS (electrophoresis grade) was obtained from Sisco Research Labs, Mumbai, India. Neutron scattering experiments were carried out using the backscattering spectrometer IRIS at the ISIS facility, UK, and the direct geometry spectrometer FOCUS at the Paul Scherrer Institute, Switzerland. IRIS was operated with the 002 pyrolytic graphite analyser providing energy resolution of  $\Delta E \sim 17 \mu\text{eV}$  (full width at half-maximum, FWHM) and with an energy transfer range of  $\pm 0.4 \text{ meV}$ . Data were recorded in the temperature range 210 - 340 K and a wave-vector transfer ( $Q$ ) range of  $0.5\text{-}1.8 \text{ \AA}^{-1}$ . FOCUS offers a much larger dynamical range compared to IRIS and is suitable for studying the present system at high temperatures. An incident wavelength of  $5.75 \text{ \AA}$  was used for the present study to achieve an energy resolution of  $\Delta E \sim 55 \mu\text{eV}$ . Data were recorded in the temperature range 300 - 400 K and at a wave vector transfer ( $Q$ ) range of  $0.4\text{-}1.73 \text{ \AA}^{-1}$ . Fixed window scans (elastic scans) were carried out as a function of temperature (in the range 175 - 400 K) using the IRIS spectrometer. Elastic scan provides an information about the existence of dynamical phase transition. Here, the elastic intensity is only measured with variation in temperature. An abrupt fall in intensity



gives an indication towards the existence of dynamical phase transition. This elastic scan is useful when there is no a priori knowledge of existence of dynamical phase transition, knowing that one can do detailed QENS study at different temperatures. The samples were placed in an aluminum can with sample thickness of 0.2 mm (which ensures no more than 10% scattering) such that multiple scattering effects are avoided. The ISIS data analysis package, MODES [62], and DAVE [74], developed by NIST, were used to carry out data reduction involving background subtraction, detector efficiency corrections etc. Differential scanning calorimetry (DSC) measurements was carried out in the temperature range 300 - 400 K at a heating rate of 5 K/min using a Setaram model No. DSC131 differential scanning calorimeter (Setaram, France).

### 3.3. RESULTS AND DISCUSSION

Elastic scans probe the mobility in samples by determining the amount of elastic scattering as a function of temperature within the used resolution of the spectrometer ( $\sim 17 \mu\text{eV}$ ). Abrupt loss of intensity in an elastic scan experiment is an indication of a phase transition associated with a change in dynamics. Fig. 3.2 shows the elastic intensity (integrated in the energy transfer range of  $\pm 10 \mu\text{eV}$ ), for SDS in the temperature range 175 - 400 K, normalised to the intensity at the lowest temperature. Fig. 3.2(a) correspond to the  $Q$  averaged elastic intensity for the range  $0.45 - 1.85 \text{ \AA}^{-1}$ . Important features observed are, the monotonic decrease of elastic intensity (almost linearly) with increasing temperature up to 360 K, much more than one would have expected due to Debye-Waller factor (Chapter 1, section 1.1.3) and a step fall in intensity is observed at 360 K indicating the existence of a dynamical transition. The monotonic decrease of intensity clearly suggests that as the temperature increases more number of hydrogen atoms take part in the dynamics. The

dynamical transition at 360 K is corroborated by the differential scanning calorimetry data where the melting transition correspond to the hydrocarbon chains is seen at ca. 375 K as shown in the inset.

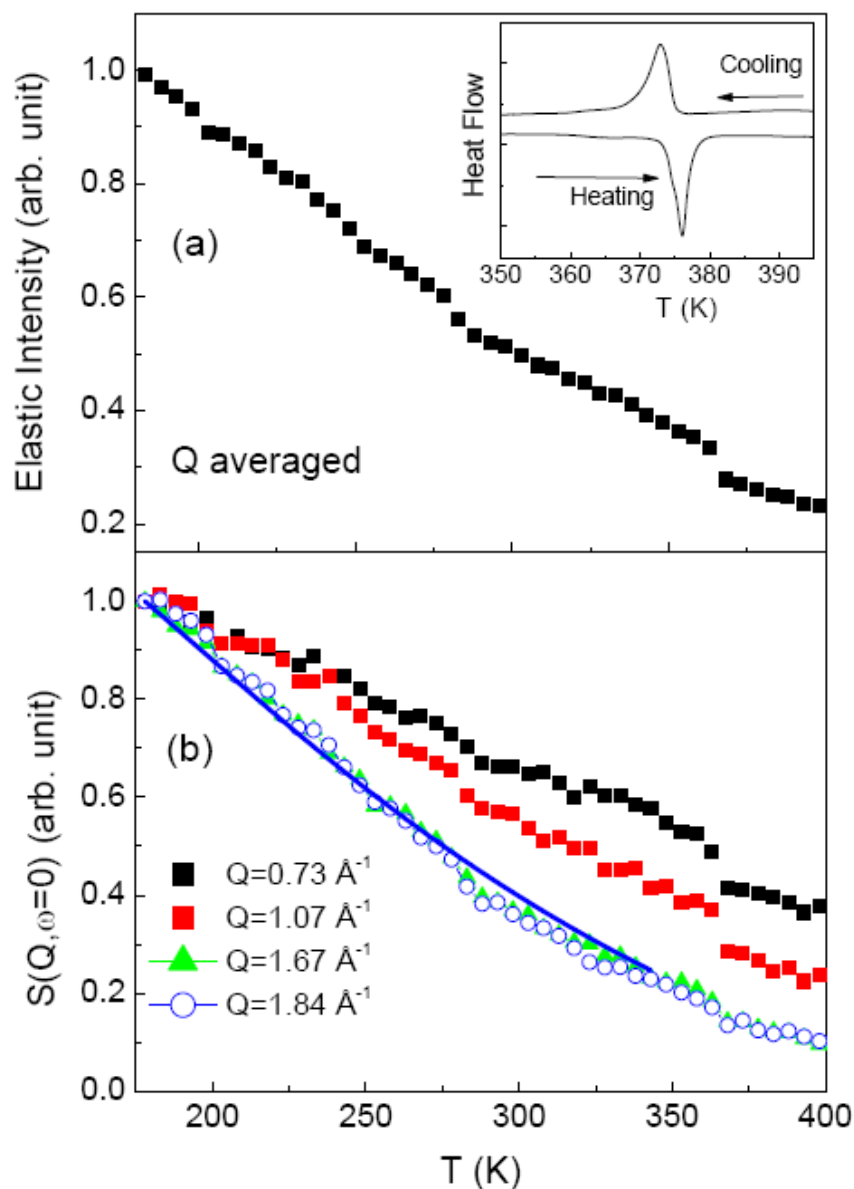


**Fig. 3.2** Temperature dependence of elastic intensity (normalised to lowest temperature studied) for, (a) average over  $Q = 0.45$  to  $1.84 \text{ \AA}^{-1}$  and (b) for different  $Q$  values. The inset represents a DSC scan at 5 K/min. A melting transition is evident.

The  $Q$  dependence of the elastic scans shows some interesting features as shown in Fig 3.2(b) for four typical  $Q$  values. It is found that the transition at 360 K is observed for the elastic scans for which the  $Q$  values are below a limiting  $Q$  value,  $Q_{\text{lim}} \sim 1.4 \text{ \AA}^{-1}$ , viz. 0.73 and  $1.07 \text{ \AA}^{-1}$ . Transitions at 360 K are clearly present in those elastic scans for which the  $Q$  values are below  $Q_{\text{lim}}$ , while for a  $Q$  value above  $Q_{\text{lim}}$  (viz.  $1.67$  and  $1.84 \text{ \AA}^{-1}$ ) the transition is not evident. This suggests that transition is observed for spatial scales  $r \geq 2\pi/Q_{\text{lim}}$  or  $4 \text{ \AA}$ . No transition is seen if one looks with spatial scale less than  $4 \text{ \AA}$ . The average lateral spacing between two SDS chains is about  $\sim 4.5 \text{ \AA}$ . It can be inferred that above the transition temperature, chains are dynamic over a larger spatial scale, but limited to the distance between the chain axes. In order to understand the nature of the dynamics, detail analysis of the quasielastic data is required.

Data from solid SDS as obtained from IRIS spectrometer showed significant quasielastic (QE) broadening over the resolution function of the instrument at  $T \geq 210 \text{ K}$ . The maximum temperature was restricted to  $400 \text{ K}$  due to poor stability of the sample at higher temperatures. The observed broadening should correspond to the stochastic dynamics of the SDS molecules. Typical QENS spectra as obtained with IRIS and FOCUS spectrometers at different temperatures are shown in Figs. 3.3(a) and (b) respectively. The evolution of the QE spectra with temperature is found to be consistent with the elastic scan data. The analysis of the data involves convolution of the appropriate scattering law  $S(Q, \omega)$  with the instrumental resolution function, determined by measuring the spectra from standard vanadium sample, and then obtain the parameters by least squares fit of the calculated spectra to the measured one.

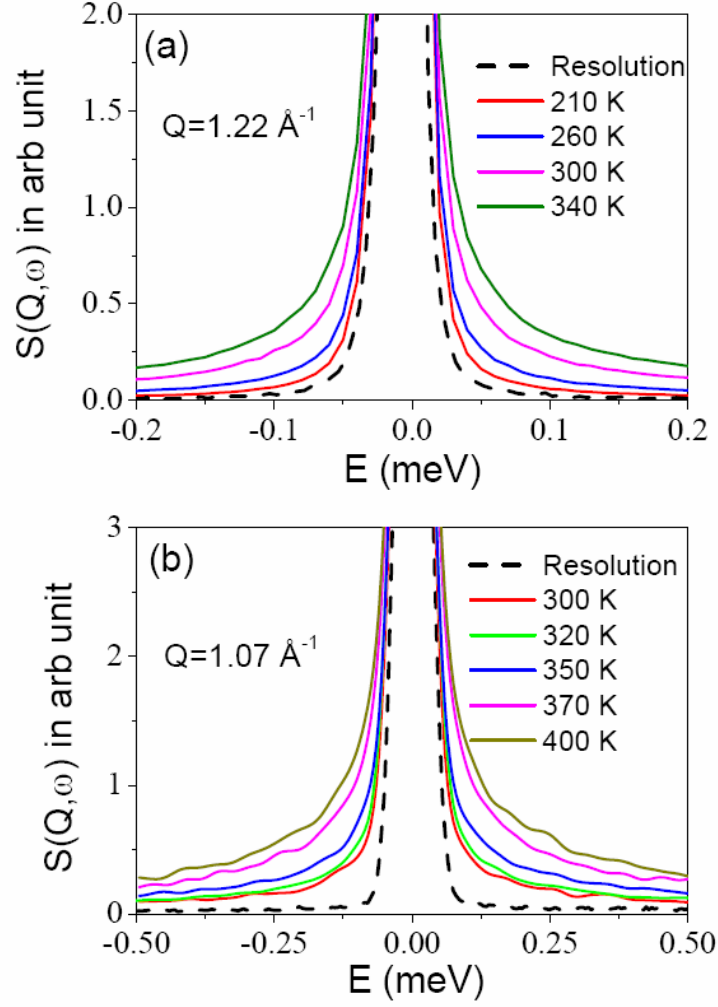


**Fig. 3.3** QENS spectra observed using (a) the IRIS and (b) the FOCUS spectrometers at different temperatures at typical  $Q$  values. Data shown are normalised to peak amplitude. The dashed line shows the instrument resolution.

The most general incoherent scattering law  $S(Q, \omega)$  without assuming any particular model can be written as ( Chapter 1, section 1.2.6)

$$S(Q, \omega) \propto A(Q)\delta(\omega) + [1 - A(Q)]L(\Gamma, \omega) \quad (3.1)$$

where,  $Q$  is the wavevector transfer and  $\hbar\omega = E - E_0$  is the energy transfer. The first term is the elastic part and second term is the quasielastic part.  $L(\Gamma, \omega)$  is a Lorentzian

function,  $L(\Gamma, \omega) = \frac{1}{\pi} \frac{\Gamma}{\Gamma^2 + \omega^2}$ ,  $\Gamma$  is the half width at half-maximum (HWHM).  $A(Q)$  in Eq. (3.1)

is nothing but the elastic incoherent structure factor (EISF) as discussed in Chapter One.

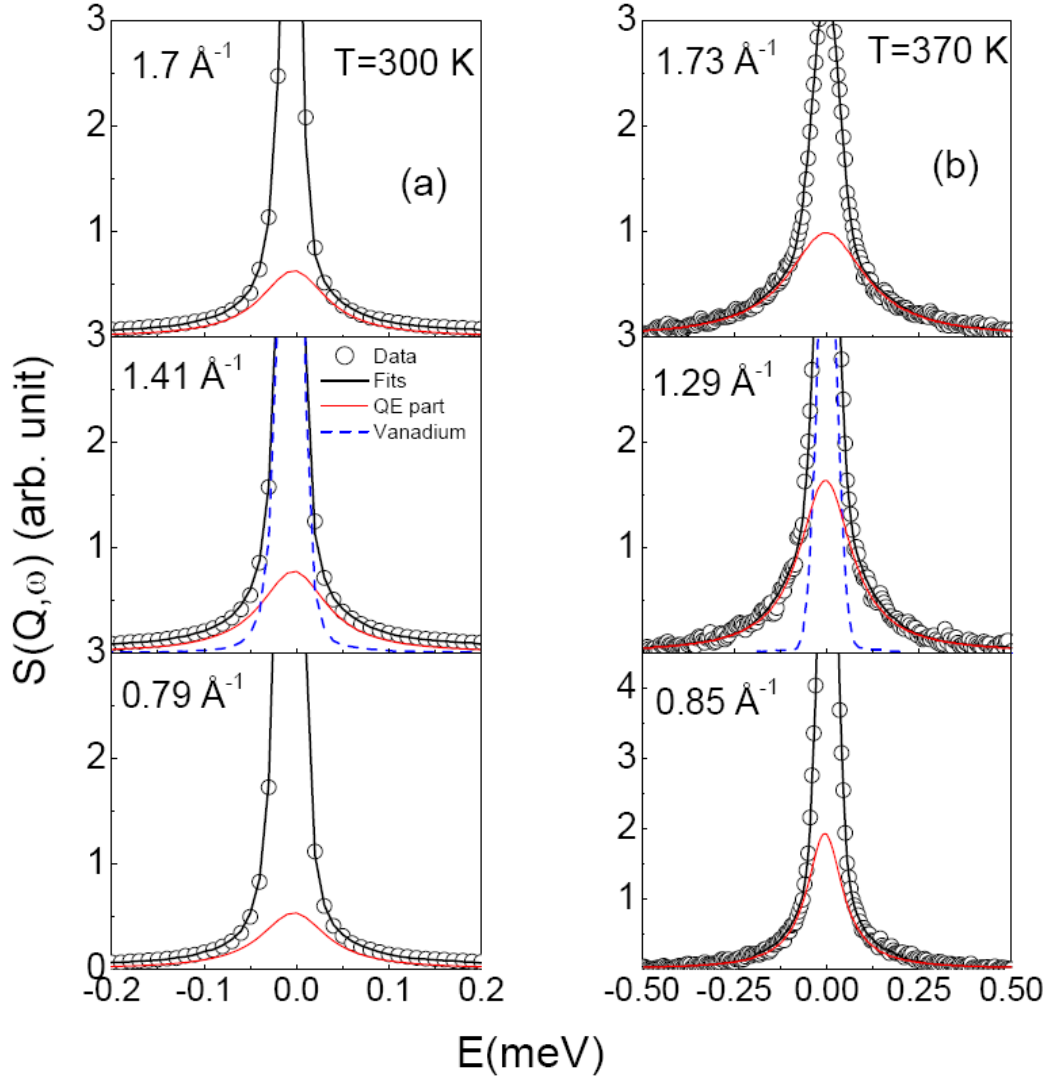


**Fig. 3.4** Typical fitted QENS spectra as observed for anhydrous SDS powder using (a) the IRIS spectrometer at 300 K and (b) the FOCUS spectrometer at 370 K at different  $Q$  values. The dashed line shows the instrument resolution in the middle panel.

To analyse the data, first the scattering law as given in Eq. (3.1) was used without assuming any specific model, with  $A(Q)$  and  $\Gamma$  as the parameters. Fits for some typical  $Q$

values are shown in Figs. 3.4 (a) and (b) at 300 and 370 K respectively. The variation of the EISF,  $A(Q)$ , as obtained from the fit, with  $Q$ , is shown in Fig. 3.5 at different temperatures. The existence of localised dynamics in SDS is evident from the behaviour of EISF. Plausible localised motions may include rotation of the whole molecule or of part of the molecule, or even individual  $\text{CH}_2$  units taking part in either diffusive or rotational motions. Fig. 3.5 shows that as the temperature is increased, the elastic component decreases systematically, suggesting increasing disorder in the system. Two scenarios are possible with increasing temperature: either (1) a higher proportion of  $\text{CH}_2$  units in the hydrocarbon chains take part in the dynamics or (2) the chains become more and more flexible. Allowing for either of these possibilities, the generalized scattering law can be written as

$$S_{inc}(Q, \omega) = (1 - p_x)\delta(\omega) + p_x [A_0(Q)\delta(\omega) + (1 - A_0(Q))L(\Gamma, \omega)] \quad (3.2)$$

where  $p_x$  is fraction of hydrogen atoms that are participating in the observed dynamics dynamically and  $(1 - p_x)$  corresponds to the immobile hydrogen atoms that would contribute towards the elastic part of the spectra.  $A_0(Q)$  is the model EISF. Therefore, the total elastic fraction in the measured spectra would be  $[p_x A_0(Q) + (1 - p_x)]$ .

From the geometry of the SDS molecule (Fig. 3.1), the simplest model for chain motion is the reorientation of the chain about its own axis, known as uniaxial rotational diffusion. Considering the molecule as rigid, i.e., alkyl chains are like rods and having uniaxial rotational diffusion around the molecular axis, the hydrogen atoms would rotate on a circle with a radius of rotation,  $a$ . The incoherent scattering law for a particle rotating among  $N$  equivalent sites equally distributed on a circle of radius ' $a$ ' for a powder sample is given in section 1.1.5.3 of chapter 1. Dianoux et al. [24], showed that for sufficiently large number of jump  $N$  ( $>6$ ) scattering law for jump diffusion on the circle is equivalent to scattering law for uniaxial rotational diffusion model for the  $Q$ -range used here. Therefore, model EISF,  $A_0(Q)$

can be written as  $\frac{1}{N} \sum_{l=1}^N j_0(2Qa \sin \frac{\pi l}{N})$ . (Chapter1, Eq. 1.72). After taking into account the immobile hydrogen atoms, the effective EISF can be written as,

$$[EISF]_{eff} = p_x \frac{1}{N} \sum_{l=1}^N j_0(2Qa \sin \frac{\pi l}{N}) + (1 - p_x) \quad (3.3)$$

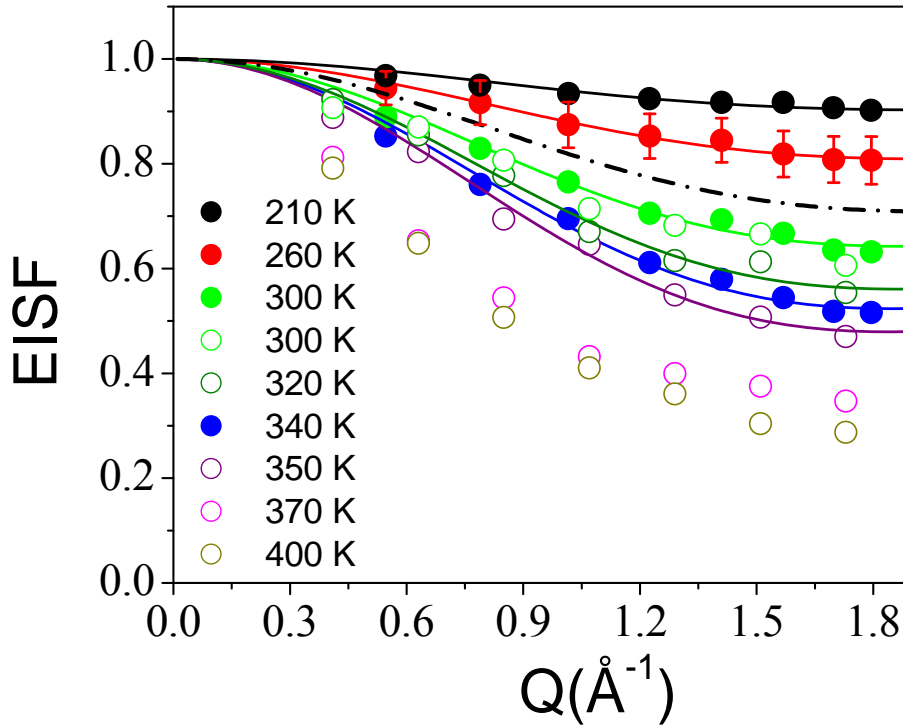


**Fig. 3.5** Variation of EISF for SDS powder with  $Q$  at different temperatures. Solid and empty circles represent data obtained with IRIS and FOCUS respectively. The solid lines represent calculated EISF for fractional uniaxial rotational diffusion model as described in text. Dashed-dotted line is for  $T=280$  K as per calculation based on fractional uniaxial rotational model (assuming  $p_x = 0.33$  &  $a = 1.55$  Å).

Parameters,  $p_x$  and  $a$  are determined by least squares fitting of the experimentally obtained  $EISF$  with this model. Fits (solid lines) are found to be reasonably good in the  $T$  range 210-350 K as shown in Fig. 3.5. Extracted values of  $p_x$  and  $a$  at different temperatures in the range 210-350 K are shown in Fig. 3.6.  $p_x$  and  $a$  are found to be  $0.11 (\pm 0.05)$  and  $1.51$

( $\pm 0.04$ ) Å respectively at 210 K. The value of ' $a$ ' the radius of rotation suggests that the alkyl chains undergo rotational diffusion about the molecular axis with a radius of rotation  $\sim 1.5$  Å, which is slightly more than average distance ( $\sim 1.4$  Å) of the hydrogen atoms from the molecular axis. This probably indicates existence of some fluctuation of the molecular axis or flexibility of the alkyl chain. The value of  $p_x = 0.11$  indicates that on the average only 11 % of a chain is contributing to the dynamics observed at 210 K. At 350 K, values of  $p_x$  and  $a$  are found to be  $0.59 (\pm 0.06)$  and  $1.6 (\pm 0.05)$  Å respectively. It is clear from Fig. 3.6 that value of  $p_x$  increases monotonically, suggesting hydrogen atoms in the chains evolve with increase in temperature. The atoms were earlier held fixed at low temperature, become mobile as the temperature increases. The radius of rotation ( $a$ ) does not change much with increasing temperature.

As can be seen from the Fig. 3.5 that EISF is found to decrease abruptly on increase of temperature from 350 to 370 K. This matches with the observation of dynamic transition at 360 K (Fig. 3.2). Uniaxial rotational diffusion model that was suitable to describe the lower temperature data is not satisfactory for  $T \geq 370$  K. This becomes more evident from the variation of the HWHM of the QE component ( $\Gamma$ ) with  $Q$  as shown in Fig. 3.7 and will be discussed later. As can be seen from the Fig 3.7, the QE width ( $\Gamma$ ) is independent of  $Q$  in the temperature range 210 to 350 K as is expected for a localised reorientational motion. However, at 370 K and above, the variation of the HWHM showed distinctly different behaviour. Scattering law for uniaxial rotational diffusion has been discussed in section 1.1.5.2 and 1.1.5.3 of chapter 1. Assuming the uniaxial rotational diffusion model, the rotational diffusion constant  $D_r$  is obtained by least squares fitting of the data in the temperature range 210 to 350 K. The radius of rotation  $a$ , as obtained from the EISF behaviour (Fig. 3.5), is used in the fitting.



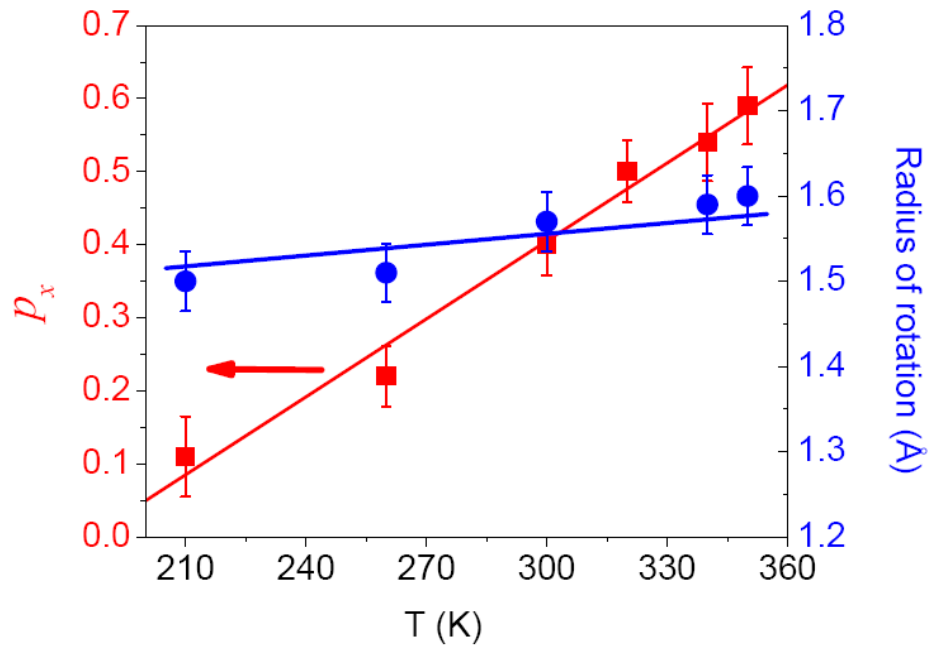


**Fig. 3.6** Variation of fractional dynamic component ( $p_x$ ) of the chains and radius of rotation (a) of the chain as obtained from the least squares fit of the EISF assuming uniaxial rotational model in the temperature range 210-350 K.

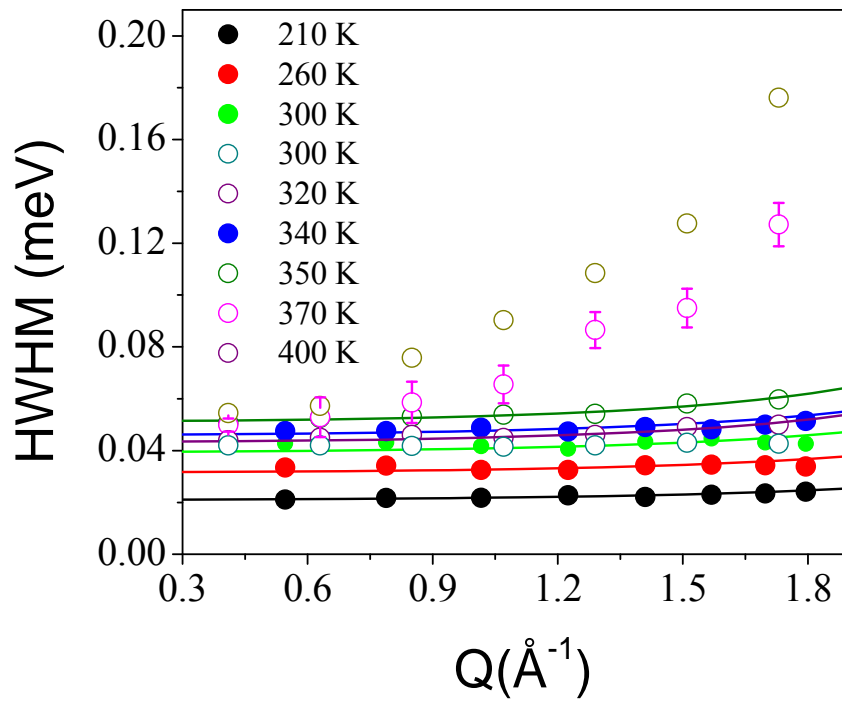


**Fig. 3.7** Variation of HWHM of a Lorentzian representing internal motion SDS powder with Q. Solid and empty circles represent data obtained with IRIS and FOCUS respectively. Solid lines are the fits with a fractional uniaxial rotational model.

Solid lines in Fig. 3.7 show that the model provides a very good description of the experimental data. An increase of width with temperature suggests a faster motion as expected for a thermally activated motion. At 210 K, the rotational diffusion coefficient of SDS chain is  $0.021 (\pm 0.008)$  meV, which increases with temperature to  $0.051 (\pm 0.01)$  meV at 350 K. The variation of rotational diffusion constant with temperature is shown in Fig. 3.8. An activation energy of  $0.9 (\pm 0.2)$  kcal/mol is obtained from the Arrhenius plot of  $D_r$  versus temperature in the range of 210 – 350 K.

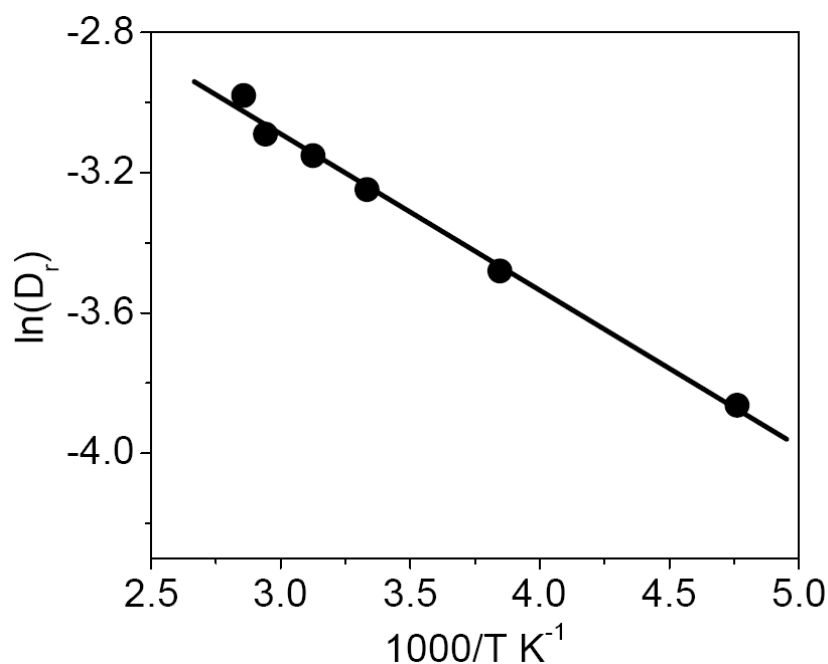


**Fig. 3.8** Variation of rotational diffusion constant ( $D_r$ ) in the temperature range 210-350 K. Arrhenius behaviour is evident.

Using the obtained values of  $p_x$  and activation energy elastic scan data could be described successfully in the temperature range up to 350 K. Elastic intensity in a fixed window experiment can be calculated as

$$I_{el}(Q, T, \omega \approx 0) \propto \int_{-\Delta\omega}^{\Delta\omega} S(Q, \omega) \otimes R(Q, \omega) d\omega \quad (3.4)$$

$S(Q, \omega)$  and  $R(Q, \omega)$  are the scattering law and instrumental resolution function respectively.  $\Delta\omega$  is the HWHM of the instrumental resolution function and  $\otimes$  represents a convolution product. As mentioned above, a uniaxial rotational diffusion model is found to describe the scattering law,  $S(Q, \omega)$  successfully. The calculated elastic intensity [shown by the solid line in Fig. 3.2(b)] assuming uniaxial rotational rotational diffusion model with the same parameter set as obtained from quasielastic data analysis is found to describe the elastic scan measurement very well. Consistency of the model describing the data for two different sets of measurements is worth noting.

So far the discussion is based on the data up to 350 K. At higher temperatures both the elastic scan as well as the QENS data showed that there exists a jump in the evolution of the dynamics. The elastic scan indicated a step decrease in intensity at 360 K. The present QENS data also show a similar effect on increasing the temperature from 350 to 370 as evident in the EISF (Fig. 3.5), which is more pronounced in the variation of HWHM (Fig. 3.7). The uniaxial rotational diffusion model could not be described the HWHM behavior at  $T \geq 370$  K. Therefore, a different model beyond the scope of uniaxial rotational diffusion framework needs to be worked out. At 360 K, SDS undergoes a structural phase transition where it goes from monoclinic to hexagonal structure at high temperature [84,85]. Due to this structural transition, the lamellar thickness decreases because of the increase in tilt angle of the hydrocarbon chain with respect to the long axis. An increase in tilt angle in hexagonal chain

packing configurations leads to an increase in molecular area in the  $a$ - $c$  plane from 20 to 24.5 Å<sup>2</sup> [84]. Therefore, one would expect much higher mobility due to the availability of more space since the molecular area increases by approximately > 20%. It is already found that at 350 K, ~ 60 % of the molecules are dynamic and with the transition, it would be likely that the whole molecule would be dynamic or in other words it could be in melt state. At this stage, phenomena such as bending, stretching of chemical bonds, large amplitude oscillations, reorientation of SDS chain etc. would likely to take place. All these various motions put together modeled as the hydrogen atoms of each CH<sub>2</sub> units undergo localized translational diffusion within the spherical volume. Since the SDS chains are expected to be flexible, the hydrogen atoms associated with different carbon atoms along the chain are more likely to encompass spheres of different volumes with different diffusivities. Therefore, we assume that hydrogen atoms belonging to different CH<sub>2</sub> units in the chain move within spheres of different radii and associated time scales are different. The distribution of radii of the spheres and associated diffusivities are assumed to increase linearly from a minimum to a maximum value. Given the structure of SDS molecules, it is expected that minimum value of radius ( $R_{\min}$ ) and diffusivity ( $D_{\min}$ ) would correspond to CH<sub>2</sub> unit nearest the head group. And as one goes away from the head group along the SDS chain, both diffusivity and radius of the sphere increase and the hydrogen atoms at the end of the tail and furthest from the head group (the CH<sub>3</sub> unit) will move within the biggest sphere of radius  $R_{\max}$  and with diffusion coefficient  $D_{\max}$ .

The EISF associated with such model can be written as

$$A_{LTD}(Q) = \frac{1}{N} \sum_{i=1}^N \left[ \frac{3j_1(QR_i)}{QR_i} \right]^2 \quad (3.5)$$

where  $N$  is total number of CH<sub>2</sub> units in the alkyl chain and  $R_i$  is the radius of the sphere associated with the  $i^{\text{th}}$  CH<sub>2</sub> unit and can be written as

$$R_i = \frac{i-1}{N-1} [R_{\max} - R_{\min}] + R_{\min} \quad (3.6)$$

The parameters,  $R_{\min}$  and  $R_{\max}$  as obtained by least squares fit of the experimentally obtained EISF using Eqs. (3.5) and (3.6) are given in Table 3.1. Solid lines in Fig. 3.9 represent the calculated EISF as per model discussed above. It is evident from Fig. 3.9 that localized translational diffusion model describe well the observed EISF at temperature  $\geq 370$  K. It is found that the value of  $R_{\min}$  is very small while the radius of the largest sphere is about 4 Å. As mentioned before the lateral spacing of the two SDS molecular chains is  $\sim 4.5$  Å. Our data show that at  $\geq 370$  K the highest spatial extent of the molecular disorder is also of a similar value.

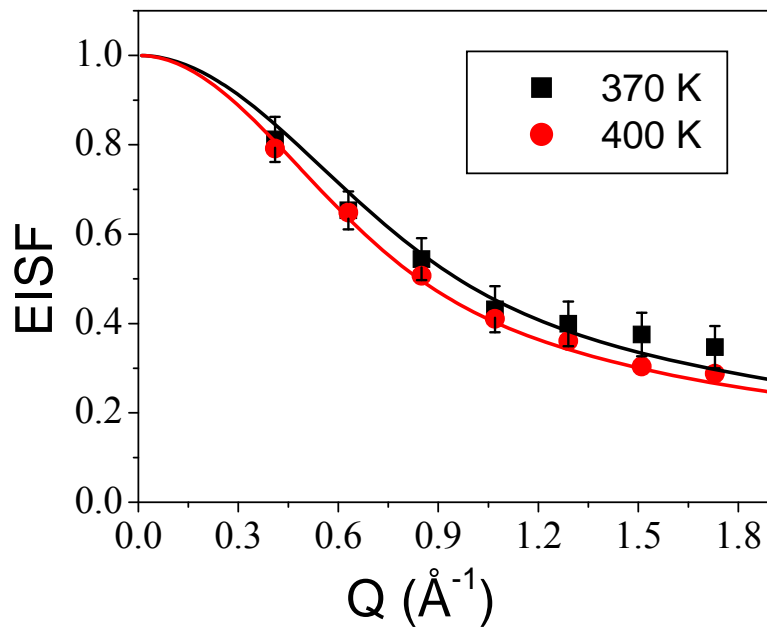


**Fig. 3.9** Variation of EISF for SDS powder with  $Q$  at 370 and 400 K. The solid lines represent calculated EISF for localised translational diffusion model as described in text.

The observed QE width has been successfully described using the same model. For this model scattering law  $S(Q, \omega)$  has been discussed in section 1.1.4.3 of chapter 1. Since no analytical expression exists for the HWHM of the quasielastic part unlike in case of the EISF, the HWHM can be calculated numerically (using Eqs. (1.61) to (1.64) from chapter 1) for

given values of  $R_{min}$ ,  $R_{max}$ ,  $D_{min}$  and  $D_{max}$ . The least squares fitting method is used to describe the observed QE width with  $D_{min}$  and  $D_{max}$  as parameters while the values of  $R_{min}$  and  $R_{max}$  are already known from the fit of the EISF (Fig. 3.9). Fig. 3.10 shows the fit of the QE widths as obtained at 370 K and 400 K assuming the localised translational diffusion model to describe the dynamics of SDS in the melt state. The  $D_{min}$  and  $D_{max}$  values obtained from the fitting are given in Table 3.1. Schematic of the dynamical feature in solid SDS below and above the transition temperature ( $T_c \sim 360$  K) is shown in Figs. 3.11(a) and 3.11(b) respectively.

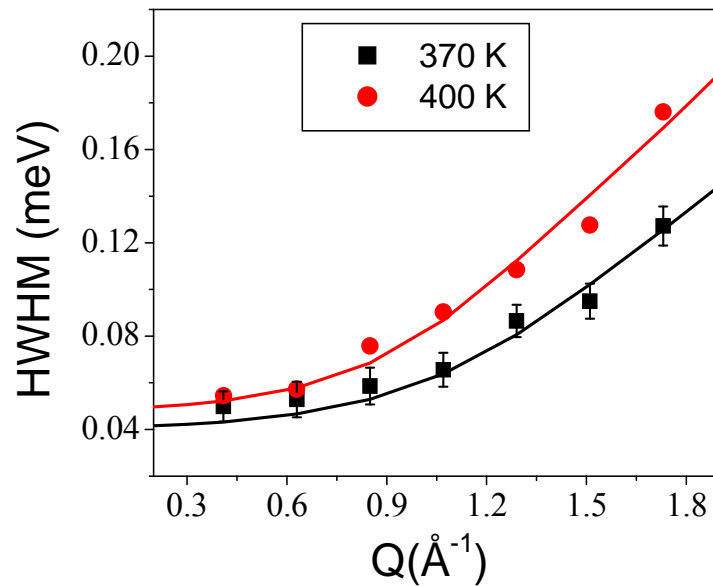


**Fig. 3.10** Variation of HWHM of a Lorentzian representing internal motion SDS powder with  $Q$  at 370 and 400 K. Solid lines are the fits with localised translational diffusion model.

We have tried to calculate the energy barrier for the rotation of the SDS molecule in the monoclinic phase of SDS. For this, a super cell of  $3 \times 5 \times 7$  unit cells was considered. In which the molecule at the center of the super cell was allowed to rotate along the molecular axis keeping all others static and potential for all the non-bonded interactions (both Coulombic and Lennard-Jones) are calculated in each rotational configuration. By

performing this exercise, one can estimate the interaction energy on the rotating molecule due to all other SDS molecule as function of rotational angle. It is found that the energy barrier for the whole molecule rotation is very high ( $\sim 400$  meV), while the same for fractional dynamics is very much feasible ( $\sim 10$  meV). This is in accordance to the neutron scattering data, which suggested a fractional reorientation of the SDS molecule in the temperature range 175 – 350 K.

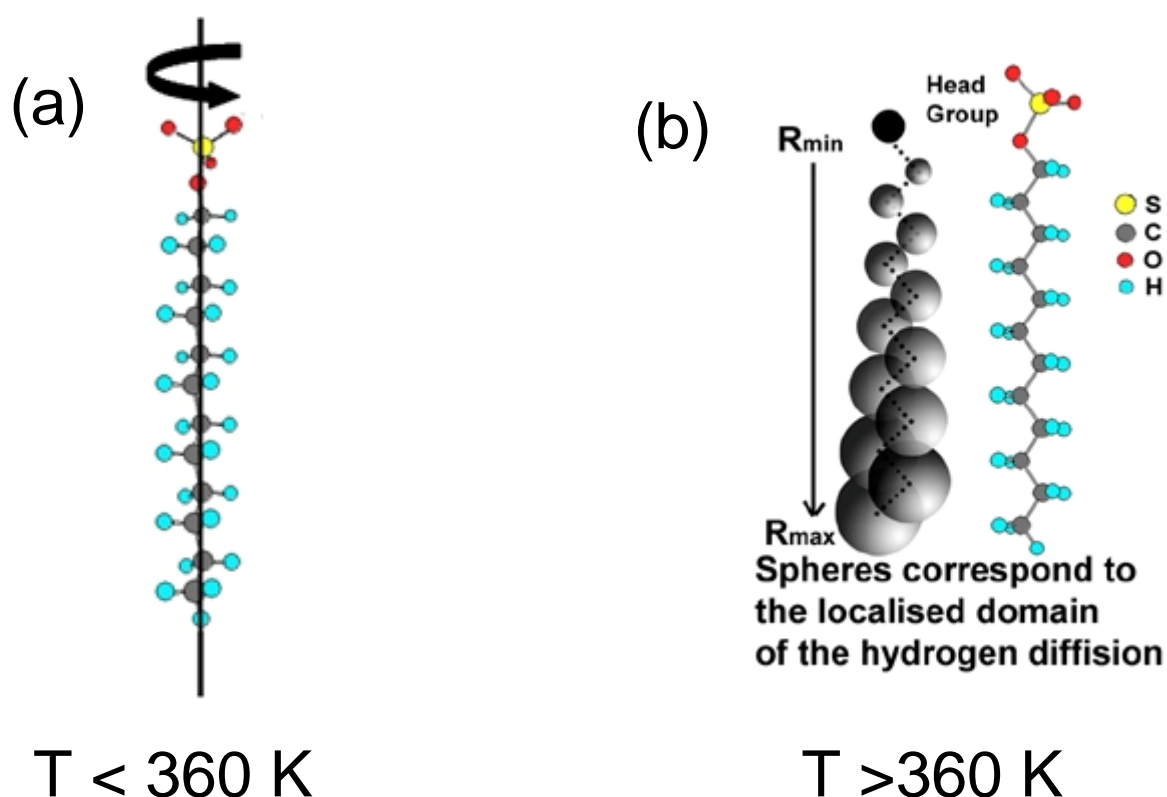


**Fig. 3.11** Schematic model of the motion in solid SDS (a) below the transition temperature ( $T=360$  K) uniaxial rotation along the molecular axis is observed and (b) above  $T=360$  K, localized translational diffusion in which hydrogen atoms of a SDS chain moving in spheres of different radii is observed. The radii of sphere are shown to increase linearly along the SDS chain.

**Table 3.1.** Radii of spheres,  $R_{\min}$  and  $R_{\max}$ , and corresponding diffusion coefficients,  $D_{\min}$  and  $D_{\max}$ , as obtained by least squares fitting of the data at high temperatures ( $>360$  K) with localized translational diffusion model.

T (K)	$R_{\min}$ (Å)	$R_{\max}$ (Å)	$D_{\min}$ $\times 10^{-5}$ (cm <sup>2</sup> /s)	$D_{\max}$ $\times 10^{-5}$ (cm <sup>2</sup> /s)
370	$0.004 \pm 0.003$	$3.89 \pm 0.3$	$0.015 \pm 0.005$	$1.78 \pm 0.3$
400	$0.002 \pm 0.001$	$4.44 \pm 0.3$	$0.06 \pm 0.005$	$2.77 \pm 0.3$

### 3.4. CONCLUSIONS

Detailed description of the reorientational motions in solid SDS in the temperature range 175 – 400 K as studied by high-resolution neutron scattering experiments is reported [86]. It is found that SDS molecules undergo fractional dynamics following a uniaxial rotation model in the temperature range 210-350 K. The fraction of SDS molecules taking part in the dynamics increases linearly with increasing temperature. Obtained rotational diffusion coefficient ( $D_r$ ) found to increase with temperature and followed Arrhenius behaviour. An activation energy of  $0.9 (\pm 0.2)$  kcal/mol is obtained from the Arrhenius plot of  $D_r$  in the temperature range of 210 – 350 K. A dynamical transition is found to exist at 360 K as seen in the elastic scan as well as quasielastic scattering data. Observed dynamical transition can be understood in conjunction with Raman spectroscopy and XRD studies on anhydrous SDS powder where a structural transition (from monoclinic to hexagonal) is seen around 360 K. This transition is accompanied with an increase in molecular area by 20%. Therefore, at high temperature ( $\geq 370$  K) there is more space for the chains, the chain experience a lower interaction potential and so the molecules can have more freedom to move, leading to more disorder and the resultant increase in the QE broadening in the high temperature chain melt state. Dynamics in



the chain melt state has been described by a localized translational diffusion model in which the hydrogen atoms associated with different CH<sub>2</sub> units of the chain diffuse within spheres of varying radii. The radii are largest at the tail end while they are smallest towards the head. Diffusivities associated with the different radii also increase from head to tail. It is interesting to compare the results from this work of anhydrous SDS to the dynamical behaviour of SDS micelles in solution described in the previous chapter. It was found that uniaxial rotation was inadequate to explain the internal motion of the SDS micelles. In case of SDS micelles, it is found that the hydrogen atoms undergo localised translational diffusion confined within spherical volumes. It is worthy to note that dynamics of SDS chain in anhydrous powder at chain melt state ( $> 360$  K) is more or less similar to the segmental motion in the micellar phase.

## CHAPTER 4

### Dynamical Landscape in CTAB Micelles

#### 4.1. INTRODUCTION

In the previous two chapters, dynamics of anionic sodium dodecyl sulfate (SDS) surfactant in the micellar as well as in solid phase are reported. SDS ( $C_{12}H_{25}OSO_3^-Na^+$ ) molecule has a head group  $OSO_3^-$  that does not contain any hydrogen, therefore the alkyl chains only contributed towards QENS data. Head group of the surfactant molecules in micelles are in contact with the surrounding water molecules and therefore the dynamics of head groups are prone to be affected by hydration. Hydration play a major role towards dynamics of head group as has been reported in model lipid systems [87,88]. Therefore, it is of interest to investigate dynamical behaviour of such surfactant molecule, which has hydrogen atoms in its head group. Cetyltrimethylammonium bromide ( $C_{16}H_{33}N^+(CH_3)_3Br^-$ ;  $C_{16}TAB$  or CTAB) has three methyl unit in its head group along with a long hydrophobic alkyl chain with 16 carbon atoms. CTAB or molecules form cationic micelles when dissolved in water above critical micellar concentration. Critical micellar concentration of CTAB molecules is found to be 0.00092 M [89], which is lower by an order of magnitude compared to SDS (0.008 M) [90]. Schematic of cationic CTAB micelles is shown in Fig. 4.1. In CTAB, apart from the dynamics of the alkyl chain, head group ( $N^+(CH_3)_3$ ) will also contribute to the observed QENS data. Phase diagram of CTAB micelles has been studied and reported in the literature [91]. Structure of CTAB micelles with surfactant concentration has been investigated in detail using small angle neutron scattering technique [92-94]. It is found that at low concentration, CTAB micelles are more or less spherical and as the concentration of surfctant increases micelles show sphere-to-rod like transition [92]. Effect of external electrolyte and temperature towards size and shape of CTAB micelles have been also studied and reported in

the literatures [94]. CTAB micelles have been the subject of a recent detailed MD simulation study on its structure [95]. However, there is not much information on the dynamics of CTAB micelles, which is widely used in the template synthesis of the inorganic compounds such as gold nano particles, SiO<sub>2</sub> nano structured materials and so forth [39,96]. Mobility of CTAB alkyl chain gives an indication of how the species inside micelles diffuse and therefore, has paramount importance in many practical applications such as micro reactor, synthesis and design of nano structures etc.

In this chapter, dynamical motions in CTAB micelles as studied using Quasielastic Neutron Scattering (QENS) technique is discussed. The details of the experiments are given in section 4.2. Results obtained from high resolution IRIS and FOCUS spectrometer discussed in section 4.3.1 and 4.3.2 respectively. The summary is depicted in section 4.4.

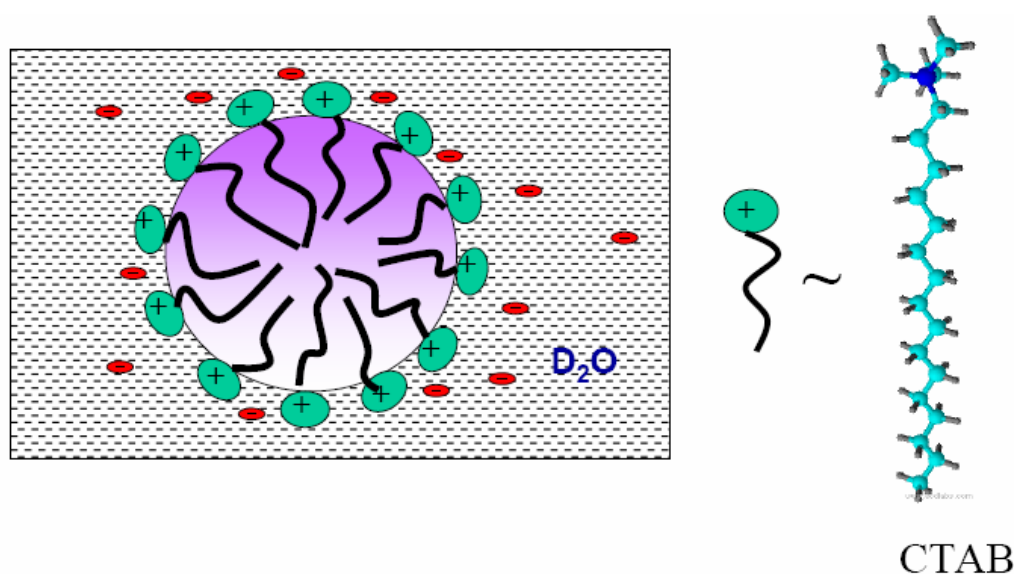


**Fig. 4.1** Schematic of cationic CTAB ( $C_{16}H_{33}N^+(CH_3)_3Br^-$ ) micellar solution.

## 4.2. EXPERIMENTAL DETAILS

CTAB surfctant was obtained from S D Fine Chemicals, Mumbai, India. For the QENS measurements, micellar solutions were prepared by dissolving CTAB in D<sub>2</sub>O (99.9% atom D purity). Experiments were carried out using the inverted geometry spectrometer IRIS (ISIS

pulsed neutron source, Didcot, UK) was operated with the 002 pyrolytic graphite analyser providing an energy resolution of  $\Delta E \sim 17.5 \mu\text{eV}$  (full width at half-maximum, FWHM) and with an energy transfer range of  $-0.3$  to  $1.2 \text{ meV}$  (in the offset mode). This instrument is suitable to study the motions with correlation time between 2 to 100 ps. Data were recorded on  $\sim 10 \%$  (w/w) aqueous CTAB micellar solution in  $\text{D}_2\text{O}$  in the temperature range of 300 - 330 K in the wave-vector transfer ( $Q$ ) range of  $0.5\text{-}1.8 \text{ \AA}^{-1}$ . The temperature range chosen is on the basis of the stability of the micelles. Experiments were also carried out using the direct geometry hybrid time of flight spectrometer FOCUS at SINQ, Paul Scherrer Institute, Switzerland, which has a relatively wider energy window, offers a much larger energy transfer range compared to IRIS and suitable to observe faster motion (0.1 ps - 30 ps). In FOCUS, the neutron beam is focused in space and time by using a doubly curved monochromator and a Fermi chopper. An incident wavelength of  $5.75 \text{ \AA}$  was used for the present study providing an energy resolution of  $\Delta E \sim 55 \mu\text{eV}$  (full width at half-maximum, FWHM). Data were recorded on 10 % (w/w) aqueous CTAB micellar solution in  $\text{D}_2\text{O}$  in the temperature range of 300 - 330 K and  $Q$  range of  $0.4\text{-}1.6 \text{ \AA}^{-1}$ . In both the spectrometer, the samples were placed in an annular aluminum can with an internal spacing of 1 mm to minimise multiple scattering and have reasonable measuring statistics. Measurements were also done on pure  $\text{D}_2\text{O}$ , to estimate the contributions from the solvent and were subtracted in order to get the contribution of micelles alone. The ISIS data analysis package, MODES [62], and DAVE [74], developed by NIST, were used to carry out data reduction involving background subtraction, detector efficiency corrections etc for IRIS & FOCUS data respectively.

### **4.3. RESULTS AND DISCUSSION**

#### **4.3.1. Results From Data Obtained Using IRIS Spectrometer**

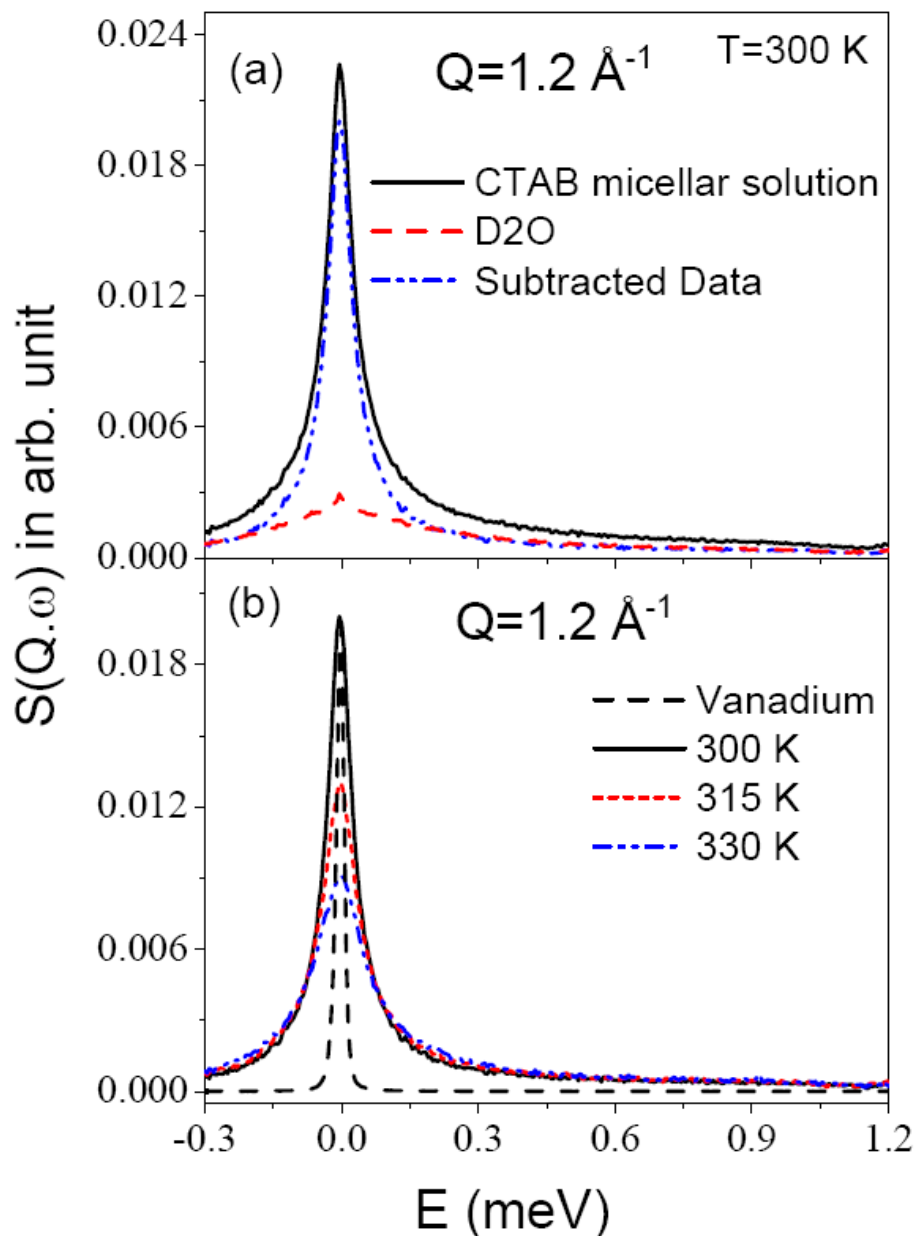


**Fig. 4.2** (a) QENS spectra from IRIS for a ~10 % (w/w) CTAB micellar solution and D<sub>2</sub>O at 300 K at  $Q=1.2 \text{ \AA}^{-1}$ . The contribution from the D<sub>2</sub>O and that from the pure micelles after the D<sub>2</sub>O subtraction are also shown (b) shows the subtracted QENS spectra at different temperatures at a typical  $Q$ -value. The instrument resolution is shown by black dashed line.

QENS data recorded for 10% (w/w) CTAB micellar solution and pure D<sub>2</sub>O at 300K at a typical  $Q$  value of  $1.2 \text{ \AA}^{-1}$  are shown in Fig. 4.2(a). The scattering law for CTAB micelles is obtained by subtracting the contribution of D<sub>2</sub>O from the CTAB micellar solution is also

shown in Fig 4.2 (a). QENS spectra for CTAB micelles are obtained similarly for other measured temperatures. Fig 4.2 (b) shows the comparison of the QENS spectra of CTAB micelles at different temperatures at a typical value of  $Q=1.2 \text{ \AA}^{-1}$ . The instrumental resolution, as measured using standard vanadium sample, is also shown in the figure for comparison. Significant quasielastic (QE) broadening over the instrumental resolution is evident at all the measured temperatures. As expected, while the peak intensity of the dynamical structure factor decreases with increasing temperature, the QE width increases.

As described in section 1.2.6 of chapter 1, scattering law for the micelles,  $S_{\text{micelles}}(\mathbf{Q}, \omega)$  can be expressed as

$$S_{\text{micelles}}(Q, \omega) = \left[ A_{\text{seg}}(Q) L_G(\Gamma_G, \omega) + (1 - A_{\text{seg}}(Q)) L_{G+\text{seg}}(\Gamma_{G+\text{seg}}, \omega) \right] \quad (4.1)$$

where,  $L_G(\Gamma_G, \omega)$  is the Lorentzian function corresponds to the global motion of the whole micelle and  $L_{G+\text{seg}}(\Gamma_{G+\text{seg}}, \omega)$  represents contribution from the combination of global micellar motion and the segmental motions, where  $\Gamma_{G+\text{seg}} = \Gamma_G + \Gamma_{\text{seg}}$ .  $A_{\text{seg}}(Q)$  is the structure factor correspond to segmental motion of the monomer. The above equation convoluted with the instrumental resolution function is used to describe the QENS data obtained for the micelles. A least square fitting method is used to fit the spectra with parameters,  $A_{\text{seg}}(Q)$ ,  $\Gamma_G$  and  $\Gamma_{G+\text{seg}}$ .

It is found that the observed spectra could be described very well by the model function depicted in Eq. (4.1). Typical fitted spectra are shown in Fig. 4.3 for the data at 330 K at some typical  $Q$  values. To gain more insight into the nature of these two dynamical processes, the parameters obtained from the fit are analyzed as a function of temperature and  $Q$ . It is expected that the global motion of the whole micelle will be slower than the segmental motion as observed in the case of anionic SDS micelles. Therefore, slower global motion will correspond to the narrower Lorentzian (hereafter referred as 1<sup>st</sup> Lorentzian),

whereas the broader Lorentzian (hereafter referred as a 2<sup>nd</sup> Lorentzian) represents the convolution of two Lorentzians, correspond to global and segmental motion of the micelles.

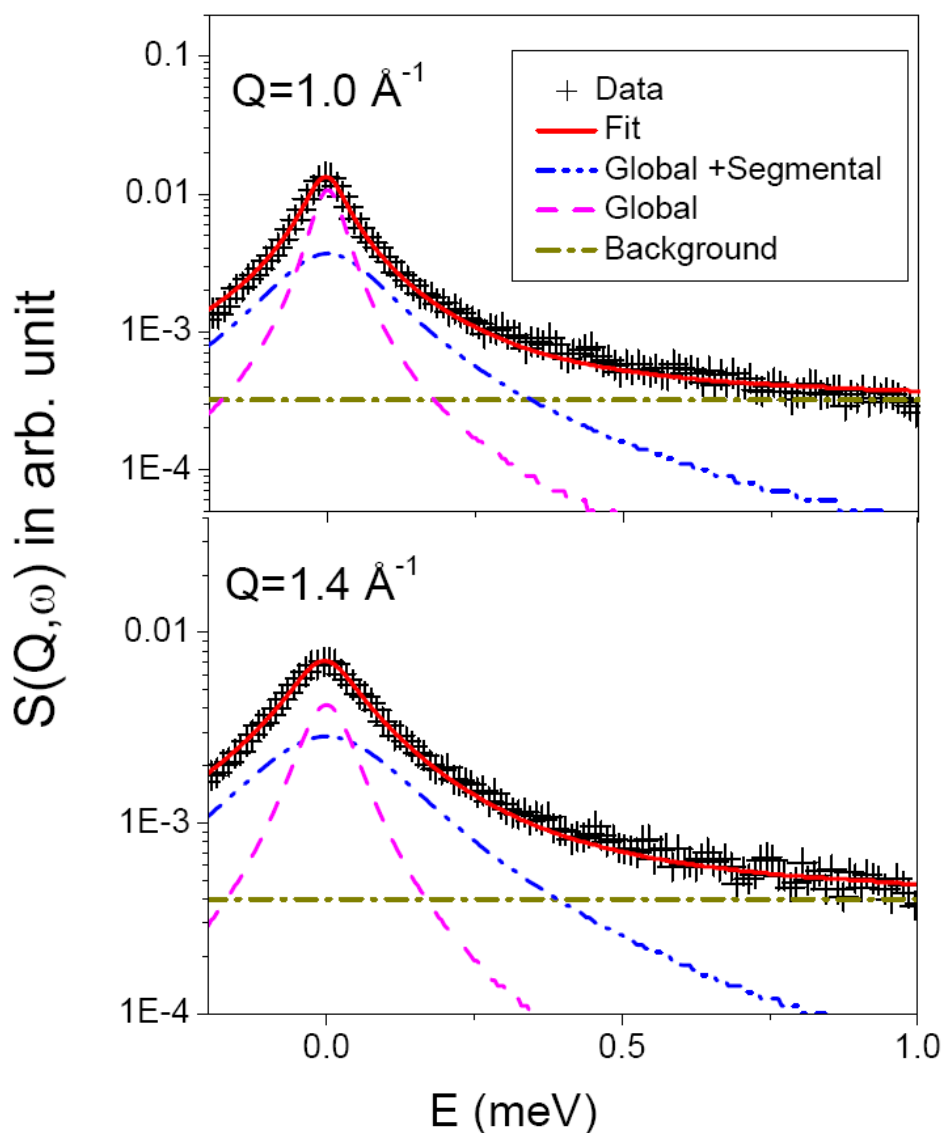


**Fig. 4.3** Typical fitted  $S(Q, \omega)$  for 10 % (w/w) CTAB micelles at 330 K, as obtained from IRIS spectrometer, assuming model function given in Eq. (4.1).

#### 4.3.1.1. Global Motion

The variation of the HWHM,  $\Gamma_G$ , of the 1<sup>st</sup> Lorentzian, with  $Q^2$  at different temperatures, is shown in Fig. 4.4 which could be described by a simple Brownian motion following Ficks

law,  $\Gamma_G = D_G Q^2$ . Here  $D_G$  is the global diffusion coefficient. Values of  $D_G$  for different temperatures are given in Table 4.1.  $D_G$  is found to increase with the temperature as expected for a thermally activated diffusive motion. Further, reduction in aggregation number of micelles with the increase of temperature also contributes to the enhanced diffusivity at high temperatures.

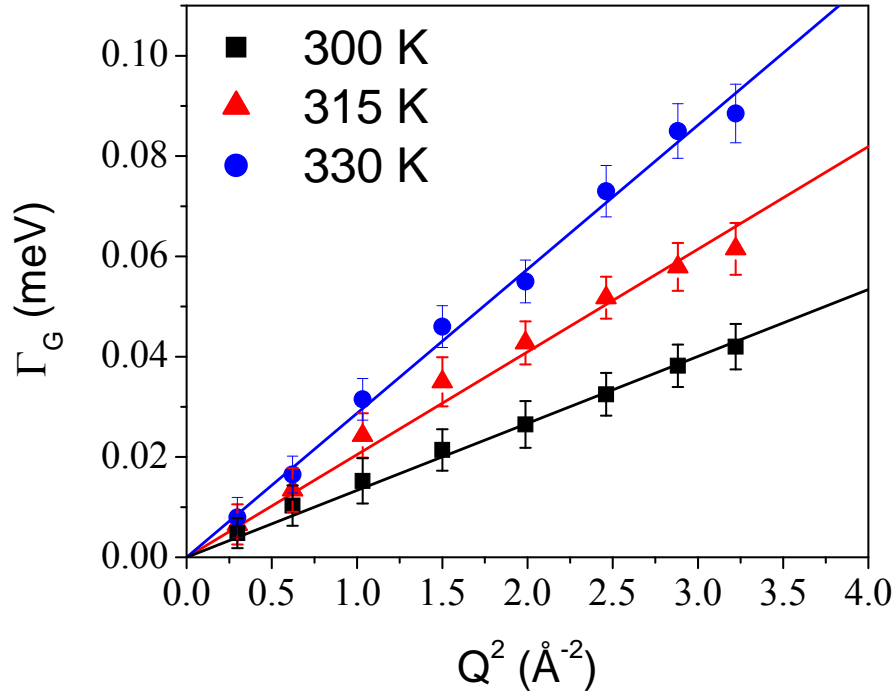


**Fig. 4.4** Variation of half width at half maxima,  $\Gamma_G$ , of the Lorentzian  $L_G(\Gamma_G, \omega)$ , which accounts for global motion of micelles in solution with  $Q^2$  at temperatures of 300 K, 315 K and 330 K. It appears that  $\Gamma_G(Q)$  is a quadratic function of  $Q$ , as expected for continuous diffusion. The solid lines correspond to a fit with Fick's law of diffusion.

According to the Stokes-Einstein relation,  $D = k_B T / 6\pi\eta R$ , one can obtain self-diffusion coefficient of a particle of radius  $R$  in a solution having viscosity  $\eta$  at a temperature  $T$ . For CTAB, estimated self diffusion coefficient is found to be  $\sim 1.0 \times 10^{-6} \text{ cm}^2/\text{s}$  (assuming viscosity of deuterated water at 300 K:  $\eta_{D2O} = 0.9 \text{ cP}$  [50] and  $R_{CTAB} \sim 22 \text{ \AA}$  as calculated from the Tanford formula [38] ) at 300 K, which is half of that obtained from the present



QENS measurement ( $2.0 \pm 0.3 \times 10^{-6} \text{ cm}^2/\text{s}$ ). As discussed in section 1.2.6 of chapter 1, global diffusion coefficient of micelles involves contributions from translational and rotational motion of the micelles leading to an apparent diffusion coefficient rather the self-diffusion coefficient. Such global diffusion coefficient has been observed for other micelles, block copolymers, and proteins in various solutions using QENS technique [50, 21,30,53] and are given in Table 4.1. Global diffusivity for CTAB micelles is found to be faster than the proteins and slower than SDS micelles owing to the difference in hydrodynamic diameters between proteins and micellar aggregates.

**TABLE 4.1** Diffusion coefficients ( $D_G$ ) corresponding to the global motion of CTAB micelles at different temperatures. Global diffusion coefficient observed for other micelles and proteins using QENS techniques [21,30,53] are also given for the comparison.

S.No	System	T (K)	$D_G (\times 10^{-6} \text{ cm}^2/\text{s})$
1.	CTAB micelles	300	$2.0 \pm 0.3$
		315	$3.1 \pm 0.4$
		330	$4.3 \pm 0.5$
2.	SDS micelles [53]	300	$2.5 \pm 0.1$
3.	Apo-calmodulin protein [21]	288	$0.65 \pm 0.04$
		323	$2.5 \pm 0.1$
4.	Myoglobin protein [30]	298	$0.82 \pm 0.02$
5.	Lysozyme protein [30]	298	$0.91 \pm 0.02$

#### 4.3.1.2. Segmental Motion

As mentioned earlier, the QENS data indicated that along with global motion there exist segmental motions of the monomers, which are faster than the global motion. As mentioned above, the 2nd Lorentzian in the scattering law arises from the contribution of both segmental and global motion as given in Eq. (4.1). The width of this Lorentzian ( $\Gamma_{G+seg}$ ) is actually sum of the widths of the Lorentzians correspond to global ( $\Gamma_G$ ) and segmental motions ( $\Gamma_{seg}$ ). As  $\Gamma_G$  is already known,  $\Gamma_{seg}$  is obtained by subtracting  $\Gamma_G$  from the  $\Gamma_{G+seg}$ . The variation of  $\Gamma_{seg}$  and  $A_{seg}(Q)$  with  $Q$  gives the detail insight about the nature of the segmental motion. The  $A_{seg}(Q)$  in Eq. (4.1) correspond to EISF for the segmental motion. Extracted EISF is shown in Fig. 4.5.

As mentioned earlier, CTAB molecule consists of a head group, consisting of three methyl groups and a long alkyl chain. Therefore, apart from the dynamics of the chain, head group would also contribute to the segmental motion of the monomer. Thus, the resultant scattering function for segmental motion of CTAB monomers can be expressed as a combination of scattering function arises from the motion of head group and the motion of the alkyl chain weighted by the number of hydrogen atoms exists in head and chain group. The resultant scattering law for segmental motion of CTAB molecules can be written as,

$$S_{seg}(Q, \omega) = P_h S_{head}(Q, \omega) + P_t S_{alkyl\ chain}(Q, \omega) \quad (4.2)$$

where  $P_h$  and  $P_t$  are the fraction of hydrogen atoms in head group and alkyl chain respectively. For CTAB molecules,  $(C_{16}H_{33}N^+(CH_3)_3Br^-)$   $P_h$  and  $P_t$  are equal to 9/42 and 33/42 respectively. In the above equation the first term correspond to motion of hydrogen atoms belonging to the head group and second term for those in the alkyl chain.

Dynamics of the methyl hydrogen atoms in the head group can be modeled by a 3-fold jump rotation in which hydrogen atoms reorient by 120° jumps on a circle about the 3 fold symmetry axis. The scattering law for the same can be written as [3]

$$S_{head}(Q, \omega) = \frac{1}{3} \left[ (1 + 2j_0(Qa)) \delta(\omega) + (2 - 2j_0(Qa)) \frac{1}{\pi} \frac{3\tau_1}{9 + \omega^2 \tau_1^2} \right] \quad (4.3)$$

where  $a$  is the H-H distance in the methyl group (1.8 Å) and  $\tau_l$  is the mean residence time at each site and  $j_0$  is spherical Bessel function of zeroth order.

In chapter 2, it was found that a model in which the hydrogen atoms move within spherical volumes; size of confining spheres and associated diffusivities varies linearly from a minimum to a maximum value. It may so happen that the CH<sub>2</sub> units near the head would have domain of dynamics the least and tail end is largest and so is the diffusivity. Same model is assumed for segmental motion of the alkyl chain of CTAB, micelles. Based on this model, the hydrogen atoms of the first ( $i=1$ ) CH<sub>2</sub> unit (nearest to the head group) will move within the smallest sphere of radius  $R_{min}$  and with the minimum diffusion coefficient  $D_{min}$ . And as one goes away from the head group along the alkyl chain, both diffusivity and radius of the sphere increase and the hydrogen atoms at the end of the tail or furthest from the head group will generate largest size sphere of radius  $R_{max}$  and with maximum diffusion coefficient  $D_{max}$ .

The scattering function for segmental motion of CTAB monomers can be written as,

$$S_{seg}(Q, \omega) = \frac{P_h}{3} \left[ (1 + 2j_0(Qa)) \delta(\omega) + (2 - 2j_0(Qa)) \frac{1}{\pi} \frac{3\tau_1}{9 + \omega^2 \tau_1^2} \right] + P_t \frac{1}{N} \sum_{i=1}^N \left[ A_0^0(QR_i) \delta(\omega) + \frac{1}{\pi} \sum_{\{l,n\} \neq \{0,0\}} (2l+1) A_n^l(QR_i) \frac{(x_n^l)^2 D_i / R_i^2}{\left[ (x_n^l)^2 D_i / R_i^2 \right]^2 + \omega^2} \right] \quad (4.4)$$

where  $N$  is the total number of carbon atoms in the alkyl chains. Rearrangement of various terms in Eq. (4.4) leads to the following equation,

$$S_{seg}(Q, \omega) = \left\{ \frac{P_h}{3} (1 + 2j_0(Qa)) + \frac{P_t}{N} \sum_{i=1}^N A_0^0(QR_i) \right\} \delta(\omega) + \frac{1}{\pi} \left[ \frac{P_h}{3} (2 - 2j_0(Qa)) \frac{3\tau_1}{9 + \omega^2 \tau_1^2} + \frac{P_t}{N} \sum_{i=1}^N \sum_{\{l,n\} \neq \{0,0\}} \left\{ (2l+1) A_n^l(QR_i) \frac{(x_n^l)^2 D_i / R_i^2}{[(x_n^l)^2 D_i / R_i^2]^2 + \omega^2} \right\} \right] \quad (4.5)$$

where  $R_i$  and  $D_i$  can be expressed as

$$R_i = \frac{i-1}{N-1} [R_{\max} - R_{\min}] + R_{\min} \quad (4.6)$$

$$D_i = \frac{i-1}{N-1} [D_{\max} - D_{\min}] + D_{\min} \quad (4.7)$$

From the Eqs. (4.5) and using  $A_0^0(QR_i) = \left[ \frac{3j_1(QR_i)}{QR_i} \right]^2$  as given in section 1.1.4.3 of chapter 1, the

EISF correspond to the segmental motion of the CTAB monomer ( $P_h=9/42$ ,  $P_t=33/42$  and  $N=16$ ) can be written as,

$$A_{seg}(Q) = \frac{1}{42} \left[ \frac{9}{3} [1 + 2j_0(Qa)] + 33 \frac{1}{16} \sum_{i=1}^{16} \left[ \frac{3j_1(QR_i)}{QR_i} \right]^2 \right] \quad (4.8)$$

$R_{\min}$  and  $R_{\max}$  are determined by least squares fit of the experimental extracted EISF with Eqs. (4.8) & (4.6). Solid lines in Fig. 4.5 represent the fit as obtained from the above description. At 300 K,  $R_{\min}$  and  $R_{\max}$  are found to be 0.02 and 2.8 Å respectively. This implies that the diffusion of hydrogen atoms in a CTAB chain are restricted to spheres of radii between 0.02 Å and 2.8 Å. With temperature, radii of sphere are found to increase and at 330 K,  $R_{\min}$  and  $R_{\max}$  are found to be 0.06 and 4.5 Å respectively. The values of these parameters at different temperatures are given in Table 4.2. A sketch to demonstrate the proposed model is shown in Fig. 4.6 where hydrogen atoms belong to head group perform 3-fold jump rotation on a circle and hydrogen atoms in the hydrophobic alkyl chain are shown to diffuse within a spherical volume of different sizes increasing linearly from head towards

tail.

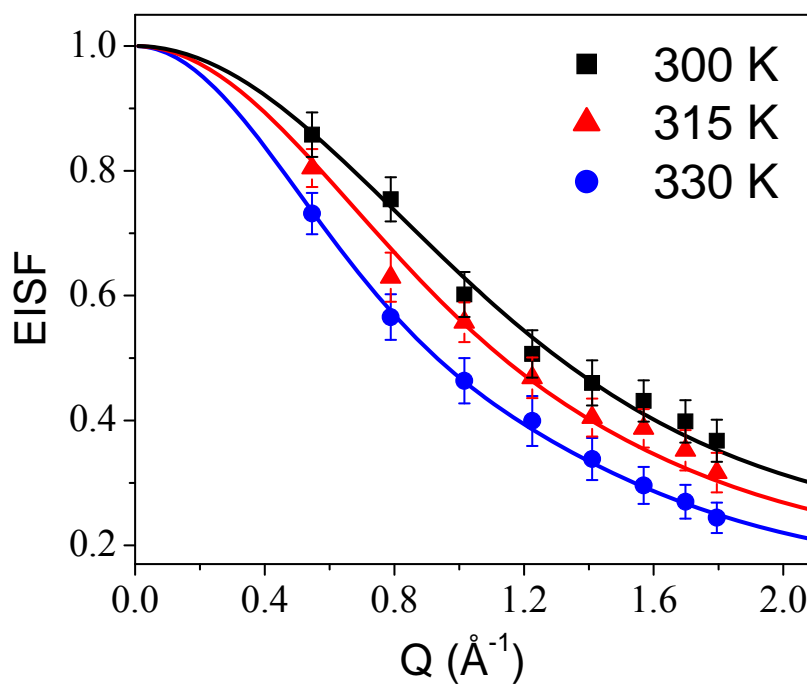


**Fig. 4.5** Variation of EISF for CTAB micellar solution with  $Q$  at temperatures of 300 K, 315 K and 330 K. The solid lines represent calculated EISF for a model described in the text.

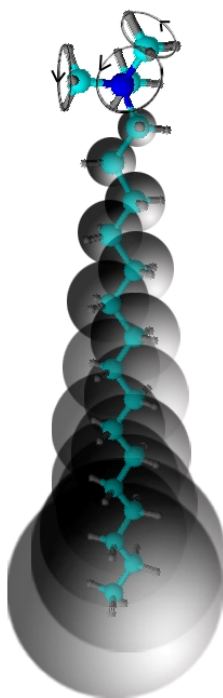


**Fig. 4.6** Schematic of the proposed model for the segmental motion of the monomer in CTAB micelles. Hydrogen atoms of the alkyl chain diffuse within spheres of different sizes,

radii of the spheres increase linearly from head towards tail. Hydrogen atoms belong to the methyl group existing in the head group performs 3-fold jump rotation.

The diffusivities associated with the different hydrogen atoms belonging to the CTAB monomer can be obtained from the  $\Gamma_{\text{seg}}(Q)$  which are obtained by subtracting  $\Gamma_G(Q)$  (width of the 1<sup>st</sup> Lorentzian) from the HWHM of the 2<sup>nd</sup> Lorentzian,  $\Gamma_{G+\text{Seg}}(Q)$  [in Eq. (4.1)]. Obtained  $\Gamma_{\text{seg}}(Q)$  is shown in Fig. 4.7 at different temperatures. As it is not possible to get an analytical expression for the HWHM of the quasielastic part for the present model, one can calculate the same numerically for given values of  $R_{\text{min}}$ ,  $R_{\text{max}}$ ,  $\tau_1$ ,  $D_{\text{min}}$  and  $D_{\text{max}}$  using Eqs. (4.5) to (4.7). The least squares fitting method is used to describe the observed QE width correspond to segmental dynamics with  $\tau_1$ ,  $D_{\text{min}}$  and  $D_{\text{max}}$  as parameters while the values of  $R_{\text{min}}$  and  $R_{\text{max}}$  are already known from the fit of the EISF (Fig. 4.5). Solid lines in Fig. 4.7 represent the fit as obtained from the above description. The obtained values of  $\tau_1$ ,  $D_{\text{min}}$  and  $D_{\text{max}}$  at different temperatures are given in Table 4.2.

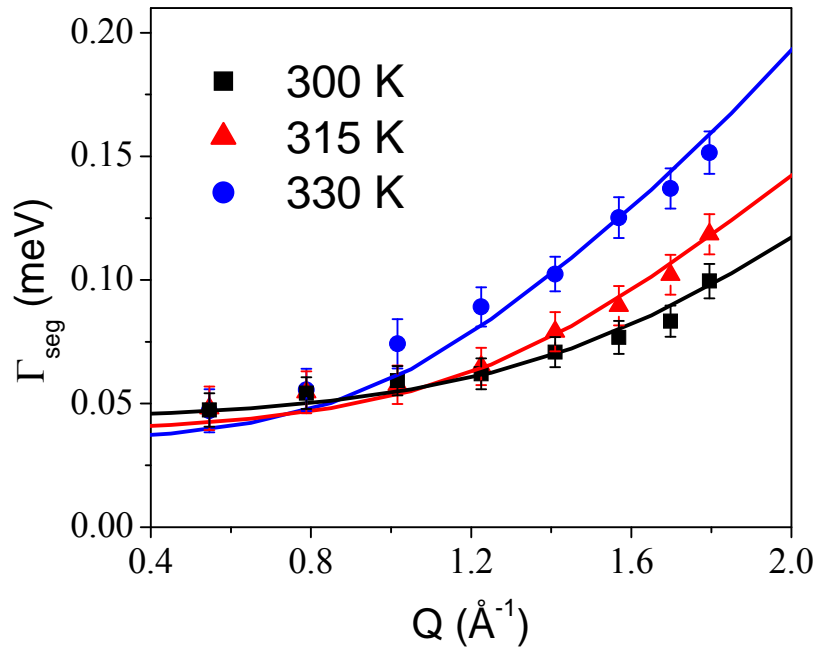


**Fig. 4.7** Variation of the half width at half maxima,  $\Gamma_{\text{seg}}$ , of the Lorentzian  $L_{\text{seg}}(\Gamma_{\text{seg}}, \omega)$ , which accounts for segmental motion of the monomer with  $Q$  at different measured

temperatures. Solid lines are the fits assuming the model as described in the text.

**TABLE 4.2** Radii of spheres,  $R_{min}$  and  $R_{max}$ , and associated diffusion coefficients,  $D_{min}$  and  $D_{max}$  for hydrocarbon chain and mean residence time ( $\tau_1$ ) for the hydrogen atoms in the head group, as obtained from the least square fitting of the data (Fig. 4.5 & 4.7) with a model discussed in the text, at different temperatures.

T(K)	$R_{min}(\text{\AA})$	$R_{max}(\text{\AA})$	$D_{min} (\times 10^{-5} \text{ cm}^2/\text{s})$	$D_{max} (\times 10^{-5} \text{ cm}^2/\text{s})$	$\tau_1$ (ps)
300	$0.02 \pm 0.01$	$2.8 \pm 0.2$	$0.1 \pm 0.04$	$1.0 \pm 0.2$	$6.5 \pm 0.6$
315	$0.03 \pm 0.02$	$3.4 \pm 0.3$	$0.1 \pm 0.04$	$1.3 \pm 0.2$	$5.2 \pm 0.5$
330	$0.06 \pm 0.03$	$4.5 \pm 0.3$	$0.2 \pm 0.05$	$1.9 \pm 0.3$	$4.0 \pm 0.5$

As shown in Table 4.2, the radii of the spheres, and the associated diffusivities increase with temperature. This can be understood in terms of various forces that govern the self-assembly process. Hydrophobic attractive forces and the interfacial free energy try to minimize the interfacial area per molecule of the micelle. However, it has to compete with the thermal energy and the repulsion between the head groups that put a constraint on the minimum area per molecule. As the temperature is increased, the monomers pack more loosely in the micelles as the distance between the two consecutive monomers increases due to thermal energy. This in turn provides more free space and increased mobility of hydrogen atoms. The values of  $\tau_1$  decreases with increase in temperature suggesting faster methyl group rotation at high temperatures.

#### 4.3.2. Results From Data Obtained Using FOCUS Spectrometer

NMR and MD simulation studies [43,45,55,56,59] on micellar systems indicate that the terminal part of the hydrocarbon chain shows the presence of a faster motion ( $\sim 1$  ps), which is ascribed to torsional oscillation of the  $\text{CH}_2$  groups. Similar fast torsional motion is also observed in anhydrous phospholipid membranes using QENS and MD simulation techniques [55]. In high-energy resolution QENS experiment (IRIS spectrometer at ISIS with  $\Delta E \sim 17.5$   $\mu\text{eV}$ ) such a fast process will contribute as a flat background, however it should be observable in a wider energy window spectrometer such as FOCUS with an energy resolution  $\Delta E \sim 55$   $\mu\text{eV}$ .

The formalism used to describe the data as obtained from IRIS spectrometer was found to be inadequate for the data from FOCUS. A broader quasielastic component is observed over and above that observed in IRIS, suggesting presence of a faster dynamical component, beyond the dynamical range of IRIS spectrometer. This could be the one associated with the conformational motion of the alkyl chain, as reported in the NMR and MD simulation studies [43,45,56,59]. Recent QENS study on lipid based vesicles indicates that only a fraction of an alkyl chain (mainly the terminal  $\text{CH}_2$  and methyl groups) participate in such fast torsional motion [81]. This is in support of other MD simulation studies, where it has been shown that probability of finding such motion is higher at the end of the alkyl chain [56,59]. Therefore, to develop the formalism for analyzing the data involving the torsional and segmental motion, two types of hydrogen atoms are assumed; (a) hydrogen atoms that experience segmental motion only (ii) hydrogen's that experience both segmental and torsional motions. Therefore resultant scattering law can be written as

$$S_{micelles}(\mathbf{Q}, \omega) = S_G(Q, \omega) \otimes \left[ P_a S_{seg}(\mathbf{Q}, \omega) + P_b \{ S_{seg}(\mathbf{Q}, \omega) \otimes S_{tor}(\mathbf{Q}, \omega) \} \right] \quad (4.9)$$

Here  $P_a$  is the fraction of hydrogen atoms take part in segmental motion and  $P_b$  is the fraction, which take part in segmental as well as in torsional motion, with  $P_a + P_b = 1$ .



For torsional motion, scattering law can be represented as a sum of elastic and quasilastic line

$$S_{tor}(Q, \omega) = A_{tor}(Q)\delta(\omega) + (1 - A_{tor}(Q))L_{tor}(\Gamma_{tor}, \omega) \quad (4.10)$$

As observed in SDS micelles here also the torsional motion is expected to be much faster than segmental motion or global motion of the whole micelle ( $\Gamma_{tor} \gg \Gamma_{seg}$  and  $\Gamma_G$ ), therefore Eq. (4.9) can be written as,

$$S_{micelles}(Q, \omega) = A_{seg}(Q)[1 - P_b + P_b A_{tor}(Q)]L_G(\Gamma_G, \omega) + (1 - A_{seg}(Q)) \\ [1 - P_b + P_b A_{tor}(Q)]L_{G+seg}(\Gamma_{seg} + \Gamma_G, \omega) + P_b(1 - A_{tor}(Q))L_{tor}(\Gamma_{tor}, \omega) \quad (4.11)$$

which comprises three Lorentzian functions. It may be noted that information about the global and segmental dynamics is already known from the data analysis of the IRIS data and those can be used while the information about the torsional motion to be extracted. This is possible as the later is much faster than the others. Therefore, to analyse the data as obtained from the FOCUS spectrometer, Eq. (4.11) can be rewritten as,

$$S_{micelles}(Q, \omega) = B_1 L_G(\Gamma_G, \omega) + B_2 L_{G+seg}(\Gamma_{seg} + \Gamma_G, \omega) + B_3 L_{tor}(\Gamma_{tor}, \omega) \quad (4.12)$$

Where  $B_1$ ,  $B_2$  and  $B_3$  are proportional to the  $A_{seg}(Q)[1 - p_b + p_b A_{tor}(Q)]$ ,  $(1 - A_{seg}(Q))[1 - p_b + p_b A_{tor}(Q)]$  and  $p_b[1 - A_{tor}(Q)]$  respectively.

$B_1$ ,  $B_2$ ,  $B_3$ ,  $\Gamma_{tor}$ ,  $\Gamma_G$  and  $\Gamma_{seg}$  are the parameters to be obtained by least squares fitting of the FOCUS data. It may be noted that  $\Gamma_G$  and  $\Gamma_{seg}$  are known from the IRIS data analysis, so only  $B_1$ ,  $B_2$ ,  $B_3$ , the weight factors and  $\Gamma_{tor}$  are only to be obtained. Eq. (4.12) is used to describe the observed QENS data with FOCUS. The fits are found to be satisfactory at all the

$Q$  values. Typical fits at 330 K, are shown in Fig 4.8. The relative area of the Lorentzian,  $L_G(\Gamma_G, \omega)$ , will define the effective EISF as

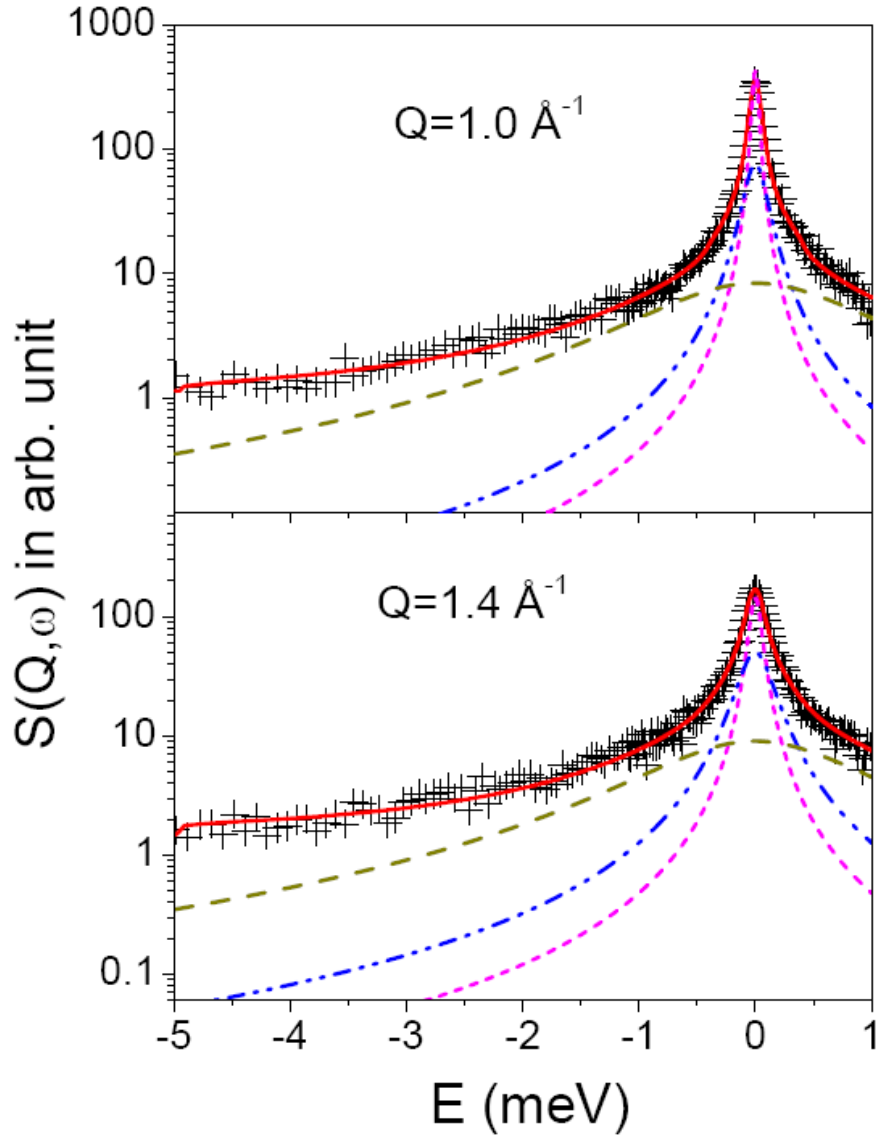


**Fig. 4.8** QENS spectra recorded for 10 % (w/w) CTAB micelles from FOCUS at the temperature 330 K. The phenomenological fit represented by the solid line is based on Eq.(4.12) sum of three Lorentzian functions. The broadest component corresponds to the torsional motion and is shown by the dashed (*dark yellow color*) line. Other components correspond to the global and segmental motions are shown by short dashed (*magenta color*) and dash-dotted (*blue color*) line respectively.

$$\frac{B_1}{B_1 + B_2 + B_3} = A_{seg}(Q)[1 - P_b + P_b A_{tor}(Q)] = (EISF)_{eff} \quad (4.13)$$

Here  $A_{seg}(Q)$  is the EISF correspond to segmental motion and  $A_{tor}(Q)$  is the EISF correspond to torsional motion and  $P_b$  is the fraction of hydrogen atoms, which are participating, in both segmental as well as in torsional motion. The EISF for the segmental motion  $A_{seg}(Q)$  is already known from the IRIS data. The obtained effective EISF is shown in Fig. 4.9. Since for the torsional motion of alkyl chain, two-fold jump rotation of  $\text{CH}_2$  unit is the best suited model [81], Eq. (4.10) can be rewritten using the scattering law for two-fold jump rotation as [3]

$$S_{tor}(Q, \omega) = \frac{1}{2}[1 + j_0(Qd)]\delta(\omega) + \frac{1}{2}[1 - j_0(Qd)]\frac{1}{\pi}\left[\frac{2\tau_2}{4 + \omega^2\tau_2^2}\right] \quad (4.14)$$

where  $j_0$  is the spherical Bessel function of zeroth order,  $d$  is the distance between the two jump sites and  $\tau_2$  is the mean residence time at each site. Eq. (4.13) can be written as,

$$(EISF)_{eff} = A_{seg}(Q)\left[1 - P_b + \frac{P_b}{2}\{1 + j_0(Qd)\}\right] \quad (4.15)$$

Eq. (4.15) is used to describe the observed effective EISF with  $P_b$  and  $d$  as the fitting parameters.

It is found that Eq. (4.15) describe the effective EISF satisfactorily with a value of  $P_b=0.24$  and  $d=(2.0 \pm 0.2) \text{ \AA}$ . The assumption of 2-fold jump diffusion for torsional motion is supported by the value obtained for the distance  $d$  ( $2.0 \text{ \AA}$ ), which is consistent with the distance between two sites which hydrogen atoms can occupy during conformational change in the alkyl chain. Only 24 % hydrogen atoms in the alkyl chain are found to participate in the faster torsional motion along with the segmental motion. NMR, MD simulation studies

[45,56,59] also suggested that only few hydrogen atoms in the tail region of alkyl chain undergo fast torsional motions.

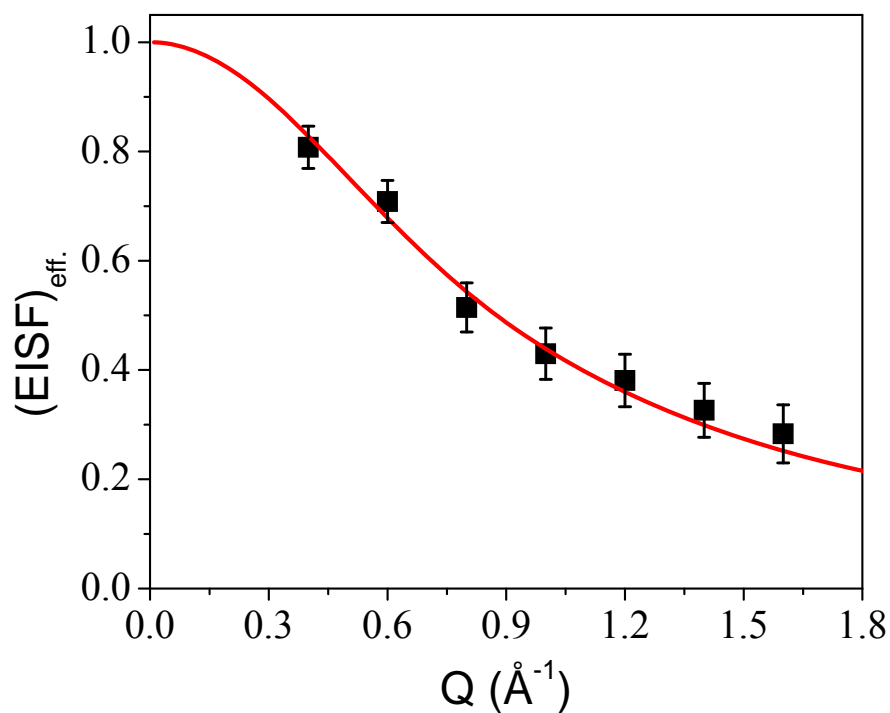


**Fig. 4.9** Variation of effective EISF with  $Q$  for CTAB micellar solution at 330 K. The solid lines represent the calculated EISF (Eq. 4.15) for a model described in the text.

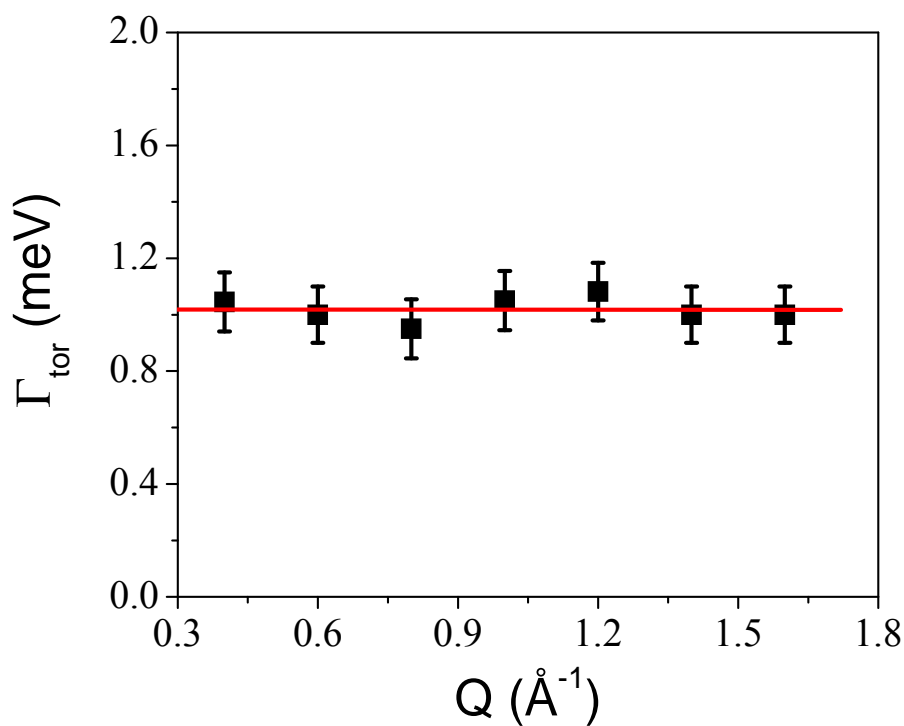


**Fig. 4.10** Variation of the half width at half maxima,  $\Gamma_{\text{tor}}$ , with  $Q$ , of the Lorentzian  $L_{\text{tor}}(\Gamma_{\text{tor}}, \omega)$ , corresponding to torsional motion.

The HWHM of the Lorentzian function ( $\Gamma_{\text{tor}}$ ) corresponding to torsional motion is shown in Fig. 4.10, which is more or less constant with  $Q$ , as expected for a 2-fold motion. The mean residence time,  $\tau_2$ , is related to  $\Gamma_{\text{tor}}$ , as  $\tau_2 = 2/\Gamma_{\text{tor}}$  [Eq. (4.14)].  $\tau_2$  is found to be  $1.3 \pm 0.2$  ps. The above methodology is found to describe the data at other temperatures consistently. It is found that while  $P_b$  reduces to 0.15 at room temperature, the residence time remains more or less same in the temperature range (300-330 K). This is consistent with the earlier MD simulation studies on short polyethylene chain in which time scale of such fast torsional motion of alkyl chain was found to be independent of wave vector transfer and the temperature [80].

Here the detailed dynamical feature exists in CTAB micelles are reported. Global diffusion of the whole micelle is found to be Fickian in nature. The QENS data presented here are compatible with proposed model that assumes the internal dynamics of micelles in terms of two independent hydrogen populations; 1) those which participate only in segmental motions and 2) those which participate in segmental as well as in fast torsional motion. Description of segmental motion of the monomer is consistent with recent MD simulation results on SDS/SDBS micelles where it was shown that the carbon atoms at the tail region undergo faster diffusion [59]. NMR spectral investigations of CTAB micellar solutions [43,45] showed that the mobility of the chains increases from the polar head to the non-polar tail. Few hydrogen atoms in the alkyl chain are also found to undergo faster torsional motion in addition to the localised translational diffusion. The observed fast torsional motion corroborates the results reported by NMR and MD simulation studies on micelles [43,45] and neutron scattering study on lipid based vesicles [81].

#### 4.4. CONCLUSIONS

The dynamics of cetyltrimethylammonium bromide (CTAB) micelles have been investigated at a molecular scale using incoherent quasielastic neutron scattering technique [10]. The dynamical features of this cationic micellar system have been investigated using two different time-of-flight spectrometers, probing a wide energy range and thus a detailed dynamical landscape is obtained. Data analysis showed the presence of both global micellar diffusion and internal motion associated with the monomer of the micelles. Global diffusion of the whole micelle is commensurate with a model which assumes Fickian diffusion of the micelle. Internal dynamics of CTAB micelles have been successfully described assuming the existence of different dynamical components: segmental motion of the monomer and additional faster torsional motion. Segmental motion has contributions from the head group in addition to the alkyl chain. While the dynamics of the methyl groups in the head group are modelled as three-fold jump rotations about the symmetry axis, the hydrogen atoms belonging to the alkyl chain, undergo localised translation diffusion confined within spheres with linear distribution of sizes. The radii of these spheres and associated diffusivity of the hydrogen atoms increase linearly from head towards tail. The observed fast torsional motion associated with some of the CH<sub>2</sub> groups belonging to the alkyl chain, most likely from the terminal part, has also been successfully described by a 2-fold jump rotation. Overall, here we have put forward a comprehensive description of complex dynamics in CTAB micelles as observed over a wide dynamical range using two different neutron spectrometers.

## CHAPTER 5

# Effect of Molecular Architecture on the Dynamics of the Ionic Micelles

### 5.1. INTRODUCTION

Dynamics of an anionic sodium dodecyl sulfate (SDS) micelles [52,53,97] as well as a cationic cetyltrimethylammonium bromide (CTAB) micelles [10] has been studied and discussed in the previous chapters. It is found that dynamics of micelles is sensitive towards the external parameters (temperature, hydration, etc.). Molecular architecture of the surfactant is an important parameter that controls the structural arrangement of the monomers in the micelles and by this one can tailor micellar system for different applications. Typical structural variations include the relative sizes of the hydrophobic tail and hydrophilic head groups, single-versus multiple-tailed surfactants, the presence of single and multiple head groups and many others. It is found that with increase in alkyl chain length aggregation number as well as the size of the micelles increases [90,93,98]. Berr [93] has shown that for 0.1 M micellar solution of  $C_n$ TAB, micelles of  $C_{12}$ TAB and  $C_{14}$ TAB are more or less spherical whereas for higher  $n$ , like  $C_{16}$ TAB, at the same concentration and temperature a more pronounced prolate ellipsoidal shape is found to accommodate the extra hydrocarbons in the core. The micelles appear to become drier, both in terms of water content and depth of water penetration as the chain length  $n$  increases. The fractional charge of the micelles is found to decrease with the alkyl chain length [93,98]. Critical micellar concentration (CMC) of the micelles is found to decrease with increase in chain length since a larger hydrophobic part of the surfactant molecule favors the micellization [93]. Recently effect of location of the phenyl ring within the alkyl tail of a series of isomeric cationic surfactants is studied [99].

CMC is found to decrease by almost an order of magnitude when the phenyl ring was moved from the tail end towards head [99]. Small angle neutron scattering (SANS) measurements revealed that the aggregation number of the micelles increases as location of phenyl ring on isomeric surfactant move towards head group. This increase in the aggregation number is accompanied by an increase in the axial ratio of the micellar aggregate and a decrease in the fractional charge. These observations have been explained in terms of decrease in cross sectional area of the alkyl chain when phenyl ring is located near the head group. Although structures (size and shape) of the micelles with change in the molecular architecture of the surfactant are well studied [90,93,98,99], there are no information on the dynamical aspect of the micelles with change in the molecular architecture. Therefore, it is of interest to investigate this to establish the correlation of the dynamics that might exist with the microstructure of the micelles. Few examples of effect towards dynamics due to change in molecular architecture are discussed in this chapter. In the category of cationic micelles, effect of chain length on the dynamics of n-alkyltrimethylammonium bromides ( $C_nH_{2n+1}N(CH_3)_3Br$ ,  $C_nTAB$ ; for  $n = 10, 12, 14, 16$ ) is of interest and discussed in this chapter. Detailed dynamical landscape in cetyltrimethylammonium bromide (CTAB or  $C_{16}TAB$ ) is reported in chapter 4, here the same is studied for the other  $C_nTAB$  ( $n=10, 12$  and  $14$ ) micelles and the dynamical features are compared. Chemical structures of  $C_nTAB$  molecules with different chain length are shown in Fig. 5.1.  $C_nTAB$  surfactant molecules ionize in aqueous solution and the corresponding micelles are aggregates of  $C_nTA^+$  ions. The micelle is positively charged and is thus called a cationic micelle. The  $Br^-$  ions, known as counterions, tend to stay near the  $C_nTA^+$  micellar surface. The counterions located at short enough distances from the micellar surface feel a very strong electrostatic attraction compared to the thermal energy and therefore these counterions are referred to as ‘bound to’ or ‘condensed on’ the micelles [90].



Similarly in the category of the anionic micelles, detailed dynamics of SDS ( $C_{12}H_{25}OSO_3Na$ ) micelles is discussed in chapter 2, here a comparison with the dynamics of a similar surfactant namely sodium dodecyl benzene sulfonate (SDBS;  $C_{12}H_{25}C_6H_4SO_3Na$ ), which has an additional phenyl ring near the head group, is discussed. It is of interest to study the effect of an additional phenyl ring towards dynamics of anionic micelles. SDBS is a major constituent of the synthetic detergents and widely used in emerging field of nano technology for graphene exfoliation, suspending fullerene or single wall nanotube in aqueous solutions, for the synthesis of nanoparticles etc. [100-102]. Recent MD simulation study by Palazzesi et al [59] on SDBS and SDS micelles showed that though structure of both the surfactants are very similar, dynamical behaviours differ significantly. The SDBS molecule contains hydrophobic dodecyl alkyl chain similar to SDS molecules. In addition, there exists a phenyl ring attached to the hydrophilic sulfonate group as shown in Fig. 5.1. It is reported that SDBS micelle shows special characteristics due to the presence of a phenyl group through the formation of  $\pi$  stack aggregates. The MD simulation study shows that dodecyl chains in SDBS micelles are less flexible than in SDS micelles [59]. Flexibility of the chain is an important issue for the release of solubilized drugs in targeted drug delivery process and, experimentally, it can be probed by quasielastic neutron scattering (QENS) technique.

The organization of this chapter is as follows: Details of the QENS experiments are given in section 5.2. Results and discussions of effect of chain length on dynamics of cationic  $C_n$ TAB micelles are discussed in section 5.3.1. Results and discussion of effect of phenyl ring on the dynamics of anionic micelles are discussed in section 5.3.2. The conclusions are depicted in section 5.4.

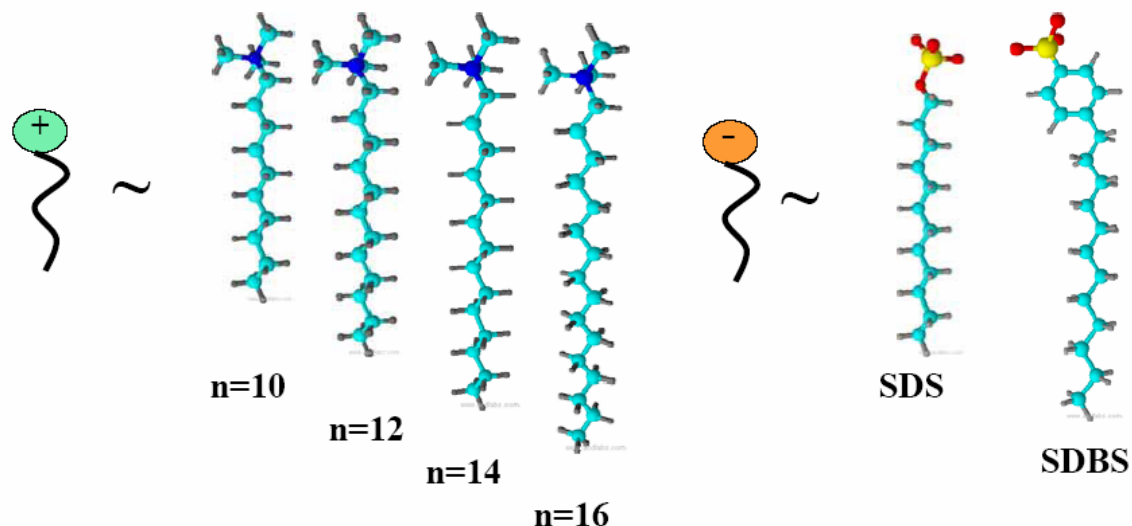


**Fig 5.1** Schematic of cationic surfactants  $C_n$ TAB having different chain length and anionic SDS and SDBS molecules.

## 5.2. EXPERIMENTAL DETAILS

All cationic surfactants  $C_n$ TAB ( $n=10,12,14$  and  $16$ ) were obtained from Aldrich.  $0.3$  M micellar solutions were prepared separately by dissolving  $C_n$ TAB in  $D_2O$  (99.9% atom D purity) for all above mentioned  $C_n$ TAB surfactants. The neutron scattering experiments have been carried out using the inverted geometry spectrometer IRIS at the ISIS pulsed neutron source, Didcot, UK. IRIS was operated with the 002 pyrolytic graphite analyser providing energy resolution of  $\Delta E \sim 17.5 \mu\text{eV}$  (full width at half-maximum, FWHM), and with the energy transfer range of  $-0.3$  to  $1.2$  meV (in the offset mode). The wave-vector transfer ( $Q$ ) range covered was  $0.5$ - $1.8 \text{ \AA}^{-1}$ . Measurements were carried out on a series of  $C_n$ TAB systems, namely,  $C_{10}$ TAB,  $C_{12}$ TAB,  $C_{14}$ TAB,  $C_{16}$ TAB. Data from pure  $D_2O$  were also recorded. To study the effect of temperature, measurements were carried out at  $300$ ,  $315$  and  $330$  K. The samples were placed in an annular aluminum can with an internal spacing of  $1$  mm to minimise multiple scattering and have reasonable measuring statistics. The ISIS data

analysis package, MODES [62], was used to carry out data reduction involving background subtraction, detector efficiency corrections etc.

Both SDBS and SDS surfactants are obtained from Aldrich. 0.3 M micellar solutions were prepared separately in D<sub>2</sub>O (99.9% atom D purity) for the both surfactants. The QENS experiments have been carried out using the time of flight spectrometer IN5 at the Institute Laue Langvin, Gernoble, France. IN5 was operated with the incident wavelength 6 Å providing an energy resolution of  $\Delta E \sim 60 \mu\text{eV}$  (full width at half-maximum, FWHM). Measurements were carried out on 0.3 M SDBS micellar solution at three different temperatures 300, 315 and 330 K in the wave-vector transfer ( $Q$ ) range 0.3-1.7 Å<sup>-1</sup>. Data were collected for pure D<sub>2</sub>O also at each temperature to estimate the contribution of the solvent. For comparison, QENS measurements have also been carried out on 0.3 M SDS micellar solution with the same instrumental set up. The samples were placed in an annular aluminum can with an internal spacing of 0.3 mm to minimize multiple scattering and have reasonable measuring statistics. Since we are interested to investigate the effect of additional phenyl group on the dynamics of anionic micelles therefore all other factors, which may affect the dynamics (molar concentration, temperatures etc) are kept identical for the both micellar solutions. The ILL data analysis package, LAMP [63], was used to carry out data reduction involving background subtraction, detector efficiency corrections, etc

### **5.3. RESULTS AND DISCUSSION**

#### **5.3.1. Effect of Chain Length on the Dynamics of Cationic CnTAB Micelles.**

QENS spectra for the CnTAB micelles is obtained by subtracting the contribution of D<sub>2</sub>O from the micellar solution and shown in Fig 5.2 (a) for a typical  $Q$  value of 1.2 Å<sup>-1</sup>. The instrumental resolution is also shown for comparison. Spectra have been normalised to the peak amplitude. Significant quasielastic (QE) broadening is observed for all C<sub>n</sub>TAB micelles

over the instrumental resolution. It is evident from the Fig.5.2 (a) that the QE broadening is found to be maximum for the smallest chain length micelle,  $C_{10}$ TAB. It decreases with increasing chain length and found to be minimum for longest chain length micelle,  $C_{16}$ TAB.

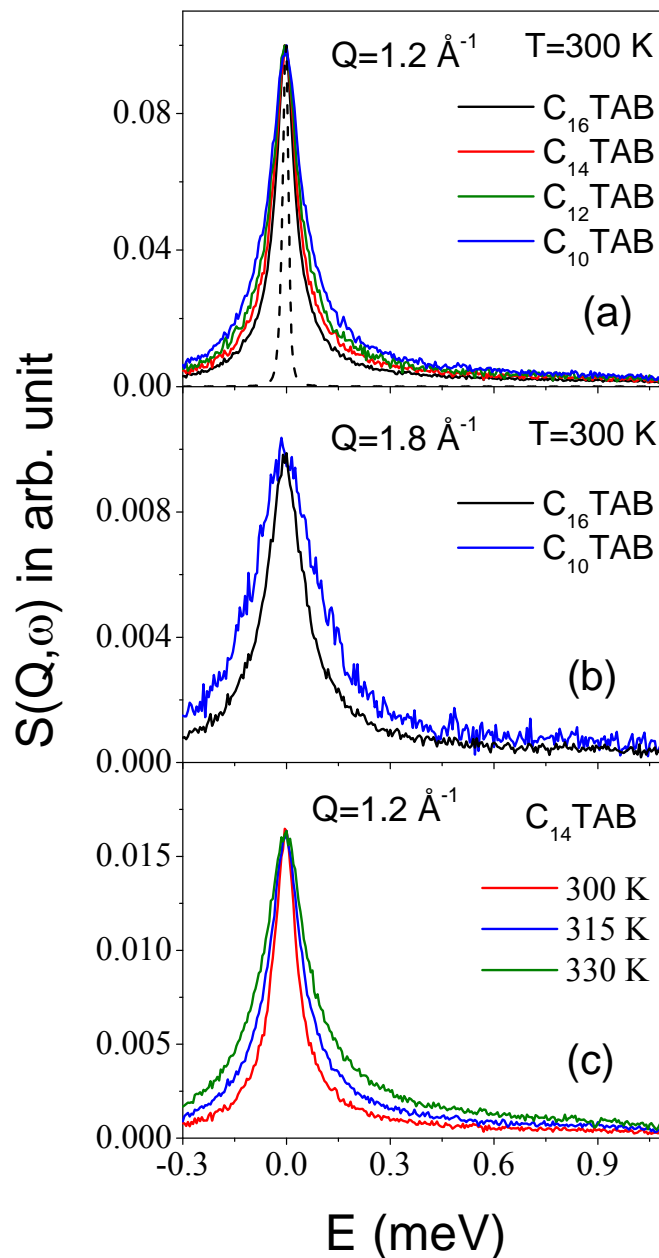


**Fig. 5.2** Typical QENS spectra for 0.3 M  $C_n$ TAB micellar solution, (a) for different chain lengths at typical value of  $Q=1.2 \text{ \AA}^{-1}$ , (b) for  $C_{10}$ TAB and  $C_{16}$ TAB micelles at  $Q=1.8 \text{ \AA}^{-1}$ , (c) for  $C_{14}$ TAB micelles at  $Q=1.2 \text{ \AA}^{-1}$  at different temperatures. All the spectra are normalised to peak amplitude. The instrument resolution is shown by dashed line.

This difference in QE broadening is more pronounced at high wave vector transfer  $Q$ . The peak normalized QENS spectra for the lowest chain length, C<sub>10</sub>TAB and highest chain length, C<sub>16</sub>TAB micelles are shown in Fig. 5.2 (b) at  $Q=1.8 \text{ \AA}^{-1}$ . The effect of temperature on the QENS spectra for C<sub>14</sub>TAB micelles is also shown in Fig. 5.2 (c). As evident the QE broadening is found to increase with the increasing temperature.

As discussed in chapter 2 and 4 that internal dynamics of micelles comprises of segmental and fast torsional motion, and it is possible to separate these contributions by using two suitable spectrometers having different energy resolutions as they are in different time scale [10,81]. Segmental motion being slower could be observed with high-energy resolution instrument where the faster torsional motion would contribute as background. The data from lower resolution instrument would have contribution from both segmental and torsional motion.

To observe the segmental motion for all CnTAB micelles, QENS data were recorded with high-energy resolution IRIS spectrometer ( $\Delta E \sim 17.5 \text{ \mu eV}$ ). Scattering law for CnTAB micelles can be written as [from Eq. (1.82)]

$$S_{micelles}(Q, \omega) = \left[ A_{seg}(Q) L_G(\Gamma_G, \omega) + (1 - A_{seg}(Q)) L_{tot}(\Gamma_{tot}, \omega) \right] \quad (5.1)$$

where  $A_{seg}(Q)$  is the elastic incoherent structure factor (EISF) for the segmental motion.  $\Gamma_{tot} = \Gamma_G + \Gamma_{seg}$  ; where  $\Gamma_G$  and  $\Gamma_{seg}$  are the half width at half maxima (HWHM) of the Lorentzian corresponding to global and segmental motions respectively. For data analysis, the scattering law [Eq. (5.1)] is convoluted with the instrumental resolution function and the parameters involved ( $A_{seg}(Q)$ ,  $\Gamma_G$  and  $\Gamma_{tot}$ ) are obtained by least squares fit with the experimental data. Typical fitted spectra for the C<sub>14</sub>TAB micelles at different temperatures are shown in Fig. 5.3(a) for  $Q=1.0 \text{ \AA}^{-1}$  and at different  $Q$  are shown in Fig. 5.3 (b) at  $T=300\text{K}$ .

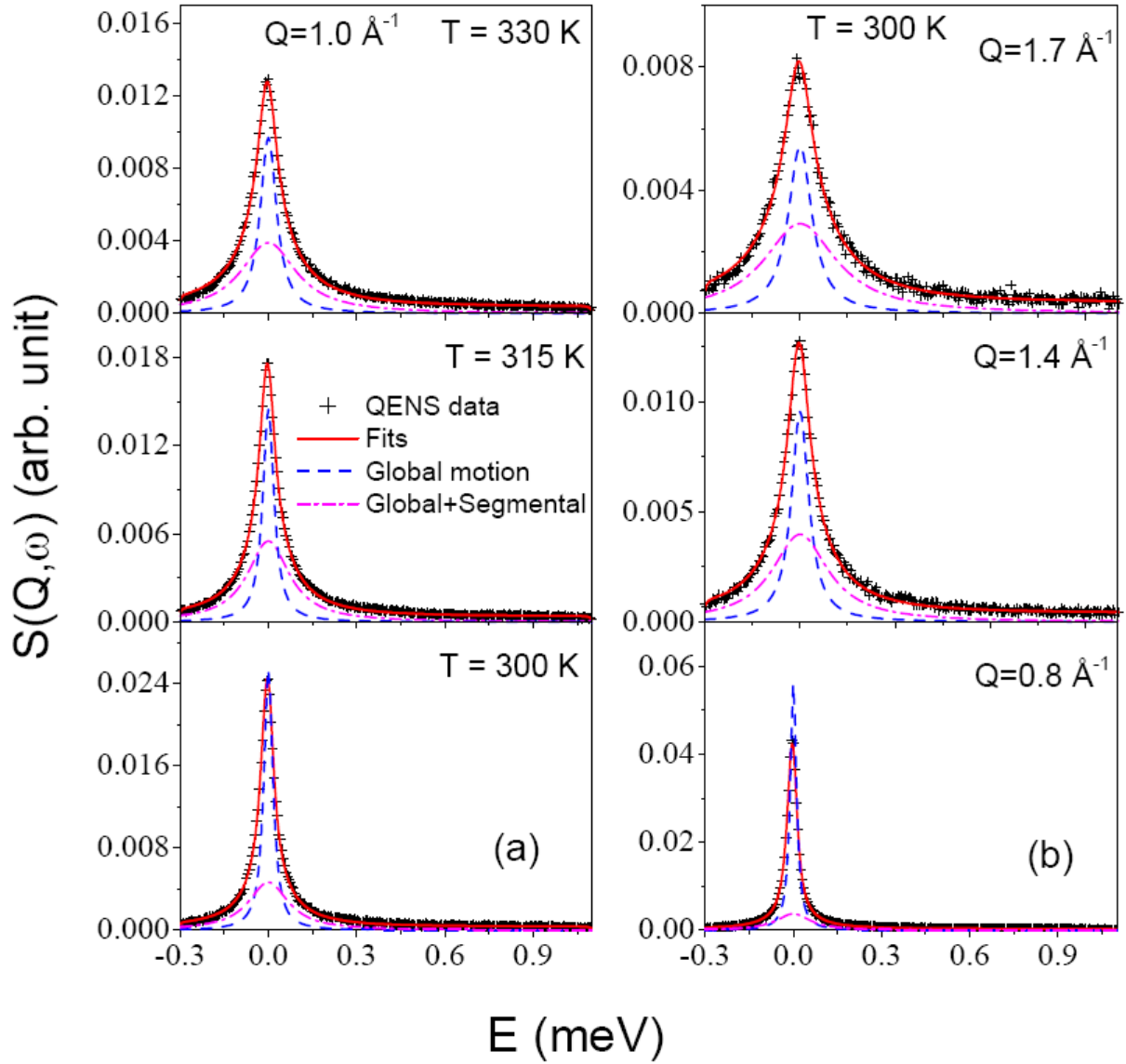


**Fig. 5.3** Typical fitted  $S_{\text{micelles}}(Q, \omega)$  for 0.3 M  $C_{14}\text{TAB}$  micelles, (a) at different temperatures at  $Q = 1.0 \text{ \AA}^{-1}$  and (b) for different  $Q$  values at  $T = 300 \text{ K}$ , assuming model function given in Eq. (5.1).

It is evident from the Fig. 5.3(a) that the HWHM of both Lorentzian functions and relative area of broader Lorentzian increases with temperature. Fitted spectra for  $C_n\text{TAB}$  ( $n=10,12,14$  and  $16$ ) micelles at a typical value of  $Q=1.2 \text{ \AA}^{-1}$  at  $300 \text{ K}$  is shown in Fig 5.4. It is evident that model scattering law [Eq. (5.1)] describes the data very well for all  $C_n\text{TAB}$  micelles at different temperatures and  $Q$  values. To gain more insight into the nature of these two dynamical processes, global and segmental, the parameters obtained from the fit are

analyzed as a function of  $Q$ . As mentioned above the global motion of the whole  $C_n$ TAB micelle is expected to be slower than the segmental motion as found for SDS and  $C_{16}$ TAB micelles described in chapter 2 and 4 respectively. Therefore, it can be assumed that the slower global motion corresponds to the narrower Lorentzian (hereafter referred as 1<sup>st</sup> Lorentzian), whereas the broader Lorentzian (hereafter referred as a 2<sup>nd</sup> Lorentzian), which represents the convolution of two Lorentzians, corresponds to both global and segmental motion of the micelles.

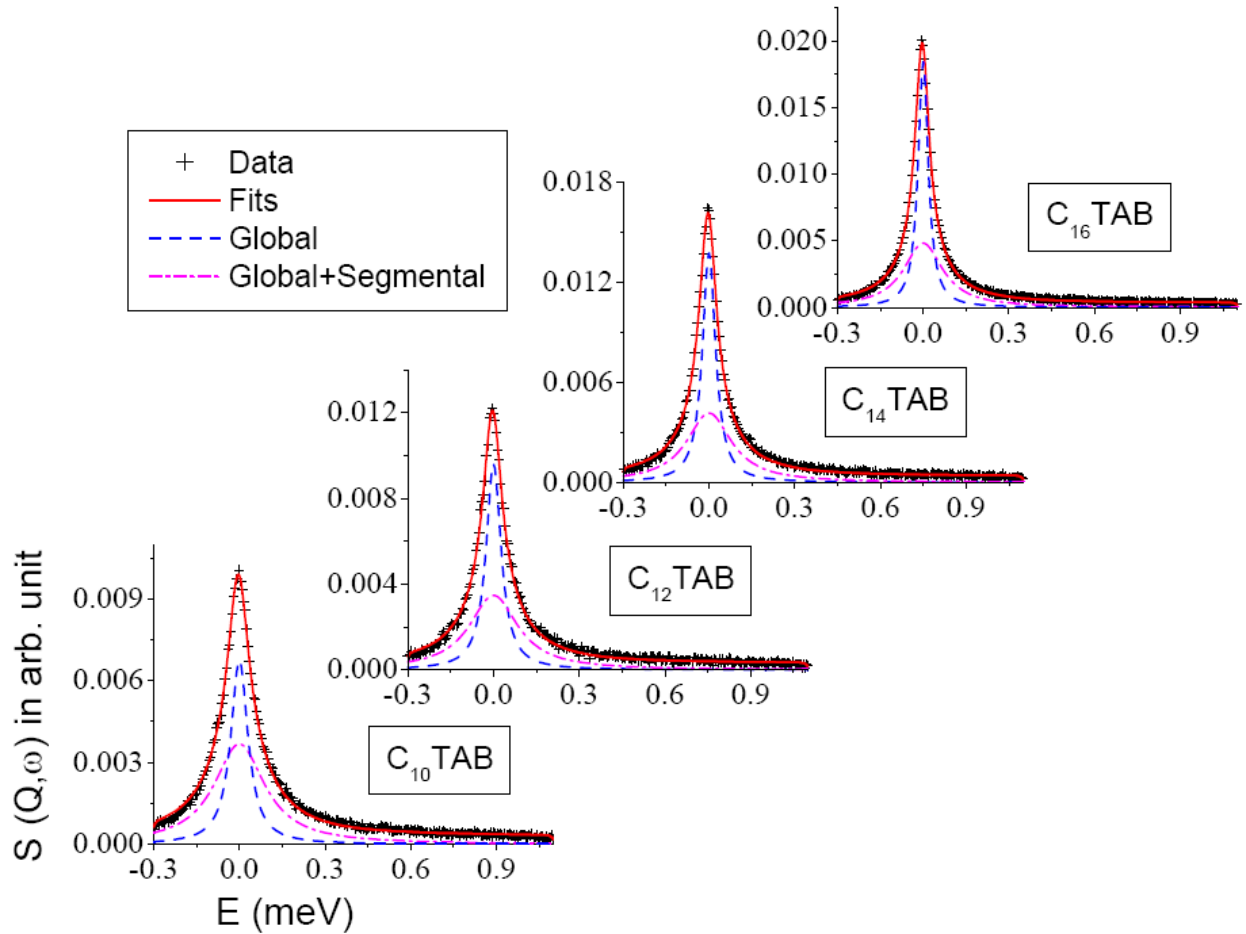


**Fig. 5.4** Typical fitted  $S_{\text{micelles}}(Q, \omega)$  for 0.3 M  $C_n$ TAB micellar solution at a typical value of  $Q=1.2 \text{ \AA}^{-1}$  at 300 K, assuming model function given in Eq. (5.1).

The variation of the HWHM,  $\Gamma_G$ , of the 1<sup>st</sup> Lorentzian, corresponding to the global dynamics of the micelles, for different  $C_n$ TAB micellar systems with  $Q^2$  is shown in Fig. 5.5. A simple Brownian motion following Ficks law,  $\Gamma_G = D_G Q^2$  is found to describe the observed behaviour quite well. Here  $D_G$  is the diffusion coefficient corresponds to the global motion. For each  $C_n$ TAB micellar systems,  $D_G$ , is obtained from the slope of  $\Gamma_G$  vs  $Q^2$ . For example,  $D_G$ , obtained for  $C_{14}$ TAB micelles are found to be  $2.5 \times 10^{-6} \text{ cm}^2/\text{s}$  at 300 K. Variation of the obtained  $D_G$  for different  $C_n$ TAB micelles at 300 K is shown in Fig 5.6.  $D_G$  obtained for  $C_{14}$ TAB micelles at different temperatures are also shown in Fig. 5.6.  $D_G$  of  $C_{14}$ TAB micelles is found to increase with the temperature as expected for a thermally activated diffusive motion.

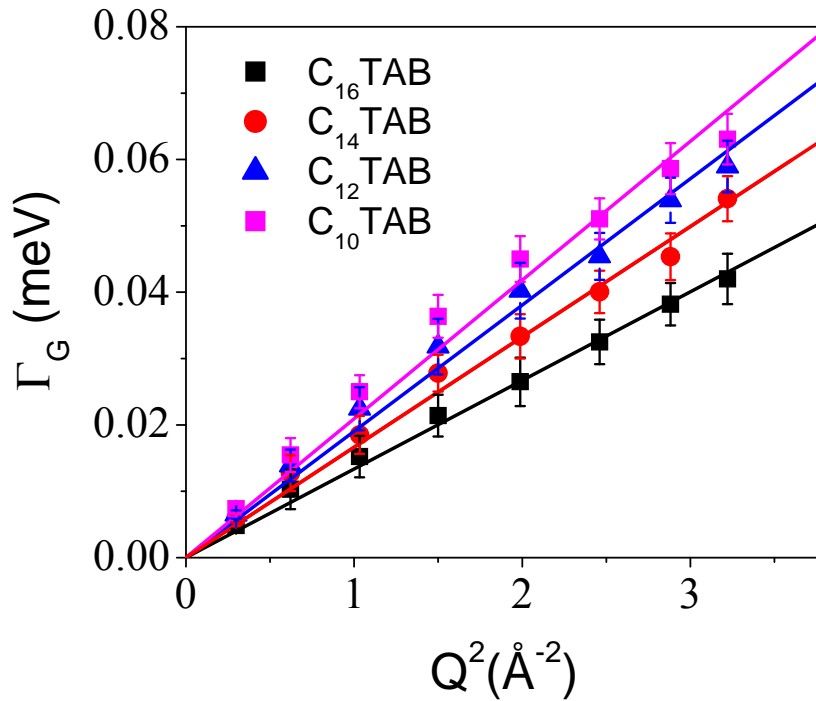


**Fig. 5.5** Variation of half width at half maxima,  $\Gamma_G$ , of the Lorentzian  $L_G$  ( $\Gamma_G$ ,  $\omega$ ), corresponds to the global motion of  $C_n$ TAB micelles (for  $n = 10, 12, 14$  and  $16$ ) with  $Q^2$  at 300 K. The solid lines correspond to fits with Fick's law of diffusion.



It is evident that diffusivity corresponds to the global motion of the  $C_n$ TAB micelles decreases with the increase of the monomer chain length. For  $C_{10}$ TAB micelles,  $D_G = 3.2 \times 10^{-6} \text{ cm}^2/\text{s}$  is obtained while for  $C_{16}$ TAB micelles, it is found to be equal to  $2.0 \times 10^{-6} \text{ cm}^2/\text{s}$ . It may be noted that small angle neutron scattering and NMR data on the  $C_n$ TAB micelles showed that aggregation number, size of micelles, etc. increase with the increase of the alkyl chain length [90,93,98,103]. Berr [93] found the values of minor and major axis for 0.1 M  $C_{12}$ TAB micelles as 21.9 Å and 26.1 Å respectively which were found to increase to 26.6 Å and 44.3 Å for 0.1 M  $C_{16}$ TAB. Aggregation number for different  $C_n$ TAB micelles found to increase from 50 to 164 as one goes from  $C_{12}$ TAB to  $C_{16}$ TAB micelles. The available structural parameters are listed in Table 5.1. The decrease in global diffusivity with the increase in chain length as observed here is the manifestation of the combined effect of the increase in hydrodynamic size and aggregation number of the micelles.

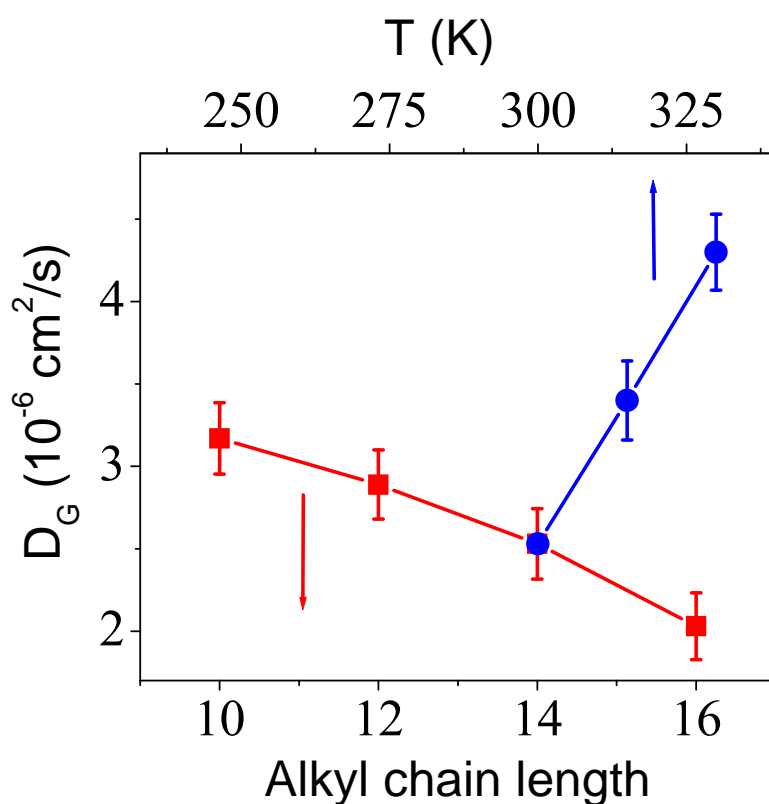


**Fig. 5.6** Variation of global diffusivity,  $D_G$  for different  $C_n$ TAB micelles with the alkyl chain length at 300 K. The temperature dependence of  $D_G$  for  $C_{14}$ TAB is also shown.

**Table 5.1** Various parameters related to shape and size of the 0.1 M  $C_n$ TAB micelles for different chain lengths as obtained using Small Angle Neutron Scattering (SANS) experiment at 298 K as taken from ref. [93].

Micelles	Aggregation Number	Micellar Charge $Z (+)$	Fractional charge $\beta (+) = Z/N$	Minor axis $A_T (\text{\AA})$	Major axis $B_T (\text{\AA})$	Axial Ratio
$C_{12}$ TAB	50	15	0.31	21.9	26.1	1.19
$C_{14}$ TAB	84	19	0.23	25.7	29.6	1.15
$C_{16}$ TAB	163	23	0.14	26.6	44.3	1.66

As mentioned above, QENS data indicated presence of two Lorentzian functions [Eq. (5.1)]: (i) first one corresponds to global motion as discussed above and (ii) 2<sup>nd</sup> Lorentzian has contribution from both segmental as well as the global motion. To investigate the segmental motion the parameters  $\Gamma_{seg}$  and EISF [ $A_{seg}(Q)$ ] are analyzed as a function of  $Q$ . Variation of EISF for different  $C_n$ TAB micellar solution with  $Q$  at 300 K is shown in Fig. 5.7 In the previous chapter, segmental motion of  $C_{16}$ TAB micelles has been described successfully assuming a model in which methyl groups in the head group undergo three-fold jump rotations about the symmetry axis and the alkyl chain undergoes localised translation diffusion confined within spheres. We found that radii ( $R_i$ ) of the sphere and associated diffusivity ( $D_i$ ) vary linearly from a minimum to maximum correspond to one near the head group & towards tail respectively. Same model is applied to describe segmental motion of all

the C<sub>n</sub>TAB micelles considered in the present study. Therefore, the general scattering law for segmental motion of C<sub>n</sub>TAB molecules can be written as [Chapter 4, Eq. (4.5)]

$$S_{seg}(Q, \omega) = \left\{ P_h B_0(Qa) + \frac{P_t}{n} \sum_{i=1}^n A_0^0(QR_i) \right\} \delta(\omega) + \frac{1}{\pi} \left[ P_h B_1(Qa) \frac{3\tau}{9 + \omega^2 \tau^2} + \frac{P_t}{n} \sum_{i=1}^n \sum_{\{l, m\} \neq \{0, 0\}} \left\{ (2l+1) A_m^l(QR_i) \frac{(x_m^l)^2 D_i / R_i^2}{[(x_m^l)^2 D_i / R_i^2]^2 + \omega^2} \right\} \right] \quad (5.2)$$

where  $P_h$  and  $P_t$  are the fraction of hydrogen atoms in head group and alkyl chain respectively. For C<sub>n</sub>TAB molecules, (C<sub>n</sub>H<sub>2n+1</sub>N<sup>+</sup>(CH<sub>3</sub>)<sub>3</sub>Br<sup>-</sup>)  $P_h$  and  $P_t$  are equal to  $9/(2n+10)$  and  $(2n+1)/(2n+10)$  respectively.  $B_0(Qa) = \frac{1}{3}[1 + 2j_0(Qa)]$  and  $B_1(Qa) = \frac{2}{3}[1 - j_0(Qa)]$  are the elastic and quasielastic structure factors in the scattering law for 3-fold jump rotation and  $j_0$  is the zeroth order spherical Bessel function.  $a$  is the distance between two hydrogen atoms in methyl group (1.8 Å) and  $\tau$  is the mean residence time at each site within the 3-fold jump rotation model.  $A_n^l(QR)$  for different  $n$  and  $l$  can be calculated by using the values of  $x_n^l$  listed in ref.[19].  $A_0^0(QR_i)$  is equal to  $\left[ \frac{3j_1(QR_i)}{QR_i} \right]^2$ , where  $j_1$  is first order spherical Bessel function.  $R_i$  and  $D_i$  can be expressed as

$$R_i = \frac{i-1}{n-1} [R_{\max} - R_{\min}] + R_{\min} \quad (5.3)$$

$$D_i = \frac{i-1}{n-1} [D_{\max} - D_{\min}] + D_{\min} \quad (5.4)$$

Therefore, the EISF correspond to the segmental motion of the C<sub>n</sub>TAB monomer can be written as,

$$EISF = \frac{1}{(2n+10)} \left[ \frac{9}{3} [1 + 2j_0(Qa)] + (2n+1) \frac{1}{n} \sum_{i=1}^n \left[ \frac{3j_1(QR_i)}{QR_i} \right]^2 \right] \quad (5.5)$$

$R_{min}$  and  $R_{max}$  are determined by a least squares fit of the extracted EISF. Solid lines in Fig. 5.7 represent the fit as obtained from the above description. The values of  $R_{min}$  and  $R_{max}$  as obtained from the fit are given in Table 5.2. For  $C_{10}TAB$ ,  $R_{min}$  and  $R_{max}$  are found to be 0.1 and 4.4 Å respectively. This implies that the diffusion of the hydrogen atoms in a  $C_{10}TAB$  chain are restricted to spheres of radii between 0.1 Å and 4.4 Å. With increase in chain length, radii of sphere are found to decrease and for higher chain length,  $R_{min}$  and  $R_{max}$  are found to be 0.02 and 2.8 Å respectively for  $C_{16}TAB$ . However with increase in temperature, radii of spheres are found to increase as shown in Table 5.2.

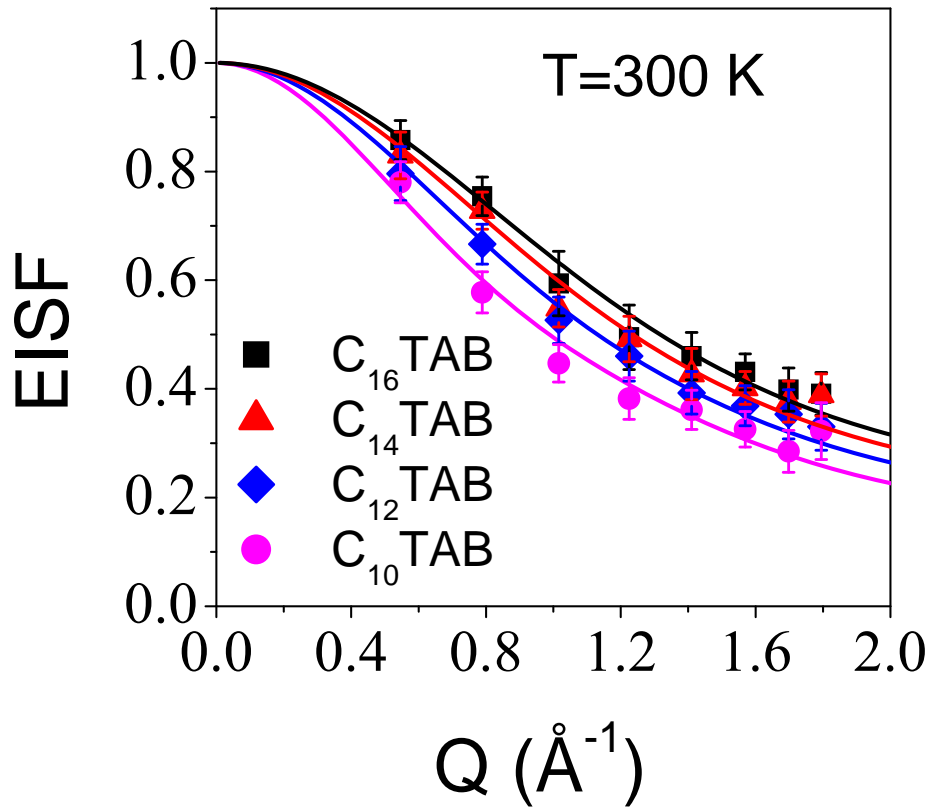


**Fig. 5.7** Variation of EISF for  $C_nTAB$  micelles ( $n = 10, 12, 14$  and  $16$ ) at 300 K. Solid lines represent calculated EISF for the model described in the text.

The diffusivities associated with the different hydrogen atoms belonging to a  $C_nTAB$  monomer can be obtained from the  $\Gamma_{seg}(Q)$  using Eq. (5.2) as done for  $C_{16}TAB$  or CTAB in the previous chapter.  $\Gamma_{seg}(Q)$  for different  $C_nTAB$  micelles is shown in Fig. 5.8 at 300 K.

The least squares fitting method is used to describe the observed QE width correspond to segmental motion,  $\Gamma_{\text{seg}}(Q)$  with  $\tau$ ,  $D_{\text{min}}$  and  $D_{\text{max}}$  as parameters while the values of  $R_{\text{min}}$  and  $R_{\text{max}}$  are already known from the fit of the EISF (Fig. 5.7). The obtained values of  $\tau$ ,  $D_{\text{min}}$  and  $D_{\text{max}}$  for different chain lengths are given in Table 5.2.

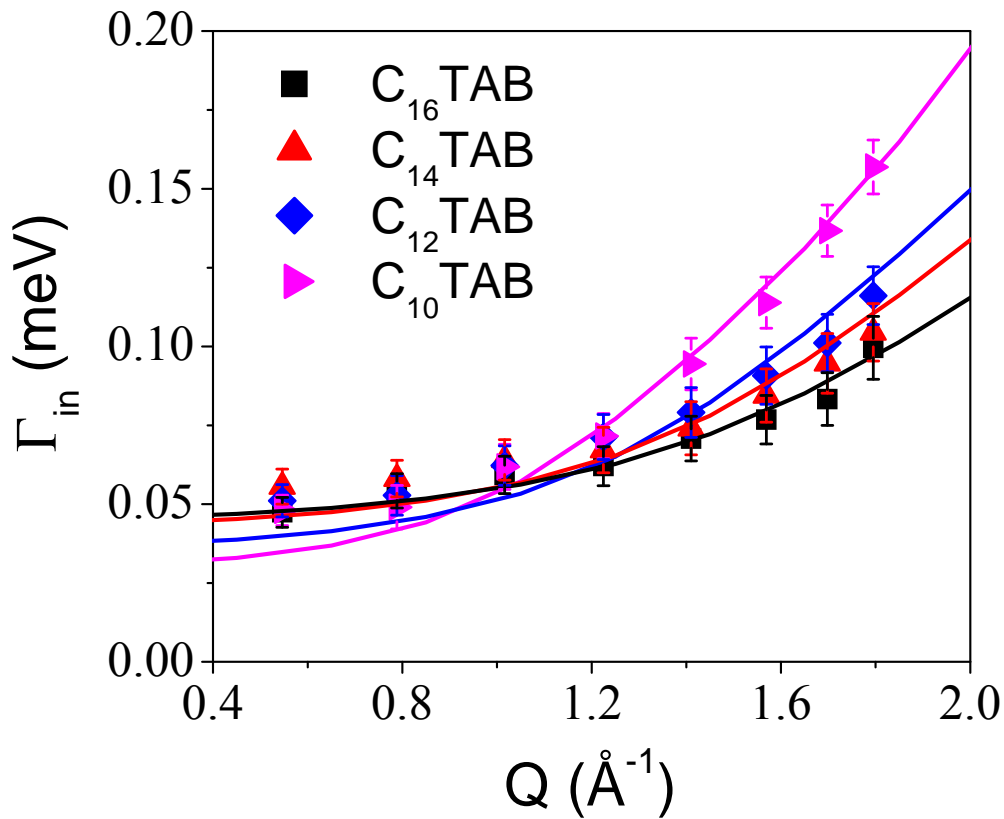


**Fig. 5.8** Variation of the HWHM,  $\Gamma_{\text{in}}$ , of the Lorentzian corresponds to segmental motion of the monomer for  $C_n$ TAB micelles with  $Q$  for different chain lengths at 300 K.

The effect of chain length on the size, shape, aggregation number and fractional charge of the micelles is studied in details and reported in the literatures [90,93,98]. The various structural parameters of  $C_n$ TAB micelles having different chain lengths as obtained from SANS experiment by Berr [93] are given in Table 5.1. The aggregation number is found to increase drastically with the increase in chain length in these micelles. On the other hand, fractional charge decreases with the increase in chain length. The variation of the length of the major axis and minor axis shows that the deformation from spherical to

ellipsoidal is more dominant for the higher chain length system. These observations have been explained in terms of increase in condensation of counterion on the micelles with the increase in the chain length of the monomer as is evident from the fractional charge on the different micelles. The increased bound counterion concentration screens electrostatic head group repulsions and allows the head groups to move closer to each other. This in turn increases packing density of the monomers within the micelles. Therefore, in case of C<sub>16</sub>TAB ( $n = 16$ ) micellar solution, there will be lesser spacing available between the monomers compared to C<sub>10</sub>TAB ( $n = 10$ ). Increased packing of the monomers also results in the removal of water molecules within the micelles and thus hydration level inside the micelles decrease with increase of the chain length. Hydration is known to influence the dynamics strongly in the case of proteins, reverse micelles, macromolecules [30,31].

**Table 5.2** Radii of spheres,  $R_{min}$  and  $R_{max}$ , and associated diffusion coefficients,  $D_{min}$  and  $D_{max}$  for hydrocarbon chain and mean residence time ( $\tau$ ) for the hydrogen atoms in the head group, as obtained from the least square fitting of the data (Figs. 5.7 & 5.8) with a model discussed in the text, for different chain length  $n$  of the molecules C <sub>$n$</sub> TAB. Global diffusion coefficient ( $D_G$ ) for C <sub>$n$</sub> TAB ( $n=10,12,14$  and  $16$ ) micelles is also compared.

Micelles	T (K)	$D_G$ ( $10^{-6}$ cm <sup>2</sup> /s)	$R_{min}$ (Å)	$R_{max}$ (Å)	$D_{min}$ ( $10^{-5}$ cm <sup>2</sup> /s)	$D_{max}$ ( $10^{-5}$ cm <sup>2</sup> /s)	$\tau$ (ps)
C <sub>10</sub> TAB	300	$3.2 \pm 0.4$	$0.10 \pm 0.03$	$4.4 \pm 0.3$	$0.30 \pm 0.06$	$1.6 \pm 0.2$	$2.6 \pm 0.2$
C <sub>12</sub> TAB	300	$2.9 \pm 0.3$	$0.04 \pm 0.02$	$3.5 \pm 0.3$	$0.15 \pm 0.03$	$1.3 \pm 0.2$	$4.0 \pm 0.3$
C <sub>14</sub> TAB	300	$2.5 \pm 0.3$	$0.02 \pm 0.01$	$3.1 \pm 0.2$	$0.08 \pm 0.02$	$1.1 \pm 0.2$	$4.8 \pm 0.4$
	315	$3.4 \pm 0.4$	$0.40 \pm 0.08$	$4.4 \pm 0.3$	$0.15 \pm 0.04$	$1.6 \pm 0.2$	$4.1 \pm 0.3$
	330	$4.3 \pm 0.5$	$0.50 \pm 0.09$	$4.8 \pm 0.4$	$0.23 \pm 0.05$	$2.3 \pm 0.3$	$3.6 \pm 0.3$

C <sub>16</sub> TAB	300	2.0 ± 0.3	0.02 ± 0.01	2.8 ± 0.2	0.1 ± 0.04	1.0 ± 0.2	6.5 ± 0.6
	315	3.1 ± 0.4	0.03 ± 0.02	3.4 ± 0.3	0.1 ± 0.04	1.3 ± 0.2	5.2 ± 0.5
	330	4.3 ± 0.5	0.06 ± 0.03	4.5 ± 0.3	0.2 ± 0.05	1.9 ± 0.3	4.0 ± 0.5

QENS results showed that internal motions get hindered with increasing chain length as shown in Table 5.2: the diffusion coefficients decrease and also the spatial extent of the dynamical domain reduced. This can be explained in terms of an increased packing density of the monomer within the micelles for chains of longer length as discussed earlier. In C<sub>10</sub>TAB micellar solution, hydrogen atoms cover a larger volume with higher diffusivity compared to that in the C<sub>16</sub>TAB micellar solution. Therefore increased chain length of the monomer reduces the flexibility of the chain and so the segmental motion becomes hindered. These results are also in agreement with the Raman scattering study on the C<sub>n</sub>TAB micellar solution. Raman scattering study on C<sub>n</sub>TAB micellar solution shows that fraction of trans/gauche conformations in alkyl chain of C<sub>n</sub>TAB increases with the increase of alkyl chain length indicating a higher degree of conformational order [104]. The NMR study on C<sub>n</sub>TAB aqueous solution (from  $n = 6$  to 12) reveals that limiting intra diffusion coefficient of C<sub>n</sub>TAB surfactant cation decreases with increasing the chain length [103]. As shown in Table 5.2, QENS results also indicate that with the increase in chain length, 3 fold rotations of CH<sub>3</sub> units belonging to head group gets slower. This may be explained due to the reduction of stern layer thickness [93]. Radii of the spheres and the associated diffusivities are found to increase with temperature as shown for C<sub>14</sub>TAB and C<sub>16</sub>TAB micelles in Table 5.2. As the temperature is increased, packing of the monomers in the micelles get reduced as the distance between the two consecutive monomers increases due to thermal energy. This in turn provides more free space and results in increased mobility of hydrogen atoms. Therefore,

with increasing temperature, the alkyl chains become more flexible and perform faster internal motion.

### 5.3.2. Effect of Phenyl ring on the Dynamics of Anionic Micelles

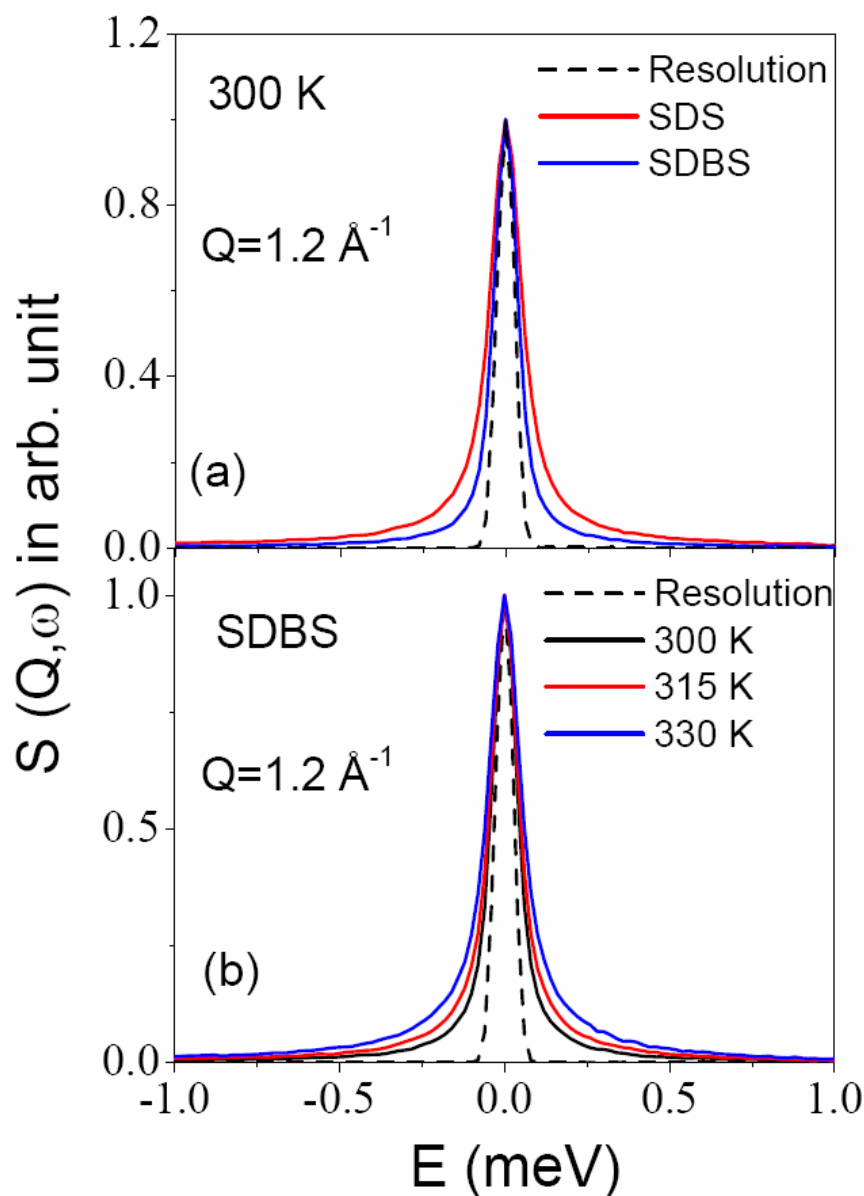


**Fig. 5.9** Comparison of QENS spectra as obtained using IN5 spectrometer at ILL for (a) 0.3 M micellar solution of SDBS and SDS at  $Q=1.2 \text{ \AA}^{-1}$  at 300 K and (b) 0.3 M SDBS micellar solution at different temperatures at  $Q=1.2 \text{ \AA}^{-1}$ . The instrument resolution is also shown by dashed line.



To investigate the effect of presence of a phenyl group in a surfactant molecule on the dynamics of anionic micelles, QENS experiments have been carried out on 0.3 M SDS and SDBS micellar solution using IN5 spectrometer with an energy resolution of  $\Delta E \sim 60 \mu\text{eV}$  (full width at half-maximum, FWHM). SDS ( $\text{C}_{12}\text{H}_{25}\text{OSO}_3\text{Na}$ ) and SDBS ( $\text{C}_{12}\text{H}_{25}\text{C}_6\text{H}_4\text{SO}_3\text{Na}$ ) molecules are very similar in structure except in SDBS there is a phenyl ring near to head group. Fig 5.9 (a) shows comparison of the QENS spectra for SDS and SDBS micelles at 300 K at a typical  $Q = 1.2 \text{ \AA}^{-1}$ . The instrumental resolution is also shown for comparison in Fig 5.9 (a). Significant quasielastic (QE) broadening is observed for both the micelles over the instrument resolution. Observed QE broadening is found to be significantly larger in case of SDS compared to SDBS. Fig 5.9 (b) shows QENS spectra measured for SDBS micelles at different measured temperatures along with instrument resolution at a typical  $Q = 1.2 \text{ \AA}^{-1}$ . QE broadening is found to increase with increase in temperature.

To investigate further, data analysis is carried out in details. In a micellar system, one is expected to observe the whole body or global motion in addition to faster internal motions [10,52,53,97]. The scattering law for a micellar system can be written as [from Eq. (1.82)]

$$S_{micelles}(Q, \omega) = \left[ A(Q) L_G(\Gamma_G, \omega) + (1 - A(Q)) L_{tot}(\Gamma_{tot}, \omega) \right] \quad (5.6)$$

where  $A(Q)$  is the EISF for internal motion.  $\Gamma_{tot} = \Gamma_G + \Gamma_{in}$  ; where  $\Gamma_G$  and  $\Gamma_{in}$  are the half width at half maxima (HWHM) of the Lorentzian function corresponding to global and internal motions respectively. It is found that the observed QENS spectra can be described by the model scattering function [Eq. (5.6)]. Typical fitted spectra for SDBS micelles at 330 K are shown in Fig. 5.10 at several  $Q$  values.

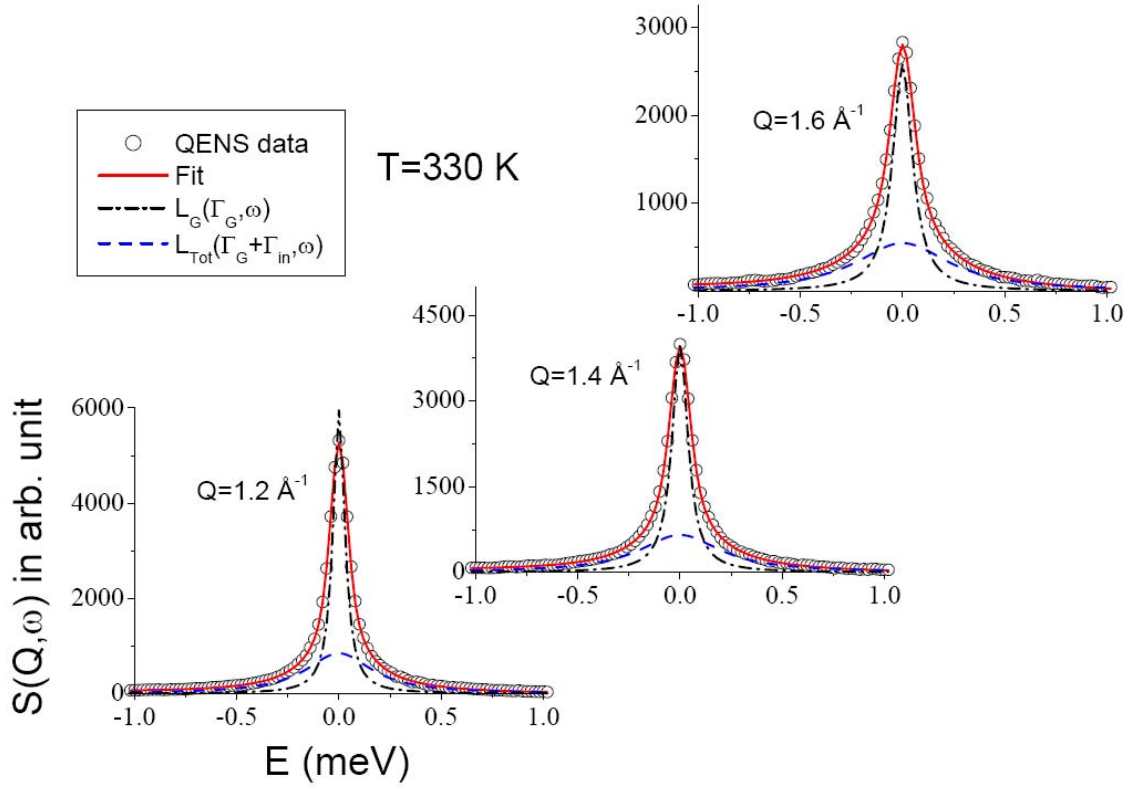


**Fig. 5.10** Typical fitted  $S(Q, \omega)$  for 0.3 M SDBS micelles at 330 K, as obtained using IN5 spectrometer at ILL, assuming scattering function given in Eq. (5.6).

The variation of the HWHM,  $\Gamma_G$ , of the Lorentzian function corresponds to global motion for SDBS micelles with  $Q^2$  at each temperature is shown in Fig. 5.11. The same for SDS micelles at 300 K is also shown in Fig. 5.11 for comparison. It is found that  $\Gamma_G$  is larger for SDS micelles than that of SDBS micelles at 300K indicating that the global motion of SDS micelles is faster than that of SDBS micelles. This could be due to the difference in the size of these micelles as observed by SANS technique [105]. Global motions for both micelles is described by Ficks law,  $\Gamma_G = D_G Q^2$  as shown by solid lines in Fig. 5.11. Here  $D_G$ , is the apparent global diffusion coefficient for micelles and can be obtained from the slope of the curve. At 300 K, global diffusivity of SDBS micelles is found to be  $(1.9 \pm 0.3) \times 10^{-6}$  cm<sup>2</sup>/sec, which is less than that obtained for SDS micelles  $(3.0 \pm 0.4 \times 10^{-6}$  cm<sup>2</sup>/sec).  $D_G$  is

found to increase with temperature as expected for a thermally activated diffusive motion and at 330 K,  $D_G$  for SDBS micelles is found to be  $(3.6 \pm 0.5) \times 10^{-6} \text{ cm}^2/\text{sec}$ .

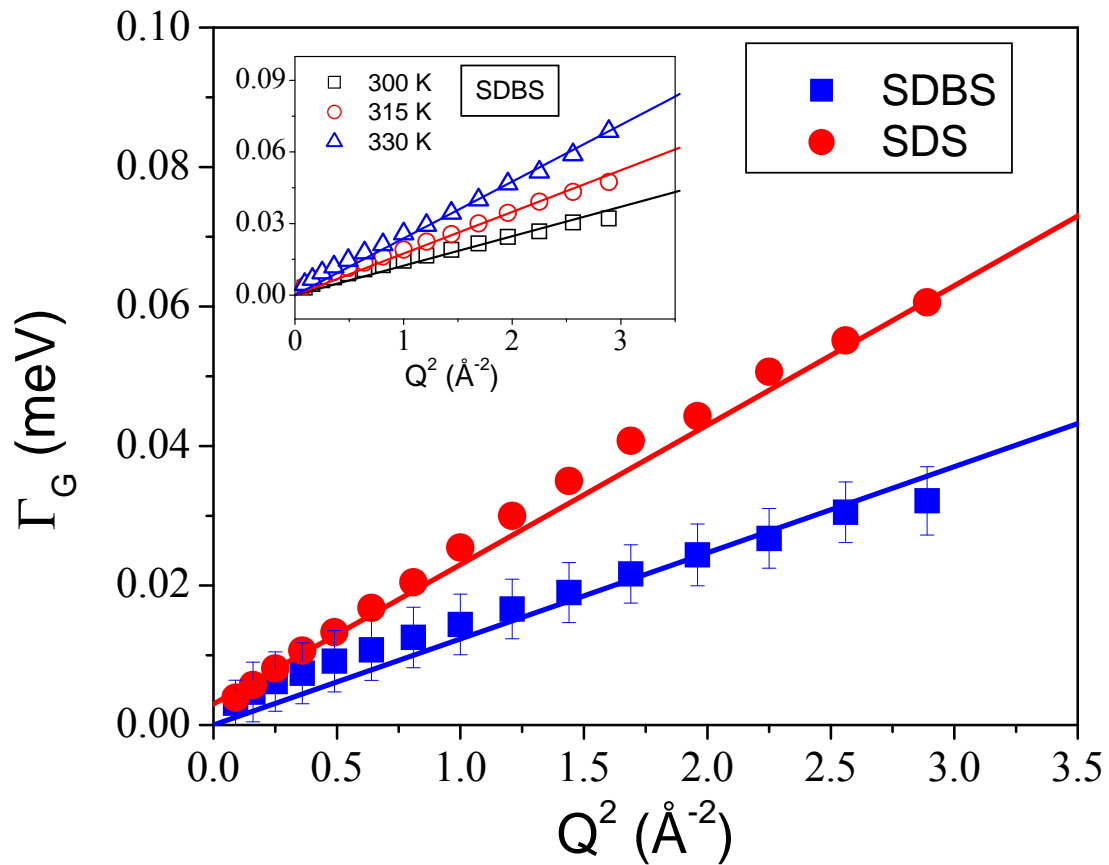


**Fig. 5.11** Variation of half width at half maxima,  $\Gamma_G$ , corresponds to global motion, with  $Q^2$  for SDBS and SDS micelles at 300 K. Inset shows the variation of  $\Gamma_G$  at different temperature for SDBS micelle. The solid lines are the fits with Fick's law of diffusion.

As mentioned earlier, internal motions of the micelles comprise of different dynamical motions including segmental and torsional motions of the monomer [10,52,53,81,97] and would be observable at IN5 spectrometer ( $\Delta E \sim 60 \text{ } \mu\text{eV}$ ) due to availability of wide energy transfer. However, it is difficult to separate all these motions and model them individually from one data set. Therefore, no attempt was made to model observed EISF quantitatively. The extracted EISF,  $A(Q)$  for the internal motion for both the

micelles are shown in Fig. 5.12. It is evident from figure that at 300 K, EISF for SDBS micelles is higher than that of SDS micelles. Alkyl chains of the both SDS and SDBS molecules are very similar and EISF for a system mainly depend on the radius of gyration. This indicates that on the average radius of gyration for internal motion of alkyl chain in SDS micelles is larger than that in SDBS micelles. Larger radius of gyration implies that alkyl chain of SDS molecules can cover large spatial extent in the micelles. This indicates that alkyl chains in SDS micelles are more flexible than in SDBS micelles. Results are consistent with the recent MD simulation study on both SDS and SDBS micelle [59]. EISF of SDBS micelles decay more rapidly with increase in temperature, suggesting increase in the flexibility of the chain at higher temperature.

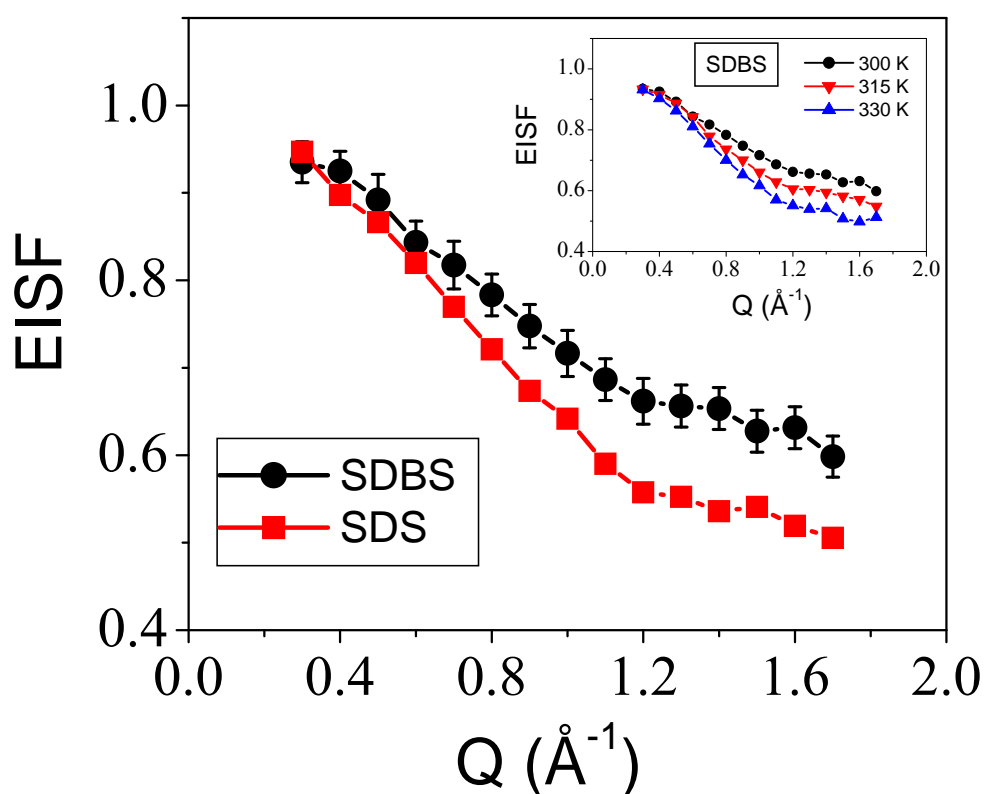


**Fig. 5.12** Variation of EISF for SDBS and SDS micellar solution with  $Q$  at 300 K. It is evident that internal dynamics of SDS micelle is more disordered than SDBS micelle at 300 K. Inset shows the EISF for SDBS micelles at different temperatures.

As mentioned earlier, internal motions of the micelles comprise of different dynamical motions, we have tried to extract the average time scale of the internal motion from the observed HWHM of 2<sup>nd</sup> Lorentzian ( $L_{tot}(\Gamma_{tot}, \omega)$ ). The 2<sup>nd</sup> Lorentzian in the scattering law arises from the contribution of both internal as well as the global motion as given in Eq. (5.6).  $\Gamma_{in}$  is obtained by subtracting  $\Gamma_G$  from the  $\Gamma_{tot}$  and is shown in Fig. 5.13 for both micelles at room temperature. The behaviour of  $\Gamma_{in}(Q)$  with  $Q$  shows characteristic features of localized translational diffusion [19]. As can be seen from the figure that HWHM  $\Gamma_{in}(Q)$  is more or less constant up to a limiting  $Q$  value and then increase linearly with  $Q^2$ . Since at higher  $Q$  values, where small distances are probed, the usual  $DQ^2$  behaviour corresponding to translational motion in an infinite medium is recovered since in this length scale, confining wall boundaries are not seen. As can be seen from Fig. 5.13, the observed HWHM follow  $D_{in}Q^2$  behaviour at higher  $Q$  values and therefore can be used to obtain average diffusivity ( $D_{in}$ ) correspond to internal motion. Average diffusivity( $D_{in}$ ) corresponds to internal motion for SDBS micelle is found to be  $(4.6 \pm 0.4) \times 10^{-6}$  cm<sup>2</sup>/sec at 300 K. The corresponding diffusivity for SDS micelles at 300 K is found to be  $(7.4 \pm 0.6) \times 10^{-6}$  cm<sup>2</sup>/sec. Therefore, internal motions in SDBS micelles are hindered vis-à-vis SDS micelles at 300 K.  $D_{in}$  for SDBS micelles increases to  $(7.5 \pm 0.6) \times 10^{-6}$  cm<sup>2</sup>/sec at 330 K. QENS results indicate that internal dynamics in anionic SDBS micelles is slow vis-à-vis SDS micelles. Our results are found to be consistent with the recent MD simulation study [59] and are found to be consistent with each other. MD simulation indicates that the mobility of alkyl chain in SDS micelles is greater than that in SDBS micelles [59]. Atom distributions calculated from center of mass of the micelles showed that the hydrophobic core of the SDBS micelle is denser or more compact than that of the SDS micelle [59]. SANS study [105] on both micelles indicates that fractional charge of SDBS micelles is smaller than that observed for SDS micelles. This might be due to more counterions condensation on SDBS micelles, which can

be understood due to additional  $\pi$  electron cloud of the benzene rings present near the SDBS micellar surface. This may lead to dense packing of the alkyl chain in the micelles. Due to increase in packing density in SDBS micelles, the protons are experience a more “viscous” (dense) medium and therefore dynamics is more constraint in SDBS than in SDS.

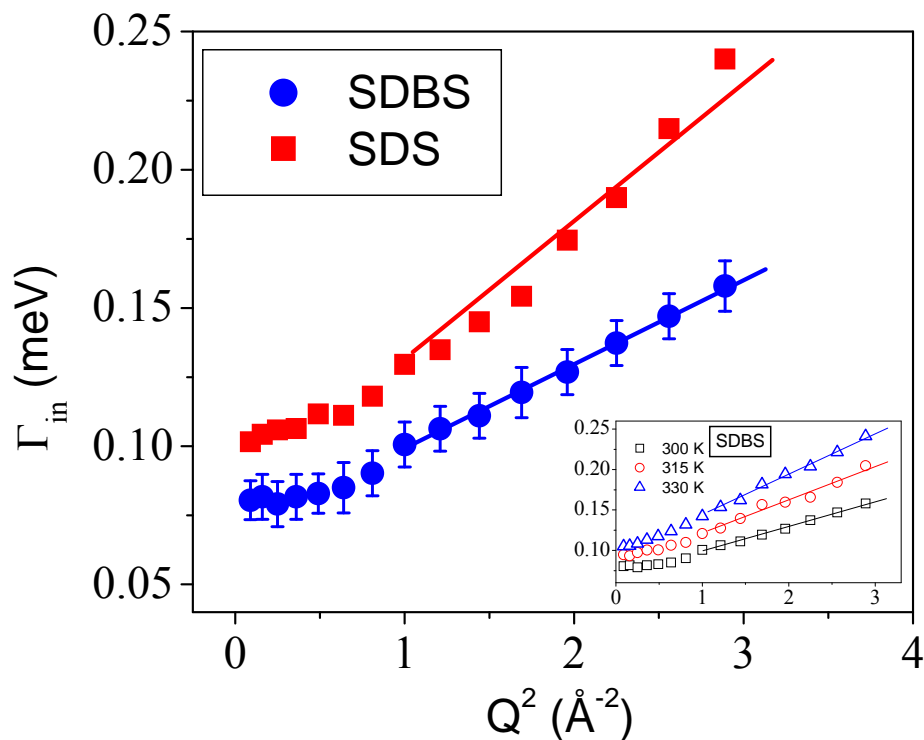


**Fig. 5.13** Variation of the HWHM,  $\Gamma_{in}$ , which correspond to the internal motion of the monomer for SDBS micelles with  $Q$  for SDS and SDBS micelle at 300 K. Inset shows the temperature dependence of  $\Gamma_{in}$  for SDBS micelle. Lines show the fits using Fick’s law.

Density profiles of surrounding solvent water molecules as calculated from MD simulation study [59] showed that the hydrophobic core of both the micelles (size  $\sim 13$   $\text{\AA}$ ) is devoid of water molecules. Therefore, there exists little chance for the carbons atoms to interact with water molecules in the core region. However, the probability distribution showed that more number of carbons atoms of the alkyl chain in SDS micelles are in the vicinity of water molecules compared to that in SDBS micelles. Thus, effectively, the aliphatic chains are

surrounded with more number of water molecules in SDS than SDBS micelles. Since hydration is known to influence the dynamics (as shown in the case of proteins, reverse micelles, macromolecules [30,31]), this could be the reason behind the hindered internal dynamics of SDBS micelles apart from the compact packing of the hydrophobic core. This is the first experimental evidence demonstrating that alkyl chains in SDBS micelles are less flexible than in SDS micelles, corroborating the recent MD simulation studies on both the micelles [59].

#### 5.4. CONCLUSIONS

Results of this study [106,107] reveal the effect of molecular architecture on the dynamics of ionic micelles. Analysis of the QENS data showed that the dynamics of the micelles could be explained in terms of global motion of whole micelle and internal motion of the monomers. The effect of chain length on the dynamics of  $C_n$ TAB micelles for varied length of the surfactant molecule ( $n = 10, 12, 14, 16$ ) has been studied. Global motion of the micelles is described by Fickian diffusion. Diffusivity correspond to the global motion is found to decrease with the increase in chain length. This may be due to the combined effect of increase in hydrodynamic size and aggregation number of the micelles with the chain length. It is found that for the smallest chain length micelle,  $C_{10}$ TAB the diffusivity associated with the internal or segmental motion is maximum and for the longest chain length micelles,  $C_{16}$ TAB has minimum. Hydrogen atoms in the alkyl chains in  $C_{10}$ TAB micelles can cover a larger volume within the micelles than those in micelles with longer chains. This indicates that alkyl chains are most flexible in the micelles with smallest chain length ( $C_{10}$ TAB). This is explained in terms of increased packing density of the monomer in the larger chain length micelles. Effect of phenyl ring in the surfactant on the dynamics of anionic micelles has been studied. While both the surfactants (SDS and SDBS) contain a hydrophobic tail of the

dodecyl alkyl chain, there exists a phenyl ring near the head group in SDBS. QENS data clearly shows that the dynamics of SDBS micelles are more restricted compared to SDS micelles. This is in accord with the recent molecular dynamics simulation study on both the micelles. Diffusivity corresponding to the global motion is found to be slower in SDBS compared to SDS micelles. The EISF corresponding to internal motion indicates that alkyl chains of SDBS molecules are less flexible than in SDS molecules. Diffusivity of the hydrogen atoms corresponding to internal motion is also found to be slower in SDBS than SDS micelle. This is explained on the basis of the denser packing of hydrophobic core and less interaction of alkyl chains with water in case of SDBS micelles.



## CHAPTER 6

# **Dynamics of Water in Restricted Geometries: Polyamide Membranes, Prussian Blue and its Analogues**

### **6.1. INTRODUCTION**

Fluids under spatially constraint within a medium are called confined fluids. The behavior of liquids in confined geometries differs from their bulk in many ways. Freezing behaviour, sorption and wetting, structure and dynamical properties, including diffusion and relaxation, of fluids may be modified under confinement [36,108]. The behaviour of fluids in restricted geometries is mainly determined by the two-factors; spatial restriction and guest-host interaction. The modification in dynamical behaviour of fluid in confined geometry compared to its bulk has considerable interest in scientific research, not only for fundamental aspects but also for practical applications in petroleum industries, catalysis, water purification and so forth. The dynamics of adsorbed species is indeed complex and depend upon a number of factors like the size and shape of the molecule, pore topology, guest-host interaction, and temperature [36,108]. Systems where water is found confined in a medium are very frequent in nature. Water in the cracks of the rocks, water inside biological membranes etc. exemplifies this class. Presence of this confined water is essential for the functioning of the cell. It is interesting to probe the influence of confinement on the properties of water. Teixeira et al have shown that the dynamical property of confined water is similar to that of the super cooled water [109]. The behavior of water in confinement or at interface is affected by the ability of water molecules to form hydrogen bonds with the substrates apart from

forming hydrogen bonds among themselves. In this chapter, dynamics of water confined in various mediums such as nanoporous polyamide membranes, Prussian blue based molecular magnet and so forth are discussed. Section 6.2 of this chapter deals with the dynamics of water in reverse osmosis and nanofiltration polyamide membranes. These polyamide membranes are widely employed for water filtration purpose. Efficiency of these membranes for filtration process depends upon their ability for water uptake. Therefore it is of interest to study the dynamical behaviour of water inside these membranes. Dynamics of water in Prussian blue and its analogues are studied using quasielastic neutron scattering (QENS) technique and discussed in section 6.3. Summary is depicted in section 4.4.

## **6.2. DYNAMICS OF WATER IN NANOPOROUS POLYAMIDE MEMBRANES**

Polyamide membranes are widely used for removal of organic substance from natural and waste water [110], desalination of sea and brackish waters [111], treatment of industrial effluents [112] and so forth. These membranes are also used in catalysis; food and dairy industries, chemical processing industries, pulp and paper industries, textile dye effluent, landfill leach treatment, and so forth. Mechanism of self-diffusion of water molecules changes on filtration through a membrane as a result of a complicated process occurring in filtration [113]. So it is of interest to study the uptake of water and its diffusion in these membranes that can be conveniently studied using Quasi elastic neutron scattering (QENS) technique. Dynamics of water in two following polyamide membranes (i) Trimesoyl chloride -m-phenylene diamine based reverse osmosis (RO) and (ii) Trimesoyl chloride - piperazine based nanofiltration (NF) have been studied using QENS technique [114-117]. Compared to the RO polyamide membrane, the NF polyamide membrane has relatively larger porosity that has molecular weight cut-off of 180 ~ 200 Daltons as determined by aqueous solution of 500 ppm concentration of organic solutes such as glucose, sucrose, polyethylene glycol etc [118].

RO and NF membranes have different electrical potentials as a result of different thickness of charged layers, which then have a direct relationship to membrane separation performances [119]. While the RO membrane rejects (95-99%) all the electrolytes including monovalent ions, the rejection selectivity (90-99%) of the NF membrane towards the divalent and multivalent ions, and less rejection towards monovalent ions (<50%) is suited for separating mixture of ions containing monovalent and divalent/multivalent ions. Therefore NF membranes are suitably used for softening of hard water, separation of monovalent from divalent ions, treatment of dye containing waste water, desalting of protein and amino acids [120]. RO membranes have been synthesized for the desalination of brackish water and sea water; and are being used to produce ultra-pure water, waste water treatment, and so on, for the last three decades [118,121-122]. As shown in the chemical structure of the RO polyamide membrane given in Fig. 6.1, the network polyamide (polymetaphenylene trimesamide) may comprise of various sub-units such as, totally cross-linked unit formed by linking all the bifunctional and trifunctional sites of reactants as well as linear network with pendant carboxylic group and terminal network with amine group.

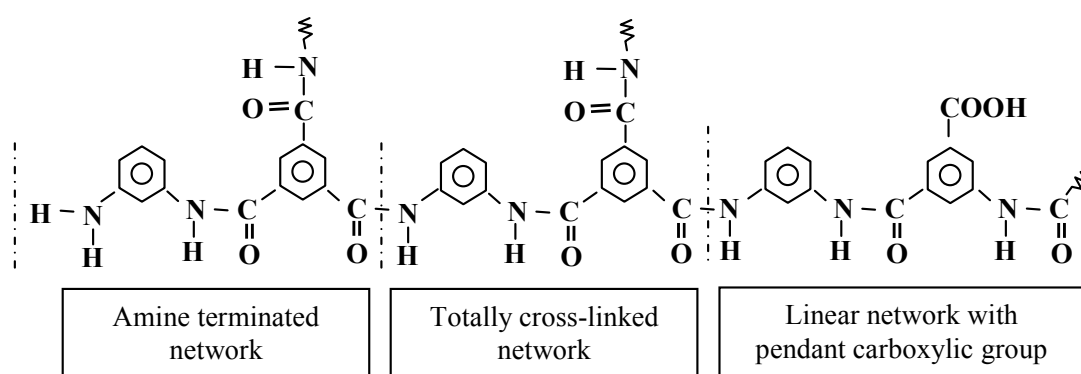


**Fig. 6.1** Chemical structure of reverse osmosis (RO) polyamide membrane.

Chemical structure of NF polyamide membranes is shown in Fig. 6.2. The piperazine monomer used in the case of the porous NF has both cross-linking sites at linear positions ( $180^\circ$ ) forming a relatively linear polymer network, whereas the cross-linking sites of m-phenylenediamine monomer of the RO are at an angular position ( $120^\circ$ ).

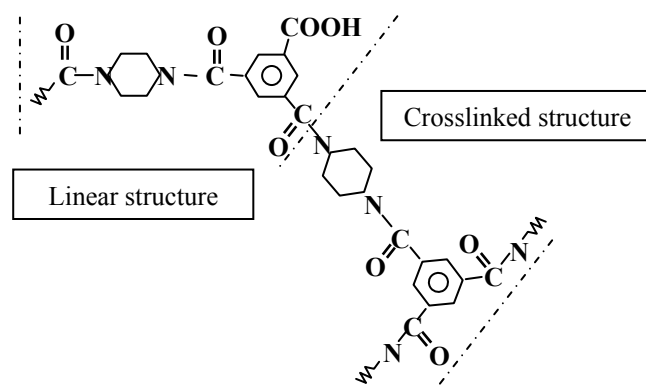


**Fig. 6.2** Chemical structure of nanofiltration (NF) polyamide membrane.

An irregular interlinking of polymer chains in these membranes can give rise to polymer free void spaces – pores [123]. These pores can have a variety of structures – open, closed, circular, non-circular, etc. and may or may not form an interconnecting network. The size of pores in porous media can in general be determined using a variety of experimental techniques including nitrogen adsorption [124], small angle neutron scattering [125] and positron annihilation lifetime spectroscopy (PALS) [126,127]. These techniques provide structural information at different length scales. PALS is an excellent technique for measuring the pore size in RO and NF membranes which are generally in order of angstroms [126-129]. PALS technique is used to characterize these polyamide membranes.

### 6.2.1. Experimental Details

RO and NF polyamide membrane samples were synthesized by our collaborator Dr. Puyam Singh at Central Salt and Marine Chemicals Research Institute, Bhavnagar, India. Both trimesoyl chloride - m-phenylene diamine based RO and trimesoyl chloride - piperazine based NF polyamide membranes were prepared by interfacial polymerization techniques [130]. A 2% (w/v) aqueous solution of m-phenylenediamine (Atul Chemicals, India) and n-hexane solution of 0.1% (w/v) trimesoyl chloride (Aldrich), which resulted in formation of polyamide layer at the water-organic interface without support. The membranes were prepared with a fixed polymerization time using the standard procedure as mentioned above. For NF membrane, 2% (w/v) solution of piperazine (Aldrich) in water was contacted with n-hexane solution of 0.1% (w/v) trimesoyl chloride (Aldrich), which resulted in the formation of polyamide layer at the water-organic interface. Both membranes subsequently were characterized by PALS and SEM techniques. SEM pictures of the samples were taken on LEO 1430VP scanning electron microscope with 5 kV accelerating voltage. For PALS measurements,  $^{22}\text{Na}$  positron source in the form of aqueous solution of NaCl folded in kapton foil was sandwiched between the layers of polymer film samples and kept between two scintillation detectors. The positrons, having acquired kinetic energy from the  $^{22}\text{Na}$  radioisotope source, are injected into the sample. The energy of positron gradually decreases upon interacting with the counter-particle in the sample before it is completely annihilated. A substantial fraction of such thermalized positrons may form positronium at the bulk-pore interface having two different spin states, either anti-parallel; *i.e.*, *para*-Positronium (*p*-Ps), or parallel, known as *ortho*-Positronium (*o*-Ps) that diffuse and localize in pores or regions of low electron density of the sample. Positron annihilation lifetime measurements were carried out using plastic scintillators coupled to fast-fast coincidence system with resolving time of

~230 ps as measured with  $^{60}\text{Co}$  source in  $^{22}\text{Na}$  energy window settings. PATFIT program [131] was used for data analysis.

Preliminary, QENS experiments have been carried out using the MARX spectrometer (Chapter 1, section 1.2.2) at Dhruva reactor, Trombay. MARX spectrometer has an energy resolution of  $\sim 200 \mu\text{eV}$  with incident energy of 5.1 meV as obtained from measuring QENS spectra standard vanadium sample. The wave vector transfer ( $Q$ ) range covered is  $0.67\text{--}1.8 \text{ \AA}^{-1}$ . QENS experiments have been carried out on both dehydrated (bare) RO and NF polyamide membranes. These membranes were hydrated by adding distilled water, adequate soaking time was allowed for water to be absorbed. QENS measurements were performed on both water sorbed RO and NF polyamide membranes. High resolution QENS experiments were also carried out on water sorbed these membranes using FOCUS (Chapter 1, section 1.2.4) spectrometer at Paul Scherrer Institute, Switzerland with incident wavelength of  $6 \text{ \AA}$  corresponding to energy resolutions of  $\Delta E \sim 45 \mu\text{eV}$ . QENS measurements were carried out on dehydrated RO and NF membranes to estimate the contribution of the membrane other than water. Experiments were performed on the heating cycle in the temperature range of  $265\text{--}325 \text{ K}$ . The quasielastic spectra were recorded in the  $Q$  range of  $0.4\text{--}1.6 \text{ \AA}^{-1}$ . Spectra were corrected for detector efficiency with standard vanadium and were normalized to monitor intensity.

## **6.2.2. Results And Discussion**

### **6.2.2.1. SEM and PALS Studies**

SEM picture showing the surface microstructure of the RO and NF polyamide samples are shown in Figs. 6.3(a) and 6.3(b) respectively. SEM pictures indicate that NF membrane has relatively smoother surface microstructure whereas the RO membrane has rough surface showing hill-valley morphology similar to the reported results of others [132].

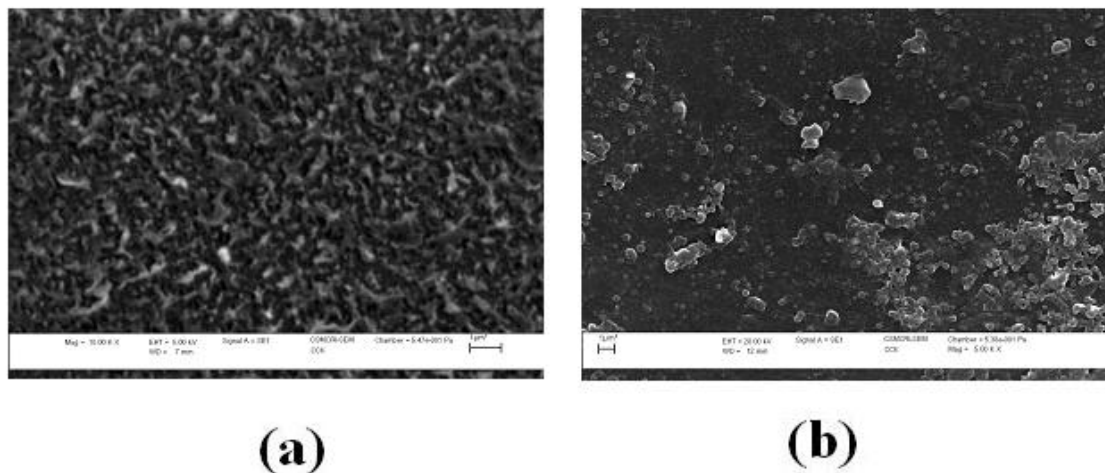


**Fig. 6.3** SEM micrograph of (a) RO and (b) NF polyamide membranes.

To measure pore size and porosity of RO and NF polyamide membranes we have carried out PALS measurement, which is based on the principle of detecting  $\gamma$ -rays, which are produced during the annihilation of positrons inside the porous material. In porous matrix, a substantial fraction of thermalized positron may form positronium (a bound state of an electron and positron) at the bulk-pore interface that diffuses and localizes in pores or regions of low electron density. Positronium may exist in two states, viz. spin singlet para-positronium (p-Ps) having small intrinsic lifetime of 0.125 ns, which decays mainly into two photons and spin triplet ortho-positronium (o-Ps), which decays mainly into three photons with much larger lifetime of 140 ns. However, in the presence of matter, o-Ps can seek out an electron of opposite spin from the pore surface and annihilate through two-photon mode known as pick-off annihilation within the time range  $\sim 1$ -10 ns. This component of positron lifetime has paramount importance, because it enables its use as nano-probe to study the microstructural properties of porous material [126-128]. The released photons mostly come out from open spaces such as holes or voids. So by measuring Ps pick-off lifetime  $\tau_p$ , one can

find out the radius of hole  $R$  according to the semi empirical equation as given below introduced by Tao and Eldrup [133,134],

$$\tau_p = \frac{1}{2} \left\{ 1 - \frac{R}{R + \Delta R} + \frac{1}{2\pi} \sin \left( \frac{2\pi R}{R + \Delta R} \right) \right\}^{-1} \quad (6.1)$$

where  $\Delta R = 1.66 \text{ \AA}$  is the thickness of the homogeneous electron layer inside the wall of free-volume hole, which is considered to be an infinite spherical potential well of radius  $R_0$  ( $=R+\Delta R$ ). Intensity is a measure of number density of the network pores, which are the inter- and intra- chain spacing of the polymer that can be varied as monomers concentration changes [128]. The parameters obtained from the present study for both RO and NF membranes are shown in Table 6.1. The lifetime of *o*-Ps is found to be slightly larger in NF membrane (1.45 ns) compared in RO membrane (1.38 ns). From Eq. (6.1), pore sizes in the RO and NF membrane are found to be 3.86 and 4.58  $\text{\AA}$  respectively, which is close to the values obtained for similar polymers [135, 136]. It is interesting to note that the intensity  $I$ , which is measure of number density of pores is found to be larger in NF membrane (10.49%) compared to RO membrane (2.34%).

**Table 6.1** Pick-off life time ( $\tau_p$ ), intensities ( $I$ ), and calculated radii ( $R, R_0$ ) of the cavities or voids in the RO and NF polyamide membranes.

System	$\tau_p$ (ns)	$I$ (%)	$R$ ( $\text{\AA}$ )	$R_0$ ( $\text{\AA}$ )
RO	1.38	2.34	2.20	3.86
NF	1.45	10.49	2.92	4.58



### 6.2.2.2. QENS Results

While the QENS spectra for dehydrated polyamide membranes did not show any quasielastic broadening, the water sorbed polyamide membranes spectra showed considerable quasielastic broadening over the instrument resolution. To analyse the data, first observed QENS spectra was attempted to separate the elastic and quasielastic contributions using the general scattering law ( Chapter 1, section 1.2.6)

$$S(Q, \omega) = A(Q)\delta(\omega) + (1 - A(Q))L(\Gamma, \omega) \quad (6.2)$$

Data from dehydrated polyamide membrane sample were used to estimate the contribution of dehydrated membrane to total spectra. Experimental QENS data obtained for both the systems are fitted using Eq. (6.2) convoluted with the instrumental resolution, by the method of least squares fitting. Typical fits of QENS data for both the system are shown in Figs. 6.4 and 6.5. Elastic component is found to insignificant and a single Lorentzian function fits the data well in both the cases. Therefore, the observed dynamics at MARX spectrometer is related to translation motion of the water molecules.

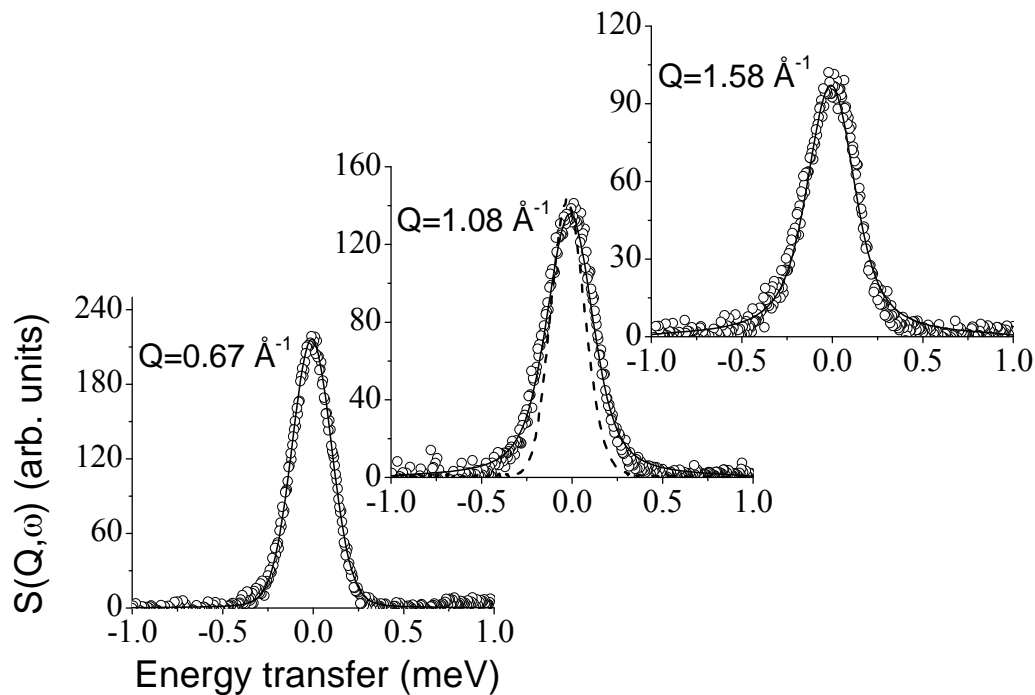


**Fig. 6.4** Fitted QENS spectra from the water-sorbed RO polyamide membrane using MARX spectrometer at some typical  $Q$ -values. Instrument resolution is shown by dashed line in the middle panel.

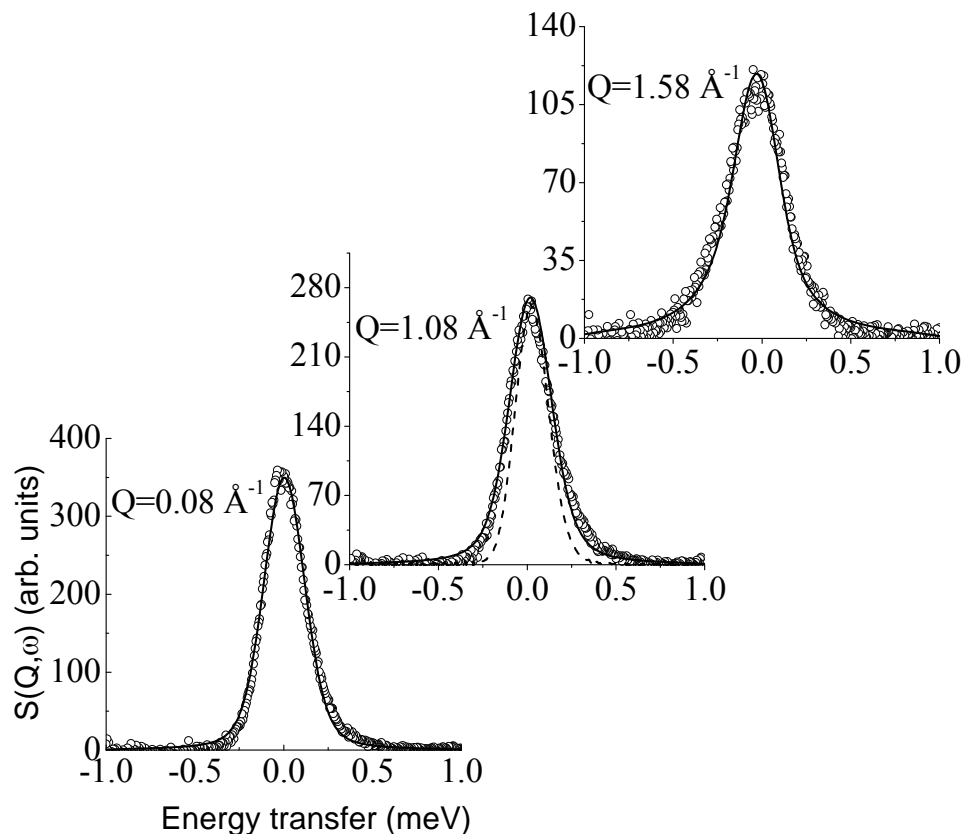


**Fig. 6.5** Fitted QENS spectra from the water sorbed NF polyamide membrane using MARX spectrometer at some typical  $Q$  values. Instrument resolution is shown by dashed line in the middle panel.

The HWHM's of the Lorentzian ( $\Gamma$ ) obtained from the fits are shown in Figs. 6.6 (a) and (b). The simplest model of translational motion is continuous diffusion (Chapter1, section 1.1.4.1), which is described by Fick's law, in which HWHM ( $\Gamma$ ) vary linearly with  $Q^2$  as  $\Gamma(Q) = DQ^2$ , where  $D$  is the self-diffusion coefficient of fluids. This occurs when the interactions between the particles are weak. In Brownian diffusion it is assumed that motion occurs via infinitely small, elementary jumps. When the intermolecular interactions are

significant, the diffusion mechanism is affected by the environment of the particle under consideration. For example, in case of a periodic lattice, the particle is more likely to be found at some energy minima, which are regularly distributed throughout the crystal. Motion of the particle in such an environment is likely to occur as jumps between these energy minima. This gives rise to a jump diffusion in which the particle remains at a site for some time called the residence time, before jumping to another site instantly. The distance covered by the particle in a jump is called the jump length. This model of jump diffusion can then be classified depending upon the degree of order in the environment, which in turn determines the distribution of jump lengths. In case of a more disordered environment like the present one where water molecules are confined within a membrane, the jump lengths could be a random or a Gaussian distribution. The corresponding jump diffusions are known as Singwi-Sjölander and Hall and Ross jump diffusions respectively (Chapter1, section 1.1.4.2). It may be noted that in all these jump diffusion models, the difference is that of a microscopic detail. In case the system is studied at a larger length scales or equivalently at smaller  $Q$  values, the information about these finer details is lost and the diffusion process looks very much like the Brownian diffusion. The variation of  $\Gamma(Q)$  with  $Q^2$  is therefore linear at low  $Q$  values and the diffusion coefficient can be obtained simply from the slope of this curve in the region of small  $Q$  values. At higher  $Q$  values, however, as finer details of the jump diffusion start to emerge, the variation of  $\Gamma(Q)$  with  $Q^2$  is no more linear and saturates to a value, which indicate that residence time is involved in the jump process. In the present case, the variation of  $\Gamma(Q)$  with  $Q^2$  obtained from the experimental data was found to be described well by the Singwi-Sjölander model of jump diffusion, which employs a random distribution of jump lengths. In this model the variation of  $\Gamma(Q)$  with  $Q^2$  is given by (Chapter1, section 1.1.4.2)

$$\Gamma(Q) = \frac{D_T Q^2}{1 + D_T Q^2 \tau} \quad (6.3)$$

where  $D_T$  and  $\tau$  are translational diffusion coefficient and residence time respectively. The solid line in Fig. 6.6 corresponds to the least squares fit of the above equation with the experimentally obtained values. The values of the parameters,  $D_T$  and  $\tau$  are obtained from the fits, for RO membrane,  $D_T$  and  $\tau$  are obtained to be  $(1.9 \pm 0.4) \times 10^{-5} \text{ cm}^2/\text{s}$  and  $(2.8 \pm 0.6) \text{ ps}$  respectively. For water diffusion in NF membrane,  $D_T$  and  $\tau$  are obtained to be  $(1.4 \pm 0.3) \times 10^{-5} \text{ cm}^2/\text{s}$  and  $(1.1 \pm 0.3) \text{ ps}$  respectively. One can obtain root mean square jump length  $l$  using the Einstein relation,  $D_T = \frac{l^2}{6\tau}$ .

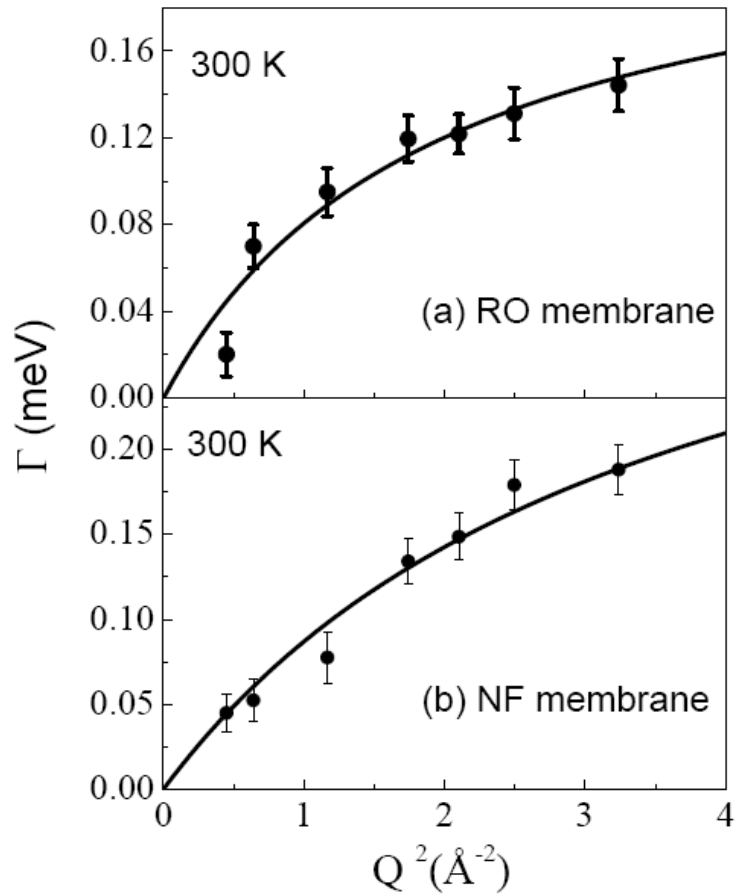


**Fig. 6.6** Variation of HWHM ( $\Gamma$ ), as obtained from QENS experiment on water sorbed in (a) RO and (b) NF polyamide membranes. The symbols represent experimental  $\Gamma$  values while the solid line is the fit with Singwi-Sjölander model.

It is of interest to investigate dynamical behavior of water especially at low temperature to

probe whether supercooling phenomena exists in the case of restricted geometries offered by the polyamide membranes. However, due to limited energy resolution and statistics, information on the dynamics of water confined in nanoporous membrane, at low temperature could not be extracted from MARX spectrometer. Therefore, further QENS experiments have been carried out on water sorbed RO and NF membranes using high-energy resolution ( $\Delta E \sim 45 \mu\text{eV}$ ) FOCUS spectrometer (Chapter1, section 1.2.4) at different temperatures. Significant quasielastic broadening is observed for both hydrated membranes at and above 268 K. Below 268 K, no quasielastic broadening was observed suggesting water molecules are frozen within the time scale of the instrument. Increase in temperature leads to continuous growth in quasielastic broadening as shown in Figs. 6.7 (a) and (b) for RO and NF polyamide membrane respectively. However, dehydrated samples did not show any QE broadening in the temperature range used for the present study. QENS spectra for dehydrated samples are used to estimate the contribution of membrane as such to total spectra. If both rotational as well as translational motion of water are present in the system, total scattering function will be a convolution of rotational and translational component assuming the two motions are uncorrelated. Therefore, general scattering law can be written as (Chapter1, section 1.2.6)

$$S_{\text{tot}}(Q, \omega) = A(Q)\delta(\omega) + [1 - A(Q)]S_{\text{rot}}(Q, \omega) \otimes S_{\text{tran}}(Q, \omega) \quad (6.4)$$

The first term accounts for the elastic scattering arising from the dehydrated membrane and the second term is for quasielastic scattering due to the mobile water molecules. Translational motion of water molecules can be described by a Lorentzian function (Chapter 1, section 1.2.4).

Rotational motion of water is known to follow isotropic rotational diffusion model [18]. Isotropic rotational diffusion model has been discussed in section 1.1.5.1 of Chapter 1. From Eqs, (6.4) and (1.68), total scattering law can be written as

$$S_{Total}(Q, \omega) = A(Q)\delta(\omega) + [1 - A(Q)] \left[ j_0^2(Qr) \frac{1}{\pi} \frac{\Gamma_T(Q)}{(\Gamma_T(Q))^2 + \omega^2} + \frac{1}{\pi^2} \sum_{l=1}^{\infty} (2l+1) j_l^2(Qr) \frac{[\Gamma_T(Q) + l(l+1)D_R]}{[\Gamma_T(Q) + l(l+1)D_R]^2 + \omega^2} \right] \quad (6.5)$$

where  $j_l$  is the spherical Bessel function of the order  $l$ ,  $\Gamma_T$  is HWHM of Lorentzian corresponding to translational motion and  $D_R$  is the rotational diffusion constant.

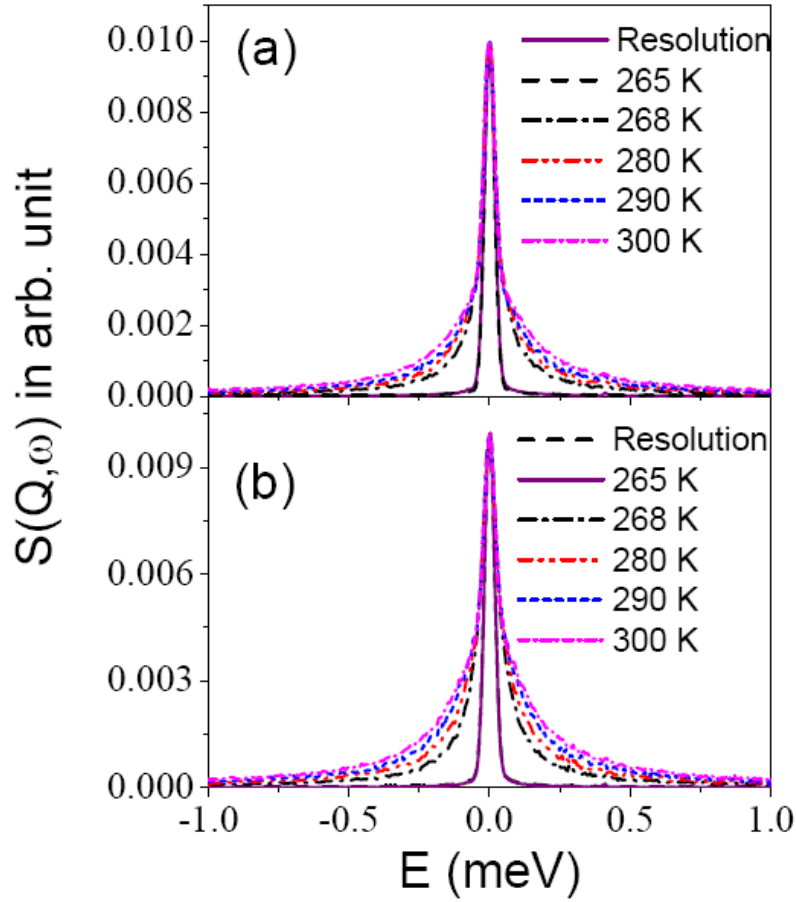


**Fig. 6.7** Typical measured QENS spectra for (a) water sorbed RO membrane and (b) water sorbed NF membrane using FOCUS spectrometer at a particular  $Q=1.0 \text{ \AA}^{-1}$ .

In practice the summation series in the above equation can be truncated at those values of  $l$  for which the Bessel functions do not contribute up to  $Q_{max}r$ . With the measured maximum wave vector transfer,  $Q_{max} = 1.6 \text{ \AA}^{-1}$  and  $r$  (radius of gyration) =  $1.0 \text{ \AA}$ , it is found that contributions of  $(2l+1)j_l^2(Qr)$  up to  $l=2$  in Eq. (6.5) are significant and thus higher orders can be neglected [18]. Eq. (6.5) with the summation truncated after  $l=2$ , convoluted

with the instrumental resolution, is used to describe the observed QENS data corresponding to the hydrated membranes. A least square fitting method is used to fit the spectra with parameters,  $\Gamma_T$  and  $D_R$ . Typical fitted spectra for water sorbed in RO and NF membranes are shown in Figs. 6.8 and 6.9 respectively.

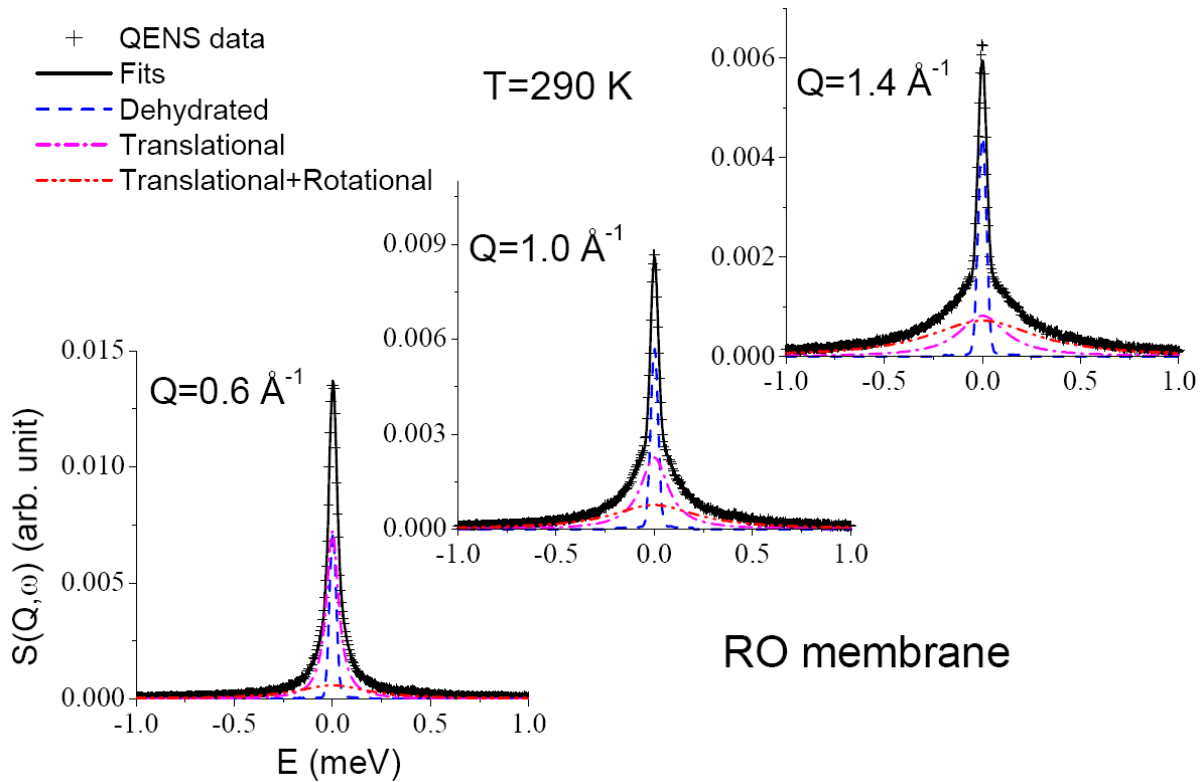


**Fig. 6.8** Fitted QENS spectra for water-sorbed RO polyamide membrane using Eq. (6.5) at some typical  $Q$  values.

As evident from both the figures, the model scattering law has provided good description of the experimental data. It is found that rotational diffusion coefficient is more or less constant with respect to  $Q$  for both the membranes and average rotational diffusion coefficients for different temperatures are given in Table 6.2. Observed rotational diffusion coefficients are compared with the bulk water [18]. It is found that the rotational diffusivity of water in these polyamide membranes does not alter much compared to its bulk value. The fact that the rotational diffusivity remains unaltered is not surprising as found in many

occasions [6,137]. The HWHM of the translational component ( $\Gamma_T$ ) for water sorbed in RO and in NF membrane, obtained from the fits are shown in Figs. 6.11 and 6.12 respectively. Random translational jump diffusion model (Chapter1, section 1.1.4.2), Eq. (6.3) is found to describe well the observed  $\Gamma_T(Q)$ . Solid lines are the fit using Eq. (6.3), where  $D_T$  and  $\tau$  are kept as parameters.  $D_T$  and  $\tau$  as obtained from the fits are shown in Table 6.2 for both the membranes at each temperature.

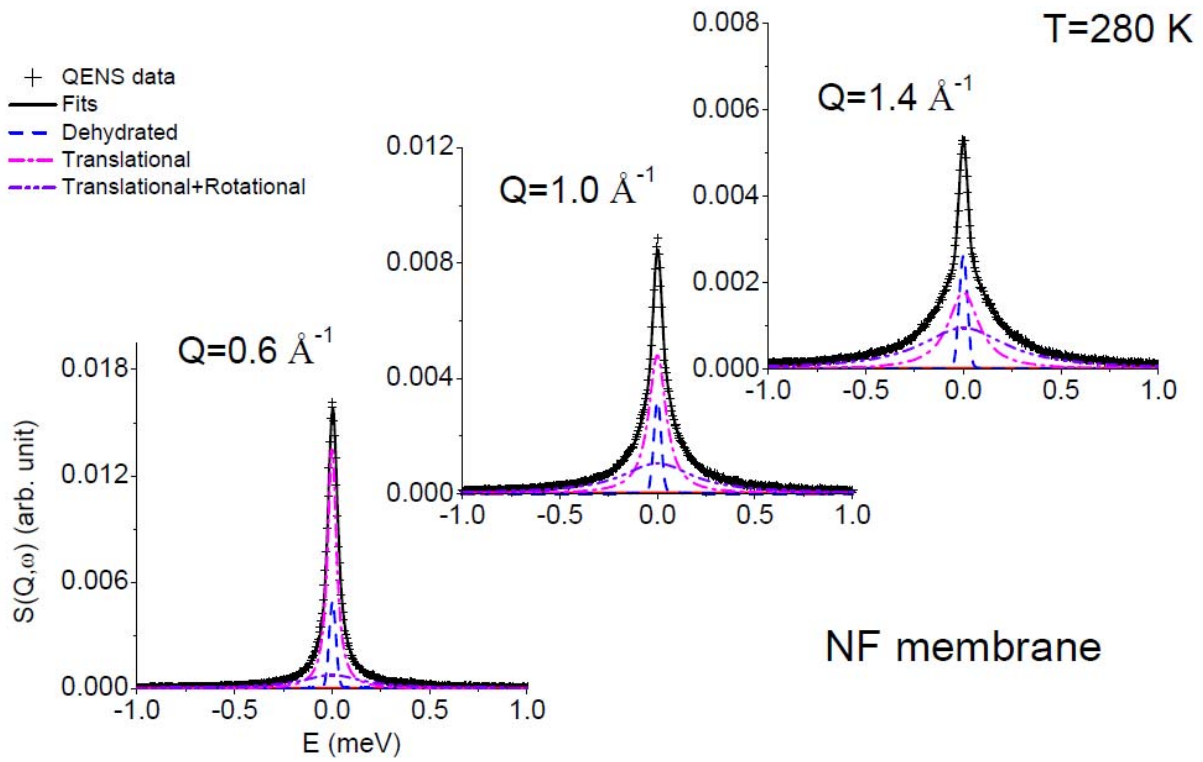


**Fig. 6.9** Fitted QENS spectra for water-sorbed NF polyamide membrane as obtained using Eq. (6.5) at some typical  $Q$  values.



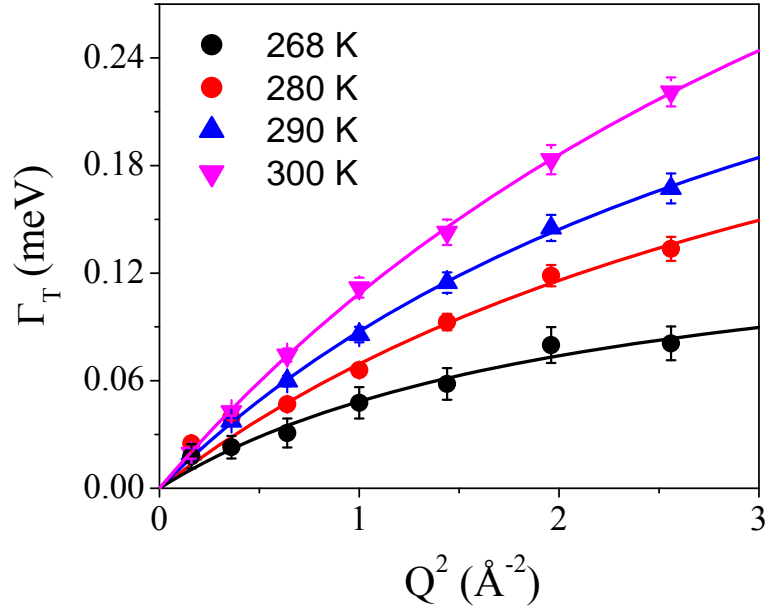


**Fig. 6.10** Variation of HWHM of Lorentzian corresponds to translation motion of water in RO membrane with  $Q^2$  at different temperatures. The solid line corresponds to the fit as per the random jump diffusion model.

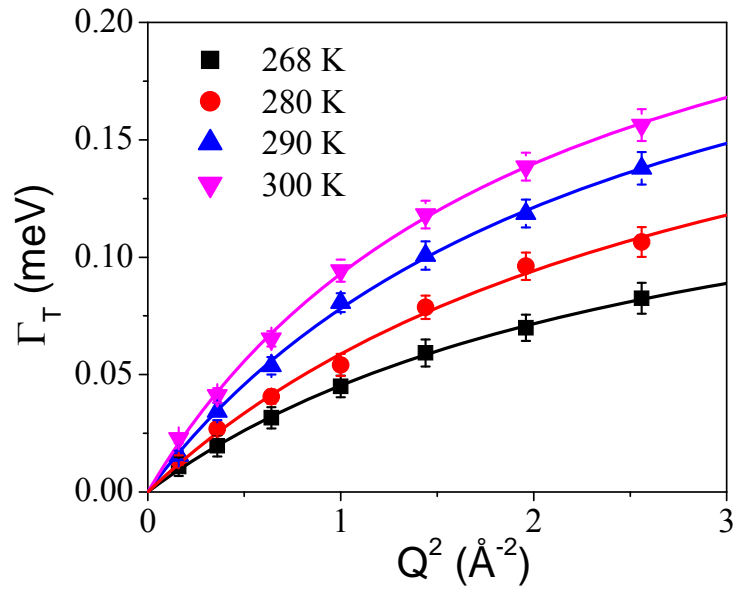


**Fig. 6.11** Variation of HWHM of Lorentzian corresponds to translation motion of water in NF membrane with  $Q^2$  at different temperatures. The solid line corresponds to the fit using Eq. (6.3) as per the random jump diffusion model.

**Table 6.2** Values of translational diffusion coefficient ( $D_T$ ), residence time ( $\tau$ ) and rotational diffusion coefficient ( $D_R$ ) of water sorbed in RO and NF membranes at different temperatures.

S. No.	T (K)	RO membrane			NF membrane		
		$D_T$ ( $10^{-5}$ cm <sup>2</sup> /s)	$\tau$ (ps)	$D_R$ ( $\mu$ eV)	$D_T$ ( $10^{-5}$ cm <sup>2</sup> /s)	$\tau$ (ps)	$D_R$ ( $\mu$ eV)
1	268	$1.0 \pm 0.3$	$4.2 \pm 0.9$	$72 \pm 8$	$0.9 \pm 0.3$	$3.8 \pm 0.6$	$71 \pm 6$
2	280	$1.3 \pm 0.1$	$1.8 \pm 0.3$	$83 \pm 9$	$1.2 \pm 0.1$	$2.8 \pm 0.3$	$81 \pm 8$
3	290	$1.7 \pm 0.1$	$1.6 \pm 0.1$	$90 \pm 10$	$1.6 \pm 0.1$	$2.4 \pm 0.2$	$93 \pm 11$
4	300	$2.0 \pm 0.1$	$1.0 \pm 0.1$	$101 \pm 11$	$2.1 \pm 0.1$	$2.3 \pm 0.1$	$102 \pm 10$

Water molecules are found to undergo restricted diffusion in these membranes especially near room temperature. Similar kind of confined behaviour was also observed for water in porous Alumina. [6]. It may be noted that diffusion of water in confining media depends on lot of factors such as pore size, connectivity within the pores, level of hydration, hydrophilic/hydrophobic interaction with substrate and so forth [137,138]. Castrillon et al. [137] had shown the effect of surface polarity on the dynamics of confined water. It was found that dynamics of water exhibited nonmonotonic dependence with hydrophobicity of substrate. Perrin et al. [138] had shown that for water in Nafion membrane, the diffusion coefficients increased with the increase in the hydration level. At room temperature and with the saturation loading, the diffusion coefficient of water in Nafion membrane is obtained as  $2.0 \pm 0.1 \times 10^{-5}$  cm<sup>2</sup>/s. A similar effect is observed in case of water dynamics in hydrotalcite [9]. It was seen that at lower hydration level, water molecules were attached to the surfaces resulting lower diffusivity of water molecules. However, with a higher hydration level, more

and more water molecules are available away from the surfaces, which leads to higher mobility of water molecules.

### 6.3. DYNAMICS OF WATER IN PRUSSIAN BLUE AND ITS ANALOGUES

Another example, which offers confinement to the water molecules is Prussian blue analogue (PBA) compounds. PBA compounds are represented by general formula  $A_x[B(CN)_6]_y \cdot zH_2O$  where  $A$  and  $B$  are 3d or 4d magnetic ions [139-143]. PBA has face centered cubic (*fcc*) structure in which  $A$  and  $B$  are surrounded octahedrally by  $N$  and  $C$  atoms, respectively. When  $x/y=1$ , the first coordination of  $A$  and  $B$  is  $\{A(NC)_6\}$  and  $\{B(CN)_6\}$  respectively. For example, in case of ferriferrocyanide  $Fe_4(II)[Fe(II)(CN)_6]_4 \cdot 16H_2O$  or  $Fe(II)[Fe(II)(CN)_6] \cdot 4H_2O$ , all water molecules are non-coordinated and occupy the interstitial positions [140]. But when  $x/y>1$ , some of the  $\{B(CN)_6\}$  sites remain vacant and the first coordination of  $A$  and  $B$  will be  $\{A(NC)_{6-n}(H_2O)_n\}$  ( $n=1,6$ ) and  $\{B(CN)_6\}$  respectively. For example,  $M_3[Fe(CN)_6]_2 \cdot 14-16 H_2O$ , 33% of the building unit ( $Fe(CN)_6$ ) sites remain vacant in the material framework creating a network of pores [142,143]. Generally, water molecules fill these vacancies. Locations of water molecules in these systems are determined using powder neutron diffraction [140-142]. Three structurally distinguishable water molecules, (i) coordinated water molecules which are coordinated to  $A$  octahedra at empty nitrogen 24e ( $x, 0, 0$ ) site, (ii) non-coordinated water molecules connected by hydrogen bonds to the coordinated ones in the spherical cavity of  $[B(CN)_6]$  at 32f ( $x, x, x$ ) site and (iii) non-coordinated water at 8c ( $1/4, 1/4, 1/4$ ) site of unit cell octants are found in these compounds [141,142]. PBA are important compounds due to its various interesting multifunctional properties upon application of external stimuli, such as temperature, magnetic field, light, pressure, humidity, etc. For humidity-sensitive characteristics, water vapour

penetrates the lattice and act on spin sites. By varying the humidity, one can tune physical as well as magnetic properties of PBA compound. For example, it has been shown that by changing the humidity content, color of cobalt based PBA is found to change between blue and pink and magnetic interaction is found to switch between ferromagnetic and antiferromagnetic coupling [144]. Therefore, role of water molecules is important in understanding the basic properties of these multifunctional molecular magnet and its possible applications in various devices.

Dynamics of water in Prussian blue (PB),  $\text{Fe(III)}_4[\text{Fe(II)(CN)}_6]_3 \cdot 14\text{H}_2\text{O}$  as well as its analogues,  $\text{Fe}_4(\text{II})[\text{Fe(II)(CN)}_6]_4 \cdot 16\text{H}_2\text{O}$  (PBA-I) and  $\text{Cu}_2\text{Mn}_2[\text{Fe(CN)}_6]_{2.67} \cdot 19\text{H}_2\text{O}$  or  $\text{Cu}_{0.75}\text{Mn}_{0.75}[\text{Fe(CN)}_6] \cdot 7\text{H}_2\text{O}$  (PBA-II) have been studied using QENS technique and discussed here. The structures of these compounds are very well studied using X-ray as well as neutron diffraction techniques [140-142,145]. In PB ( $\text{Fe(III)}_4[\text{Fe(II)(CN)}_6]_3 \cdot 14\text{H}_2\text{O}$ ), owing to the 4:3 (x: y) stoichiometry, the charge neutrality necessitates that 1/4 of the  $\text{Fe(CN)}_6$  sites are vacant and they are filled by the water molecules [141]. All three structurally distinguishable kinds of water molecules as mentioned above are found in PB. Out of 14 water molecules, six water molecules are coordinated to Fe(III) at empty nitrogen sites 24e (x, 0, 0) site, four non-coordinated water molecules at 32f (x, x, x) site inside the spherical cavity and remaining four non-coordinated water molecules are found at 8c (1/4, 1/4, 1/4) site of unit cell octants [141]. Similarly in PBA-II ( $\text{Cu}_2\text{Mn}_2[\text{Fe(CN)}_6]_{2.67} \cdot 19\text{H}_2\text{O}$ ), 1/3 of the  $\text{Fe(CN)}_6$  sites are vacant and they are filled by the water molecules [142]. On the average, out of nineteen water molecules, eight are coordinated at 24e site, six are non-coordinated at 32f site in the spherical cavity and remaining five water molecules are non-coordinated at 8c interstitial site out side the cavity [142]. The diffraction pattern shows a distinct broad peak at the (100) Bragg position at room temperature, which is forbidden under the *fcc* (Fm3m) space group [142]. The RMC analysis of the neutron scattering data [142]

infers that the broad peak at (100) is attributed to clustering of O atoms of coordinated as well as non-coordinated water molecules in the empty  $\text{Fe}(\text{CN})_6$  sites. Fig. 6.12(a) shows the formation of spherical cavity by coordinated water molecules as obtained from the structural analysis. The non-coordinated water molecules are omitted for clarity. Most likely cause of the clustering of 'O' atoms is that the non-coordinated water molecules at 32f crystallographic site are mainly confined in a spherical cavity formed by coordinated water molecules. The diameter of the cavity, estimated by positions of oxygen atoms of the coordinated water molecules, is  $\sim 5.1$  Å. However, in PBA-I ( $\text{Fe}_4(\text{II})[\text{Fe}(\text{II})(\text{CN})_6]_4 \cdot 16\text{H}_2\text{O}$ ), owing to the 1:1 (x:y) stoichiometry, no  $\text{Fe}(\text{CN})_6$  sites are vacant [Fig. 6.12(b)]. Ferriferrocyanide has only one kind of water molecules, which are non-coordinated and at the interstitial sites [140]. Combinations of these samples provide an ideal combination to distinguish dynamics of different kind of water.

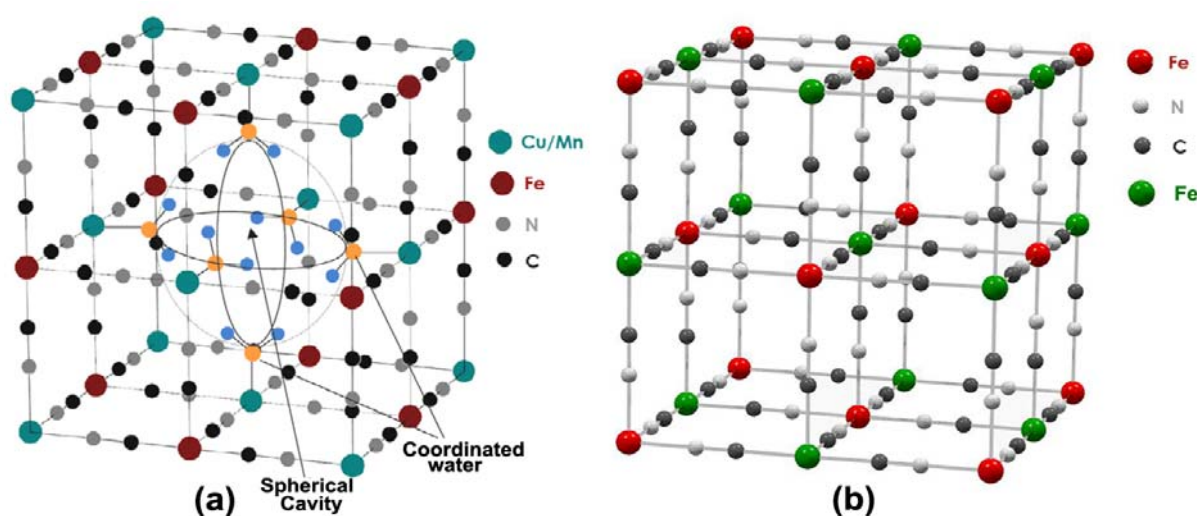


**Fig. 6.12** Unit cell of (a) PBA-II ( $\text{Cu}_2\text{Mn}_2[\text{Fe}(\text{CN})_6]_{2.67} \cdot 19\text{H}_2\text{O}$ ) and (b) PBA-I ( $\text{Fe}_4(\text{II})[\text{Fe}(\text{II})(\text{CN})_6]_4 \cdot 16\text{H}_2\text{O}$ ) and as obtained from the structural analysis [140,142]. The spherical cavity formed by coordinated water molecules in PBA-II is also indicated. The non-coordinated water molecules within the cavity as well as at octants are omitted for clarity.

### 6.3.1. Experimental Details

The polycrystalline samples of PB, PBA-I and PBA-II are prepared by the precipitation method. PB ( $\text{Fe(III)}_4[\text{Fe(II)(CN)}_6]_3 \cdot 14\text{H}_2\text{O}$ ) is prepared by mixing 0.1 M aqueous solution of  $\text{K}_4\text{Fe(CN)}_6$ , to rapidly stirred aqueous solution of 0.1 M  $\text{FeCl}_3$ . For PBA-I ( $\text{Fe}_4(\text{II})[\text{Fe(II)(CN)}_6]_4 \cdot 16\text{H}_2\text{O}$ ), 0.1 M  $\text{K}_3\text{Fe(CN)}_6$  aqueous solution was slowly added to 0.1 M  $\text{FeCl}_3$  aqueous solution in the appropriate proportions and the resulting solution was heated up to 325 K. The hot solution was allowed to cool at room temperature and diluted to double of its initial volume after cooling. PBA-II ( $\text{Cu}_2\text{Mn}_2[\text{Fe(CN)}_6]_{2.67} \cdot 19\text{H}_2\text{O}$ ) was prepared by mixing 0.1 M aqueous solutions of  $\text{Cu(NO}_3)_2$  and  $\text{Mn(NO}_3)_2$  to rapidly stirred aqueous solution of 0.1 M  $\text{K}_3[\text{Fe(CN)}_6]$  in the appropriate proportions,. Obtained precipitates were filtered, washed many times with distilled water and finally dried at room temperature. These samples are well characterized by X-ray as well as neutron diffraction techniques. Compound is found to be in *fcc* crystalline phase with  $\text{Fm}\bar{3}\text{m}$  space group.

QENS measurements have been carried out on PB ( $\text{Fe(III)}_4[\text{Fe(II)(CN)}_6]_3 \cdot 14\text{H}_2\text{O}$ ), PBA-I ( $\text{Fe}_4(\text{II})[\text{Fe(II)(CN)}_6]_4 \cdot 16\text{H}_2\text{O}$ ) and PBA-II ( $\text{Cu}_2\text{Mn}_2[\text{Fe(CN)}_6]_{2.67} \cdot 19\text{H}_2\text{O}$ ) as well as on dehydrated sample of each with an incident wavelength of 6 Å corresponding to an energy resolution (FWHM) of  $\Delta E \sim 45 \mu\text{eV}$ . QENS experiments were performed in the temperature range 260-360 K using hybrid time of flight spectrometer ‘FOCUS’ (Chapter-1, section-1.2.4) at SINQ, Paul Scherrer Institut, Switzerland. The samples were placed in a flat rectangular aluminum can with an internal spacing of 0.2 mm (which ensures no more than 10% scattering) such that multiple scattering effects can be neglected. The quasielastic spectra were recorded in the  $Q$  range of  $0.4\text{-}1.6 \text{Å}^{-1}$ . Spectra were corrected for detector efficiency with standard vanadium and were normalized to monitor intensity. As experimental Bragg peak positions are known from the diffraction pattern, during  $Q$  binning such  $Q$  values (where Bragg peaks occur) are avoided. The DAVE software [74] developed

by NIST was used to carry out data reduction involving background subtraction, detector efficiency corrections, etc. Data from the dehydrated sample were used to estimate the contribution from the sample other than water. For dehydration, sample was heated at 420 K under vacuum (15 mb) for a period of about 10 h. Dehydrated sample is then sealed in a glove box and used for the neutron scattering measurements. Weight of the sample is recorded before and after dehydration process. Weight loss as observed after dehydration is also independently confirmed by Thermo Gravimetric Analysis (TGA) measurements. Thermogravimetric measurements are carried out with Mettler thermogravimetric analyzer (TG 50). The thermograms are recorded in air atmosphere at a heating rate of 5 °C min<sup>-1</sup> in the temperature range 40–300°C. Diffraction pattern recorded for the dehydrated sample confirm the same *fcc* crystal structure with space group Fm3m.

### 6.3.2. Results and Discussion

Significant quasielastic (QE) broadening for Prussian blue and its analogues is observed over the instrument resolution whereas no QE broadening is observed for dehydrated samples. Therefore, observed QE broadening correspond to dynamics of water. This is also corroborated by the vibrational density of states (DOS) as obtained from the time of flight data for all the compounds and their dehydrated form using the following simplified expression [146]

$$g(E) \cong \frac{E}{Q^2} \left[ 1 - \exp\left(-\frac{E}{K_B T}\right) \right] S(Q, E) \quad (6.6)$$

where  $K_B$  is Boltzman constant,  $T$  is temperature and  $E$  is energy transfer. The peak at about 8 meV, corresponding to the intermolecular bending motions of the water molecules [146,147], observed in Prussian blue and its analogues, is found to be absent in the dehydrated form. For examples, vibrational DOS as obtained for PBA-II and its dehydrated

form are shown in Fig. 6.13. Peak at 8 meV, observed in PBA-II, is found to be absent in the dehydrated form suggest that dehydrated sample is devoid of any water remained. The loss of water molecules in the is clearly evident. Data as obtained from the dehydrated sample were subtracted from that of the hydrated sample to extract the contribution from the water alone. Observed QENS spectra for all three compounds (PB, PBA-I and PBA-II) are compared. Typical QENS spectra for these compounds are shown at  $Q=1.0 \text{ \AA}^{-1}$  at 330 K as shown in Fig. 6.14. For all the compounds, QENS spectra are found to be comprised of at least two contributions, a narrow elastic peak that reflects scattering from species, which are static or moving slower than the instrumental resolution, and a quasielastic broadening arising from the mobile species.

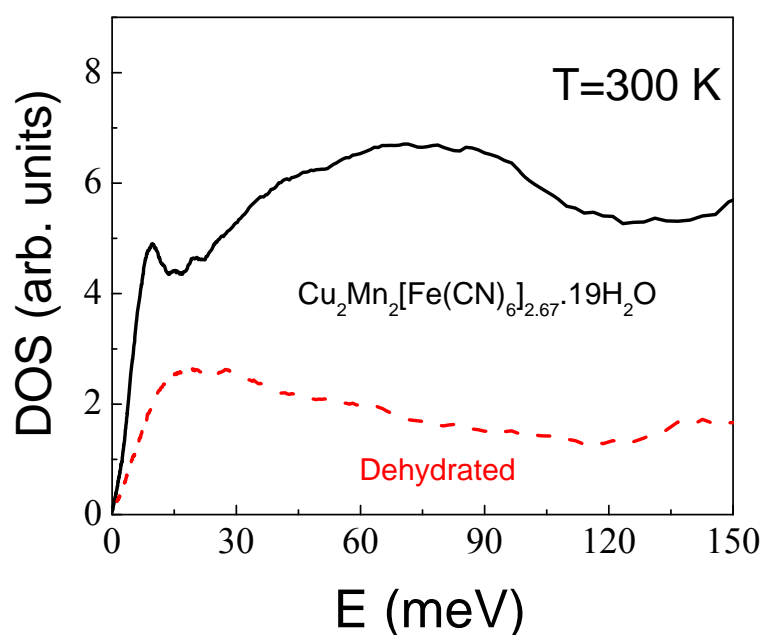


**Fig. 6.13** Vibrational DOS for PBA-II ( $\text{Cu}_2\text{Mn}_2[\text{Fe}(\text{CN})_6]_{2.67} \cdot 19\text{H}_2\text{O}$ ) and its dehydrated form at 300 K. A peak around 8 meV in  $\text{Cu}_2\text{Mn}_2[\text{Fe}(\text{CN})_6]_{2.67} \cdot 19\text{H}_2\text{O}$  is not seen in the dehydrated sample.



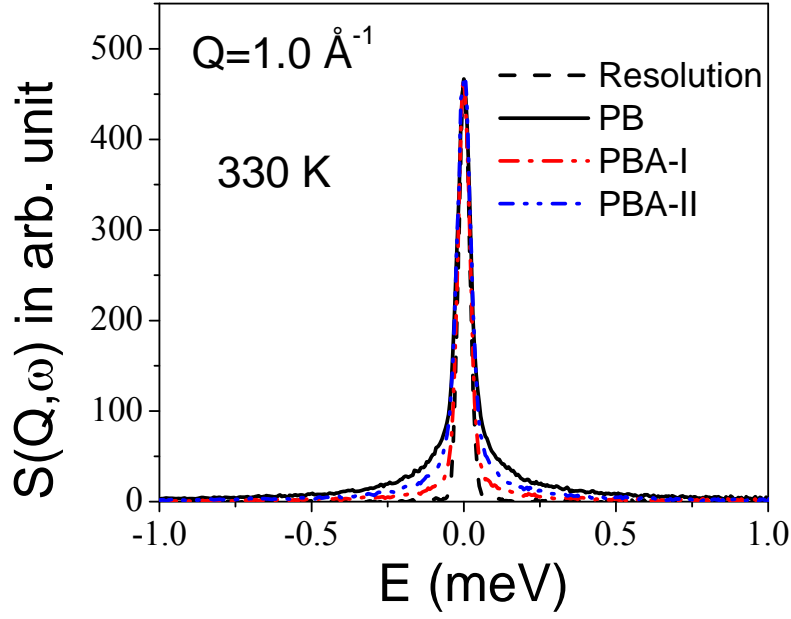


**Fig. 6.14** Comparison of QENS spectra as obtained for PB, PBA-I and PBA-II at  $Q=1.0 \text{ \AA}^{-1}$  at 330 K. The instrument resolution as obtained from a standard vanadium sample is shown by a dashed line. Spectra have been normalized to maximum peak intensity of vanadium.

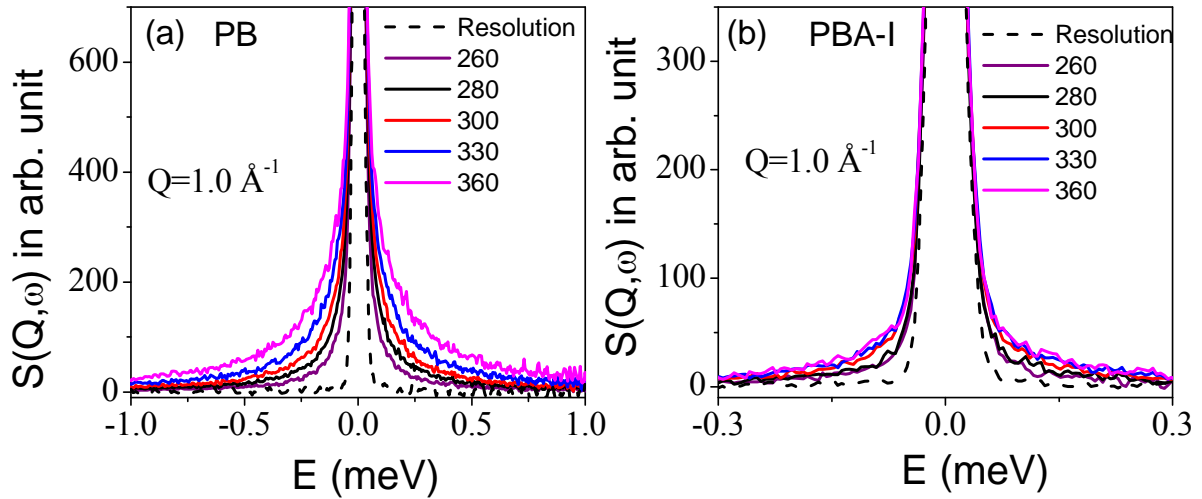


**Fig. 6.15** QENS spectra recorded for (a) PB and (b) PBA-I at different temperatures at  $Q=1.0 \text{ \AA}^{-1}$ . Contribution from dehydrated sample has been subtracted. A dashed line shows the instrument resolution. Spectra have been normalized to maximum peak intensity.

On increase of temperature from 260 K to 360 K, the QE broadening is found to increase in all the compounds. Typical evolution in the QENS spectra for PB and PBA-I at the observed temperature range 260 K-360 K are shown in the Fig. 6.15(a) and (b) respectively. It is found that evolution in quasielastic broadening for PBA-I (which don't have cavities) is slower than other compounds PB and PBA-II (which have cavities due to vacant  $\text{Fe}(\text{CN})_6$  units). To proceed with the analysis, it is required to separate the elastic and quasielastic components of the subtracted data. For that, model scattering law is given in Eq. (6.2). (Chapter 1, section 1.2.6). Eq. (6.2) is convoluted by the instrumental resolution function and the parameters  $A(Q)$  and  $\Gamma(Q)$  were determined by least squares fit with the measured data. QENS spectra at different temperatures for all the compounds are satisfactorily described using a finite elastic incoherent structure factor [EISF:  $A(Q)$ ], along with  $Q$  dependent quasielastic broadening [ $\Gamma(Q)$ ]. Fits for some typical  $Q$  values at  $T = 300$  K for PB, PBA-I and PBA-II are shown in Fig. 6.16, 6.17 and 6.18 respectively. Presence of elastic contribution,  $A(Q)$  is surprising, in general it is not expected for bulk water but as the water here are kind of confined they might undergo localised motion and presence of elastic component indicate the same. If this localized motion is due to the rotational motion of water molecules, the possible models could be, 1) 2-fold jump rotation (Chapter 1, section 1.1.5.3) around an axis which is perpendicular to the molecular plane and passing through oxygen atom, 2) isotropic rotation (Chapter 2, section 1.1.5.1) where molecular reorientation is assumed to take place through small-angle random rotations on surface of a sphere i.e. on a time average, no most probable orientation exists. From the behaviour of the variation of the QE width with  $Q$ , as discussed later, it is clear that the observed dynamics cannot be 2-fold jump rotation. Also the behaviour of calculated EISF (as shown in Fig. 6.19) based on isotropic rotational model (Chapter 1, section 1.1.5.1) clearly indicates that it is not a feasible model to describe the observed data. Therefore, most likely process could be localized

translational diffusion (Chapter 1, section 1.1.4.3), which is observed in case of water confined in porous alumina gel [6].

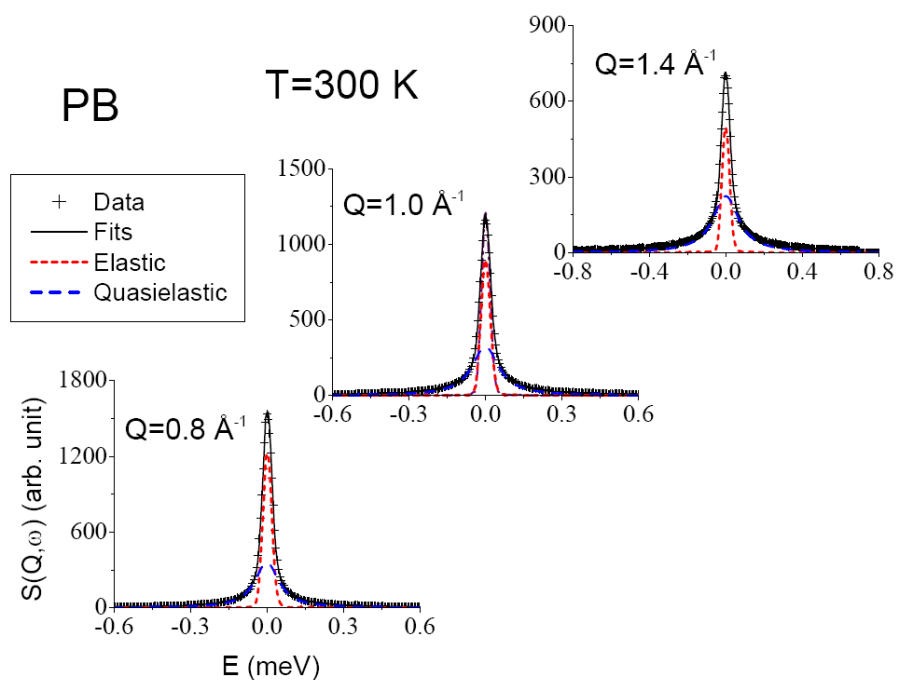


**Fig. 6.16** Fitted subtracted QENS spectra for PB ( $\text{Fe}_4(\text{II})[\text{Fe}(\text{II})(\text{CN})_6]_3 \cdot 14\text{H}_2\text{O}$ ) at some typical  $Q$  values. Instrument resolution is shown by the dashed line in the middle panel.

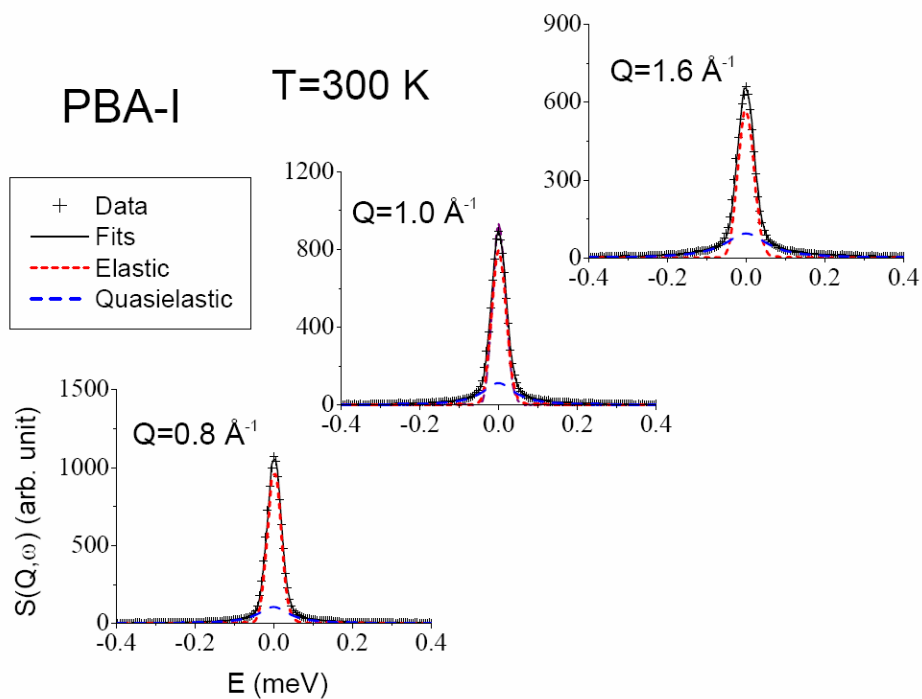


**Fig. 6.17** Fitted subtracted QENS spectra for PBA-I ( $\text{Fe}_4(\text{II})[\text{Fe}(\text{II})(\text{CN})_6]_4 \cdot 16\text{H}_2\text{O}$ ) at some typical  $Q$  values. Instrument resolution is shown by the dashed line in the middle panel.

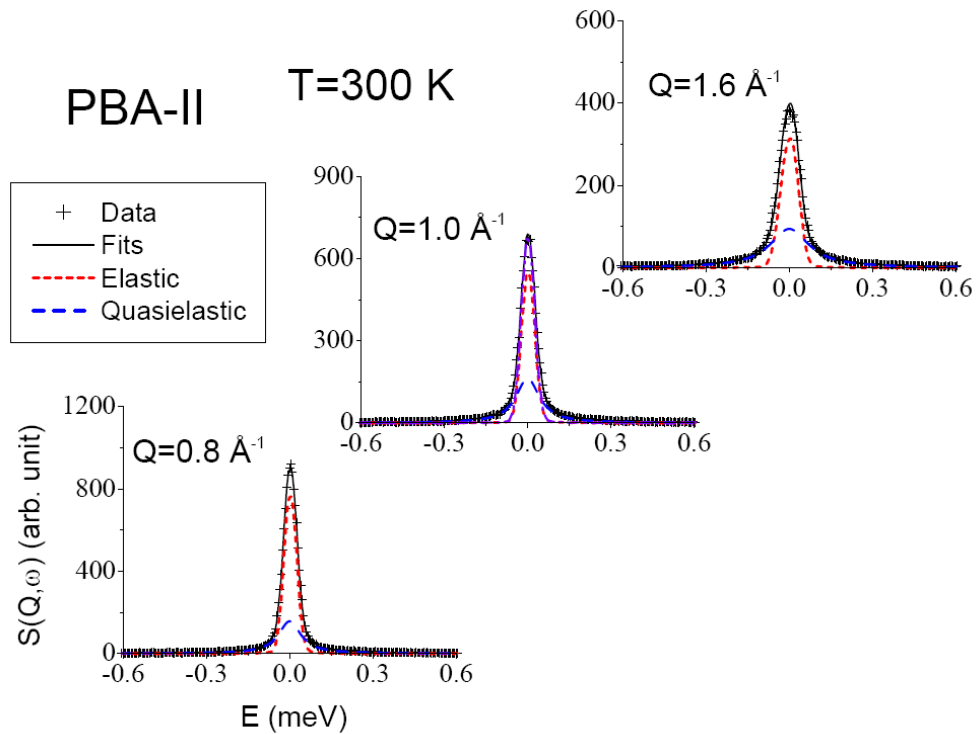


**Fig. 6.18** Fitted subtracted QENS spectra for PBA-II ( $\text{Cu}_2\text{Mn}_2[\text{Fe}(\text{CN})_6]_{2.67} \cdot 19\text{H}_2\text{O}$ ) at some typical  $Q$  values. Instrument resolution is shown by the dashed line in the middle panel.

The variation of EISF at different temperatures (Fig. 6.19) indicates that there is an evolution of dynamics as the temperature is increased. This is more pronounced in the compounds ( $x/y > 1$ ), which have cavities such as PB and PBA-II. In PBA-I, which does not have cavities, change in EISF with temperature is found to be very small. Evolution in dynamics suggests that as temperature is increased, more number of water molecules contribute to the dynamics. Considering all the facts a generalized scattering law for a system where fraction of the water molecules ( $p_x$ ) contribute to the dynamics can be written as,

$$S(Q, \omega) = (1 - p_x) \delta(\omega) + p_x \left[ A_0(Q) \delta(\omega) + (1 - A_0(Q)) L(\Gamma, \omega) \right] \quad (6.7)$$

where  $A_0(Q)$  is the model EISF and the total elastic fraction would be,  $[p_x A_0(Q) + (1 - p_x)]$ .

In case of translational diffusion of particles within a sphere of radius  $a$  enclosed by impermeable boundary,  $A_0(Q)$  can be given as (Chapter 1, section 1.1.4.3)

$$A_0(Q) = \left[ \frac{3j_1(Qa)}{Qa} \right]^2 \quad (6.8)$$

The effective EISF can be written as,

$$A(Q) = \left[ p_x \left( \frac{3j_1(Qa)}{Qa} \right)^2 + (1 - p_x) \right] \quad (6.9)$$

Here  $j_1(Qa)$  is the first-order spherical Bessel function. It is found that the above equation could describe the observed EISF for all the samples at different temperatures very well, as shown by the solid lines in Fig 6.19. The mobile fraction of the water molecules,  $p_x$ , and radius of the spherical cavity within which the molecules undergo localized dynamics,  $a$ , are the parameters determined by least squares fitting of the experimentally obtained *EISF* are given in Table 6.3. For example, at 260 K, the values of  $p_x$  and  $a$  for water in PBA-II are found to be  $0.30 \pm 0.04$  and  $3.0 \pm 0.2$  Å respectively, suggesting that about 30 % of water molecules are mobile and contributing to the observed dynamics. Variation of  $p_x$  for all the compounds are shown in Fig 6.20. Fraction of mobile water molecules in PB and PBA-II ( $x/y > 1$ ) are found to be more than PBA-I ( $x/y = 1$ ). In case of PB and PBA-II, fraction of mobile water molecules increases significantly with temperature unlike in PBA-I. Obtained value of the size of sphere ( $a$ ) for PB and PBA-II is found to be very similar to the size of the cavity (radius  $\sim 2.55$  Å) formed due to the vacant sites of  $\text{Fe}(\text{CN})_6$ .

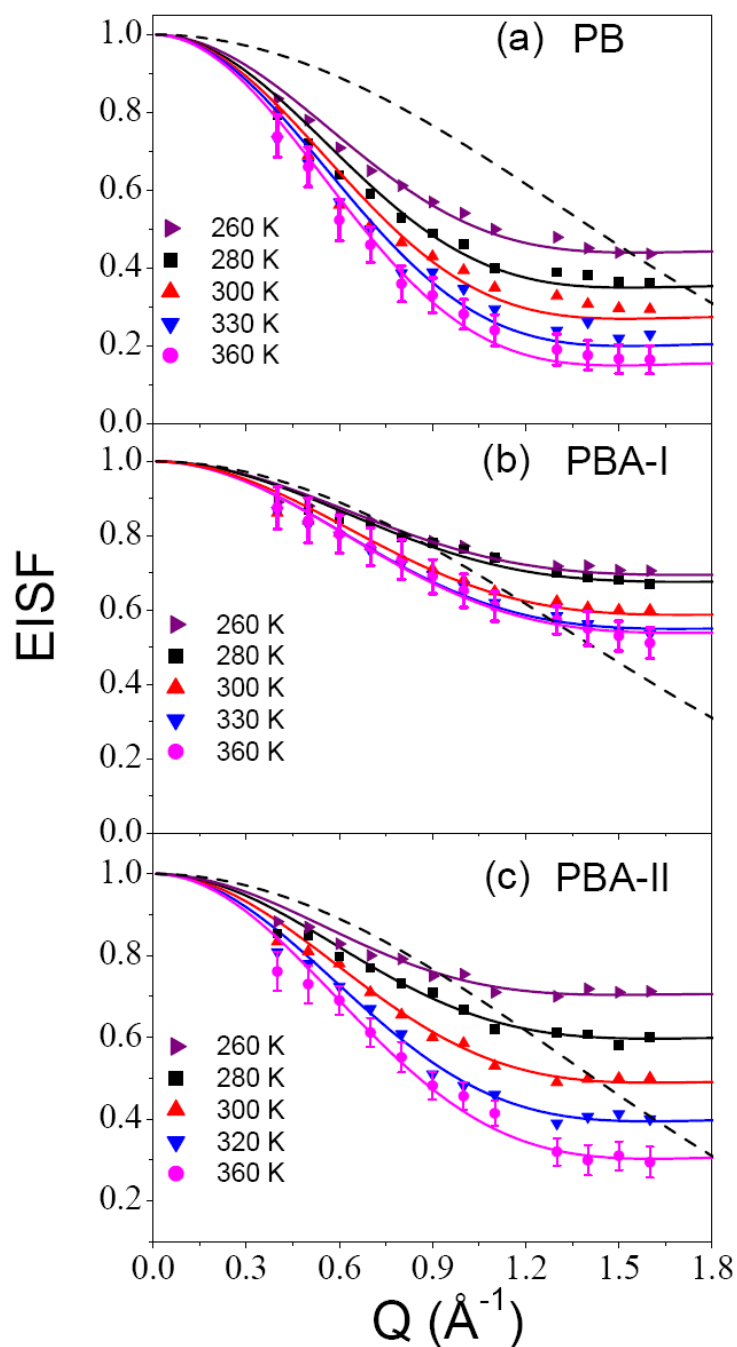


**Fig. 6.19** Variation of EISF for (a) PB ( $\text{Fe}_4(\text{II})[\text{Fe}(\text{II})(\text{CN})_6]_3 \cdot 14\text{H}_2\text{O}$ ), (b) PBA-I ( $\text{Fe}_4(\text{II})[\text{Fe}(\text{II})(\text{CN})_6]_4 \cdot 16\text{H}_2\text{O}$ ) and (c) PBA-II ( $\text{Cu}_2\text{Mn}_2[\text{Fe}(\text{CN})_6]_{2.67} \cdot 19\text{H}_2\text{O}$ ) as obtained from QENS data with  $Q$  at different temperatures. Solid lines show the fits to the EISF using a localized translational diffusion model with immobile fraction [Eq.(6.9)] of water molecules. A dashed line shows the calculated EISF as per the model based on isotropic rotation just for comparison.

**Table 6.3** Fraction of water molecules taking part in the dynamics ( $p_x$ ) and localization radius of sphere ( $a$ ) for PB ( $\text{Fe}_4(\text{II})[\text{Fe}(\text{II})(\text{CN})_6]_3 \cdot 14\text{H}_2\text{O}$ ), PBA-I ( $\text{Fe}_4(\text{II})[\text{Fe}(\text{II})(\text{CN})_6]_4 \cdot 16\text{H}_2\text{O}$ ) and PBA-II ( $\text{Cu}_2\text{Mn}_2[\text{Fe}(\text{CN})_6]_{2.67} \cdot 19\text{H}_2\text{O}$ ) as obtained from the least square fitting of the data (Fig. 6.19) with a model discussed in the text, in the temperature range 260-360 K.

S.No	T (K)	Fraction of mobile water ( $p_x$ )			$a$ (Å)		
		PB	PBA-I	PBA-II	PB	PBA-I	PBA-II
1	260	0.56	0.31	0.30	2.90	2.64	3.0
2	280	0.65	0.32	0.40	2.94	2.64	2.80
3	300	0.73	0.41	0.51	2.96	2.64	2.80
4	330	0.80	0.45	0.63	2.95	2.67	2.82
5	360	0.85	0.46	0.70	3.0	2.64	2.80

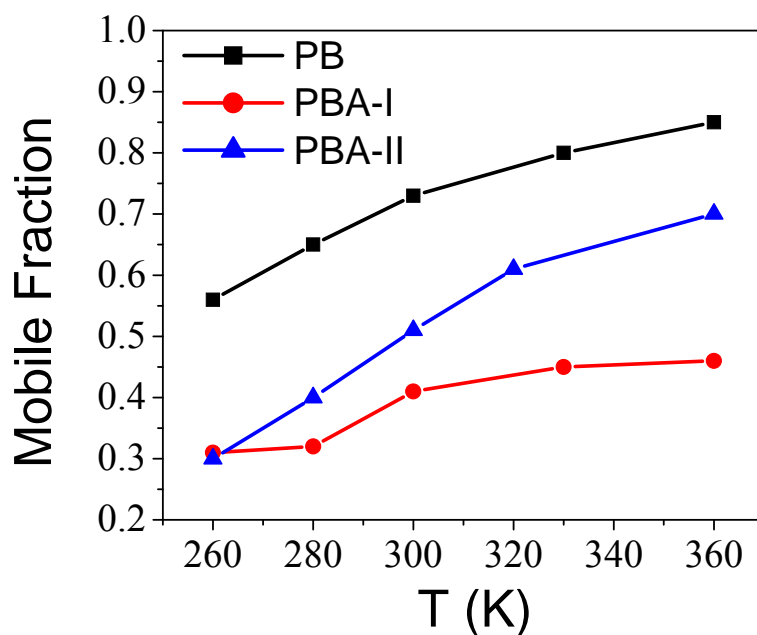


**Fig. 6.20** Variation of fraction of water molecules taking part in the dynamics in PB ( $\text{Fe}_4(\text{II})[\text{Fe}(\text{II})(\text{CN})_6]_3 \cdot 14\text{H}_2\text{O}$ ), PBA-I ( $\text{Fe}_4(\text{II})[\text{Fe}(\text{II})(\text{CN})_6]_4 \cdot 16\text{H}_2\text{O}$ ) and PBA-II

( $\text{Cu}_2\text{Mn}_2[\text{Fe}(\text{CN})_6]_{2.67} \cdot 19\text{H}_2\text{O}$ ) as obtained from the model fit in the temperature range 260–360 K.

The most likely picture emerging from the data analysis is that in PBA-I ( $x/y=1$ ), which has only one kind of water molecules (non-coordinated at 32f site), only a small fraction is mobile. This might be due to the difference in local structure of 32f site. Fraction of mobile water molecules does not change much with the temperature and even at 360 K (highest measured temperature), more than 50 % of water molecules remain immobile. However, in PB and PBA-II ( $x/y>1$ ), there exists three kinds of water molecules, the first kind is the coordinated water molecules located at 24e site (on the surface of the cavity formed by vacant  $\text{Fe}(\text{CN})_6$  units) and do not participate in the dynamics at low temperature. The second kind is the non-coordinated water molecules residing at the 8c ( $1/4, 1/4, 1/4$ ) interstitial sites (i.e. outside the cavity) and most of these water molecules remain immobile even at highest measured temperature. The third kind of water molecules is non-coordinated at 32f sites (i.e., inside the cavity formed by vacant  $\text{Fe}(\text{CN})_6$  units) confined in the spherical cavity ( $d \sim 5.1 \text{ \AA}$ ) undergoing localised translational motion. Dynamics of the coordinated water molecules evolve with increase of temperature as found in PB and PBA-II where fraction of mobile water molecules increases significantly with the temperature. For example, in PBA-II, fraction of mobile water molecules,  $p_x$  as extracted from the QENS data is found to be 30% at 260 K. Interestingly, if the non-coordinated water molecules which lie inside the cavity only be dynamic (6 out of total 19 molecules in the formula unit), one can expect the value of  $p_x$  to be  $\sim 30 \%$ . As the temperature increases, coordinated water molecules gain enough thermal energy to break the coordination (bonding from 3d element) and participate in the dynamics. It has been shown that in  $(\text{Co}_x\text{Mn}_{1-x})_{1.5}[\text{Fe}(\text{CN})_6] \cdot z \text{H}_2\text{O}$ , the coordination geometry of  $\text{Co}^{\text{II}}$  changes from a 6-fold coordination to 4 fold due to desorption of coordinated water molecules from Co/Mn sites which results change the magnetic interaction



between ferromagnetic and antiferromagnetic coupling [144]. At 360 K,  $p_x$  is found to 70 % as extracted from the QENS data. This is feasible, if all the coordinated water molecules participate in the dynamics along with non-coordinated ones that lie inside the cavity (that amounts to 14 out of total 19 molecules), then one can expect the value of  $p_x$  to be  $\sim 70$  %. Therefore, one can infer that at low temperature most of the mobile water molecules in Prussian blue or its analogues having cavities ( $x/y > 1$ ) corresponds to those present inside the cavities (non-coordinated at 32 f site). As temperature increases, coordinated water molecules located at 24e site start to participate in the dynamics and at high enough temperature ( $\sim 360$  K) all the immobile water molecules correspond to non-coordinated water molecules at 8c site (outside the cavities).

The variations of the HWHM of QE component ( $\Gamma$ ) as a function of  $Q$  for PB, PBA-I and PBA-II at different temperatures are shown in Fig. 6.21. As can be seen from the figure, the QE width ( $\Gamma$ ) is more or less constant up to a limiting  $Q$  value ( $\sim 1.0 \text{ \AA}^{-1}$ ) and then increases. It is very clear that the variation of the QE width is very different than that observed in bulk water [18] or water in nanoporous polyamide membranes [114-116] (as discussed earlier). In case of bulk water, HWHM increases linearly with  $Q^2$  and then saturates to a constant value indicating a dynamics typified by jump diffusion (Chapter 1, section 1.1.4.2). In the present case, the HWHM shows significantly different behaviour at low  $Q$  than that of bulk water. At lower  $Q$  ( $Qa < \pi$ ), i.e., when larger distances are probed, behavior of HWHM approaches a constant value, which is independent of  $Q$ . This is due to the fact that in this length scale, confining cavity boundaries manifest themselves and the water molecules are seen to perform localised dynamics. Therefore, behaviour of quasielastic width in this  $Q$  range resembles that of rotational model. However, at larger  $Q$  values ( $Qa > \pi$ ), where small distances are probed, usual  $DQ^2$  behaviour corresponds to translational motion in

an infinite medium is recovered since in this length scale, i.e., when probed inside the cavity, confined wall boundaries are not seen.

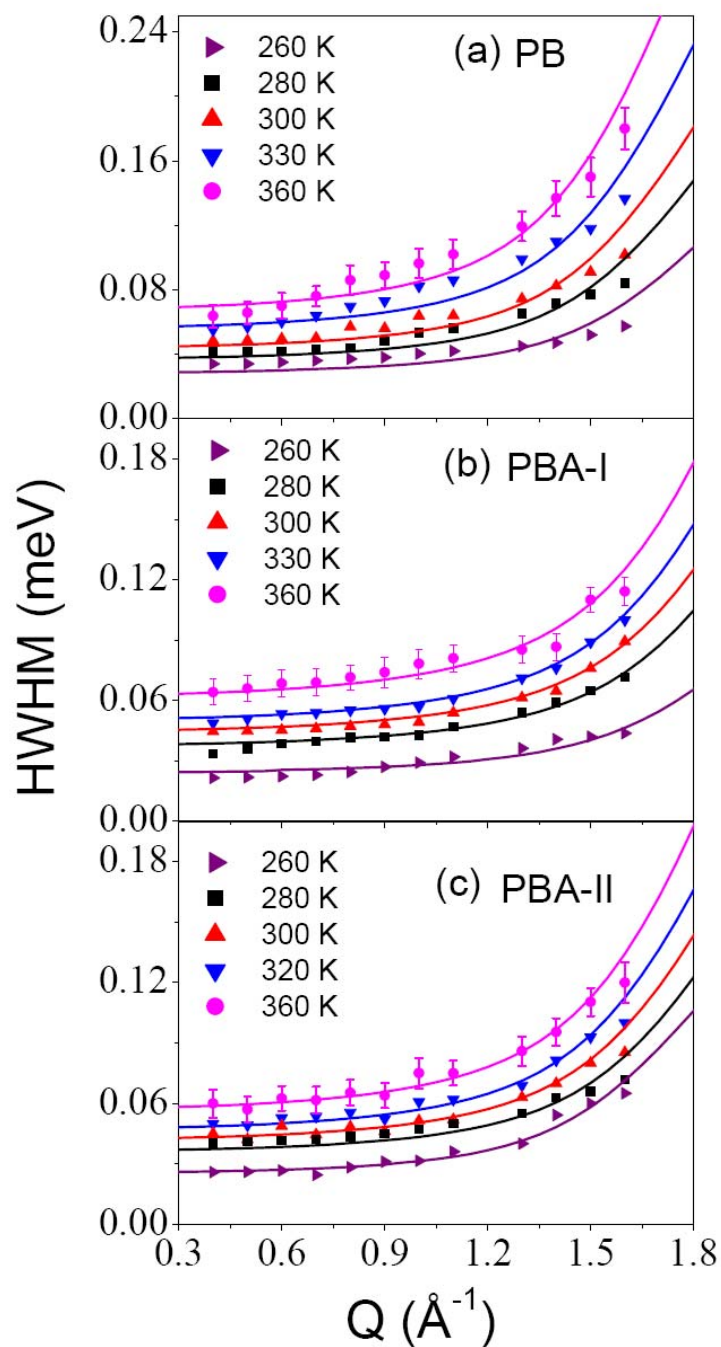


**Fig. 6.21** Variation of half width at half maxima (HWHM) of a Lorentzian representing water dynamics in (a) PB ( $\text{Fe}_4(\text{II})[\text{Fe}(\text{II})(\text{CN})_6]_3 \cdot 14\text{H}_2\text{O}$ ), (b) PBA-I ( $\text{Fe}_4(\text{II})[\text{Fe}(\text{II})(\text{CN})_6]_4 \cdot 16\text{H}_2\text{O}$ ) and (c) PBA-II ( $\text{Cu}_2\text{Mn}_2[\text{Fe}(\text{CN})_6]_{2.67} \cdot 19\text{H}_2\text{O}$ ) with  $Q$ . Solid

lines are the fit with a model based on localized translational diffusion as described in Eq. (6.10).

The model scattering function for the water molecules performing localised translational diffusion inside a spherical cavity can be given as (Chapter-1, section 1.1.4.3)

$$S(Q, \omega) = (1 - p_x) \delta(\omega) + p_x \left[ A_0^0(Qa) \delta(\omega) + \frac{1}{\pi} \sum_{\{l,n\} \neq \{0,0\}} (2l+1) A_n^l(Qa) \frac{(x_n^l)^2 D_{loc} / a^2}{\left[ (x_n^l)^2 D_{loc} / a^2 \right]^2 + \omega^2} \right] \quad (6.10)$$

Here, the first term represents the elastic contribution due to immobile water molecules. Second term represents the scattering function for localised translational diffusion weighted by the fraction of mobile water molecules. Here,  $D_{loc}$  is the localised diffusion coefficient and  $x_n^l = a \sqrt{\lambda_n^l}$  are dimensionless numbers, values of first 99 are tabulated in ref. [19].  $A_n^l(Qa)$  for different  $n$  and  $l$  can be calculated by using the expression given in ref. [19]. In the limit  $Qa \rightarrow \infty$ , the second term of Eq. (6.10) reduces to a scattering law for translational motion (a single Lorentzian) in infinite medium.

Since no analytical expression exists for the HWHM of the quasielastic part unlike that in case of EISF, the HWHM can be calculated numerically (using Eq. 6.10) for given values of  $a$  and  $D_{loc}$ . The least-squares fitting method is used to describe the observed QE width with  $D_{loc}$  as parameter while the values of  $a$  are already known from the fit of the EISF. Fig. 6.21 shows the fit of the QE widths as obtained assuming the localised translational diffusion model to describe the dynamics of water in the PB, PBA-I and PBA-II respectively. Obtained value of diffusion coefficient at each temperature for all the systems are given in Table 6.4. It is found that dynamics of water molecules in PBA-I ( $x/y=1$ ) is more hindered compared to PB and PBA-II ( $x/y>1$ ). While comparing between PB and PBA-II, both the systems have cavities however diffusivity of water is larger in PB vis-à-vis PBA-II.

This may be due to loose binding of water molecules in PB vis-à-vis PBA-II as suggested by thermogravimetric measurements as discussed later. Diffusion coefficient of water in all the systems increase with the temperature as expected for a thermally activated motion. The variation of diffusion constant with temperature is shown in Fig. 6.22. Activation energy for diffusion of water in each system is obtained from the Arrhenius plot of  $D_{loc}$  vs. temperature (Fig. 6.22). Activation energy for water diffusion in PBA-I (7.40 KJ/mol) is found to be higher than PBA-II (6.11 KJ/mol) and PB (7.11 KJ/mol).

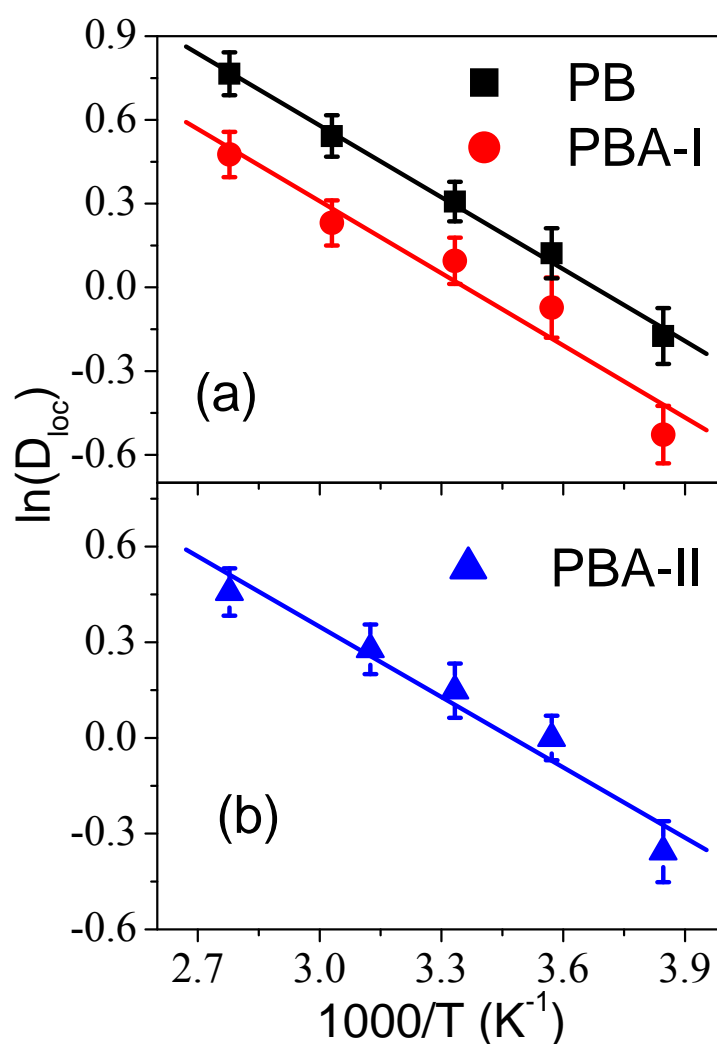


**Fig. 6.22** Variation of localized diffusion constant ( $D_{loc}$ ) of water in (a) PB( $Fe_4(II)[Fe(II)(CN)_6]_3 \cdot 14H_2O$ ) and PBA-I ( $Fe_4(II)[Fe(II)(CN)_6]_4 \cdot 16H_2O$ ) and (b) PBA-II

( $\text{Cu}_2\text{Mn}_2[\text{Fe}(\text{CN})_6]_{2.67} \cdot 19\text{H}_2\text{O}$ ) in the temperature range 260–360 K. Arrhenius behaviour is evident within the measured temperature range.

Results are also compared with the thermo gravimetric measurements. Fig. 6.23 shows the thermograms of PB, PBA-I and PBA-II. In PB, both coordinated and non-coordinated waters are weakly bonded, and under the heating the crystal water evolves at a relatively low temperature below 100°C. The thermogram of PBA-I ( $x/y=1$ ) is different from that of PB or PBA-II ( $x/y>1$ ). It is found that PB and PBA-II show sharp weight loss compared to PBA-I indicating that water molecules are relatively loosely bound in PB and PBA-II. While comparing in PB and PBA-II, it is found that weight loss is sharper in PB compared to PBA-II. Results are consistent with the QENS measurement, which indicates that more fractions of water molecules are mobile with high diffusivity in PB compared to PBA-I and PBA-II.

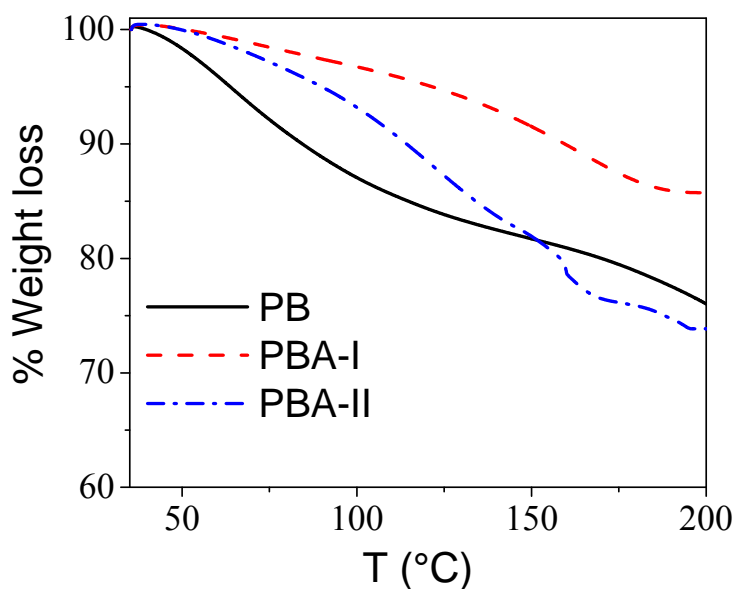


**Fig. 6.23** Thermo-gravimetric curves for  $\text{PB}(\text{Fe}_4(\text{II})[\text{Fe}(\text{II})(\text{CN})_6]_3 \cdot 14\text{H}_2\text{O})$ ,  $\text{PBA-I}(\text{Fe}_4(\text{II})[\text{Fe}(\text{II})(\text{CN})_6]_4 \cdot 16\text{H}_2\text{O})$  and  $\text{PBA-II}(\text{Cu}_2\text{Mn}_2[\text{Fe}(\text{CN})_6]_{2.67} \cdot 19\text{H}_2\text{O})$  compounds. Sharp loss in weight of PB compared to PBA-I and PBA-II is evident.

Results are compared with the recent QENS study on dynamics of water confined in NaX and NaA zeolites [148]. Both mobile and immobile water molecules are found to coexist in these systems as well. In these zeolites, fraction of mobile water molecules was seen to increase with temperature in the low temperature regime and was found to be constant at higher temperatures. Most of the immobile water molecules corresponds to those present in the  $\beta$  cages of the zeolite and are in the vicinity of the charged surface and cations of zeolites. It is also found that at higher temperatures, most of the water molecules in the  $\alpha$  cages are mobile. These two types of water molecules showed different dynamical behaviours similar to the present system. This indicates that not only the bonding but also the physical environment is important in determining dynamics of water molecules in such a system.

**Table 6.4** Localised Diffusion coefficients,  $D_{loc}$  of water in  $PB(Fe_4(II)[Fe(II)(CN)_6]_3 \cdot 14H_2O)$ , PBA-I ( $Fe_4(II)[Fe(II)(CN)_6]_4 \cdot 16H_2O$ ) and PBA-II ( $Cu_2Mn_2[Fe(CN)_6]_{2.67} \cdot 19H_2O$ ) compounds as obtained from the least square fitting of the data (Fig. 6.21) with the localised translational diffusion model as discussed in the text.

T (K)	$D_{loc}(\times 10^{-5} \text{ cm}^2/\text{s})$		
	PB	PBA-I	PBA-II
260	0.84	0.59	0.7
280	1.13	0.93	1.00
300	1.36	1.1	1.16
330	1.72	1.26	1.32
360	2.15	1.6	1.6

## 6.4. CONCLUSIONS

Dynamics of water in nanoporous reverse osmosis (RO) and nanofiltration (NF) polyamide membranes as studied using quasielastic neutron scattering (QENS) technique are reported [114-117]. Both RO and NF polyamide membrane are synthesized using interfacial polymerization techniques and widely used for water treatments. Both membranes are characterized using scanning electron microscope (SEM) and positron annihilation lifetime spectroscopy (PALS) techniques. SEM pictures indicate that NF polyamide membrane has relatively smoother surface microstructure compared to RO polyamide membrane, which has relatively rough surface, showing hill–valley microstructure morphology. PALS measurement shows that both membranes consist of pore of size  $\sim 5$  Å although density of pores is found to be larger in NF membrane (10.49%) compared to RO membrane (2.34%). QENS measurements have been carried out on both water sorbed RO and NF polyamide membranes. QENS experiments have also been carried out on both dehydrated membranes. Significant quasielastic (QE) broadening is observed for water sorbed RO and NF membranes over the instrument resolution whereas no QE broadening is observed for dehydrated samples. QENS data show that translational motion got modified due to the confinement effect while the rotational motion did not. Jump diffusion model with random distribution of jump lengths was found to describe the translational motion of adsorbed water in both the membranes.

Dynamics of crystal-water in Prussian Blue (PB;  $\text{Fe}_4(\text{II})[\text{Fe}(\text{II})(\text{CN})_6]_3 \cdot 14\text{H}_2\text{O}$ ) and its analogues PBA-I ( $\text{Fe}_4(\text{II})[\text{Fe}(\text{II})(\text{CN})_6]_4 \cdot 16\text{H}_2\text{O}$ ) and PBA-II ( $\text{Cu}_2\text{Mn}_2[\text{Fe}(\text{CN})_6]_{2.67} \cdot 19\text{H}_2\text{O}$ ) based molecular magnet have been investigated using QENS technique [149,150]. It is found that dynamical behaviour of the water molecules depends on the location of them in the crystal lattice. In PB and PBA-II, the water molecules are located at 8c, 24e and 32f crystallographic sites. Further, spherical cavities are created due to the vacant sites by the absent  $\text{Fe}(\text{CN})_6$  units. The 24e and 32f sites are located inside the cavity

and the water molecules at 24e are coordinated and 32f are non-coordinated. The site 8c lies outside the cavity and the water molecules are non-coordinated. However, in PBA-I, which does not have any vacant  $\text{Fe}(\text{CN})_6$  units, has only one kind of water molecules, these are non-coordinated and located at 32f crystallographic sites. It is found that in case of PB, QE broadening is large compared to PBA-I and PBA-II. In all the compounds, QE broadening is found to be temperature dependent and increases on increase of temperature. However, in case of PB and PBA-II, increase in QE broadening is more prominent than PBA-I. The observed data could be described well assuming localized translational diffusion model. Dynamics of water in PBA-I, which does not have any vacant  $\text{Fe}(\text{CN})_6$  units is found to be much hindered vis-à-vis PB and PBA-II. Fraction of mobile water molecules in PBA-I does not change much with the temperature and even at 360 K, more than 50 % of water is found to be immobile. However, in case of PB and PBA-II, fraction of mobile water molecules increases sharply with the temperature. This may be due to the fact that coordinated water molecules, immobile at low temperature, may start to participate in the dynamics at high temperature. Non-coordinated water molecules inside the spherical cavities are found to be mobile at all measured temperatures. For example, in case of PBA-II, while ~30 % of the water molecules contribute to the dynamics at 260 K which goes up to ~70% at 360 K. Data analysis showed that the dimension of the dynamical regime within which the water molecules are confined correspond to the diameter of the spherical cavity mentioned above. At low temperatures, non-coordinated water molecules contribute to the dynamics and with increase of temperature the coordinated ones become dynamic progressively. Diffusion coefficients as obtained from the data analysis found to follow Arrhenius law with activation energy 7.11, 7.40 and 6.11 KJ/mol for PB, PBA-I and PBA-II respectively.

Effect of confinement on dynamics of water in different systems such as polyamide membranes, Prussian blue and its analogues based molecular magnet are studied. It is found



that dynamics of water is very different than bulk water. Furthermore, it is found to be quite complex and depend on many factors such as host structure, guest-host interaction, temperature and so forth. Next chapter which is based on the discussion on dynamics of different guest molecules confined in zeolitic framework will throw more light on these factors and their effect on the dynamics of confined fluid.

## **CHAPTER 7**

# **Dynamics of Adsorbed Molecules in Nanoporous Zeolitic Framework**

### **7.1. INTRODUCTION**

Zeolites are crystalline microporous aluminosilicates, well known for their molecular sieving cation exchange and catalytic properties and are used extensively in petrochemical & refining industries [151,152]. One of the most unique cation exchange properties of zeolites that is used for purification of water is that of removing dissolved cations (e.g.  $\text{NH}_4^+$ ) which are not favourable to human or animal health by exchanging with biologically acceptable cations such as  $\text{Na}^+$ ,  $\text{Mg}^{+2}$  etc. Because of their acid strength and shape selectivity, zeolites offer a wide range of catalytic applications also in the petrochemical industry. One particular reaction, which is of immense interest to the automobile industry, is the selective catalytic reduction of nitric oxide (NO). In a review on this topic, Amiridis et al [153] have highlighted the fact that unsaturated hydrocarbons (e.g., propylene) under excess oxygen condition inside a ZSM5 zeolite pore have a tremendous potential in reducing NO.

Diffusion of adsorbed guest molecules in zeolites, determines the performance of zeolitic materials in catalytic, sorption, separation and ion exchange applications. Apart from the practical applications, well ordered porous structure of zeolites makes them an ideal tool

to experimentally study the phenomenon of molecular dynamics in confined geometries. Diffusion of adsorbed species depends on many factors that include the host-zeolite interaction, the shape of the host, the volume of the cages and their potential energy landscape, temperature etc [7,8,154-169]. All these make the study of diffusion of hydrocarbons in zeolites interesting and essential. A diffusion anomaly as a function of molecular length in hydrocarbons adsorbed in zeolite was reported earlier [170]. Quasielastic neutron scattering (QENS) [7,8,154-163] and pulsed field gradient NMR [164,165] are the two main experimental techniques to study self-diffusivity of hydrocarbons confined in zeolites pores. During the past three decades molecular dynamics (MD) simulations have been used to study diffusion of guest molecules confined in zeolites [166-170]. Experimental and MD simulation studies are even more powerful when they are used in conjunction with each other. Our group at Solid State Physics Division, Bhabha Atomic Research Centre is using both QENS and MD techniques to study the dynamics of various adsorbed species in the zeolites [7,8, 156-163, 168,169]. Dynamics of benzene [156,157] and cyclohexane [158] adsorbed in ZSM5 zeolite is studied using QENS technique. A network of two different channel systems (straight as well as sinusoidal) typifies the structure of ZSM5 zeolite. There are straight channels with an elliptical cross section of approximately 5.7-5.2 Å running along the crystallographic axis '*b*'. These are intersected by sinusoidal channels with nearly circular cross section of 5.4 Å in the '*a-c*' plane as shown in Fig. 7.1 (a). The resulting intersections are elongated cavities up to 9 Å in diameter. In both cases, only rotational motion was observed. This is expected because the size of these molecules (benzene ~ 5.8 Å and cyclohexane ~6 Å) is large compared to the channel dimension (~5.4 Å) of ZSM5 zeolite, making it difficult for these molecules to transport in channels and therefore they are trapped at intersection of channels (9 Å), undergoing rotational motion in the time scale of a few picoseconds. There might be translational motion within intersection of channels but that is

expected to be very slow and hence not observable in QENS technique. Further it was found that cyclohexane performs 3-fold jump rotational motion whereas benzene molecule 6-fold jump rotation. Thus symmetry of the molecular species has also been found to play an important role in deciding the dynamical properties of the adsorbed molecules. Dynamics of different hydrocarbons such as propane [7,8], acetylene [159,160,168], 1,3 butadiene [161,169] and propylene [162,163,171] confined in Na-Y zeolite have been studied using QENS and MD simulation techniques by our group. Unlike ZSM5, a network of almost spherical supercages, which are interconnected with each other in a tetrahedral manner by 12 membered oxygen rings forming windows, characterizes Na-Y zeolite. The diameter of these windows is about 7.8 Å while the supercages themselves have a diameter of 11.8 Å. It is found that translational motion of guest molecules is actually a multi component process and the dynamics observed in QENS experiment is just one part of the complex dynamics.

Dynamics of propylene in ZSM5 zeolite as studied using QENS and MD simulation technique is discussed in this chapter. To probe the effect of guest-host interaction, QENS study on another guest species ethylene glycol (EG) in ZSM5 zeolite is also discussed in this chapter. The details of the experiments and simulation are given in section 7.2 and 7.3 respectively. Results and discussions of dynamics of propylene in ZSM5 zeolite are discussed in section 7.4.1. Results and discussion of dynamics of ethylene glycol in ZSM5 are discussed in section 7.4.2. The conclusions are depicted in section 7.5.

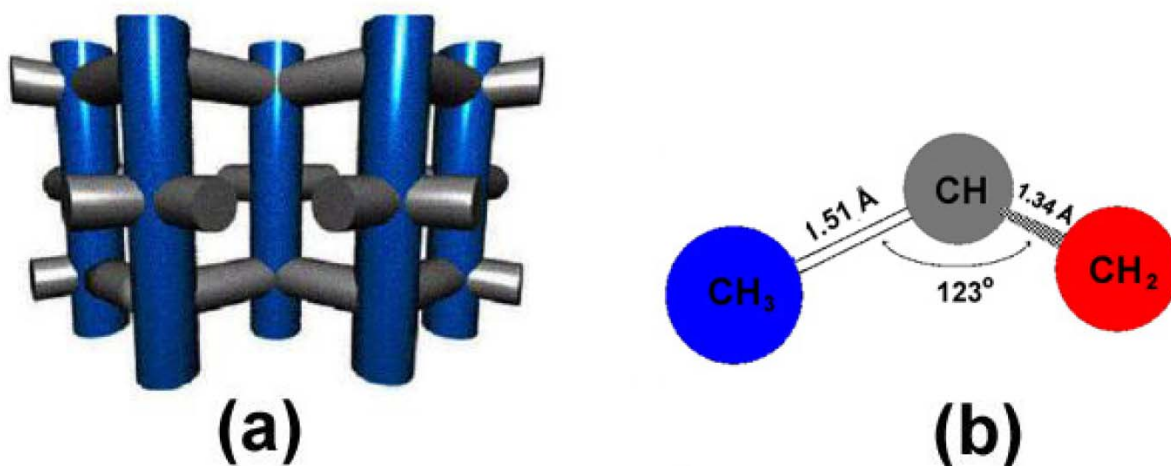


**Fig. 7.1** (a) Straight and sinusoidal channel structure of ZSM5 zeolite (b) Propylene molecule as a united atom model as used in simulation.

## 7.2. EXPERIMENTAL DETAILS

The ZSM5 samples used in the QENS study were obtained from Sud-Chemie. For ascertaining crystalline nature of the samples, we have carried out X-ray diffraction, which revealed that the sample is crystalline with a high degree of order. The zeolite samples were put in two flat rectangular aluminum sample cells and dehydrated by evacuating for a period of about 48 hours at a temperature 573 K under vacuum ( $10^{-5}$  torr). One of them was loaded with propylene gas (purity > 99.99%) to saturation at ambient pressure. QENS measurements were performed for both dehydrated (bare) zeolite and zeolite with propylene gas. Two instruments having different energy windows, MARX spectrometer and Triple Axis Spectrometer (TAS) at Dhruva, Trombay were used to record the QENS spectra. Details of both spectrometers are discussed in section 1.2.1 and 1.2.2 respectively. MARX spectrometer has an energy resolution of  $\sim 200$   $\mu\text{eV}$  with incident energy of 5.1 meV as obtained from standard vanadium sample. The wave vector transfer ( $Q$ ) range covered is  $0.67\text{-}1.8$   $\text{\AA}^{-1}$ . The TAS was used in inverted geometry in which incident energy  $E_i$  was varied and final energy

was kept fixed at  $E_f = 20$  meV. In this configuration, this has energy resolution  $\sim 3$  meV in the  $Q$  range  $0.8\text{-}2.5 \text{ \AA}^{-1}$ . QENS experiments have been also carried out on EG sorbed in ZSM5 zeolite at 300 K using MARX spectrometer. Data from the bare zeolite were used to estimate the contribution from the bare zeolite.

### 7. 3. MD SIMULATION DETAILS

MD simulation of propylene molecules confined in ZSM5 zeolite at saturation loading ( $\sim 8$  molecules per unit cell) has been carried out in the micro-canonical ensemble. Atomic positions of ZSM5 zeolite as reported by Koningsveld et al [172] have been used in the simulation. The simulation cell consists of  $(2 \times 2 \times 2)$  unit cells of ZSM5 zeolite with size of  $40.044 \times 39.798 \times 26.766 \text{ \AA}$ . Test runs made with larger system sizes did not lead to significant changes in the results. Periodic boundary conditions as discussed in section 1.3.3 of chapter 1 are used in all three directions. The framework of zeolite is assumed to be rigid since earlier study showed that flexibility of the framework has a marginal effect on the diffusivity of the guest molecules at higher loadings [173]. Therefore, the framework of zeolite is kept fixed and propylene molecules were allowed to move during the simulation. Propylene molecule was modelled as three interacting sites ( $\text{CH}_3\text{-CH-CH}_2$ ) under united atom model making an angle of  $123^\circ$  as shown in Fig. 7.1 (b). The propylene is considered as a rigid molecule and therefore the bond angle and bond lengths between the sites are kept constant throughout the simulation. The rotational degrees of freedom are modelled using quaternion formalism [32]. Equations of motions for both translational and rotational motion are integrated using the leapfrog form of the Verlet algorithm. A simulation time step of 1 fs was used in the simulation, which gave good energy conservation. The temperature of the system was adjusted to 300 K at each step for the first 300ps. Subsequently production run of 1.3 ns was carried out.

Intermolecular interactions were modelled by Lennard-Jones (6-12) potential. The guest-guest as well as the guest-zeolite interaction could thus be written as

$$\Phi(r_{ij}) = 4\varepsilon_{ij} \left[ \left( \frac{\sigma_{ij}}{r_{ij}} \right)^{12} - \left( \frac{\sigma_{ij}}{r_{ij}} \right)^6 \right] \quad (7.1)$$

where  $\Phi$  is the potential between the interacting species  $i$  and  $j$ , separated by a distance  $r_{ij}$ . The interaction parameters  $\varepsilon_{ij}$  and  $\sigma_{ij}$  used in the simulation are as available in the literature [174,175]. The Lorentz –Berthelot combination rule was used to obtain the cross or mixed terms. A cutoff radius of 13 Å is employed for guest-guest and guest-zeolite interaction.

## 7.4. RESULTS AND DISCUSSION

### 7.4.1 Dynamics of Propylene in ZSM5 Zeolite

The quasielastic spectra were recorded for both bare and propylene-loaded ZSM5 zeolite samples on MARX spectrometer ( $\Delta E \sim 200 \mu\text{eV}$ ) at Dhruva, India. Significant quasi elastic broadening was observed in case of propylene loaded zeolite sample whereas the bare zeolite did not show any broadening over the instrument resolution. Thus, this broadening is related to the dynamical motion of propylene molecules adsorbed in ZSM5 zeolite. The bare zeolites spectra were used to estimate the elastic contribution from the zeolites alone. To analyse the data, elastic and quasielastic contributions to QENS spectra were separated using the general scattering law as described in Eq. (1.74). It was found that elastic part due to the adsorbed propylene is insignificant and a single Lorentzian function fits the data very well (Fig. 7.2).

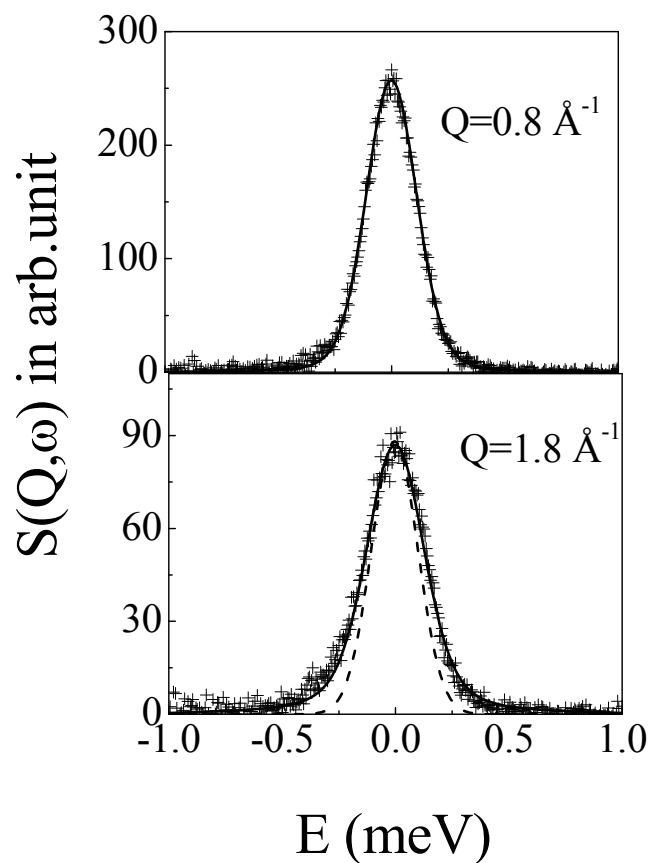


**Fig. 7.2** Fitted QENS spectra from the propylene adsorbed in ZSM5 zeolite using MARX spectrometer at some typical  $Q$  values. Instrument resolution is shown by dashed line.

Therefore, it could be concluded that the observed dynamics is related to pure translation motion of the propylene molecules. Variation of observed HWHM of the Lorentzian ( $\Gamma_T$ ) with  $Q^2$  is shown in Fig. 7.3.

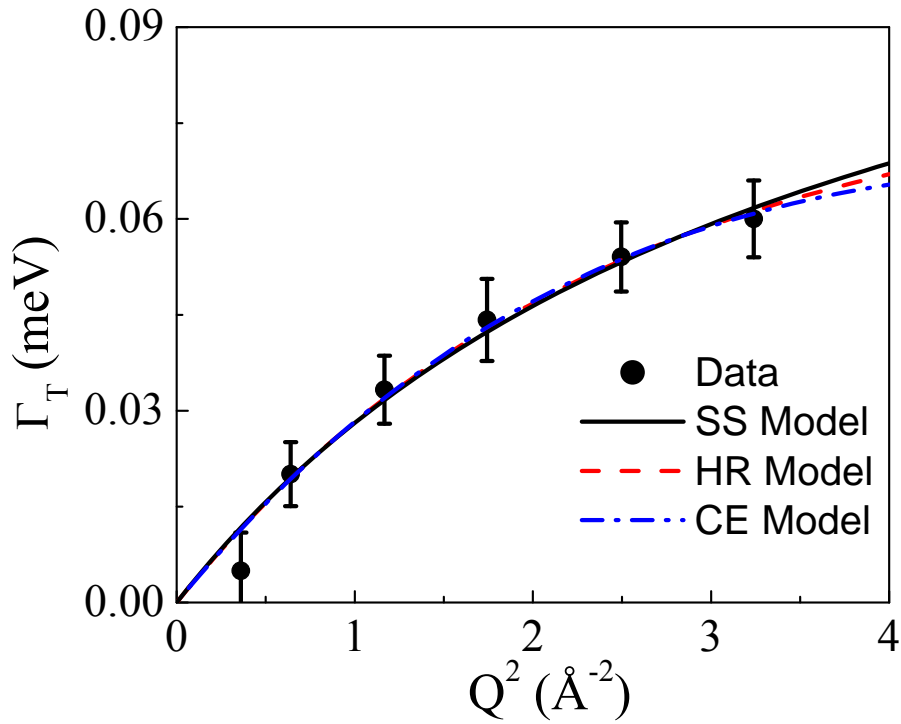


**Fig. 7.3** Variation of HWHM ( $\Gamma_T$ ) with  $Q^2$ . The lines correspond to the fit assuming different models as described in the text.

In case of simple Brownian diffusion the variation of  $\Gamma_T$  with  $Q^2$  is expected to be linear. Here  $\Gamma_T$  values seem to be saturated at higher  $Q$  values, which is an indication of jump diffusion mechanism. In jump diffusion, it is assumed that diffusion occurs through jumps, i.e., for a time interval  $\tau$ , a species remains at a given site, oscillating about the center of equilibrium and after it moves to another site in a negligible time. The time  $\tau$ , spent at a given site is called the residence time. Several different models of jump diffusion can be envisaged differing in the distribution of jump lengths, viz. Chudley and Elliott (CE), Singwi and Sjölander (SS) and Hall and Ross (HR) models which are the plausible ones for the present situation.

As discussed in section 1.1.4.2 of chapter1, in Chudley and Elliott model, molecules are assumed to undergo jumps of a fixed length  $l$  i.e., all the jumps are identical and hence



there is no distribution of jump lengths. In this case, behaviour of HWHM of the Lorentzian function can be written as,

$$\Gamma_T(Q) = \frac{6D_T}{l^2} \left[ 1 - \frac{\sin(Ql)}{Ql} \right] \quad (7.2)$$

Singwi and Sjölander in their model, implicitly employed a random jump length distribution, where the variation of HWHM of the Lorentzian function would be,

$$\Gamma_T(Q) = \frac{6D_T Q^2}{(6 + l^2 Q^2)} \quad (7.3)$$

Hall and Ross proposed a situation where the distribution of jump lengths in any direction exhibits a simple Gaussian behaviour. According to Hall and Ross model variation of HWHM of Lorentzian takes the form

$$\Gamma_T(Q) = \frac{6D_T}{l^2} \left[ 1 - \exp\left(-\frac{Q^2 l^2}{6}\right) \right] \quad (7.4)$$

where  $D_T$  is translational diffusion coefficient and  $l$  is the root mean square jump length. All three models mentioned above were tried to fit the experimentally obtained HWHM as shown by the lines in Fig. 7.3. As evident from the figure, all the three models give the similar quality of fit with the QENS data. The parameters, root mean square jump length  $l$ , and translational diffusion coefficient  $D_T$  as obtained from the fits are given in Table 7.1.

Residence time  $\tau$ , can be determined using Einstein relation  $D_T = \frac{l^2}{6\tau}$ .

**Table 7.1** Root mean square jump length ( $l$ ) and translational diffusion coefficient ( $D_T$ ) for propylene in ZSM5 zeolite as obtained from the fits shown in Fig 7.3.

Model	$l$ (Å)	$D_T$ ( $10^{-5}$ cm <sup>2</sup> /sec)
-------	---------	---

CE	1.9	0.50
SS	1.3	0.56
HR	1.6	0.53

If the jump length distribution is very sharp then all the three models look alike. In case of ZSM5 equipotential sites available for a guest molecule are also arranged in a complex but regular manner [176]. This would imply that in zeolites the jump length would not be constant although the spread in the jump length distribution will be very small making all the three distributions cited above look alike. Indeed, it was found that all the models fitted with the QENS data with more or less the same accuracy.

From the MD simulation study, intermediate scattering functions (as discussed in section 1.4.3) corresponding to translational as well as rotational motion of the propylene molecule within channels of ZSM5 zeolite are calculated using Eqs. (7.5) and (7.6) respectively.

$$I^T(Q, t) = \frac{1}{N} \sum_i \overline{\langle \exp[i\mathbf{Q} \cdot (\mathbf{r}_i^{CM}(t + t_0) - \mathbf{r}_i^{CM}(t_0))] \rangle} \quad (7.5)$$

$$I^R(Q, t) = \frac{1}{N} \sum_i \overline{\langle \exp[i\mathbf{Q} \cdot (\mathbf{d}_i(t + t_0) - \mathbf{d}_i(t_0))] \rangle} \quad (7.6)$$

where bar denotes the average over all possible orientations of the  $\mathbf{Q}$  vectors,  $\mathbf{r}_i^{CM}$  is the position vector of the centre of mass of the  $i^{\text{th}}$  propylene molecule with respect to a space fixed reference frame and  $\mathbf{d}_i$  denoting the position of a  $\text{CH}_3$  species in the centre of mass frame.

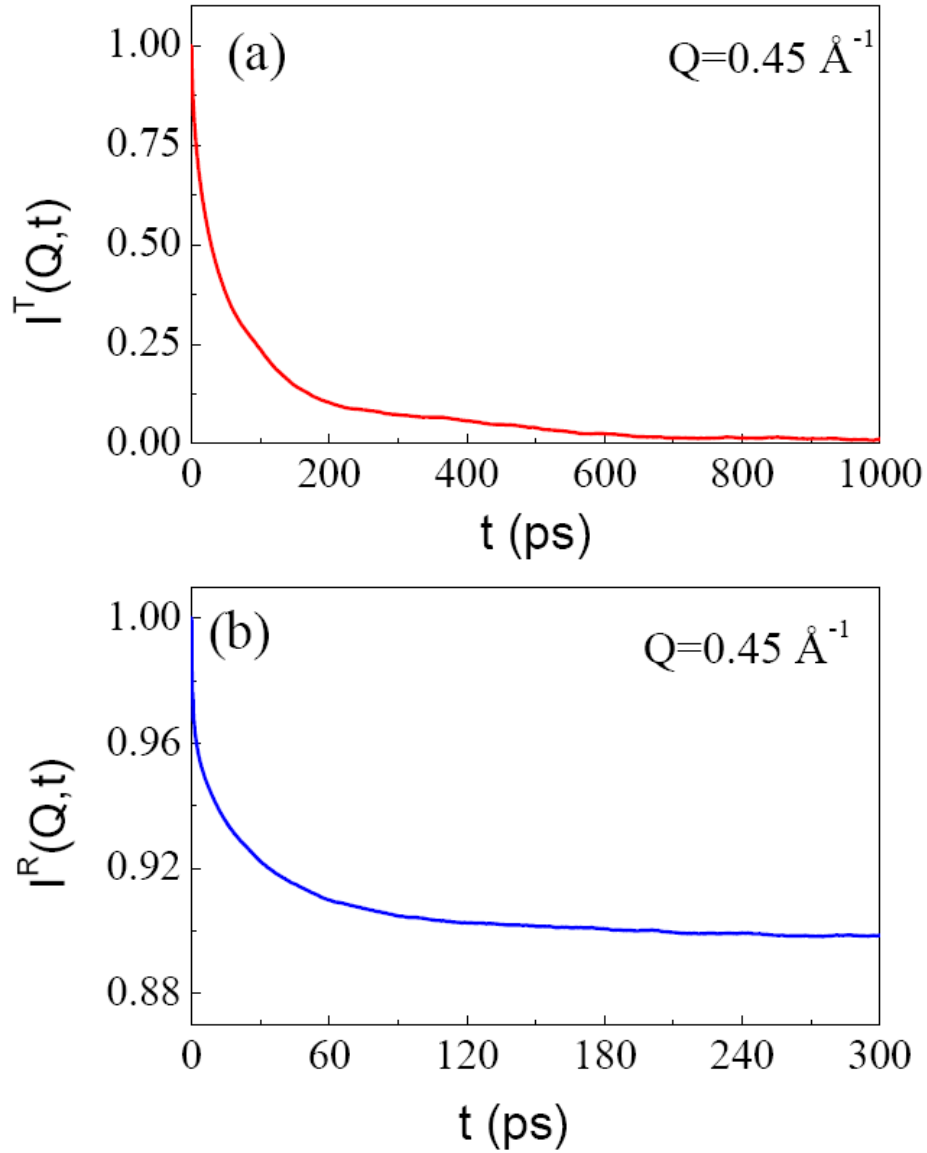


**Fig.7.4** Variation of (a) translational and (b) rotational intermediate scattering functions calculated from MD simulation trajectories with time  $t$  at  $Q=0.45 \text{ \AA}^{-1}$ .

Very different features can be noted from the behaviour of the calculated intermediate functions corresponding to translational and rotational motions as shown in Fig. 7.4(a) and (b) respectively for a typical value of  $Q = 0.45 \text{ \AA}^{-1}$ . The intermediate scattering function corresponds to the rotational motion reaches to a non-zero minimum value within  $t \sim 150$  ps whereas that of the translational motion goes to zero at  $t \sim 900$  ps. The non-zero value of the minimum in case of rotational intermediate scattering function is due to the presence of local

motions. This non-zero value provides information towards EISF as discussed in section 1.4.3. A much faster decay of the rotational component indicates an order of magnitude faster motion than translation. This is corroborative to the fact that rotational motion was not observed in the QENS measurement described above.

To investigate the faster rotational dynamics of propylene molecules adsorbed in ZSM5 zeolite, as predicted by the MD simulation results, QENS experiments have been carried out using another instrument TAS having wider energy resolution ( $\Delta E \sim 3$  meV) at Dhruva, Trombay. Indeed significant quasielastic broadening was observed for the propylene loaded ZSM5 zeolite whereas no broadening was observed for the bare ZSM5 zeolite. Data for the bare zeolite was subtracted from propylene loaded ZSM5 data to get the contribution from the propylene molecules alone. Here both the fast and slow components are expected to contribute to the data and therefore the scattering law would have the contribution from both translation and rotation as a convolution product and can be written as (Chapter 1, Eq. (1.78))

$$\begin{aligned}
 S_{Total}(Q, \omega) &= \left[ B(Q)\delta(\omega) + (1-B(Q))\frac{1}{\pi} \frac{\Gamma_R(Q)}{(\Gamma_R(Q))^2 + \omega^2} \right] \otimes \frac{1}{\pi} \frac{\Gamma_T(Q)}{(\Gamma_T(Q))^2 + \omega^2} \\
 &= \left[ B(Q)\frac{1}{\pi} \frac{\Gamma_T(Q)}{(\Gamma_T(Q))^2 + \omega^2} + (1-B(Q))\frac{1}{\pi^2} \frac{[\Gamma_T(Q) + \Gamma_R(Q)]}{[\Gamma_T(Q) + \Gamma_R(Q)]^2 + \omega^2} \right] \quad (7.7)
 \end{aligned}$$

where  $B(Q)$  is the EISF for rotational motion and  $\Gamma_R$  is HWHM of the half width at half maximum (HWHM) of the Lorentzian function corresponding to rotational motion. The solace is the translational contribution ( $\Gamma_T$ ) is already available from the measurement of the MARX spectrometer and using that as known parameter ( $\Gamma_T$ ), the contribution of the rotational part are evaluated. Eq. (7.7) is used to least squares fit of the measured QENS spectra with the  $B(Q)$  and  $\Gamma_R$  the parameters. It is found that Eq. (7.7) describes the observed

QENS data very well as shown in Fig. 7.5. The EISF,  $B(Q)$  extracted from the fit is shown in Fig. 7.6. Out of the various plausible models that can be envisaged for describing the rotational motion of the propylene adsorbed in ZSM5, isotropic rotational diffusion (Chapter1, section 1.1.5.1),  $B(Q) = j_0^2(Qr)$  describes the experimental EISF very well as evident in Fig. 7.6. Radius of gyration ( $r$ ) is obtained as  $1.91 \pm 0.01 \text{ \AA}$  which is equal to the average distance of all the hydrogen atoms from the center of mass of a propylene molecule.

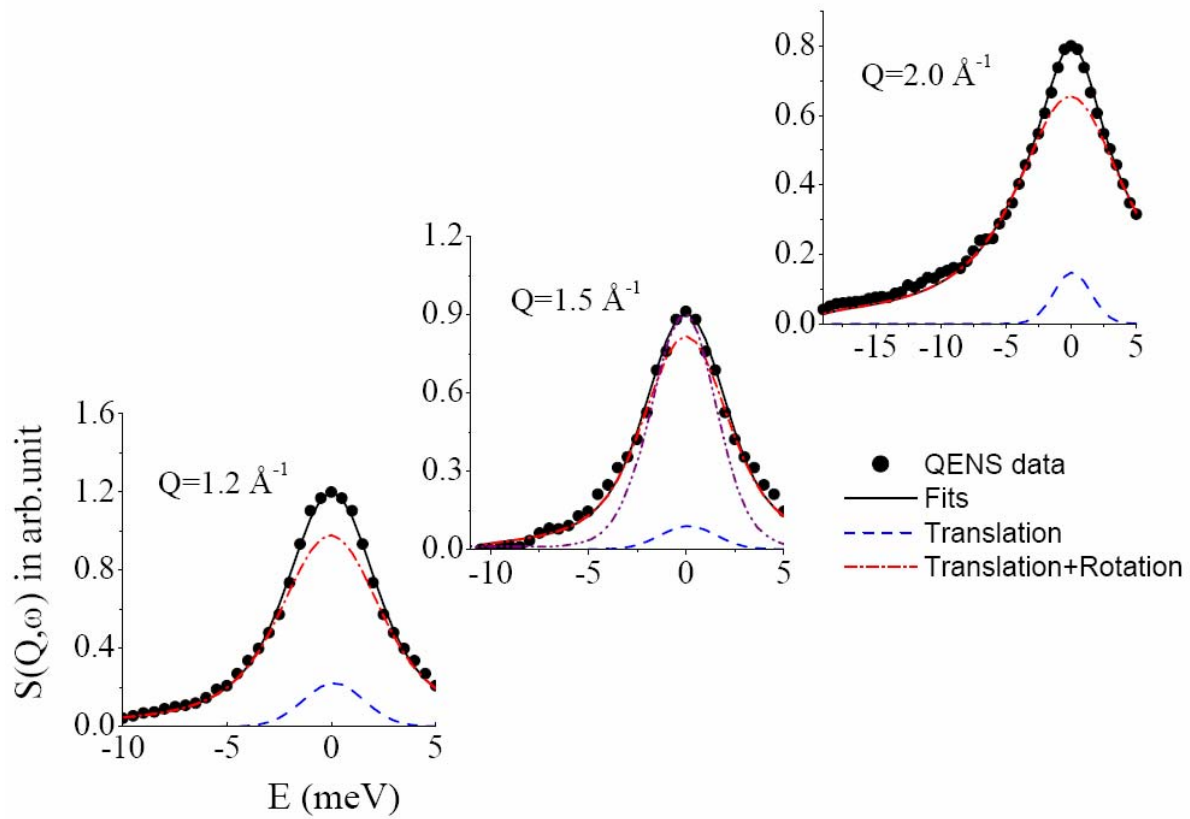


**Fig. 7.5** QENS spectra from the propylene adsorbed in ZSM5 zeolite at TAS at some typical  $Q$ -values. Instrument resolution is shown by dash dot dotted line in middle panel.

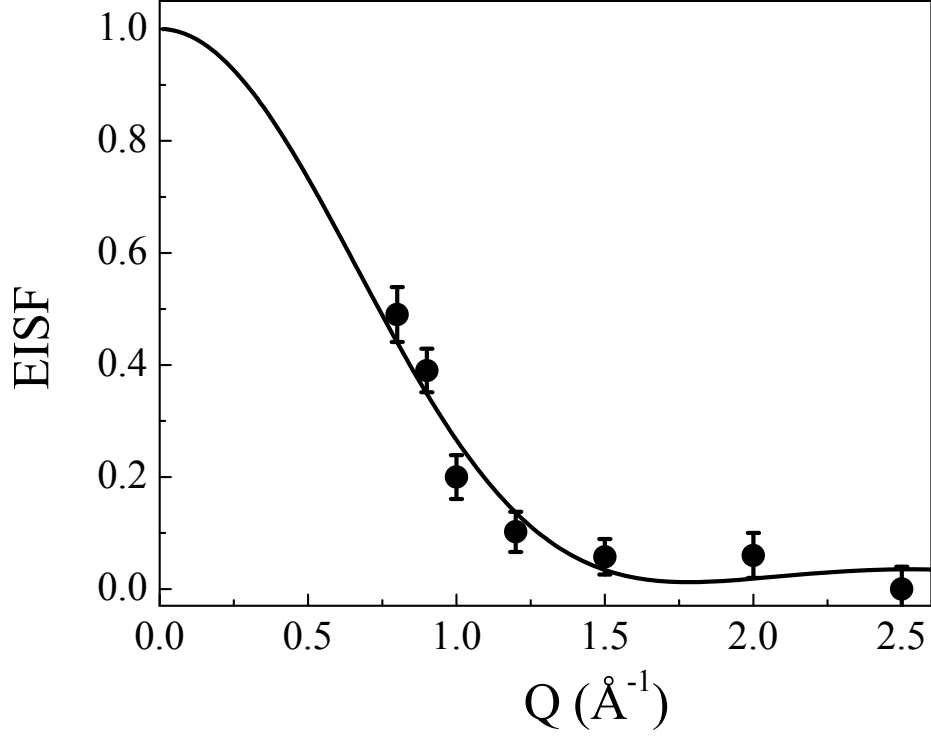


**Fig. 7.6** Variation of EISF for propylene adsorbed in ZSM5 zeolite as obtained from QENS data using TAS with respect to wave vector  $Q$ . The solid line corresponds to the isotropic rotational diffusion model.

The scattering law for isotropic rotational diffusion (Chapter1, section 1.1.5.1) can be written as

$$S_{iso}^R(Q, \omega) = j_0^2(Qr) \delta(\omega) + \frac{1}{\pi} \sum_{l=1}^{\infty} (2l+1) j_l^2(Qr) \frac{l(l+1)D_R}{(l(l+1)D_R)^2 + \omega^2} \quad (7.8)$$

where  $j_l(Qr)$  are the spherical Bessel functions of order  $l$ ,  $r$  is the radius of gyration and  $D_R$  is the rotational diffusion coefficient. Therefore, from Eq. (7.7) and (7.8), total scattering law can be written as

$$S_{Total}(Q, \omega) = j_0^2(Qr) \frac{1}{\pi} \frac{\Gamma_T(Q)}{(\Gamma_T(Q))^2 + \omega^2} + \frac{1}{\pi^2} \sum_{l=1}^{\infty} (2l+1) j_l^2(Qr) \frac{[\Gamma_T(Q) + l(l+1)D_R]}{[\Gamma_T(Q) + l(l+1)D_R]^2 + \omega^2} \quad (7.9)$$

In practice the summation series in the 2<sup>nd</sup> term of Eq. (7.9) can be truncated at those values of  $l$  for which the Bessel functions do not contribute up to  $Q_{max}r$ . In the present case with  $Q_{max}= 2.5 \text{ \AA}^{-1}$  and  $r= 1.91\text{\AA}$  it can be readily seen from Fig. 7.7 that terms above  $l=6$  do not have significant contribution. The experimental spectra were therefore fitted with Eq. (7.9) with the summation truncated after  $l=6$  with least squares fit having  $D_R$  as the parameter. The fitted spectra at typical  $Q$  values are shown in Fig. 7.8. As evident from the figure the model has provided a very good description of the experimental data. Variation of rotational diffusion coefficients obtained from fits is shown in Fig. 7.9. It is found that rotational diffusion coefficient is more or less constant with respect to  $Q$ . An average rotational diffusion coefficient of  $D_R=0.37 \text{ meV}$  is obtained.

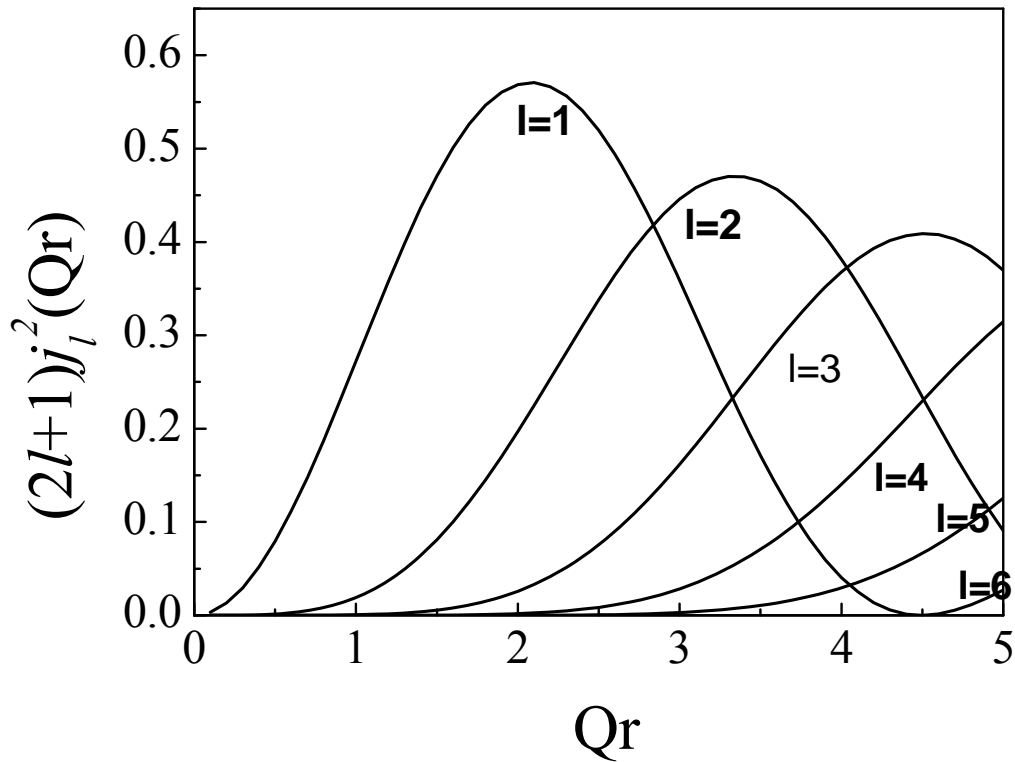


**Fig.7.7** Variation of quasielastic structure factor  $(2l+1)j_l^2(Qr)$  with  $Qr$  at some typical  $l$  values.

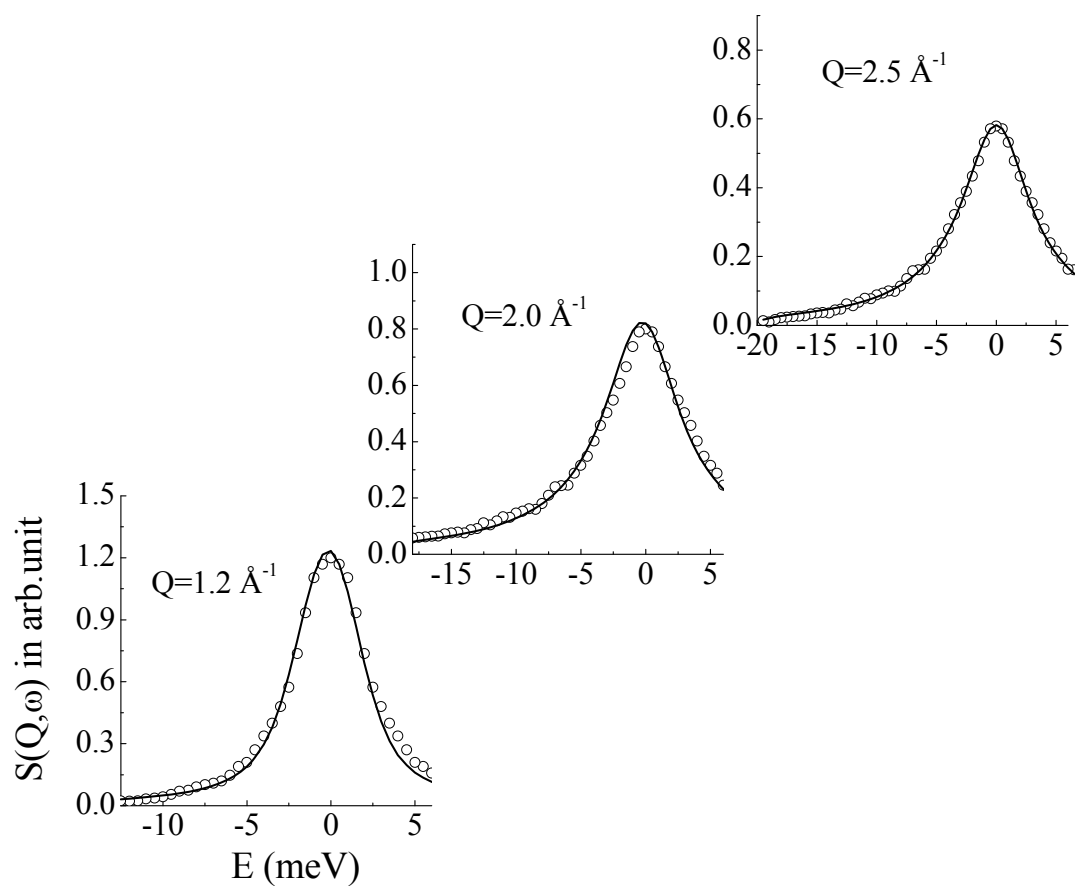


**Fig. 7.8** Typical fitted experimental data observed with TAS assuming isotropic rotational diffusion model for propylene adsorbed in ZSM5 zeolite at some typical  $Q$  values.

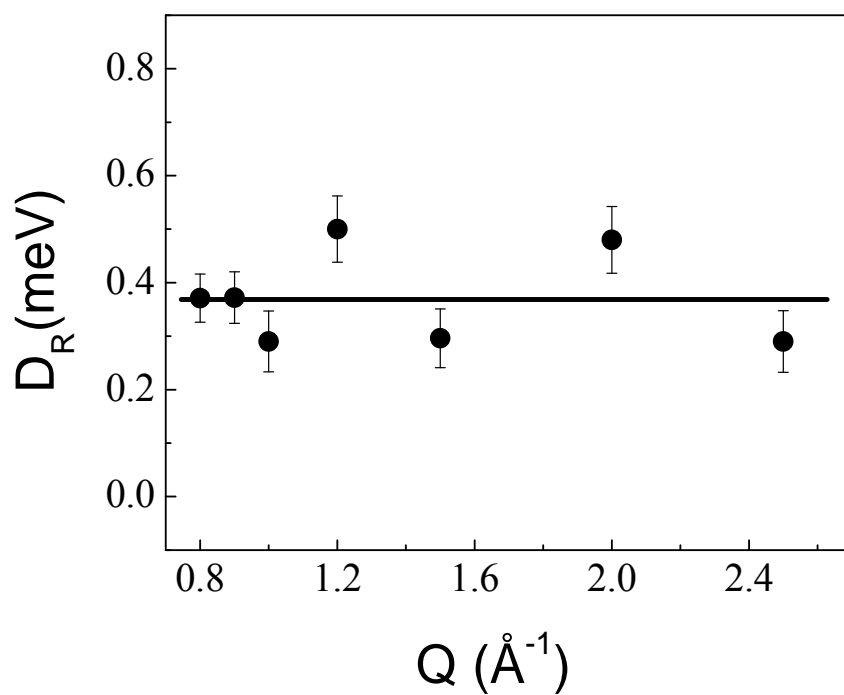


**Fig. 7.9** Variation of rotational diffusion coefficient ( $D_R$ ) with  $Q$ .



For isotropic rotational motion the trajectory, as obtained from MD simulation, of a  $\text{CH}_3$  site of the propylene molecule with respect to the center of mass should trace a sphere in 3 dimensions. Trajectories of the  $\text{CH}_3$  site of the propylene molecule with respect to the center of mass is plotted in X-Y plane for a) up to 1311 ps b) up to 140 ps and c) up to 200 ps and shown in Fig. 7.10. It is clearly seen from Fig. 7.10(a) that the path traced by the  $\text{CH}_3$  site with respect to the center of mass of the molecule encompasses the surface of a sphere at long times, thereby showing that the molecule has had all the possible orientations during the time interval of the simulation. This shows that the rotational motion is indeed isotropic on the average over large time. This is also corroborated by the fact that the variation of EISF as obtained from long time behaviour of calculated  $I^R(Q, t)$  with  $Q$  is described well by the isotropic rotation as shown in Fig 7.11. However, as evident from Fig 7.10 (b) and Fig 7.10 (c) that at short time, the motion is restricted by channel framework and not truly isotropic. To understand the detailed mechanism of the rotational motion inside zeolitic channels, the intermediate scattering function  $I^R(Q, t)$  calculated from MD simulation was compared with theoretical models.

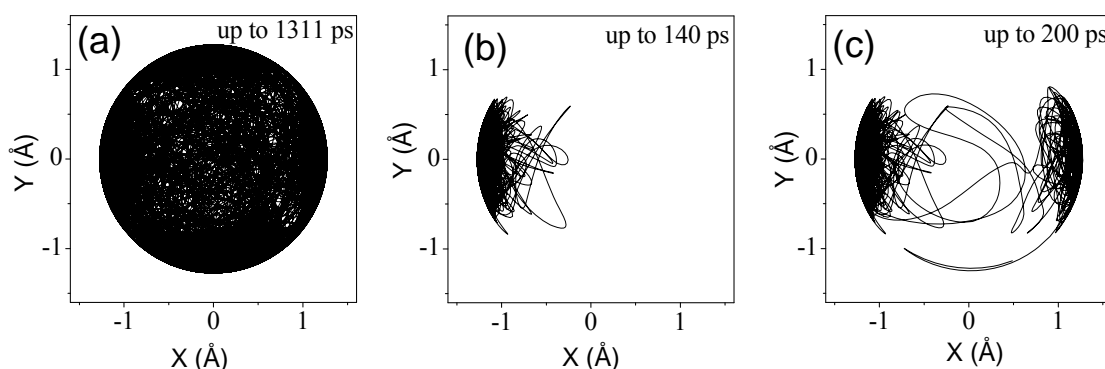


**Fig 7.10** Trajectory of the  $\text{CH}_3$  site with respect to the center of mass of the molecule for (a) 1311 ps, (b) first 140 ps and (c) first 200 ps of the simulation production run in X-Y plane.

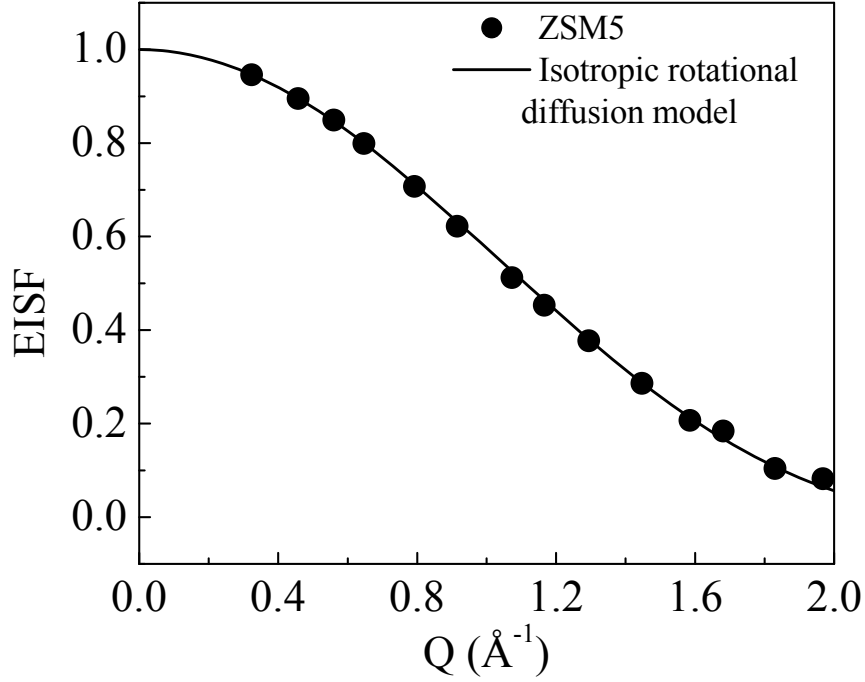


**Fig. 7.11** Variation of  $EISF$  as obtained from long time behaviour of  $I^R(Q, t)$  calculated using MD simulation trajectories of the propylene molecules in ZSM5 zeolite. The solid curve corresponds to the calculated variation for isotropic rotational diffusion.

Variations of  $I^R(Q, t)$  with  $Q$  at some typical  $Q$  values are shown in Fig. 7.12. For isotropic rotation, the rotation axis is not unique and distributed isotropically. In this case,  $I^R(Q, t)$  can be written as [23],

$$I^R(Q, t) = \sum_{l=0}^{\infty} (2l+1) j_l^2(Qr) C_l(t) \quad (7.10)$$

where  $j_l$ 's are Bessel functions,  $r$  is the radius of gyration and  $C_l$  are the orientational correlation functions defined as,

$$C_l(t) = \langle P_l(\mathbf{e}(t) \cdot \mathbf{e}(0)) \rangle \quad (7.11)$$

$P_l$  is the Legendre polynomial of order  $l$  and  $\mathbf{e}$  is a unit vector directed towards the  $\text{CH}_3$  site with respect to center of mass of the propylene molecule. Therefore, evolution of  $\mathbf{e}$  with time

can be analysed to get the details of rotational motion of the propylene molecule. In particular, in the case of isotropic rotational diffusion through small angular jumps, the orientational correlation functions in Eq. (7.11) can be expressed in terms of the rotational diffusion coefficient ( $D_R$ ) as

$$C_l(t) = \exp(-l(l+1)D_R t) \quad (7.12)$$

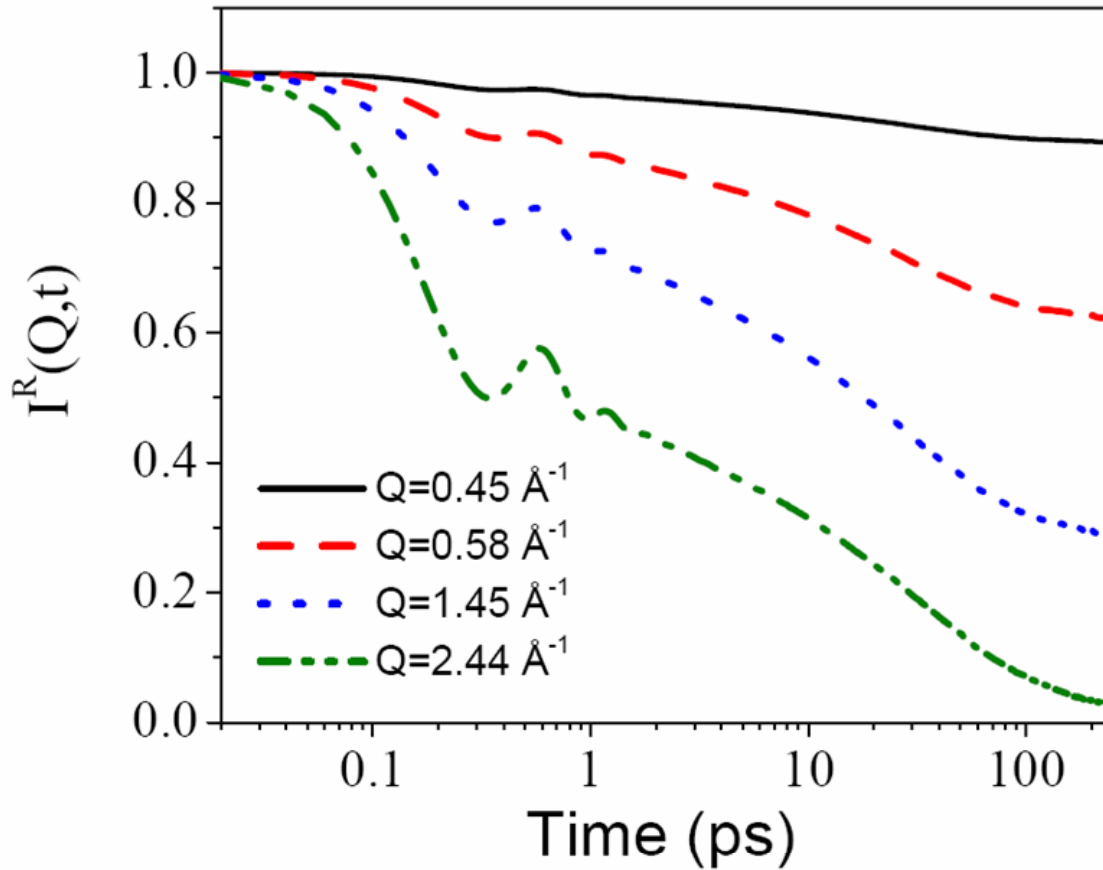


**Fig.7.12** Variation of  $I^R(Q,t)$  of propylene molecules within ZSM5 zeolite at typical  $Q$  values.

As shown earlier that in case of propylene, the factor  $(2l+1)j_l^2(QR)$  has significant contributions only up to  $l=6$  for all the  $Q$  values up to  $2.5 \text{ \AA}^{-1}$  and therefore, the summation over infinite terms can be truncated at  $l=6$  in Eq. (7.10). It is found that  $I^R(Q,t)$  functions do not follow the simple exponential decay characteristic of isotropic rotational diffusion model

(Fig 7.12). In addition, data show some oscillations at short times (Fig.7.12), which was investigated further as described below.

As can be seen from Eq. (7.10), the time dependence of the intermediate scattering function for rotational motion comes exclusively from the orientational correlation functions. The orientational correlation functions of different orders were calculated and shown in Fig. 7.13. The functions show conspicuous wobbling before decaying to lower values instead of a simple exponential decay. Oscillations in these functions indicate that the molecules undergo librational motion [177]. Rotational dynamics of the trapped molecule inside the channel may consist of oscillations of the molecule as a whole until the molecule experiences a suitable torque and space to rotate freely. Oscillations of the trapped molecule as a whole also known as librational motion was also observed by NMR studies on butane adsorbed in ZSM5 zeolite [178].

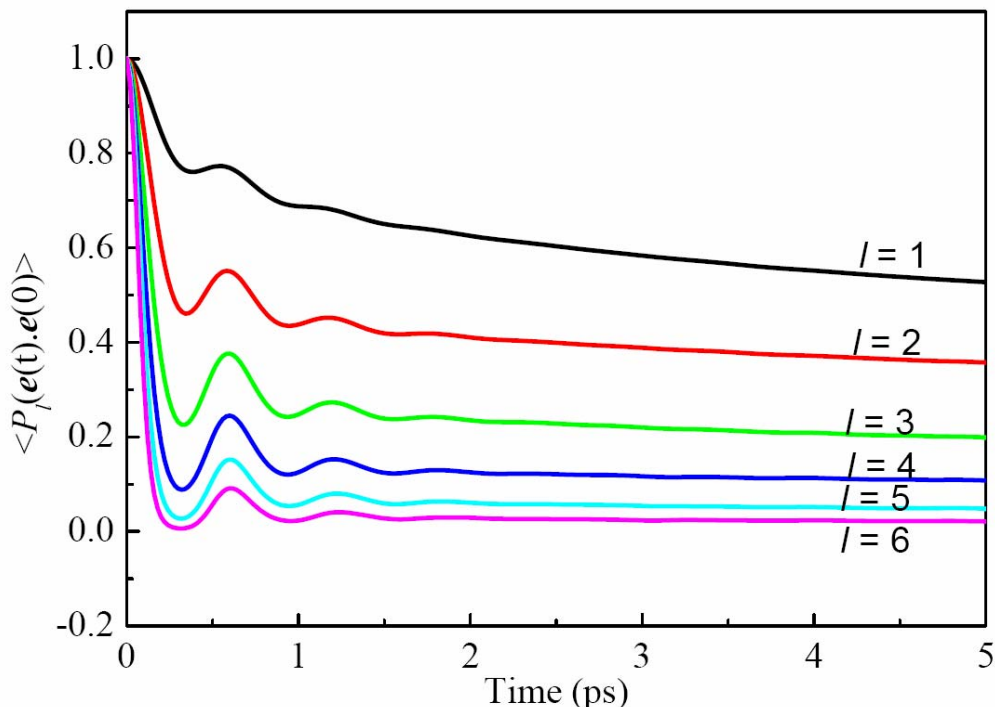


**Fig. 7.13.** The behavior of the first six orientational correlation functions,  $\langle P_l(e(t).e(0)) \rangle$  with time.

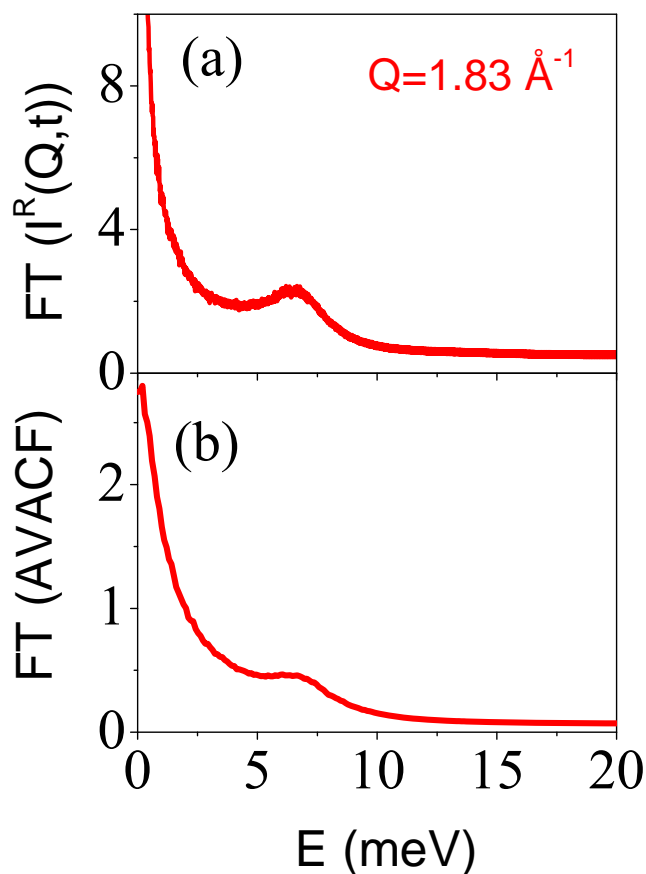


**Fig. 7.14** (a) Fourier Transform of  $I^R(Q,t)$  for propylene in ZSM5 zeolite at typical Q-value of  $1.8 \text{ \AA}^{-1}$ . A peak around  $\sim 7 \text{ meV}$  is observed. (b) Fourier Transform of AVACF for propylene in ZSM5 zeolite. Inset: FT of AVACF in an expanded scale, the peak around  $\sim 7 \text{ meV}$  is evident.

Existence of libration motion for propylene in ZSM5 zeolite is further confirmed from the calculated Fourier transform (FT) of  $I^R(Q,t)$  and angular velocity auto correlation functions (AVACF) which are related to dynamical structure factor  $S^R(Q,\omega)$  for rotational motion and rotational density of state respectively. FT of  $I^R(Q,t)$  and AVACF are shown in Figs. 7.14(a) and (b) respectively. The peak at  $7 \text{ meV}$  as observed in both the figures corresponds to the existence of libration of propylene molecule.

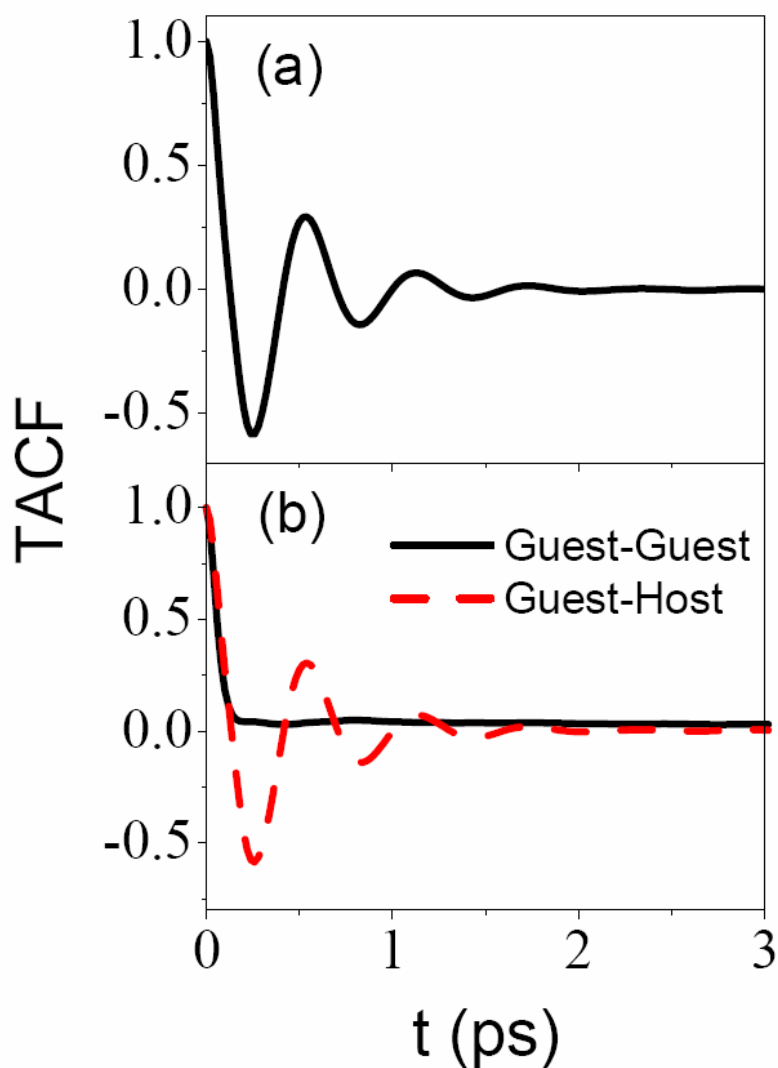


**Fig. 7.15** (a) Torque auto correlation function (TACF) for propylene in ZSM5 zeolite. Presence of oscillations is observed. (b) TACF for due to guest-guest as well as guest host interaction. TACF due to guest-host interaction is seen to be responsible for the oscillations.

Torque autocorrelation function (TACF) is also calculated for propylene adsorbed in ZSM5 zeolite in order to investigate the nature of torque responsible for the rotational motion of propylene molecule inside the zeolitic cavity. Large amplitude oscillation in TACF is found as shown in Fig. 7.15 (a). The torque on a particular propylene molecule consists of two parts; first arises due to all other propylene molecules present in the zeolitic cavity (guest-guest) and second is due to the zeolite framework atoms (guest-host). In order to

examine the origin of large oscillations in TACF for ZSM5 zeolite, torque due to guest-guest interactions and torque due to guest-host interactions are separately calculated. TACF due to guest-guest interaction and guest-host interaction for ZSM5 zeolite are separately shown in Fig. 7.15 (b). It can be seen from the figure that the large oscillations are mostly due to guest-host interaction rather than guest-guest interaction.

One can obtain the value of the libration angle for propylene molecules in ZSM5 zeolite by using Eq. (7.11) and setting  $P_l(\cos(\theta_m)) = C_l(t_m)$ , where  $t_m$  is the time at which the first minimum occurs in the orientational correlation functions (Fig. 7.13). This leads to a mean libration angle of  $40^\circ$  for propylene adsorbed in ZSM5 zeolite. Correlation times,  $\tau_l$ , associated with orientational correlation functions can be calculated as

$$\tau_l = \int_0^\infty C_l(t) dt = \int_0^\infty \langle P_l(\mathbf{e}(t) \cdot \mathbf{e}(0)) \rangle dt \quad (7.13)$$

Values of correlation times,  $\tau_l$  and  $\tau_2$  obtained from the orientational correlation functions using Eq. (7.13) are  $38 \pm 3$  and  $94 \pm 4$  ps respectively.

To probe the nature of motion, the time evolutions of  $\cos(\theta)$ ,  $\theta$  being the angle of a unit vector  $\mathbf{e}$  attached to a tagged propylene molecule adsorbed in ZSM5 with the X, Y and Z-axis in the space fixed frame are shown in Fig. 7.16 (a). It is found that the angular jumps do not comprise of all the possible angles uniformly in all the X,Y,Z directions. It is found that while these are similar in Y & Z directions it is different in X direction indicating a clear anisotropic motion. The angular jumps in Y and Z direction are limited to a small angular band indicating restricted rotations. However, in X direction, the distribution of angular jumps is limited to a much smaller value and the test molecule found to flip at  $\sim 140$  ps and again performs restricted rotation. Due to comparable size of propylene molecules and ZSM5 channel diameter, reversal of orientation of the molecule is possible in two cases: 1) while translating, the molecule finds a channel intersection which provides an opportunity to

change its orientation before entering into another channel again and 2) due to the collision with the other guest molecules. To probe the cause of this reversal of orientation, torque due to guest-guest and guest-zeolite interaction is calculated for the same test molecule. Fig. 7.16(b) shows the time evolutions of torque in the X direction due to guest-guest interactions only. It can be seen from Fig. 7.16(b), that around 140 ps, torque in the X direction due to guest-guest interaction shows some peaks suggesting collisions due to other guest molecules. Although not shown here, torque due to guest-host interaction shows no such change. Therefore, the flipping orientation of the molecule is mainly due to guest-guest interaction.

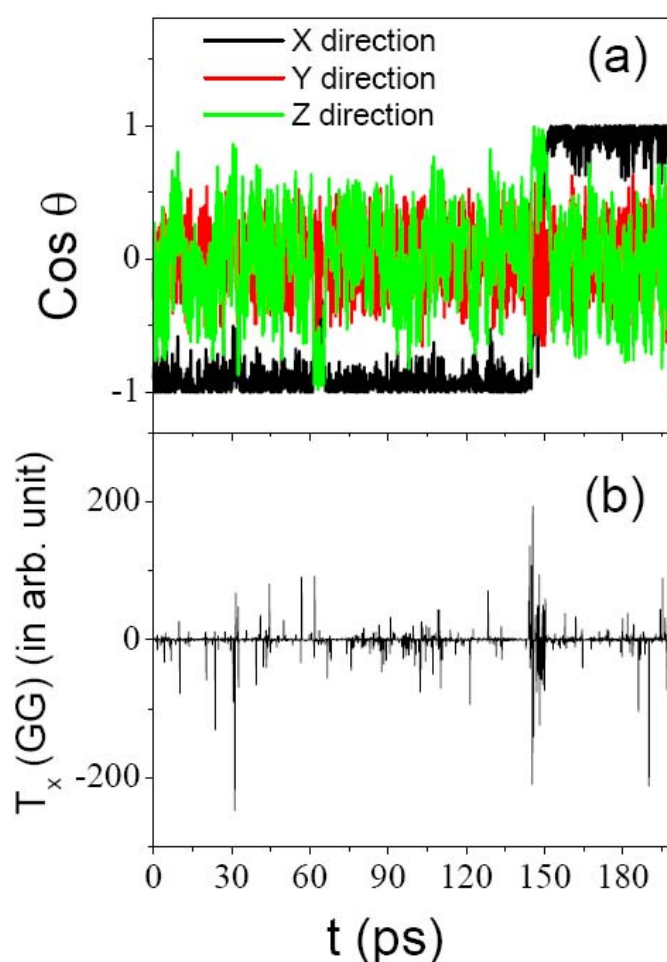


**Fig. 7.16** (a) Projection of a unit vector  $e$  (directed towards  $\text{CH}_3$  site) with respect to center of mass in space fixed coordinate for short time for a tagged molecule in ZSM5 zeolite. (b) Torque exerted on the molecules in the X direction due to guest-guest interaction.



Therefore, in general, rotation of a propylene molecule inside ZSM5 zeolite is characterised by restricted rotations for short times, then flips its orientation and continues restricted rotations. It can clearly be seen in Fig. 7.10(b) and 7.10(c), where trajectories of a CH<sub>3</sub> site of a tagged propylene molecule with respect to the center of mass is plotted in X-Y plane, upto 140 ps and 200 ps respectively. Restriction of  $\theta$  to a small value suggests that the molecule confined in ZSM5 zeolite performs a restricted rotation, possibly libration as indicated in the rotational density of states (Fig. 7.14 (b))

It is clear from Fig. 7.16 (a) that the tagged molecule prefers a specific orientation inside ZSM5 zeolitic channel in X direction. To probe whether this is the case in general for all the propylene molecules inside the zeolite, the projection angles of the unit vector  $\mathbf{e}$  were binned for all the molecules at all times. Histogram of the distribution of projection angles of unit vector  $\mathbf{e}$  to different axis in case of propylene adsorbed in ZSM5 zeolite is shown in Fig. 7.17 (a). Two extra peaks apart from a peak at 90 degree are observed for projection angles with respect to X and Y axis as shown in Fig. 7.17 (a). These extra peaks are found to be absent for projection angles with respect to Z-axis. The origin of the peak around 90 degree in the distribution of projection angles can be explained as follows: When a unit vector performs isotropic rotation, after a sufficient time, tip of the vector covers a sphere as shown in Fig. 7.17 (b). Surface of the sphere is equally populated by the trajectories of the tip of the vector. At any given time, orientational configuration of the unit vector will be determined by the position of the tip in the surface of the sphere. Total number of orientational configurations having projection angle  $\theta$  will be proportional to the length of circumference of the circle with radius  $\sin\theta$  as shown in Fig. 7.17(b). All the points (representing orientational configurations of the unit vector) in that circumference will have the same projection angle  $\theta$ . Since circumference is maximum for the projection angle  $\theta=90$  degree, total number of orientational configurations will be maximum for projection angle,  $\theta=90$

degree. Distribution centred around 90 degree with respect to X, Y and Z-axis is thus a consequence of purely isotropic distribution of the projections. Appearance of two extra peaks that are observed for projection angles with respect to X and Y-axes (Fig. 7.17(a)) shows that inside ZSM5 zeolite channel, molecules do not have random orientations; instead, there exists a preferred orientation. Calculation showed that the preferred angles correspond to the orientation when the molecular axis lies parallel to the channel axes. Further, these preferred orientations were observed only in X and Y direction, and not in Z direction. This is expected as ZSM5 zeolite consists channels in X and Y direction only and no channels in Z direction. Therefore, it can be inferred that while diffusing, propylene molecules are aligned along the channels. To check whether this is a consequence of channel structure or geometrical restriction or both, MD simulation of propylene adsorbed in two another zeolites (Na-Y and  $\text{AlPO}_4\text{-5}$ ) has been carried out [171,176,179,180].  $\text{AlPO}_4\text{-5}$  has only straight channel along the z direction with larger diameter ( $\sim 11 \text{ \AA}$ ) than ZSM5 zeolite ( $\sim 5.4 \text{ \AA}$ ) and provides enough space for propylene molecules to orient itself inside the channel. Unlike ZSM5 and  $\text{AlPO}_4\text{-5}$ , Na-Y has almost spherical supercages (size  $\sim 11.8 \text{ \AA}$ ), which are interconnected with each other in a tetrahedral manner by 12 membered oxygen rings forming windows (size  $\sim 7.8 \text{ \AA}$ ). Rotational motion of propylene has been studied in both the  $\text{AlPO}_4\text{-5}$ , Na-Y zeolites [171,180]. Intermediate scattering function corresponding to rotation motion,  $I^R(Q,t)$  for propylene in Na-Y zeolite is well described by Eq. (7.10) and (7.12) indicating isotropic rotation of propylene molecules [171,180]. Neither preferred orientation nor libration motion was observed for propylene in Na-Y zeolite. However in case of  $\text{AlPO}_4\text{-5}$ , preferred orientation of propylene was observed along the channel direction. Histograms of the distribution of projection angles of unit vector  $\boldsymbol{e}$  as described above to different axis in case of propylene adsorbed in Na-Y and  $\text{AlPO}_4\text{-5}$  zeolite are shown in Fig. 7.18(a) and 7.18(b) respectively. It is evident from Fig 7.18 that in case of  $\text{AlPO}_4\text{-5}$  preferred orientation

of propylene is observed only in Z direction, and not in X or Y direction. It may be noted that AlPO<sub>4</sub>-5 zeolite consists channels only in Z direction. However, no signature of libration motion was found in this case, may be due to the larger diameter of the channels. Thus, it can be inferred that the preferred orientation of the guest molecule inside a host zeolite is mainly due to the shape of host structure rather than size of channels whereas librational motion arises mainly due to the geometrical restriction.

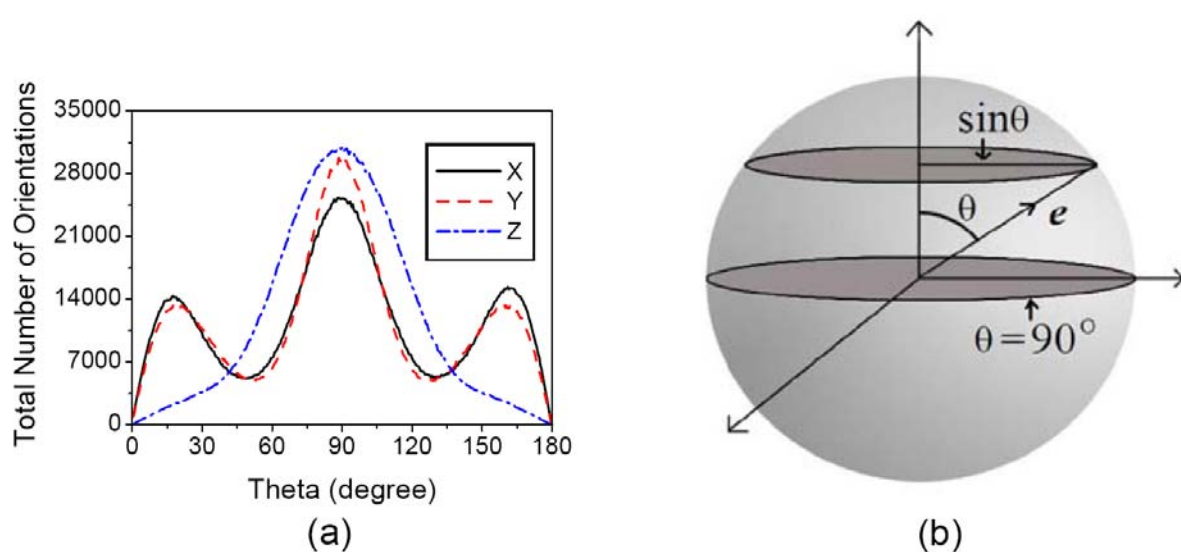


**Fig. 7.17** (a) Histogram of the distribution of projection angles of unit vector (from center of mass to a CH<sub>3</sub> site) to different axis in case of propylene adsorbed in ZSM5 zeolite. (b) Schematic of a sphere covered by the tip of a unit vector  $e$  performing isotropic rotation.

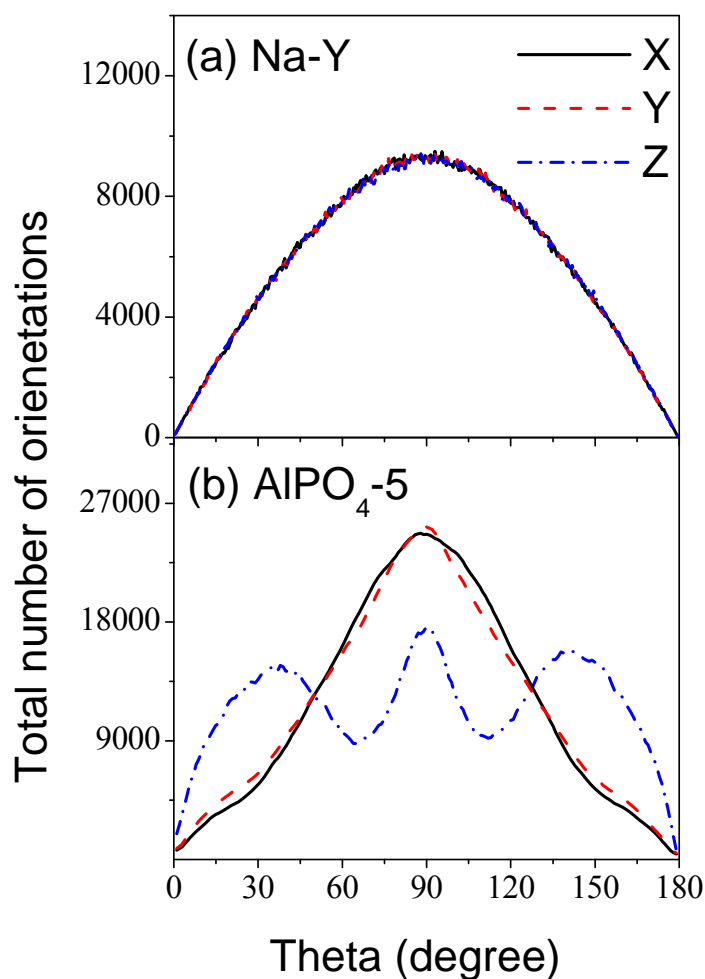


**Fig. 7.18** Histograms of the distribution of projection angles of unit vector (from center of mass to a  $\text{CH}_3$  site) to different axis in case of propylene adsorbed in (a) Na-Y and (b)  $\text{AlPO}_4$ -5 zeolites.

#### 7.4.2. Dynamics of Ethylene Glycol (EG) in ZSM5 Zeolite

As mentioned earlier dynamics of guest molecules depends upon many factors including the host-zeolite interaction. Therefore, it is of interest to investigate the effect of guest-host interaction on the dynamics of sorbed species. QENS experiments have been carried out on ethylene glycol (EG;  $\text{C}_2\text{H}_6\text{O}_2$ ) sorbed in ZSM5 at MARX spectrometer ( $\Delta E \sim 200 \mu\text{eV}$ ) at Dhurva, Trombay at 300 K. EG can form interfacial hydrogen bond with the oxygen of the host zeolitic ZSM5 (unlike propylene). QENS data from EG sorbed in ZSM5 zeolite showed

significant quasielastic broadening whereas dehydrated ZSM5 showed no quasielastic broadening over the instrument resolution. Thus, this broadening is related to the dynamical motion of EG molecules sorbed in ZSM5 zeolite. Data from the dehydrated zeolite was subtracted from that of EG adsorbed in ZSM5 zeolite. Subtracted QENS data was separated out into elastic and quasielastic contributions by fitting the scattering law (given in Eq. (1.74)) after convoluting with the instrumental resolution function. Typical QENS data and fits are shown in Fig.7.19.

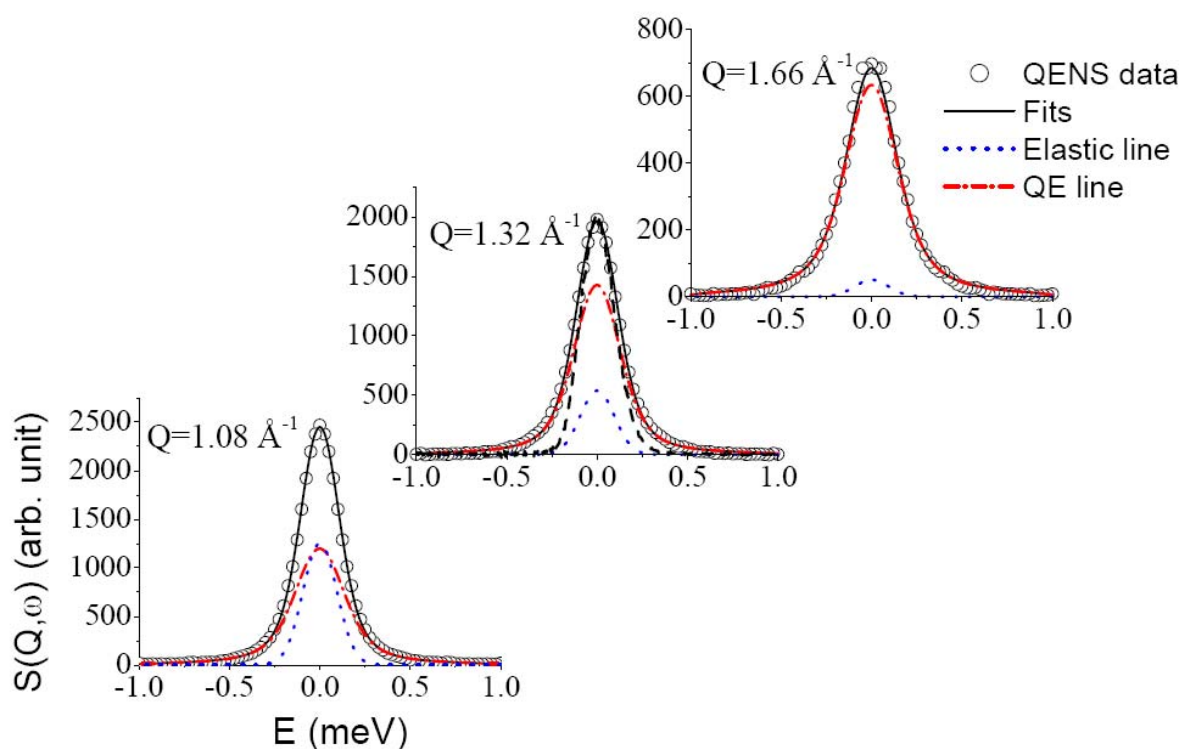


**Fig. 7.19** Fitted QENS spectra from EG adsorbed in ZSM5 zeolite at some typical  $Q$  values. Solid lines represent the fit while dash-dot and dash-dot-dot lines represent quasielastic and elastic components respectively. Instrument resolution is shown by dashed line in middle panel.

Analysis of QENS data showed a non-zero value of EISF, which indicates the presence of localized motion of EG inside the pores. Extracted EISF (Fig. 7.20) is compared with various models of localized motions as discussed in chapter 1. It is found that the isotropic rotational diffusion model (Chapter 1, section 1.1.5.1) describes the EISF well as shown by solid line in Fig 7.20. Radius of gyration is found to be 1.9 Å, which is equivalent to average distance of all hydrogen atoms from center of mass of EG molecules. Schematic of EG molecules is shown in Fig. 7.20 (b).

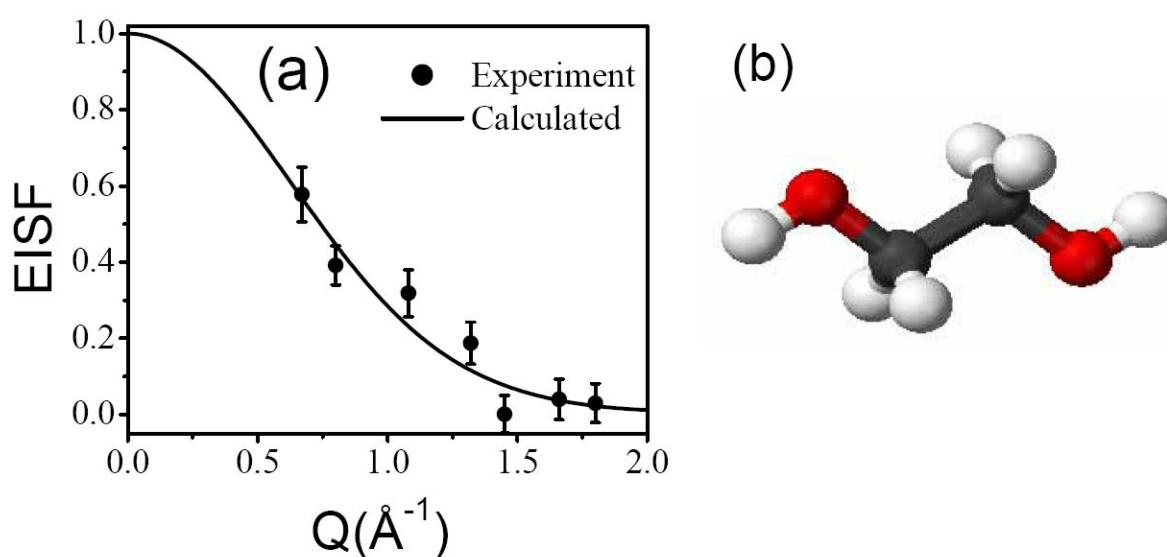


**Fig. 7.20** (a) Variation of EISF as obtained from QENS data of EG loaded in ZSM5 using MARX spectrometer with respect to wave vector  $Q$ . The solid line corresponds to the isotropic rotational diffusion model. (b) Schematic of EG molecule.

After establishing the rotational geometry of the EG, the whole QENS spectra was analysed assuming the scattering law correspond to isotropic rotational diffusion as given in Eq. (7.8). In the present case,  $Q_{max}$  and  $r$  are equal to  $1.8 \text{ \AA}^{-1}$  and  $1.9 \text{ \AA}$  respectively. It can be readily seen from Fig. 7.7 that terms only up to  $l=5$  contribute in the scattering law of

isotropic rotation as given in Eq. (7.8). QENS spectra were therefore fitted with Eq. (7.8) with the summation truncated after  $l=5$  with least square fits having rotational diffusion coefficient ( $D_R$ ) as the parameter. Fits are found to be reasonably good as shown in Fig. 7.21, which gives an extra support to the reliability of the model. Variation of rotational diffusion coefficient,  $D_R$  as obtained from the fits is shown in Fig 7.22. It is found that  $D_R$  more or less constant with  $Q$  and an average value of 16  $\mu\text{eV}$  is obtained for rotation motion of EG confined in ZSM5 zeolite.

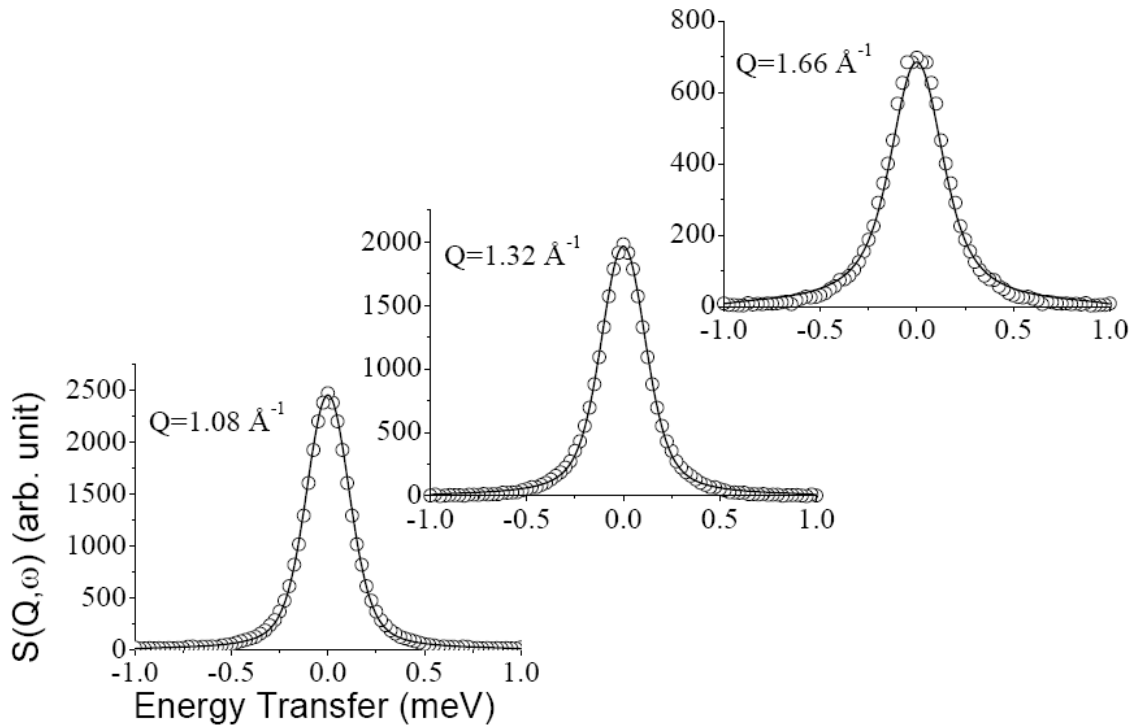


**Fig. 7.21** Typical fitted QENS spectra for EG sorbed in ZSM5 zeolite assuming isotropic rotational diffusion model at some typical  $Q$  values.

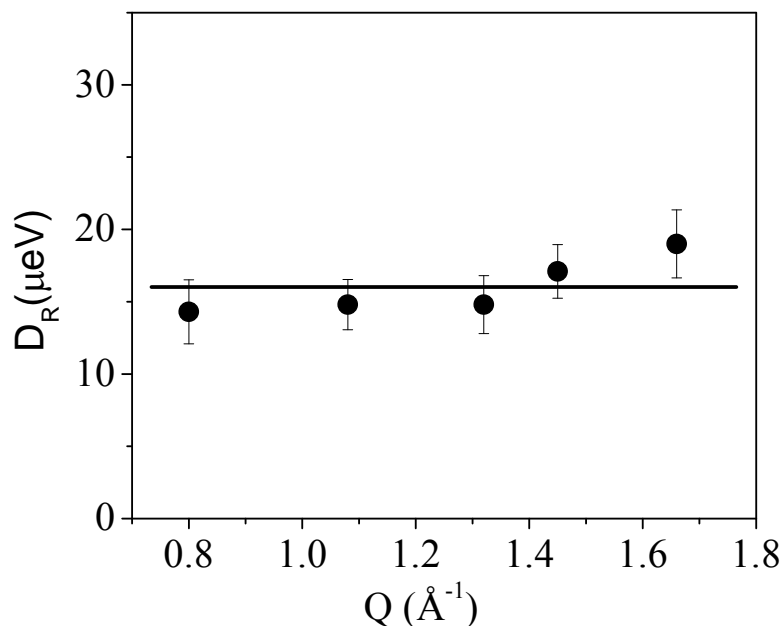


**Fig. 7.22** Variation of rotational diffusion coefficient,  $D_R$  of EG sorbed in ZSM5 with  $Q$ .

Obtained rotational diffusion coefficient,  $D_R = 16 \mu\text{eV}$  is compared with that of bulk EG. It is found that the rotational diffusion coefficient of EG confined in ZSM5 is much less compared to its bulk value ( $39 \mu\text{eV}$ ) at room temperature [181]. Results can be compared with the dynamical parameters of other hydrocarbons such as benzene and propylene adsorbed in ZSM5 zeolite. It is found that propylene and EG both show isotropic rotation while six fold rotational jump motion was observed in case of benzene. Rotational diffusion coefficient of EG is almost one order of magnitude less than propylene ( $370 \mu\text{eV}$ ) and almost comparable to benzene ( $20 \mu\text{eV}$ ) [156] in ZSM5 in spite of the fact that EG is having a lower moment of inertia and less symmetric than benzene. Therefore, main cause of hindered rotation may be the strong attractive interaction between EG molecules and ZSM5 zeolite. This should reflect in the freezing behavior of EG confined in ZSM5 zeolite, as freezing temperature of fluids in confined media is strongly affected by the strength of forces between fluid molecules and the pore walls [182-186]. Miyahara et al [182] in a molecular simulation study of freezing of simple fluids in slit pores showed that freezing temperature,  $T_f$  is



strongly affected by the strength of forces between fluid molecules and the pore walls. For repulsive and weakly attractive potentials, the shift in freezing temperature  $\Delta T_f = (T_f)_{\text{confined}} - (T_f)_{\text{bulk}}$  is negative. However, for strongly attractive interaction  $\Delta T_f$  was observed to be positive. Experimentally this can be studied using positron annihilation spectroscopy (PAS) technique, which is an *in-situ* and non-destructive and well suited for the study of phase transition of confined molecules [184-186].

Temperature dependent PAS study was carried out to probe the freezing behavior of EG confined in ZSM5 zeolite. The variation in Doppler broadened S-parameter with temperature showed discontinuity at a temperature (270 K) higher than the bulk freezing point of EG (260 K) [185,186]. Moreover, lifetime of ortho-Positronium (o-Ps) and its intensity also showed discontinuity at 270 and 260 K during the cooling cycle [185]. The transition at 270 K may be attributed to the freezing of ethylene glycol confined in micropores of ZSM5, which is 10 K above the bulk freezing temperature. Such an elevation in freezing point of confined molecules signifies an attractive interaction between the fluid molecules and the pore wall, which, in the present case is a consequence of the interfacial hydrogen bonding between ethylene glycol and ZSM5 pore surface. Existence of hydrogen bonding between ethylene glycol and ZSM5 pore surface is also confirmed by NMR results [185]. Depression in freezing temperature was also observed for benzene adsorbed in ZSM5, which corresponds to the weakly attractive or repulsive interaction between the benzene molecules and pore-surface [184]. Therefore, hindered rotational dynamics of EG is a consequence of the strong hydrogen bonding between ethylene glycol and zeolite surface.

## 7.5. CONCLUSIONS

Dynamics of guest molecules (propylene and ethylene glycol) absorbed in channel framework of ZSM5 have been studied in details [171,176,179,180,186]. Translational as

well as rotational motion of propylene inside ZSM5 zeolite are investigated [171,176,179,180]. Slower translational motion of propylene is studied using MARX spectrometer having energy resolution of  $\sim 200 \mu\text{eV}$  and the data are found to be describable by jump diffusion models. MD simulation studies suggest that rotational motion of propylene is almost an order of magnitude faster than the translational motion. This is confirmed by measurements carried out using a much wider energy window spectrometer ( $\Delta E \sim 3 \text{ meV}$ ) and it is found that propylene undergoes isotropic rotational diffusion in the channels of ZSM5 zeolite. MD simulation also indicates, on the average, rotational motion of propylene is isotropic which is consistent with the experimental results. However, at shorter times, deviation from isotropic behaviour is observed. Detailed analysis of trajectories revealed that the rotational dynamics of propylene adsorbed in ZSM5 zeolite is quite complex and simple isotropic rotation could not explain the intermediate scattering functions correspond to rotational motion [179]. In addition, orientational correlation function shows presence of librational motion. This is confirmed by rotational density of states and the dynamic structure factor calculated by Fourier transform of angular velocity auto correlation function and intermediate scattering function respectively. MD simulation study also indicates that the propylene molecules prefer to be oriented along the channel direction during diffusion through the ZSM5 zeolite [179]. It is found that the preferred orientation of the guest molecule inside a host zeolite is due to the shape of host structure rather than the size of the channels whereas librational motion arises mainly due to the geometrical restriction. Here experiments and simulation are carried out simultaneously and independently [171,176,179,180]. The results as obtained from these studies not only gave insight of the total dynamical process but also consistent within each other. To investigate the effect of guest-host interaction, QENS experiments have been carried out on EG adsorbed in ZSM5 [186]. EG can form strong hydrogen bond with the host structure of ZSM5 zeolite (unlike

propylene). Only rotation motion of EG is observed at MARX spectrometer ( $\sim 200 \mu\text{eV}$ ). There might be translational motion of EG within the channels of ZSM5 zeolite but that is expected to be slow and hence not observable in QENS technique. Although, both propylene and EG show isotropic rotation inside ZSM5 zeolite, rotational diffusion coefficient of EG is found to be one order of magnitude less than propylene [171,186]. The nature of guest-host interaction is probed using Positron Annihilation Spectroscopy by observing the freezing behaviour of the guest molecules inside the host. It is found that the guest-host interaction has a predominant role in determining the dynamical behavior of adsorbed molecules.

## CHAPTER 8

### Summary and Future Direction

#### 8.1. SUMMARY

The research work presented in the thesis showed that quasielastic neutron scattering (QENS) measurements have been successfully used to study stochastic molecular dynamics occurring typically in picoseconds time scale, present in variety of complex systems. MD simulation technique has been employed to gain deeper insights on dynamical processes and compliment the results obtained through QENS technique. Suitable models are developed to describe the experimental data and related to dynamics are obtained to understand the relevant physics. Other experimental techniques such as dynamic light scattering (DLS), differential scanning calorimetry (DSC), scanning electron microscope (SEM), small angle neutron scattering (SANS), positron annihilation spectroscopy (PAS), Thermal gravimetric analysis (TGA) are employed to obtain various other informations which were also used explaining the results obtained through QENS technique.

Study of SDS based anionic micelles revealed a very complex dynamical landscape, covering wide time scale ranges, exists in the micelles. Distinct motions namely global diffusion of whole micelles, segmental motion of the alkyl chain and additional fast torsional motion are observed. The global diffusion associated with the whole micelle was found to be Fickian in nature and the corresponding diffusion coefficient was found to be consistent with those obtained from DLS measurement and MD simulation results. Internal motion of the monomer was found to comprise of segmental as well as torsional motion of the alkyl chain. A model in which the hydrogen atoms undergo localised translational diffusion confined within spherical volumes successfully described segmental motion of the SDS molecules. The

volume and the associated diffusivity of the confining sphere found to have a linear relationship with the position of hydrogen atom on the alkyl chain. Fraction of alkyl chain was found to perform fast torsional motion that was described by 2-fold rotation. The studies presented in this thesis lead to first effort to understand the details of internal dynamics of ionic micelles.

Results of QENS studies have provided a detailed insight into the reorientational motions of alkyl chain in solid phase of SDS. It was found that SDS molecules undergo fractional dynamics following a uniaxial rotation model in the temperature range 210-350 K. The fraction of SDS molecules taking part in the dynamics was found to increase linearly with increasing temperature. Obtained rotational diffusion coefficient followed Arrhenius behavior. A dynamical transition was found to exist at 360 K. This was understood in conjunction with Raman spectroscopy and diffraction studies on anhydrous SDS powder where a structural transition (from monoclinic to hexagonal) had been observed around 360 K [84,85]. It was found that uniaxial rotation was inadequate to explain the dynamics above the transition temperature (~360 K). Localized translational diffusion model in which the hydrogen atoms associated with different CH<sub>2</sub> units of the chain diffuse within the spheres of varying radii was found to describe the observed dynamics above 360 K. It is worthy to note that dynamics of SDS chain in anhydrous powder above the transition temperature (~360 K) is very similar to the segmental motion in the micellar phase.

Detailed dynamical landscape of CTAB (C<sub>16</sub>H<sub>33</sub>N(CH<sub>3</sub>)<sub>3</sub>Br; C<sub>16</sub>TAB) based cationic micelles has been investigated using QENS technique. This study was undertaken with the objective of understanding the dynamics of head group, which are in contact with surrounding water molecules and therefore are prone to be affected by hydration. Unlike SDS, head group in CTAB molecule consists of three methyl units and therefore it is observable by neutrons. Data analysis showed the presence of global micellar diffusion and

internal motion associated with the monomer of the micelles. Global diffusion of the whole micelle was found to commensurate with a model, which assumed Fickian diffusion of the micelle. Internal dynamics of CTAB micelles have been successfully described assuming the existence of different dynamical components: segmental motion of the alkyl chain, fast torsional motion like SDS and also contributions from the head group. While the dynamics of the methyl groups in the head group were modeled as three-fold jump rotations about the symmetry axis, the hydrogen atoms belonging to the alkyl chain, were found to undergo localised translation diffusion confined within spheres with linear distribution of sizes. The observed fast torsional motion associated with some of the CH<sub>2</sub> groups belonging to the alkyl chain has also been successfully described by a 2-fold jump rotation.

Effect of molecular architecture on the dynamics of ionic micelles has been studied. In the category of cationic micelles, effect of chain length on the dynamics of *n*-alkyltrimethylammonium bromides (C<sub>*n*</sub>H<sub>2*n*+1</sub>N(CH<sub>3</sub>)<sub>3</sub>Br, C<sub>*n*</sub>TAB; for *n* = 12,14,16)) for varied length of the surfactant molecule has been investigated. Both global as well as segmental motions of C<sub>*n*</sub>TAB micelles have been affected with the alkyl chain length of the surfactant. Global as well as segmental motion found to slow down with increase in chain length. Furthermore, it was found that in micelles with shorter chain length, the hydrogen atoms in the alkyl chains covered a larger volume than those with longer chains. Therefore, it can be concluded that alkyl chains are more flexible in the micelles with shorter chain length and as chain length of surfactant molecules increases, flexibility of the alkyl chain decreases. This was explained in terms of increased packing density of the monomer in the larger chain length micelles. In the category of anionic micelles, SDBS (C<sub>12</sub>H<sub>25</sub>C<sub>6</sub>H<sub>4</sub>SO<sub>3</sub>Na) and SDS (C<sub>12</sub>H<sub>25</sub>OSO<sub>3</sub>Na) are of very similar structure except SDBS contains an additional phenyl ring near to head group. It was found that presence of the phenyl ring significantly modifies the dynamics, both global as well as internal motion found to slow down. Interestingly our

experimental results are found to be consistent with recent MD simulation study on both the micelles [59]. Elastic incoherent structure factor corresponding to internal motion indicated that alkyl chains of SDBS molecules are less flexible than in SDS molecules. Diffusivity of the hydrogen atoms corresponding to internal motion is also found to be slower in SDBS than SDS micelle. This has been explained on the basis of the denser packing of hydrophobic core and lesser hydration level of alkyl chains in case of SDBS micelles.

Results of QENS studies have also provided considerable insight into the dynamical properties of water inside nanoporous reverse osmosis (RO) and nanofiltration (NF) polyamide membranes, Prussian blue and its analogues. Translational motion of water molecules has been found to follow random jump diffusion in these membranes and corresponding diffusivity was found to be hindered vis-à-vis bulk water. QENS studies carried out on the crystal-water in Prussian Blue (PB;  $\text{Fe}_4(\text{II})[\text{Fe}(\text{II})(\text{CN})_6]_3 \cdot 14\text{H}_2\text{O}$ ) and its analogues PBA-I ( $\text{Fe}_4(\text{II})[\text{Fe}(\text{II})(\text{CN})_6]_4 \cdot 16\text{H}_2\text{O}$ ) and PBA-II ( $\text{Cu}_2\text{Mn}_2[\text{Fe}(\text{CN})_6]_{2.67} \cdot 19\text{H}_2\text{O}$ ) based molecular magnet, showed that dynamics of water could be best described by localized translational diffusion. It was shown that dynamical behaviour of the water molecules depend on the location of them in the crystal lattice. Dynamics of water in PBA-I, which did not have any vacant  $\text{Fe}(\text{CN})_6$  units was found to be more hindered than in PB and PBA-II. Fraction of immobile water molecules in PBA-I was found to be larger compared to PB and PBA-II and does not change much with temperature. However, in case of PB and PBA-I, fraction of mobile water molecules increased sharply with temperature. This might be due to the fact that coordinated water molecules exist in PB and PBA-II immobile at low temperature and start to participate in the dynamics at high temperature. QENS studies presented in this thesis are the first studies to understand the dynamics of water in polyamide membranes and Prussian blue analogous.

Dynamics of guest molecules confined in channel framework of ZSM5 zeolite revealed that exact mechanism of dynamics depend on the shape and size of guest host systems and on the interactions between them. Dynamics of two different guest molecules namely ethylene glycol (EG) and propylene in ZSM5 zeolite was studied in detail. EG can form hydrogen bond with the oxygen of zeolite framework unlike propylene. MD simulation studies suggested that rotational motion of propylene is almost an order of magnitude faster than the translational motion and hence two suitable spectrometers were used to separate the contribution of translational and rotational motion. Translational and rotational motion of propylene was found to follow jump diffusion and isotropic rotational diffusion respectively. However, intermediate scattering functions corresponding to the rotational motion as calculated from the trajectories of MD simulation indicated a complex and anisotropic rotational motion of the propylene molecule at short times. Orientational correlation functions indicated that propylene molecule performs librations at short times. Calculated rotational density of states and dynamic structure factor further confirmed this. It was also observed that while diffusing, propylene molecules prefer an orientation in which the long molecular axis aligns along the channel. It was found that the preferred orientation of the guest molecule inside a host zeolite is more due to the shape of host structure rather than the size of the channels whereas librational motion arises mainly due to the geometrical restriction. To investigate the effect of guest-host interaction, QENS studies on EG confined in ZSM5 have been carried out. Only rotational motion of EG was observed, as translational motion should be slow to be observable in QENS technique. Rotational motion of EG was found to follow isotropic rotation and observed rotational diffusion coefficient was found to be one order of magnitude less than propylene. This might be due to the strong attractive interaction between EG and zeolite framework as observed with PAS by investigating the freezing behaviour of the EG inside the ZSM5 zeolite.



## 8.2. FUTURE DIRECTION

The experience gained during thesis work would be useful for studying the stochastic dynamics of more complex biological systems such as vesicles, lipid membrane, proteins and so forth. In fact, QENS experiment on dynamics of cat-anionic vesicles, which undergo multi to unilamellar Transition ( $\sim 45^\circ \text{C}$ ), is scheduled to be carried out in July 2013 at IRIS spectrometer, ISIS facility, UK. The author has also recently taken up MD simulations studies on self-assembled structure in collaboration with Prof. M. Johnson at ILL, Grenoble, France. This would be helpful in planning the QENS experiments and visualization of the stochastic motions in complex systems. Some of MD simulation and QENS experiment noted below carried out since submission of the synopsis and is not a part of this thesis.

MD simulation carried out on series of cationic micelles,  $\text{C}_n\text{TAB}$  ( $n = 12, 14, 16$ ). Preliminary analysis of trajectories reveals that both global as well as internal motion of  $\text{C}_n\text{TAB}$  micelles gets hindered with increase in chain length. This is consistent with our QENS results as discussed in chapter 5 of this thesis. Detailed analysis of the trajectories can reveal more insight about the dynamics of these cationic micelles. Effect of external electrolyte on the structure of ionic micelles is well known and studied in detail using small angle scattering techniques [94,187,188]. It has been shown that addition of electrolyte enhance the growth of ionic micelles and leads to transition from spherical to rod like micelles [187,188]. Therefore, it is of interest to investigate the effect of external electrolyte on the dynamics of ionic micelles. QENS experiments have been carried out on SDS as well as CTAB micelles in presence of external electrolytes (NaCl, KBr, Sodium salicylate etc) at ISIS facilities, UK and ILL, Grenoble. In parallel, MD simulations on these ionic micelles in presence of external electrolyte are also being carried out. Question is whether the dynamics of ionic micelles is affected by addition of external electrolyte? If yes, then what is the

correlation with the microstructure of ionic micelles? All these are likely to be answered from the analysis of the experimental data and simulation trajectories.

Effect of an additional phenyl ring of the surfactant on the dynamics of anionic micelles has been studied and discussed in chapter 5. It has been shown that due to phenyl ring, dynamics of SDBS micelles gets hindered vis-à-vis SDS micelles. MD simulation has also been carried out on SDBS micelles and results are compared with the SDS micelles. It is found that both global as well as internal dynamics of SDBS micelles are slower compared to SDS micelles. This is consistent with the QENS results on both the ionic micelles. MD simulation indicates that hydration and packing of alkyl chain in the micelles are the major factors for slowing down of the internal dynamics of SDBS micelles. In SDBS molecules, phenyl ring is located near the head group. It is of interest to investigate the effect of location of the phenyl ring within the alkyl tail on the dynamics of ionic micelles. A series of isomeric ionic surfactants has been synthesized in the collaboration of Bio-organic Division (BOD) of BARC. QENS experiments on the ionic micelles based on these surfactants are scheduled in July 2013 at ILL, Grenoble.

With regard to dynamics of water in confinement, clays provide an ideal environment for the study of confined water and are of relevance to many research subjects, such as cement chemistry [189] hydrogeological and petrological processes [190] and so forth. In general, clay belongs to the phyllosilicate family comprising layer structures. The layers possess a net framework negative charge originating from the substitution of one cation for another, either in the tetrahedral or octahedral layers. This charge is compensated by adding suitable cations in the hydrated form in the interlayer spacing of the clay. QENS experiments have been carried out on water confined in various saponite clays [191,192] having different concentration of charge balancing cations. Data analysis would reveal the effect of concentration of charge balancing cation on the dynamics of water in saponite clays. Another

type of clay namely, bentonite clay exhibits high swelling capacity for water, making this suitable as a buffer material in sealants and barriers. Dynamics of water in bentonite has been also studied [193] through QENS technique. To understand the role of water molecules in the gelation of aluminium slurry, QENS experiments have been also carried out on water in the alumina slurry in the as-prepared condition and after exposing to the temperature range of 55° C where a sharp enhancement in the viscosity is observed in rheological measurements. Preliminary QENS data analysis indicated the reduction in diffusivity of water in alumina slurry exposed at 55 C *vis-a-vis* slurry prepared at room temperature [194].

It is of interest to investigate dynamical behaviour of different guest molecules confined in novel nanoporous material, metal organic framework (MOF) [195-200]. In general, MOF materials consist of metal clusters and organic linkers and can be synthesized in a modular fashion and are thus tunable. Therefore, MOFs are advantageous over the other micro-porous materials and conventional zeolites. MD simulation studies on different hydrocarbons confined in different frameworks have been carried out. For example, dynamics of acetylene in copper 1, 3, 5-benzenetricarboxylate (CuBTC) MOF has been studied [201]. Various interesting results such as increase in diffusivity with the concentration of acetylene molecules are observed which are understood by studying the evolution of the trajectories and free energy map. It will be interesting to study the dynamics of mixture of different hydrocarbons in CuBTC metal organic framework. This can be useful to use MOF as molecular sieving for separation of different hydrocarbons. Efforts are being made to study this system using MD simulation technique.

## REFERENCES

- [1] P. A. Egelstaff (Ed.), *Thermal Neutron Scattering* (London: Academic Press, 1965)
- [2] W. Marshall and S.W. Lovesey, *Theory of Thermal Neutron Scattering* (Oxford: Clarendon Press, 1971)
- [3] M. Bée, *Quasielastic Neutron Scattering* (Bristol: Adam Hilger, 1988).
- [4] R. Hempelmann, *Quasielastic Neutron Scattering and Solid State Diffusion* (Oxford: Clarendon Press, 2000)
- [5] W. G. Williams, *Polarized Neutrons* (Oxford: Clarendon Press, 1988)
- [6] S. Mitra, R. Mukhopadhyay, I. Tsukushi and S. Ikeda, *J. Phys.: Cond. Matt.* **13** (2001) 8455.
- [7] R. Mukhopadhyay, A. Sayeed, S. Mitra, A. V. Anil Kumar, Mala N. Rao, S. Yashonath and S. L. Chaplot, *Phys. Rev. E* **66** (2002) 061201.
- [8] A. Sayeed, S. Mitra, A.V. Anil Kumar, R. Mukhopadhyay, S.Yashonath, and S.L. Chaplot, *J. Phys. Chem. B* **107** (2003) 527.
- [9] S. Mitra, A. Pramanik, D. Chakrabarty, F. Jurányi, S. Gautam and R. Mukhopadhyay, *J. Phys.: Conf. Series* **92** (2007) 012167
- [10] V.K. Sharma, S. Mitra, V. Garcia Sakai, P.A. Hassan, J. Peter Embs and R.Mukhopadhyay, *Soft Matter* **8** (2012) 3151.
- [11] G.H. Vineyard, *Phys. Rev.*, **110** (1958) 999
- [12] B. A. Dassanacharya and K. R. Rao, *Phys. Rev.* **137** (1965) A417.
- [13] C.T. Chudley and R.J. Elliot, *Proc. Phys. Soc.* **77** (1961) 353.
- [14] P. A. Egelstaff, *An Introduction to the Liquid State* (London :Academic Press, 1967).
- [15] J. M. Rowe, J. J. Rush, L. A. de Graaf and G. A. Ferguson, *Phys. Rev. Lett.* **29** (1972) 1250

- [16] P.L. Hall and D.K. Ross, *Mol. Phys.* **42** (1981) 673.
- [17] K.S. Singwi and A. Sjolander, *Phys. Rev.* **119** (1960) 863.
- [18] J. Tiexiera, M.-C. Bellissent-Funel, S. H. Chen, and A. J. Dianoux, *Phys. Rev. A* **31** (1985) 1913
- [19] F. Volino and A.J. Dianoux, *Mol. Phys.* **41** (1980) 271
- [20] S. Dellerue, A. J. Petrescu, J. C. Smith, and M. C. Bellissent-Funel, *Biophysical Journal* **81** (2001) 1666.
- [21] G. Gibrat, F. L. Assairi, Y. Blouquit, C. T. Craescu, and M.-C. Bellissent-Funel, *Biophysical Journal* **95** (2008) 5247.
- [22] L. Carpentier, M. Bée, A. M. Giroud-Godquin, P. Maldivi, and J. C. Marchon, *Mol. Phys.* **68** (1989) 1367.
- [23] V.F. Sears, *Can. J. Phys.*, **44** (1966) 1999.
- [24] A.J. Dianoux, F. Volino and H. Hervet, *Mol. Phys.* **30** (1975) 1181
- [25] S.L. Chaplot, R. Mukhopadhyay, P.R. Vijayaraghavan, A.S. Deshpande, and K.R. Rao, *Pramana–J. Phys.* **33** (1989) 59
- [26] R. Mukhopadhyay, S. Mitra, S.K. Paranjpe, and B.A. Dasannacharya, *Nucl. Instrum. Methods Phys. Res. A* **474** (2001) 55.
- [27] Disk chopper time-of-flight spectrometer IN5 available at <http://www.ill.eu/instruments-support/instruments-groups/instruments/in5>
- [28] Direct geometry time-of-flight spectrometer FOCUS available at <http://spectroscopy.web.psi.ch/focus/>
- [29] IRIS-time of flight backscattering spectrometer available at <http://www.isis.stfc.ac.uk/instruments/iris/iris4691.html>
- [30] J. Perez, J. M. Zanotti, and D. Durand, *Biophysical Journal* **77** (1999) 454.
- [31] M. Freda, G. Onori, A. Paciaroni, and A. Santucci, *Phy. Rev E* **68** (2003) 021406.

- [32] M. P. Allen and D. J. Tildesley, *Computer Simulation of Liquids*, (Oxford: Clarendon Press, 1987).
- [33] L. Verlet, *Phys. Rev.* **165** (1967) 98.
- [34] C. W. Gear, Report, ANL7126 Argonne National Laboratory (1966).
- [35] E.O.Brigham, *The Fast Fourier Transform*; Prentice Hall, Englewood Cliffs (NJ) USA (1974).
- [36] D. R. Cole, E. Mamontov, G. Rother : *In Neutron Applications in Earth, Energy and Environmental Sciences*; Eds. L. Liang,. R. Rinaldi,. H. Schober: (Berlin: Springer-Verlag, 2009) Chapter 19, p.547
- [37] J. C. T. Kwak, *Polymer-Surfactant Systems* (New York: Marcel Dekkar, 1998).
- [38] C. Tanford, *The Hydrophobic Effect: Formation of Micelles and Biological Membranes* ( New York: Wiley, 1973).
- [39] B. Jönsson, B. Lindman, K. Holmberg and B. Kronberg, *Surfactants and Polymers in Aqueous Solution* (New York: John Wiley & Sons, 1998).
- [40] A.V. Zvelindovsky (Ed.), *Nanostructured Soft Matter: Experiment, Theory, Simulation and Perspectives* (London: Springer, 2007)
- [41] Y Chevalier and T Zemb, *Rep. Prog. Phys.* **53** (1990) 279
- [42] P. S. Goyal and V. K. Aswal, *Current Science* **80** (2001) 972
- [43] P. J. Bratt, D. G. Gillies, L. H. Sutcliffe, and A. J. Williamst *J. Phys. Chem.* **94** (1990) 2727
- [44] O. Söderman, G. Carlstrom, U. Olsson and T. C. Wong *J. Chem. Soc. Faraday Trans.* **84** (1988) 4475
- [45] A. Belmajdoub, K. Elbayed, J. Brondeau, D. Canet, I. Rico, and A. Lattes, *J. Phys. Chem.*) **92** (1988) 3569.

- [46] Gunjan Verma V. K. Aswal, S. K. Kulshreshtha, P. A. Hassan, and Eric W. Kaler, *Langmuir* **24** (2008) 683.
- [47] J. Appell, G. Porte, and E. Buhler *J. Phys. Chem. B* **109** (2005) 13186.
- [48] D. J. Cebula, R. H. Ottewill, J. Ralstons and P. N. Pusey *J. Chem. SOC., Faraday Trans*, **77** (1981), 2585.
- [49] J. Tabony, A. Llor, and M. Drifford, *Colloid & Polymer Sci.* **261** (1983) 938.
- [50] V. Castelletto, I. W. Hamley, Z. yang, W. Haeussler, *J. Chem. Phys.* **119** (2003) 8158.
- [51] P. Brocca, L. Cantu, F. Cavatorta, M. Corti, E. Del Favero, A. Deriu and M. Di Bari, *Physica B* **350** (2004) e619.
- [52] V. K. Sharma, Gunjan Verma, S. Gautam, P. A. Hassan, S. Mitra and R. Mukhopadhyay, *Z. Phys. Chem.* **224** (2010) 253.
- [53] V. K. Sharma, S. Mitra, G. Verma, P. A. Hassan, V. Garcia Sakai, R. Mukhopadhyay, *J. Phys. Chem. B* **114** (2010) 17049.
- [54] V. García Sakai and A. Arbe, *Current Opinion in Colloid & Interface Science* **14** (2009) 381.
- [55] M. Doxastakis, V. Garcia Sakai, S. Ohtake, J. K. Maranas and J. J. de. Pablo, *Biophysical Journal* **92** (2007) 147.
- [56] A. D. Mackerell, *J. Phys. Chem.* **99** (1995) 1846.
- [57] T. Wymore, X.F. Gao, T.C. Wong, *J. of Molecular Structure* **485–486** (1999) 195.
- [58] S. Abel, F. Sterpone, S. Bandyopadhyay, and M. Marchi, *J. Phys. Chem. B* **108** (2004) 19458.
- [59] F. Palazzesi, M. Calvaresi and Francesco Zerbetto, *Soft Matter* **7** (2011) 9148.
- [60] C. D. Bruce, M. L. Berkowitz, L. Perera and M. D. E. Forbes, *J. Phys. Chem. B.* **106** (2002) 3788.

- [61] G. F. Cata, H. C. Rojas, A. P. Gramatges, C. M. Zicovich-Wilson L. J. Alvarez and C. Searle, *Soft Matter* **7** (2011) 8508.
- [62] MODES, <http://www.isis.stfc.ac.uk/instruments/iris/data-analysis/modes-v3-user-guide-6962.pdf>.
- [63] LAMP, [http://www.ill.fr/data\\_treat/lamp/lamp.html](http://www.ill.fr/data_treat/lamp/lamp.html).
- [64] N. J. Turro and A. Yekta, *J. Am. Chem. Soc.* **100** (1978) 5951.
- [65] Croonen, Y.; Geladt, E.; Van der Ziegel, M.; Van der Auweraer, H.; Vandendriessche, F. C.; DeSchryver, F. C. *J. Phys. Chem.* **87** (1983) 1426.
- [66] B. L. Bales, L. Messina, A. Vidal and M. Peric, *J. Phys. Chem. B* **102** (1998) 10347.
- [67] M. Sammalkorpi, M. Karttunen and M. Haataja, *J. Phys. Chem. B* **111** (2007) 11722.
- [68] M. Sammalkorpi, M. Karttunen and M. Haataja, *J. Phys. Chem. B* **113** (2009) 5863.
- [69] J. C. Phillips, R. Braun, W. Wang, J. Gumbart, E. Tajkhorshid, E. Villa, C. Chipot, R. D. Skeel, L. Kale, and K. Schulten, *Journal of Computational Chemistry* **26** (2005) 1781.
- [70] CHARMM, [http://mackerell.umaryland.edu/CHARMM\\_ff\\_params.html](http://mackerell.umaryland.edu/CHARMM_ff_params.html)
- [71] W. L. Jorgensen, J. Chandrasekhar, J. D. Madura, R. W. Impey, M. L. Klein, *J. Chem. Phys.* **79** (1983) 926.
- [72] D. Frenkel and B. Smit, *Understanding Molecular Simulation From Algorithms to Applications*, (San Diego: Academic Press, 1996).
- [73] S. E. Feller, Y. Zhang, R. W. Pastor, and B. R. Brooks, *J. Chem. Phys.* **103** (1995) 4613.
- [74] R.T. Azuah, L.R. Kneller, Y. Qiu, P.L.W. Tregenna-Piggott, C.M. Brown, J.R.D. Copley, and R.M. Dimeo, *J. Res. Natl. Inst. Stan. Technol.* **114** (2009) 341.
- [75] M. V. Bockstaele, J. Gelan, H. Martens, J. Put, F-C. D. Schryver and J.C. Dederen, *Chem. Phys. Lett.* **70** (1980) 605.
- [76] D. E. Koppel, *J. Chem. Phys.* **57** (1971) 4814.
- [77] M. Bergstrom and Jan S. Pedersen *Phys. Chem. Chem. Phys.* **1** (1999) 4437



- [78] D. Bendedouch, S. H. Chen and W. C. Koehler, *J. Phys. Chem.* **87** (1983) 153.
- [79] nMoldyn, <http://dirac.cnrs-orleans.fr/plone/software/nmoldyn/>
- [80] G. Ariedi, J. Ryckaert and D. N. Theodorou, *Chem. Phys.* **292** (2003) 371.
- [81] Y. Gerelli, V. Garcia Sakai, J. Ollivier and A. Deriu, *Soft Matter* **7** (2011) 3929.
- [82] B. Aoun, V. K Sharma, S. Mitra, M. Johnson and R. Mukhopadhyay (to be submitted).
- [83] L. A. Smith, R.B. Hammond, K.J. Roberts, D. Machin, G. McLeod, *Journal of Molecular Structure* **554** (2000) 173.
- [84] S. Sundell *Acta Chem. Scandinavica* **31** (1977) 799.
- [85] M. Picquart, *J. Phys. Chem.* **90** (1986) 243
- [86] S. Mitra, V. K. Sharma, V. Garcia Sakai, J. Peter Embs and R. Mukhopadhyay, *J. Phys. Chem. B* **115** (2011) 9732.
- [87] M. Trapp, T. Gutberlet, F. Juranyi, T. Unruh, B. Demé, M. Tehei, and J. Peters, *J. Chem. Phys.* **133** (2010) 164505.
- [88] P. Berntsen, C. Svanberg and J. Swenson, *J. Phys. Chem. B* **115** (2011) 1825.
- [89] J. M. Neugebauer, *Meth. Enzymol.* **182** (1990) 239.
- [90] P. Mukerjee and K. J. Mysels, *NSRDS-NBS 36*, US. Government Printing Office, Washington, D.C. (1971).
- [91] X. Auvray, C. Petipas, R. Anthore, I. Rico and A. Lattes, *J. Phys. Chem.* **93** (1989) 7458.
- [92] V. K. Aswal and P.S. Goyal, *Chem. Phys. Lett.* **368** (2003) 59.
- [93] S. S. Berr, *J. Phys. Chem.* **91** (1987) 4760.
- [94] V. K. Aswal and P. S. Goyal, *Chem. Phys. Lett.* **357** (2002) 491. .
- [95] G. F. Cata, H. C. Rojas, A. P. Gramatges, C. M. Zicovich-Wilson L. J. Alvarez and C. Searle, *Soft Matter* **7** (2011) 8508.
- [96] Qiang Xu (Ed.), ‘*Nanoporous Materials: Synthesis and Applications*’ CRC press (2013)

- [97] V. K. Sharma, S. Mitra, G. Verma, P. A. Hassan, V. Garcia Sakai and R. Mukhopadhyay, *AIP Conf. Proc.*, **1349** (2011) 995.
- [98] J. V. Joshi, V. K. Aswal, and P. S. Goyal, *J. Macromolecular Science B* **47** (2008) 338.
- [99] Swati De, Vinod K. Aswal, and S. Ramakrishnan, *Langmuir* **26** (2010) 17882.
- [100] B. R. Priya and H. J. Byrne, *J. Phys. Chem. C* **112** (2008) 332.
- [101] M. Lotya, Y. Hernandez, P. J. King, R. J. Smith, V. Nicolosi, L. S. Karlsson, F. M. Blighe, S. De, Z. Wang, I. T. McGovern, G. S. Duesberg and J. N. Coleman, *J. Am. Chem. Soc.* **131** (2009) 3611.
- [102] X.-J. Wu and D. Xu, *J. Am. Chem. Soc.* **131** (2009) 2774.
- [103] Gerardino D'Errico, Ornella Ortona, Luigi Paduano, and Vincenzo Vitag, *J. of Colloid and Interface Science* **239** (2001) 264.
- [104] C. R. Haramagatti, “*Structure, Dynamics and Phase Behaviors of Cationic Micellar Solutions: Raman and Neutron Scattering Study of Alkyltrimethylammonium Bromides*”. Doctoral Thesis, Georg-August- Universität zu Göttingen, Göttingen, Germany, 2006
- [105] S. Kumar, Daksha Sharma, Deepti Sharma and Kabir-ud-Din *J. Surfactants and Detergents*, **9** (2006) 77.
- [106] V. K Sharma, S. Mitra, V. Garcia Sakai and R. Mukhopadhyay, *J. Phys. Chem. B* **116** (2012) 9007.
- [107] V. K. Sharma, S. Mitra, M. Johnson and R. Mukhopadhyay, *J. Phys. Chem. B* (2013) (in Press) DOI 10.1021/jp401831y
- [108] R.Kimmich, S.Stapf , A.I.Maklakov , V.D.Skirda , E.V.Khozina *Mag.Res. Im.* **14** (1996) 793
- [109] J. Texeira, J.-M. Zanotti, M.-C. Bellissent-Funel and S. H. Chen, *Physica B* **234-236** (1997) 370
- [110] M. Alborzfar, G. Jonsson, C. Grøn, *Wat. Res.* **32** (1998) 2983.

- [111] Sourirajan, T. Matsuura, *Reverse Osmosis/Ultrafiltration Process Principles National Research Council Canada, Ottawa* 1985, pp. 848–884.
- [112] C.A. Buckley, C.J. Brouckaert, C.A. Kerr, Reverse osmosis application in brackish water desalination and in the treatment of industrial effluents, in: Z. Amjad (Ed.), *Reverse Osmosis*, Van Nostrand Reinhold, New York, 1993. pp. 275–299.
- [113] T. V. Karmazina, A. A. Kavitskaya, V. I. Slisenko, A. A. Petrachkov, A. A. Vasilkevich, *Desalination*, **184** (2005) 337.
- [114] V.K. Sharma, P.S. Singh, S. Gautam, P. Maheshwari, D. Dutta and R. Mukhopadhyay, *J. Membr. Sci.* **326** (2009) 667.
- [115] V.K. Sharma, P.S. Singh, S. Gautam, S. Mitra and R. Mukhopadhyay, *Chem. Phys. Lett.* **478** (2009) 56.
- [116] V. K. Sharma, S. Mitra, Puyam Singh, Fanni Jura'ny, and R. Mukhopadhyay *Euro. Phys. Journal ST* **189** (2010) 217.
- [117] V. K. Sharma, S. Mitra and R. Mukhopadhyay (To be submitted)
- [118] R. J. Petersen, *J. Membr. Sci.* **83** (1993) 81.
- [119] V. Freger, *Langmuir* **19** (2003) 4791.
- [120] M. Ulbricht, *Polymer* **47** (2006) 2217.
- [121] J. E. Cadotte, R. S. King, R. J. Majerle and R. J. Petersen, *J. Macromol. Sci., Chem.* **A15** (1981) 727.
- [122] P. W. Morgan, *Condensation Polymers by Interfacial and Solution Methods* (New York: Interscience, 1965).
- [123] T. D. Nguyen, K. Chan, T. Matsuura, S. Sourirajan, *Ind. Eng. Chem. Prod. Res. Dev.* **23** (1984) 501.
- [124] S. J. Gregg, and K. S. W. Sing, *Adsorption, Surface Area and Porosity* (New York: Academic Press, 1982).

- [125] P.S. Singh, V. K. Aswal *J. Phys. Chem. C* **111** (2007) 16219
- [126] D. M. Schreider, Y. C. Jean, in D. M. Schreider, Y. C. Jean (Eds.) *Positron and Positronium Chemistry* (New York: Elsevier, 1988).
- [127] H. H. Yin, Y. Zejie, M. Weitao, Z. Daming, *Plasma Sci. Tech.* **7** (2005) 3062.
- [128] D. Dutta, A. Bhattacharya, B. N. Ganguly, *J. Mem. Sci.* **224** (2003) 127.
- [129] A. Shimazu, K. Ikeda, T. Miyazaki, Y. Ito, *Radiat. Phys. Chem.* **58** (2000) 555.
- [130] P.S. Singh, S.V. Joshi, C.V. Devmurari, J.J. Trivedi, A.P. Rao and P.K. Ghosh, *J. Mem. Sci.* **278** (2006) 19.
- [131] P. Kirkgaard, N. J. Pedersen and M. Eldrup, *PATFIT-88, Risø-M-2740*; Roskilde, Denmark, 1989.
- [132] S.– Y. Kwak, D. W. Ihm, *J. Mem. Sci.* **158** (1999) 143.
- [133] S. J. Tao, *J. Chem. Phys.* **56** (1972) 5499.
- [134] M. Eldrup, D. Lightbody and J. N. Sherwood, *Chem. Phys.*, **63** (1981) 51.
- [135] C.L. Li, S.H. Huang, W.S. Hung, S.T. Kao, D.M. Wang, Y.C. Jean, K.R. Lee, J.Y. Lai, *J. Memb. Sci.* **313** (2008) 68.
- [136] K. Boussu, J. De Baerdemaeker, C. Dauwe, M. Weber, K.G. Lynn, D. Depla, S. Aldea, I.F.J. Vankelecom, C. Vandecasteele, B. Van der Bruggen, *Chem. Phys. Chem* **8** (2007) 370.
- [137] S.R.V. Castrillon, N. Giovambattista, I.A. Aksay, P.G. Debenedetti, *J. Phys. Chem. B* **113** (2009) 1438.
- [138] J.C. Perrin, S. Lyonnard, F. Volino, *J. Phys. Chem. C* **111** (2007) 3393.
- [139] S. M. Yusuf, Amit kumar and J. V. Yakhmi, *Applied Phys. Lett.* **95** (2009) 182506.
- [140] A. Kumar, S.M. Yusuf and L. Keller, *Phys. Rev. B* **71** (2005) 054414.
- [141] P. Herren, P. Fischer, A. Ludi and W. Halg, *Inorg. Chem.* **19** (1980) 956.
- [142] Amit Kumar, S. M. Yusuf, L. Keller and J.V. Yakhmi, *Phys. Rev. Lett.* **101** (2008) 207206.

- [143] R. Martinez-Garcia, M. Knobel, and E. Reguera, *J. Phys. Chem. B* **110** (2006) 7296.
- [144] S. I. Ohkoshi, K. I. Arai, Y. Sato and K. Hashimoto, *Nature Mater.* **3** (2004) 857.
- [145] H. J. Buser, D. Schwarzenbach, W. Petter, A. Ludi, *Inorg. Chem.* **16** (1977) 2704.
- [146] D. Russo, J. Teixeira, L. Kneller, John R. D. Copley, J. Ollivier, S. Perticaroli, E. Pellegrini and M. A. Ganzalez, *J. Am. Chem. Soc.* **133**, (2011) 4882.
- [147] M-C Bellissent-Funel, S.H. Chen, J.-M. Zanotti, *Phys. Rev. E* **51** (1995) 4558.
- [148] W. A. Kamitakahara and N. Wada, *Phys. Rev. E* **77** (2008) 041503.
- [149] V.K. Sharma, S. Mitra, A. Kumar, S. M.Yusuf, Fanni Jurányi and R. Mukhopadhyay, *J. Phys. Cond. Mat.* **23** (2011) 446002.
- [150] V.K. Sharma, S. Mitra, N. Thakur, S. M.Yusuf, Fanni Jurányi and R. Mukhopadhyay  
(To be submitted)
- [151] G. Tomlinson, *Modern Zeolites, structure and function in detergents and petrochemicals* (Switzerland: Traw Tech Publications Ltd., 1998).
- [152] D. L. Bish and D. W. Ming, (Eds.) *Natural Zeolites: Occurrence, Properties, Applications* Reviews in Mineralogy and Geochemistry Volume 45 p 207-216.
- [153] M. D. Amiridis, T. Zhang and R.J. Farrauto, *Applied Catalysis B: Environmental*, **10** (1996) 203
- [154] H. Jobic, J. Karger and M. Bée, *Phys. Rev. Lett.*, **82** (1999) 4260.
- [155] H. Jobic and D. N. Theodorou, *Micropor. Mesopor. Mater.* **102** (2006) 21.
- [156] A.K. Tripathi, A. Sahasrabudhe, S. Mitra, R. Mukhopadhyay and N.M. Gupta *Phys. Chem. Chem. Phys.*, **3** (2001) 4449.
- [157] S. Mitra, R. Mukhopadhyay, A.K. Tripathi and N.M. Gupta, *Applied Physics A*, **74** (2002) S1308.
- [158] A. Sahasrabudhe, S. Mitra, A. K. Tripathi, R. Mukhopadhyay and N.M. Gupta, *Phys. Chem. Chem. Phys.* **5** (2003) 3066.

- [159] S. Mitra, S. Sumitra, A.M. Umarji, R. Mukhopadhyay, S. Yashonath and S. L. Chaplot, *Pramana - J. Phys.* **63** (2004) 449.
- [160] S. Mitra, Siddharth Gautam, R. Mukhopadhyay, S. Sumitra, A.M. Umarji, S. Yashonath, S.L. Chaplot, *Physica B* **385-386** (2006) 275.
- [161] S. Gautam, S. Mitra, A. Sayeed, S. Yashonath, S.L. Chaplot and R. Mukhopadhyay, *Chem. Phys. Lett.* **442** (2007) 311.
- [162] V. K. Sharma, Mala N. Rao, Siddharth Gautam, A. K. Tripathi, V. S. Kamble, S. L. Chaplot and R. Mukhopadhyay, *Pramana - J. Phys.*, **71** (2008) 1165.
- [163] Siddharth Gautam, A. K. Tripathi, V. S. Kamble, S. Mitra and R. Mukhopadhyay, *Pramana - J. Phys.*, **71** (2008) 1153.
- [164] J. Kärger, and D.M. Ruthven, *Diffusion in Zeolites and Other microporous solids* (Wiley –Interscience, New York 1992).
- [165] J. Caro, M. Bülow, W. Schiner, J. Kärger, W. Heink, H. Pfeifer and S. P. Zdanov, *J. Chem. Soc., Faraday Trans. 1*, **81** (1985) 2541.
- [166] D. Dubbeldam and R. Q. Snurr, *Molecular Simulation* **33** (2007) 305.
- [167] P. Demontis and G. B. Suffritti, *Chem. Rev.* **97** (1997) 2845.
- [168] Siddharth Gautam, S. Mitra, R. Mukhopadhyay and S.L. Chaplot, *Phys. Rev. E* **74** (2006) 041202.
- [169] Siddharth Gautam, S. Mitra, S.L. Chaplot and R. Mukhopadhyay, *Phys. Rev. E* **77** (2008) 061201.
- [170] Pradip Kr. Ghorai, Subramanian Yashonath, Pierfranco Demontis and Giuseppe B. Suffritti, *J. Am. Chem. Soc.*, **125** (2003) 7116.
- [171] V. K. Sharma, S. Gautam, S. Mitra and R. Mukhopadhyay, *Z. Phys. Chem.* **224** (2010)133.
- [172] H. van Koningsveld, H. van Bekkum and J. C. Jansen, *Acta Cryst.*, **B43** (1987) 127.

- [173] F. Leroy, B. Rousseau and A. H. Fuchs, *Phys. Chem. Chem. Phys.* **6** (2004) 775.
- [174] T. Vlugt, R. Krishna and B. Smit, *J. Phys. Chem. B* **103** (1999) 1102.
- [175] W. L. Jorgensen, J. D. Madura, and C. J. Swenson, *J. Am. Chem. Soc.* **106** (1984) 6638.
- [176] V.K. Sharma, S. Gautam, S. Mitra, Mala N. Rao, A. K. Tripathi, S. L. Chaplot and R. Mukhopadhyay, *J. Phys. Chem. B* **113** (2009) 8066
- [177] R.W. Impey, P.A. Madden, I. R. McDonald, *Mol. Phys.* **46** (1982) 513.
- [178] D. I. Kolokolov, H. Jobic and A.G. Stepanov, *J. Phys. Chem. C* **114** (2010) 2958.
- [179] Siddharth Gautam, V. K. Sharma, S. Mitra, S. L. Chaplot and R. Mukhopadhyay *Chem. Phys. Lett* **501** (2011) 345.
- [180] V. K. Sharma, S. Mitra, S.L. Chaplot and R. Mukhopadhyay *AIP Conf. Proc.*, **1313** (2010) 325.
- [181] A. Novikov, M. Rodnikova, O. Sobolev, *Physica B* **350** (2004) e363.
- [182] M. Miyahara and K. E. Gubbins, *J. Chem. Phys.* **106** (1997) 2865.
- [183] R. Radhakrishnan, K. E. Gubbins, A. Watanabe, K. Kaneko, *J. Chem. Phys.* **111** (1999) 9058.
- [184] D. Dutta, A. Sachdeva and P. K. Pujari, *Chem. Phys. Lett.* **432** (2006) 116.
- [185] P. Maheshwari, D. Dutta, S.K. Sharma, K. Sudarshan, P.K. Pujari, M. Majumder, B. Pahari, B. Bandyopadhyay, K. Ghoshray and A. Ghoshray, *J. Phys. Chem. C* **114** (2010) 4966
- [186] V. K. Sharma, S. Mitra, P. Maheshwari, D. Dutta, P. K. Pujari, and R. Mukhopadhyay, *Euro. Phys. Journal ST* **189** (2010) 273.
- [187] S. S Berr, R. R. M. Jones, *Langmuir* **4** (1988) 1247.
- [188] G. Garg, P. A Hassan, V. K Aswal and S. K. Kulshreshtha, *J. Phy. Chem. B* **109** (2005) 1340.

- [189] H. V. Damme, A. Gmira, In *Handbook of Clay Science*; Eds., F. Bergaya, B. K. G. Theng and G. Lagaly (Amsterdam: Elsevier, 2006) pp 1113.
- [190] F. K. North, *Petroleum Geology* (Boston: Unwin-Hyman, 1990)
- [191] S. A. Prabhudesai, V. K. Sharma, S. Mitra, D. Chakrabarty, M.A. Vicente, J. Peter Embs and R. Mukhopadhyay, *J. Phys. Soc. Japan* **82** (2013) SA009.
- [192] S. Mitra, S. A. Prabhudesai, D Chakraborty, V. K. Sharma, M. Vicente, J.P. Embs and R. Mukhopadhyay, *Phys. Rev. E* **87** (2013) 062317.
- [193] R. R. Dessai, V. K. Sharma, S. A. Prabhudesai, S. Mitra, J. A. E. Desa and R. Mukhopadhyay, *J. Phys. Soc. Japan* **82** (2013) SA008.
- [194] P. Biswas, S. Chaitanya, R. Johnson, S. Prabhudesai, V. K. Sharma, S. Mitra and R. Mukhopadhyay, *Open Journal of Inorganic Chemistry* **3** (2013) 48.
- [195]. A.I. Skoulidas, *J. Am. Chem. Soc.* **126**, 1356 (2004).
- [196] Q. Yang, C. Xue, C. Zhong, J.-F. Chen, *AIChE J.* **53** (2007) 2832.
- [197] Y.X. Hu, S.C. Xiang, W.W. Zhang, Z.X. Zhang, L. Wang, J.F. Bai, B.L. Chen, *Chem. Commun.* **48** (2009) 7551.
- [198] S. Amirjalayer, R. Schmid, *Micropor. Mesopor. Mater.* **125** (2009) 90.
- [199] D.C. Ford, D. Dubbeldam, R.Q. Snurr, V. Kunzel, M. Wehring, F. Stallmach, J. Karger, U. Muller, *J. Phys. Chem. Lett.* **3** (2012) 930.
- [200] P. Canepa, N. Nijem, Y. J. Chabal and T. Thonhauser, *Phys. Rev. Lett.* **110** (2013) 026102.
- [201] S. A. Prabhudesai, V. K. Sharma, S. Mitra, R. Mukhopadhyay, *Euro. Phys. J. B* **86** (2013) 145.



## LIST OF PUBLICATIONS

1. Dynamics in Anionic Micelles: Effect of Phenyl Ring  
**V. K. Sharma**, S. Mitra, M. Johnson and R. Mukhopadhyay, *J. Phys. Chem. B* 117 (2013) 6250.
2. Dynamics of Molecular Species in Confined Geometry  
**V. K. Sharma**, S. Mitra and R. Mukhopadhyay, *J. Phys. Soc. Japan* 82 (2013) SA006
3. Dynamical features in Cationic Micelles of Varied Chain Length  
**V. K. Sharma**, S. Mitra, V. Garcia Sakai and R. Mukhopadhyay, *J. Phys. Chem. B* 116 (2012) 9007.
4. The dynamical landscape in CTAB micelles  
**V. K. Sharma**, S. Mitra, V. Garcia Sakai, P.A. Hassan, J. Peter Embs and R. Mukhopadhyay, *Soft Matter* 8 (2012) 7151.
5. Understanding the dynamics of everyday-use surfactant micelles  
**V. K. Sharma**, S. Mitra, P. A. Hassan, R. Mukhopadhyay and V. Garcia Sakai, *Highlights ISIS Annual Report* (2012).
6. Diffusion of Water in Molecular Magnet  $\text{Cu}_{0.75}\text{Mn}_{0.75}[\text{Fe}(\text{CN})_6]\cdot 7\text{H}_2\text{O}$   
**V. K. Sharma**, S. Mitra, Amit Kumar, S. M. Yusuf, Fanni Juranyi and R. Mukhopadhyay, *J. Phys. Cond. Mat.* 23 (2011) 446002.
7. Molecular Mobility in Solid Sodium Dodecyl Sulphate  
S. Mitra, **V. K. Sharma**, V. Garcia Sakai, J. Peter Embs and R. Mukhopadhyay, *J. Phys. Chem. B* 115 (2011) 9732.
8. Rotational Dynamics of Propylene in ZSM-5 Zeolitic Frameworks  
Siddharth Gautam, **V. K. Sharma**, S. Mitra, S. L. Chaplot and R. Mukhopadhyay *Chem. Phys. Lett* 501 (2011) 345.

9. Internal Dynamics in SDS Micelles: Neutron Scattering Study  
**V. K. Sharma**, S. Mitra, G. Verma, P. A. Hassan, V. Garcia Sakai and  
 R. Mukhopadhyay, *J. Phys. Chem. B* 114 (2010) 17049.
10. Effect of Guest-Host interaction on the Dynamics of Ethylene Glycol in H-ZSM5 Zeolite  
**V. K. Sharma**, S. Mitra, P. Maheshwari, D. Dutta, P. K. Pujari, and  
 R. Mukhopadhyay, *Euro. Phys. Journal ST* 189 (2010) 273.
11. Diffusion of Water in Nano-porous Polyamide Membranes: Quasielastic Neutron Scattering Study  
**V. K. Sharma**, S. Mitra, Puyam Singh, Fanni Jura'ny, and R. Mukhopadhyay  
*Euro. Phys. Journal ST* 189 (2010) 217.
12. Dynamics of Propylene adsorbed in Na-Y and Na-ZSM5 Zeolites: A QENS and MD Simulation Study  
**V. K. Sharma**, S. Gautam, S. Mitra and R. Mukhopadhyay (Mini-Review)  
*Z. Phys. Chem.* 224 (2010) 133.
13. Monomer Dynamics in SDS Micellar Solution  
**V. K. Sharma**, Gunjan Verma, S. Gautam, P. A. Hassan, S. Mitra and  
 R. Mukhopadhyay, *Z. Phys. Chem.* 224 (2010) 253.
14. Dynamics of Adsorbed Hydrocarbon in Nanoporous Zeolite Framework  
**V. K. Sharma**, S. Gautam, S. Mitra, Mala N. Rao, A. K. Tripathi, S. L. Chaplot and  
 R. Mukhopadhyay, *J. Phys. Chem. B* 113(2009) 8066.
15. Dynamics of Water Sorbed in Reverse Osmosis Polyamide Membrane  
**V. K. Sharma**, P.S. Singh, S. Gautam, P. Maheshwari, D. Dutta and R.  
 Mukhopadhyay, *J. Membrane Science* 326(2009) 667.

16. Dynamics of Water in Nanofiltration Polyamide Membrane  
**V. K. Sharma**, P.S. Singh, S. Gautam, S. Mitra and R. Mukhopadhyay  
*Chem. Phys. Lett.* 478 (2009) 56.
17. Fluctuating Surfaces of Micelles: Observation and Consequences  
 B. Aoun, **V. K. Sharma**, E. Pellegrini, S. Mitra, M. Johnson and R. Mukhopadhyay  
 (Submitted)
18. Diffusion of hydrocarbon in Zeolite and Effect due to Pore Topology: Neutron Scattering and MD Simulation Studies  
 S. Mitra, **V. K. Sharma**, S.L. Chaplot and R. Mukhopadhyay  
 (Submitted)
19. Dynamics of Water in Prussian Blue and Green Compounds.  
**V. K. Sharma**, S. Mitra, S. M. Yusuf, Fanni Juranyi and R. Mukhopadhyay  
 (Manuscript under preparation)
20. Complex dynamical behaviour of SDS micelles as studied using MD simulation and QENS techniques  
 B. Aoun **V. K. Sharma**, S. Mitra, M. Johnson and R. Mukhopadhyay  
 (Manuscript under preparation)
21. Dynamics of Water in nanoporous water filtration polyamide membranes  
**V. K. Sharma**, S. Mitra and R. Mukhopadhyay  
 (Manuscript under preparation)
- 22\*. Effect of Surface Passivation in Spinel Slurry towards Hydrolysis: Neutron Scattering and Rheological Studies  
 K. Rajeswari, Papiya Biswas, Roy Johnson, S. Prabhudesai, **V. K. Sharma**, S. Mitra and R. Mukhopadhyay, *J. Disp. Sc. Tech.* (in press)

- 23\*. Diffusion of Water in Bentonite Clay  
R. R. Dessai, **V. K. Sharma**, S. A. Prabhudesai, S. Mitra, J. A. E. Desa and R. Mukhopadhyay, *J. Phys. Soc. Japan* 82 (2013) SA008.
- 24\*. Dynamics of Water Confined in Saponite Clay  
S.A. Prabhudesai, **V. K. Sharma**, S. Mitra, D. Chakrabarty, M.A. Vicente, J. Peter Embs and R. Mukhopadhyay, *J. Phys. Soc. Japan* 82 (2013) SA009.
- 25\*. Thermally Induced Gelation of Alumina Shaping- Neutron Scattering and Rheological Measurements  
P. Biswas, S. Chaitanya, R. Johnson, S. Prabhudesai, **V. K. Sharma**, S. Mitra and R. Mukhopadhyay, *Open Journal of Inorganic Chemistry* 3 (2013) 48.
- 26\*. Transport of Acetylene Adsorbed in CuBTC Metal Organic Framework  
S. A. Prabhudesai, **V. K. Sharma**, S. Mitra, R. Mukhopadhyay, *Euro. Phys. J. B* 86 (2013)145
- 27\*. Dynamics of Water in Synthetic Saponite Clays: Effect of Trivalent Ion Substitution  
S. Mitra, S. A. Prabhudesai, D Chakraborty, **V. K. Sharma**, M. Vicente, J.P. Embs and R. Mukhopadhyay, *Phys. Rev. E* 87 (2013) 062317.
- 28\*. Rotational dynamics of propylene inside Na-Y zeolite cages  
**V. K. Sharma**, Mala N Rao, Siddharth Gautam, A K Tripathi, V S Kamble, S L Chaplot and R. Mukhopadhyay, *Pramana-J. Phys.* 71 (2008) 1165.
- 29\*. Impact of rare earth magnetic moment on ordering of Ru in Sr<sub>2</sub>RuREO<sub>6</sub>(RE=Gd and Eu)  
V.P.S.Awana, Rahul Tripathi, **V. K. Sharma**, H. Kishan, E.T.-Muromachi and I.Felner, *Journal of Magnetism and Magnetic Material* 312 (2007) 290.

\*Publications not included in the thesis.